Helmholtz-Zentrum Berlin für Materialien und Energie und Institut für Physik,
Universität Potsdam

Spin textures and electron scattering in nanopatterned monolayer graphene

Dissertation
zur Erlangung des akademischen Grades
"doctor rerum naturalium" (Dr. rer. nat.)
in der Wissenschaftsdisziplin Experimentalphysik

eingereicht an der
Mathematisch-Naturwissenschaftlichen Fakultät
der Universität Potsdam

von
Maxim Krivenkov

Universität Potsdam,
11. November 2020

Hauptbetreuer: apl. Prof. Oliver Rader

Zweitbetreuer: Prof. Dr. Alexei Erko

Mentor: Dr. Andrei Varykhalov

Gutachter: Prof. Dr. Markus Donath

Gutachter: Prof. Dr. Ján Minár

https://doi.org/10.25932/publishup-48701
https://nbn-resolving.org/urn:nbn:de:kobv:517-opus4-487017

To my parents Irina and Sergei, my wife Natasha
and to my best friend Ksenia.

Acknowledgements

I would like to thank all the people who supported me during the course of this work and contributed to it.

First of all, I would like to acknowledge Prof. Oliver Rader for the opportunity to work in his group and his guidance throughout all these years.

I would like to express my sincere gratitude to my mentor Dr. Andrei Varykhalov for introducing me to the synchrotron world and for his unlimited support in all kinds of questions. His dedication to science and systematic approach were the best role model for me.

I would like to give my deepest acknowledgement to Dr. Dmitry Marchenko, with whom I had a pleasure to share many synchrotron beamtimes and to learn best practices and clever tricks in the experimental design and data analysis. Without his scientific curiosity and meticulous attention to details the last part of this work would not be possible.

I am indebted to Dr. Evangelos Golias, all the density functional theory calculations were done together with him and their results directly contributed to our theoretical understanding of the spin textures in graphene. I am thankful for his keen interest and support during the whole course of this work.

I am very thankful to Dr. Sánchez-Barriga for sharing his knowledge with me, his invaluable help and many fruitful discussions.

I am very grateful to Dr. Alexander Fedorov for all the deep scientific advice, discussions and help.

I am glad to acknowledge Dr. Emile Rienks who have always been open for discussions and ready to help.

I also express my gratitude to Dmitry Smirnov and Dr. Anna Makarova for all their support and encouragement.

I would like to thank all my colleagues at BESSY for very friendly environment throughout these years, especially fellow PhD students: Maryam Sajedi, Vladimir Voroshnin and Friedrich Freyse.

Finally, I thank all my family, especially my parents, my wife Natalia and her sister Ksenia for their patience, encouragement and support over the years.

Contents

Contents iii

List of Figures vii

Abbreviations ix

1 Introduction 1
- 1.1 Motivation 1
- 1.2 Graphene. Overview and applications 4
  - 1.2.1 Structure 5
  - 1.2.2 Electronic structure of free-standing monolayer graphene 6
  - 1.2.3 Effect of sublattice asymmetry 11
  - 1.2.4 Bychkov-Rashba and intrinsic spin-orbit interactions in graphene 11
- 1.3 Methodical background 18
  - 1.3.1 Technique of spin- and angle-resolved photoemission spectroscopy 18
    - 1.3.1.1 Three-step model of photoemission. Step one. 19
    - 1.3.1.2 Three-step model of photoemission. Step two. 22
    - 1.3.1.3 Three-step model of photoemission. Step three. 24
    - 1.3.1.4 Many-body interactions. 25
    - 1.3.1.5 ARPES spectrometer. 27
    - 1.3.1.6 Spin-resolved ARPES. 31
  - 1.3.2 Technique of scanning tunneling microscopy 34
  - 1.3.3 Technique of low energy electron diffraction 38
  - 1.3.4 Graphene preparation 41
  - 1.3.5 Moiré patterns 43
  - 1.3.6 Density functional theory 45
- 1.4 Experimental aspects 46
  - 1.4.1 UHV 46
  - 1.4.2 ARPES 47
  - 1.4.3 STM 48
  - 1.4.4 Software used for data analysis 48

2 Giant Rashba effect in graphene intercalated with gold nanoclusters 49
- 2.1 Introduction . . . 50
- 2.2 Historical overview . . . 51
- 2.3 Experimental details . . . 52
  - 2.3.1 Sample preparation and experimental details . . . 54
    - 2.3.1.1 Sample preparation procedure . . . 54
    - 2.3.1.2 Details of DFT calculations . . . 55
- 2.4 Results and discussion . . . 55
  - 2.4.1 Structure of the graphene/Au/Ni(111) interface . . . 55
    - 2.4.1.1 Phase I. Continuous monolayer of intercalated Au with triangular pattern . . . 56
    - 2.4.1.2 Phase II. Ordered arrays of intercalated Au nanoclusters 60
  - 2.4.2 DFT modelling of the cluster structures . . . 65
    - 2.4.2.1 Au_1 relaxed structures . . . 66
    - 2.4.2.2 Au_1 band structure calculations . . . 67
    - 2.4.2.3 Au_3 relaxed structures . . . 69
  - 2.4.3 Origin of the giant Rashba-effect . . . 70
- 2.5 Summary of conclusions . . . 72

3 Origin of the band gap in Bi-intercalated graphene on Ir(111) 73
- 3.1 Introduction . . . 73
  - 3.1.1 ARPES intensity distribution in the Dirac cone of graphene . . . 74
  - 3.1.2 Overview of Gr/Ir(111) and Gr/Bi interfaces . . . 78
- 3.2 Experimental details . . . 81
- 3.3 Experimental results and discussion . . . 83
  - 3.3.1 Preparation and core-level spectroscopy . . . 83
  - 3.3.2 Preparation and characterization by LEED and ARPES . . . 85
  - 3.3.3 Dependence on Bi concentration . . . 87
  - 3.3.4 Structural study with STM . . . 90
    - 3.3.4.1 Comparison of Gr/Bi/Ir(111) and Gr/Ir(111) . . . 90
    - 3.3.4.2 Standing waves of electronic density due to scattering on defects . . . 92
    - 3.3.4.3 Multilayer intercalation . . . 93
    - 3.3.4.4 Local observation of $(\sqrt{3} \times \sqrt{3})\ R30^\circ$ structure . . . 93
- 3.4 Origin of the band gap in Gr/Bi/Ir(111) . . . 95
  - 3.4.1 Spin-resolved ARPES results . . . 95
  - 3.4.2 Corrugation effects and local rehybridization . . . 97
  - 3.4.3 Hybridization with substrate states . . . 98
  - 3.4.4 Sublattice asymmetry . . . 99
- 3.5 Summary of conclusions . . . 102

4 Electronic scattering resonances in photoemission from monolayer graphene 103
4.1 Introduction . . . 103
  4.1.1 Surface states and surface related effects in ARPES . . . 104
  4.1.2 Electronic surface scattering resonances . . . 105
  4.1.3 Historical overview . . . 107
4.2 General theoretical picture of surface scattering resonances . . . 109
  4.2.1 Two-layer scattering model . . . 109
    4.2.1.1 How does it apply to ARPES? . . . 113
  4.2.2 Phase accumulation (interference) model . . . 114
    4.2.2.1 Phase shift due to underbarrier scattering . . . 114
    4.2.2.2 Possible origins of deviations from interference model . 119
4.3 Experimental details . . . 122
4.4 Results and discussion . . . 123
  4.4.1 Occurrence and general properties of scattering resonances in ARPES 123
  4.4.2 Crossing positions and the effect of doping . . . 127
  4.4.3 Controlling the resonances . . . 131
    4.4.3.1 Corrugation enhancement . . . 132
    4.4.3.2 Hydrogenation . . . 134
4.5 Summary of conclusions . . . 138

Bibliography 139

Publications related to this thesis 167

Other publications 167

Summary 170

Zusammenfassung 172

This page was intentionally left empty.

List of Figures

1.1 Graphene lattice, unit cell and Brillouin zone 6
1.2 Plot of tight binding graphene band structure 9
1.3 Rashba-type SOI in typical semiconductors and graphene 14
1.4 Combined effect of Rashba and intrinsic SOI on the Dirac cone 16
1.5 Scheme of electron photoemission spectroscopic measurements 23
1.6 Inelastic mean free path of electrons of different energy in solids 24
1.7 ARPES setup and hemispherical deflection analyzer working principle . 29
1.8 Schematic representation of Mott scattering 33
1.9 Tunneling between sample and tip in the STM experiment 35
1.10 STM working principle and modes of operation 37
1.11 Schematic representation of LEED setup and its working principle . . . 40
1.12 Scheme of graphene preparation by CVD process 42
1.13 Formation of moiré patterns 44

2.1 Dependence of Rashba Δ_{SO} in Gr/Au/Ni(111) on Gr-Au separation . . 53
2.2 Comparison of two types of Ni(111) substrate 54
2.3 LEED of Gr/Au/Ni(111) 56
2.4 Triangular pattern in Gr/Ni(111) intercalated with Au 57
2.5 A hardball structural model of the triangular pattern in Au/Ni(111) . . 58
2.6 STM of Gr/Au/Ni(111) for submonolayer Au coverages 60
2.7 STM observation of arrays of intercalated clusters 61
2.8 Au nanocluster structure in Gr/Au/Ni(111) on a thin film Ni substrate . 64
2.9 Estimation of surface area occupied by clusters 65
2.10 DFT modelling of graphene supported by Au nanoclusters (structure) . 66
2.11 DFT modelling of graphene supported by Au nanoclusters (band structure) 68
2.12 Backfolding in Brillouin zones of $(k \times k)$ hexagonal supercells 68

3.1 ARPES intensity distribution in the Dirac cone of graphene 74
3.2 PES intensity modulation due to the interference effect 77
3.3 Large scale constant energy surfaces for π and π^* bands 78
3.4 PES intensity distribution in graphene with broken sublattice symmetry 79

3.5 Replica cones and mini-BZs of Gr/Ir(111) in ARPES mapping. 80
3.6 Schematic sample preparation procedure for Gr/Bi/Ir(111) 82
3.7 Core-level spectroscopy study of Bi intercalation process 84
3.8 Comparison of Gr/Ir(111) and Gr/Bi/Ir(111) by LEED and ARPES . . 86
3.9 Evolution of Gr/Bi/Ir(111) ARPES spectra with Bi concentration. . . . 88
3.10 STM characterization and comparison of Gr/Ir(111) and Gr/Bi/Ir(111). 91
3.11 Intercalation site of Bi with multilayer thickness. 93
3.12 Local observation of low-density Bi phase 94
3.13 Spin-resolved PES of the Dirac cone in Gr/Bi/Ir(111) 97
3.14 Photoelectron interference effects in Gr/Bi/Ir(111) 100

4.1 Surface potential and types of surface related states 105
4.2 Basic principle of interference model of ScR 106
4.3 Example of surface scattering resonances in ARPES 107
4.4 Electron reflection and emission pathways in a two-layer model 110
4.5 Rydberg series of scattering resonance states 112
4.6 Photoemission thresholds in extended zone scheme 115
4.7 Fine-structure thresholds for a hexagonal lattice 115
4.8 Modeling of ScR in phase accumulation framework 117
4.9 Sketch of realistic surface potential compared to image potential 118
4.10 Low kinetic energy spectral features far from normal emission 120
4.11 Geometry of ARPES experiment 122
4.12 Observation of scattering resonances at different photon energies 124
4.13 Full photoemission mapping of ScR 125
4.14 Scattering resonances overlapping with valence bands 127
4.15 Extra crossings and energy shifts in ScR 128
4.16 Correlation between the ScR crossings and shift of the Dirac point . . . 129
4.17 The effect of the substrate on ScR and DC in graphene 130
4.18 Effect of rehybridization by Ir nanoclusters on ScR in Gr/Ir(111) 133
4.19 Influence of hydrogenation on ScR in Gr/Ir(111) 135
4.20 Dirac cone dispersion in Gr/Ir(111) after hydrogenation 135
4.21 STM characterization of hydrogenated Gr/Ir(111) 136

Abbreviations

Common abbreviations

2D, 3D	two-dimensional, three-dimensional
BZ	Brillouin zone
CES	constant energy surface
DC	Dirac cone
DOS	density of states
F(H)WHM	full (half) width at half maximum
fcc	face-centered cubic (lattice)
FT	Fourier transform
hcp	hexagonal close packed (lattice)
IPS	image potential state
LDOS	local density of states
ML	monolayer
ScR	scattering resonances
SOI	spin-orbit interaction
SPB	surface potential barrier
UHV	ultra-high vacuum
E_F	Fermi level

Methods

(V)LEED	(very) low energy electron diffraction
ARPES	angle resolved photoemission spectroscopy
CVD	chemical vapor deposition
DFT	density functional theory
ESCA	electron spectroscopy for chemical analysis
LDA	local density approximation
LEEPS	low energy electron point source
PEEM	photoemission electron microscopy
PES	photoelectron spectroscopy

SPELEEM	spectroscopic photoemission low energy electron microscopy
STM	scanning tunneling microscopy
TB	tight binding
XPS	x-ray photoelectron spectroscopy

Symbols, units, definitions

$\hbar$	reduced Planck constant	1.055×10^{-34} J · s
c	speed of light in vacuum	2.998×10^{10} cm/s
k_B	Boltzmann constant	8.617×10^{-5} eV/K
m_e	electron rest mass	9.109×10^{-31} kg
Å	angstrom	10^{-10} m
eV	electron volt	1.602×10^{-19} J

Chapter 1

Introduction

1.1 Motivation

Graphene, a two-dimensional crystal formed by carbon atoms residing in a honeycomb lattice, is a truly unique material. Despite its very simple structure, the science around graphene covers a range of physical phenomena spanning from half-integer quantum Hall effect to solid-state analogues of effects in relativistic physics. The history of graphene is full of surprising discoveries, starting from its first isolation by Novoselov and Geim in 2004 [1], despite the theory predicted that such 2D crystals *could not exist* being thermodynamically unstable.

In the following years it was found that graphene has a rich and unexpected physics. Its band structure is hosting a feature with linear energy dispersion relation – the Dirac cone, that became a topic of thousands of research papers. First of all, the Dirac cone provides a deep link between the low-energy quasiparticle excitations in graphene with massless relativistic particles, but at the same time it is responsible for the unique and practically important electronic properties of graphene, such as extremely high electron mobility at room temperature (exceeding 1.4×10^5 cm^2/(V·s) [2]). One can say without much exaggeration that a separate branch of physics has sprouted from studying the complex physics of this "simple" material. Chapter 1 of the current thesis is dedicated to introduce to the reader the basics of graphene physics, especially the aspects important for the further discussion, and the experimental methods used in this work.

After more than a decade of intense research the properties of free-standing graphene have been studied rather well, but there is still a great interest in the ways how they can be controlled and modified. This is not only of a fundamental interest, but also important for the use of graphene in certain applications, for example, in *spintronic* devices. Spintronics is a perspective field of electronics that exploits the electron spin degree of freedom in addition to its charge. In a free-standing graphene electrons can travel long distances (on the micron scale) without changing the projection of their spin, thus graphene can act as a perfect conductor of spin-polarized currents. What is more important, there is a possibility to realize *manipulation* of spin currents on the basis of graphene as well. The devices like Datta-Das spin-transistor [3] exploit the rotation of electron's spin in the areas with finite spin-orbit interaction (SOI). To realize this type of device in graphene, areas with enhanced SOI has to be created, since carbon has a negligible strength of SOI. This can be done by bringing graphene into contact with specific substrates, such as heavy transition metals. Particularly interesting system of this kind is graphene on Ni(111) substrate, intercalated by gold. In this system graphene was shown to be quasi-free-standing and at the same time to exhibit a large Rashba-type spin-splitting of the Dirac cone [4]. The large Rashba-SOI induced in graphene was attributed to the electronic hybridization between the out-of-plane p_z orbitals of graphene and 5d orbitals of Au. Surprisingly, the strength of this effect was an order of magnitude higher than the theoretical prediction. Details of the mechanism leading to such strong splitting were not completely clear and Chapter 2 is focused on the investigation of possible *structural* origins of this effect.

However, even more tempting would be to find a way to introduce another type of spin-dependent term in the graphene Hamiltonian – so-called "intrinsic SOI" [5], which, in contrast to Rashba-term, should lead to opening of gaps of opposite signs in the band structure of graphene and realize a long-sought quantum spin Hall phase in graphene [5]. This effect should manifest itself in the presence of robust one-dimensional spin-polarized electronic states at the edge of the graphene sheet.

One of the suggested ways to induce an *intrinsic* SOI is by bringing graphene into contact with heavy post-transition metals [6]. In this case lack of d-states additionally excludes the $\pi - d$ hybridization scenario that plays a major role for the strong induced *Rashba*-SOI. The heavy *sp*-metal Bi is one of the least explored possibilities for creating such an interface to graphene. In Chapter 3 we present an extensive study of graphene on Ir(111) substrate intercalated by Bi. Our results reveal an unreported structural phase which is characterized by a remarkable, nearly ideal graphene band structure manifesting a suppressed interaction with the underlying substrate. The focus of the study is on the minor band gap at the Dirac point and investigation of its origin.

Graphene is not only an important and interesting object of study on its own, but it can also be used as a great test model to study very general surface science phenomena. The reason is that it is well studied, has a simple structure, easy to handle (stable, inert) and at the same time it is very versatile – there are many ways how the parameters of graphene can be gradually modified in the experiment: by selection of substrate, intercalation, decoration with atoms or clusters, by nanopatterning and so on.

In the Chapter 4 we use graphene to study in detail the effect of *surface scattering resonances* – trapping of electrons in the quasi-bound states under the surface potential barrier. This topic is not only of fundamental interest – better understanding of this process will allow to extract important information about the shape of the surface potential barrier and the structure of the surface layer.

Moreover, this effect is important from the instrumental point of view. One of the main experimental methods used in the current thesis is angle-resolved photoemission spectroscopy (ARPES), a very powerful technique that provides rich information about the band structure of the sample. However, a detailed analysis and interpretation of the experimental data can sometimes be challenging. In particular, some spectral features are not directly related to the band structure and their appearance can be confusing for the experimentalist. The phenomenon of surface scattering resonances is one of the lesser known sources of such features, it manifests itself in the ARPES spectra as sharp lines of reduced or enhanced photoemission intensity. Such modulation of intensity in the spectrum means that in certain directions the number of electrons travelling with certain kinetic energy is strongly suppressed and this effect can find application in the optoelectronic devices.

1.2 Graphene. Overview and applications

Graphene is a two-dimensional (2D) crystal formed by carbon atoms arranged in a honeycomb lattice. Carbon appears in this form naturally in every single sheet of the layered graphite structure. Theoretical calculations for a single layer of graphite predicted the unusual linear "massless" and gapless energy dispersion in the band structure already in 1947 [7]. However, for a long time it was considered that a strictly 2D isolated single layer of graphite is thermodynamically unstable, as well as any other one- or two-dimensional crystals [8–10]. Only in 2004 it was proved that despite this theoretical restriction, atomically thick crystals can exist[*]. First Novoselov et al. reported isolation of stable few-layer graphite flakes by mechanical exfoliation [1] then followed the exfoliation of a *single* layer free-standing graphene[†]and a study of its electronic properties [12, 13] that revealed a list of very unusual transport phenomena, proving the theoretical predictions for 2D massless fermions. These studies opened the door to completely new interesting physics available in the labs all around the world. For these groundbreaking experiments Andre Geim and Konstantin Novoselov were awarded the Nobel Prize in Physics in 2010.

Not only the electronic, but also mechanical properties of graphene are exceptional owing to the strong covalent σ-bonds realizing the in-plane connection between the carbon atoms. With astonishing tensile strength of 130 GPa and Young modulus of 1.0 TPa [15] graphene appears to be the strongest material ever measured, even though it is only one atom thick.

Moreover, graphene has extremely high thermal conductivity, it can be used to make atomically thin membranes and it is nearly transparent for electromagnetic waves from visible to near infrared range — one layer adsorbs only $\approx \pi\alpha = 2.3\%$ of incident radiation (α is the fine structure constant) [16, 17]. In combination with conductive properties such low opacity paves the way for use of graphene in transparent electronics.[‡]

All of these unique properties of graphene are investigated by scientists and engineers to test if they can provide advances in a wide range of applications, such as supercapacitors, water deionization, solar cells, photodetectors, flexible electronics, touch screens, chemical sensors, DNA sequencing and spintronics.

The focus of this thesis is on the fundamental properties of the electronic band structure of graphene. In the next section we will discuss in detail the structure of graphene and the origin of its fascinating electronic properties.

---

[*] The apparent contradiction is usually explained by the fact that the 2D crystallite exists in a metastable condition: its structure was formed as a 3D crystal and thermal fluctuations cannot create crystalline defects due to the strong interatomic bonds of graphene. Another point to consider is the rippled surface of the real-life graphene that makes it not strictly 2D and also helps to suppress the thermal vibrations that are very large for 2D systems [11].

[†] Graphene is not unique in this case, almost at the same time the same authors reported a list of other 2D materials, prepared by similar technique, including single layers of boron nitride, several dichalcogenides, and complex oxides [14].

[‡] At the same time, 2.3% is enough to make a single layer of graphene visually distinguishable in the *optical* microscope.

1.2.1 Structure

Carbon, the building block of graphene, is the 6th element of the periodic table, therefore, its atom has 6 electrons and it has the ground state electron configuration $1s^2 2s^2 2p^2$, i.e. the inner shell 1s is filled (it is localized close to the nucleus and thus can be neglected in the discussion of chemical reactions) and 4 electrons occupy the outer shell of 2s and 2p orbitals. Because the 2p orbitals ($2p_x$, $2p_y$, and $2p_z$) are 4 electronvolts (eV) higher in energy than the 2s orbital, it is energetically favourable to put 2 electrons in the 2s orbital and only 2 of them in the 2p orbitals. However, in some cases of bonding to other atoms it may become favourable to excite one electron from the 2s to the third 2p orbital, in order to form covalent bonds, since the energy gain may be larger than the 4 eV needed for the electronic excitation. In this excited state of the carbon atom there are four orbitals with unpaired electrons, namely, $2s$, $2p_x$, $2p_y$, and $2p_z$. A quantum-mechanical superposition of the state $2s$ with n $2p_i$ states is called sp^n hybridization (n=1,2,3) and it is essential for the formation of covalent bonds with carbon.

In the case of sp^1 hybridization the two sp-hybridized orbitals have club shape and are oriented in the opposite directions, such hybridization is involved for example in the formation of the strong covalent σ bond in acetylene.

As for sp^2 hybridization, the three hybrid orbitals are oriented in the same plane with 120° angles between them and the remaining p-orbital is oriented perpendicular to this plane. This is the hybridization type responsible for planar structures and it is present for example in benzene rings, graphite and graphene.

The remaining possibility is sp^3 hybridization when all three 2p orbitals are in a superposition with 2s. This leads to a set of four club-shaped orbitals oriented in the vertexes of a tetrahedron with equal angles between them ≈109.5°. This kind of hybridization is present in methane and diamond, and it is one of the reasons why diamond is one of the hardest materials — all its bonds are strong covalent σ bonds.

As it was stated above, graphene is formed by sp^2 hybridized carbon atoms arranged in a planar honeycomb lattice.* The unit cell of this lattice [see Fig. 1.1, left] contains two atomic sites, A and B. This lattice can be imagined as two interpenetrating triangular sublattices, each composed of sites of only one sort (A or B). The unit lattice vectors are $\vec{\mathbf{a}}_1$ and $\vec{\mathbf{a}}_2$, their length is $a = |\vec{\mathbf{a}}_1| = |\vec{\mathbf{a}}_2| = 1.42 \times \sqrt{3} = 2.46$ (Å), where 1.42 Å is the nearest neighbor distance in graphene (b). The reciprocal lattice vectors [Fig. 1.1, right] have magnitude $\frac{4\pi}{\sqrt{3}a}$ and the first Brillouin zone (BZ) is a hexagon with distances $\Gamma\mathrm{M} = \frac{2\pi}{\sqrt{3}a} \approx 1.47$ Å^{-1} and $\Gamma\mathrm{K} = \frac{4\pi}{3a} \approx 1.70$ Å^{-1}.

---

[*] The honeycomb atomic structure and long-range crystalline order of the free-standing graphene were confirmed in early transmission electron microscopy (TEM) experiments [18].

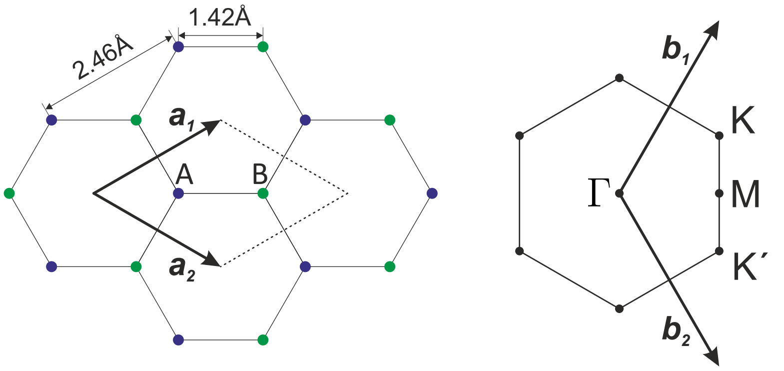

Figure 1.1: Graphene honeycomb lattice and its Brillouin zone. Left: lattice structure and unit cell of graphene containing two atoms (A and B) in the unit cell ($\vec{\mathbf{a}}_1$ and $\vec{\mathbf{a}}_2$ are the lattice unit vectors). Blue and green green circles mark A and B sublattice sites, respectively. Right: corresponding Brillouin zone with reciprocal unit vectors $\vec{\mathbf{b}}_1$ and $\vec{\mathbf{b}}_2$. The Dirac cones are located at the K and K' points.

1.2.2 Electronic structure of free-standing monolayer graphene

In the following we will be mostly interested in the band-structure of graphene supported by different substrates. First of all it is essential to take a look at the electronic structure of free-standing graphene, which is rather simple and can be well described using a tight-binding Hamiltonian, leading to analytical solutions for the electronic eigenstates and energy dispersion. The first to derive this band structure was Wallace [7], already in 1947 he performed analytical calculations for a graphite monolayer and showed its unusual dispersion relation.

To describe the electronic structure one can first note that there are four valence electrons in carbon atoms in graphene, three of them occupy the $2s$, $2p_x$ and $2p_y$ orbitals, which hybridize (sp^2 hybridization) and form in-plane σ^* (antibonding or unoccupied) and σ (bonding or occupied) orbitals, responsible for tight in-plane bonding with neighboring carbon atoms. The remaining fourth electron in the $2p_z$ state makes up the π-bond with its symmetry axis oriented perpendicular to the graphene plane.

The unit cell of the honeycomb graphene lattice contains 2 atoms, A and B. The electronic wave functions of A and B atoms overlap and lateral interaction between p_z orbitals creates delocalized bonding π and antibonding π^* orbitals. At the same time, the overlap between the π and σ orbitals is strictly zero by symmetry. Thus, the π bands in graphene can be treated independently from the other valence electrons.

The σ bands can be completely neglected since their energies fall too far away from the Fermi level. Only the remaining one conduction electron in the $2p_z$ state is thus needed to describe the low-energy electronic properties of graphene in the first approximation [19].

Let us now calculate the energy dispersion of the $2p_z$ state using the tight binding approximation and following Wallace [7]. We will label the normalized $2p_z$ orbital wave function for an isolated atom as $X(\vec{\mathbf{r}})$, then the electronic wave function can be constructed as the following linear combination of Bloch functions:

$$\psi = c_1\phi_1 + c_2\phi_2 \tag{1.1}$$

where

$$\begin{cases} \phi_1 & = \sum_A e^{i(\vec{\mathbf{k}}\vec{\mathbf{r}}_A)} X(\vec{\mathbf{r}} - \vec{\mathbf{r}}_A), \\ \phi_2 & = \sum_B e^{i(\vec{\mathbf{k}}\vec{\mathbf{r}}_B)} X(\vec{\mathbf{r}} - \vec{\mathbf{r}}_B). \end{cases} \tag{1.2}$$

The two sums are taken over all A or B sites, respectively (N sites of each type). The coefficients c_1 and c_2 should realize the minimum energy of the system $E(c_1, c_2)$. To minimize this function with respect to coefficients, we first substitute wave function in the stationary Schrödinger equation as in Eq. (1.1) (we switch to bra–ket notation from now on for brevity):

$$\begin{gathered} H\left|\psi\right\rangle = E\left|\psi\right\rangle, \\ \left\langle\psi\right| H \left|\psi\right\rangle = \left\langle\psi|E|\psi\right\rangle, \\ \left\langle c_1\phi_1 + c_2\phi_2\right| H \left|c_1\phi_1 + c_2\phi_2\right\rangle = \left\langle c_1\phi_1 + c_2\phi_2\right| E \left|c_1\phi_1 + c_2\phi_2\right\rangle. \end{gathered} \tag{1.3}$$

H denotes Hamiltonian of the system. Applying the variational principle to the last equation we take partial derivatives over the coefficients, that results in a following system of secular equations:

$$\begin{cases} c_1\left\langle\phi_1|H|\phi_1\right\rangle + c_2\left\langle\phi_1|H|\phi_2\right\rangle & = c_1E\left\langle\phi_1|\phi_1\right\rangle + c_2E\left\langle\phi_1|\phi_2\right\rangle, \\ c_1\left\langle\phi_2|H|\phi_1\right\rangle + c_2\left\langle\phi_2|H|\phi_2\right\rangle & = c_1E\left\langle\phi_2|\phi_1\right\rangle + c_2E\left\langle\phi_2|\phi_2\right\rangle \end{cases} \tag{1.4}$$

or,

$$\begin{cases} c_1H_{11} + c_2H_{12} & = c_1ES + c_2E\left\langle\phi_1|\phi_2\right\rangle, \\ c_1H_{21} + c_2H_{22} & = c_1E\left\langle\phi_2|\phi_1\right\rangle + c_2ES \end{cases} \tag{1.5}$$

where

$$\begin{gathered} H_{11} = \left\langle\phi_1|H|\phi_1\right\rangle, \quad H_{12} = H_{21}^* = \left\langle\phi_1|H|\phi_2\right\rangle, \quad H_{22} = \left\langle\phi_2|H|\phi_2\right\rangle \\ \text{and} \quad S = \left\langle\phi_1|\phi_1\right\rangle = \left\langle\phi_2|\phi_2\right\rangle. \end{gathered} \tag{1.6}$$

By neglecting in Eq. (1.5) the overlap between p_z wave functions located on different sites ($\left\langle\phi_1|\phi_2\right\rangle = \left\langle\phi_2|\phi_1\right\rangle = 0$) we can simplify the system even further (neglect of overlap integrals defines the so-called orthogonal tight-binding schemes) and we end up with the secular equations determinant

$$\begin{vmatrix} H_{11} - ES & H_{12} \\ H_{21} & H_{22} - ES \end{vmatrix} = 0 \tag{1.7}$$

Solving Eq. (1.7) we obtain the energy dispersion relation in terms of matrix elements:

$$E = \frac{1}{2S}(H_{11} + H_{22} \pm \sqrt{(H_{11} - H_{22})^2 + 4|H_{12}|^2}) \tag{1.8}$$

From A-B sublattice symmetry it follows that $H_{11} = H_{22}$, moreover

$$S = \sum_{1}^{N} \langle \phi_1 | \phi_1 \rangle = N \tag{1.9}$$

then (1.8) simplifies as

$$E = \frac{1}{N}(H_{11} \pm |H_{12}|). \tag{1.10}$$

Now one has to calculate matrix elements H_{11} and H_{12}.

$$H_{11} = \sum_{A,A'} \exp\Big(-i\vec{\mathbf{k}}(\vec{\mathbf{r}}_A - \vec{\mathbf{r}}_{A'})\Big) \int X^*(\vec{\mathbf{r}} - \vec{\mathbf{r}}_A) H X(\vec{\mathbf{r}} - \vec{\mathbf{r}}_{A'})\, \mathrm{d}\tau \tag{1.11}$$

$$H_{12} = \sum_{A,B} \exp\Big(-i\vec{\mathbf{k}}(\vec{\mathbf{r}}_A - \vec{\mathbf{r}}_B)\Big) \int X^*(\vec{\mathbf{r}} - \vec{\mathbf{r}}_A) H X(\vec{\mathbf{r}} - \vec{\mathbf{r}}_B)\, \mathrm{d}\tau \tag{1.12}$$

If we limit our calculation only to nearest and next-nearest neighbors (A-B for H_{12} and A-A for H_{11}), we get

$$\frac{H_{11}}{N} = E_0 - 2\gamma_0'\Big(\cos(k_y a) + 2\cos\Big(k_x\sqrt{3}a/2\Big)\cos(k_y a/2)\Big), \tag{1.13}$$

$$\frac{H_{12}}{N} = -\gamma_0\left(\exp\left(-ik_x\frac{a}{\sqrt{3}}\right) + 2\cos(k_y a/2)\exp\left(ik_x\frac{a}{2\sqrt{3}}\right)\right), \tag{1.14}$$

where

$$E_0 = \int X^*(\vec{\mathbf{r}}) H X(\vec{\mathbf{r}})\, \mathrm{d}\tau\,; \tag{1.15}$$

$$\gamma_0 = -\int X^*(\vec{\mathbf{r}} - \vec{\rho}_{AB}) H X(\vec{\mathbf{r}})\, \mathrm{d}\tau\,; \quad \gamma_0' = -\int X^*(\vec{\mathbf{r}} - \vec{\rho}_{AA'}) H X(\vec{\mathbf{r}})\, \mathrm{d}\tau \tag{1.16}$$

E_0 is the energy of $2p_z$ electron in carbon, γ_0 and γ_0' are called transfer or hopping integrals. The vectors $\vec{\rho}_{AB}$ and $\vec{\rho}_{AA}$ are joining nearest neighbors (of different type) and next-nearest neighbors (same type), respectively. Here we made use of the fact that the atomic p_z orbitals have rotational symmetry.

Having calculated the matrix elements and after some simple arithmetic we can finally provide the analytical result for the dispersion of the bands (π and π^* for $-$ and $+$ sign, respectively):

$$\begin{aligned} E_\pm(\vec{\mathbf{k}}) &= E_0 \pm \gamma_0\sqrt{3 + f(\vec{\mathbf{k}})} - \gamma_0' f(\vec{\mathbf{k}}), \\ f(\vec{\mathbf{k}}) &= 2\cos(k_y a) + 4\cos\Big(k_x\sqrt{3}a/2\Big)\cos(k_y a/2) \end{aligned} \tag{1.17}$$

The values of γ_0 and γ_0' can be estimated by fitting the results of experiments or *ab initio* calculations. This gives $-3\,\mathrm{eV} \lesssim \gamma_0 \lesssim -2.5\,\mathrm{eV}$ and $0.02\gamma_0 \lesssim \gamma_0' \lesssim 0.2\gamma_0$ [20]. Typically value $\gamma_0 = -2.7\,\mathrm{eV}$ is used.

Two calculated band structures with different values of γ_0, γ_0' of (1.17) are shown in Fig. 1.2. First case [$\gamma_0 = -3.0$ eV, $\gamma_0' = 0.2\gamma_0$, Fig. 1.2 (a)] shows the effect of large next-nearest hopping energy γ_0': the electron-hole symmetry is broken and the π and π^* bands become asymmetric, while in the second case [$\gamma_0 = -2.7$ eV, $\gamma_0' = 0.02\gamma_0$, Fig. 1.2 (b)] the band structure is almost symmetric.

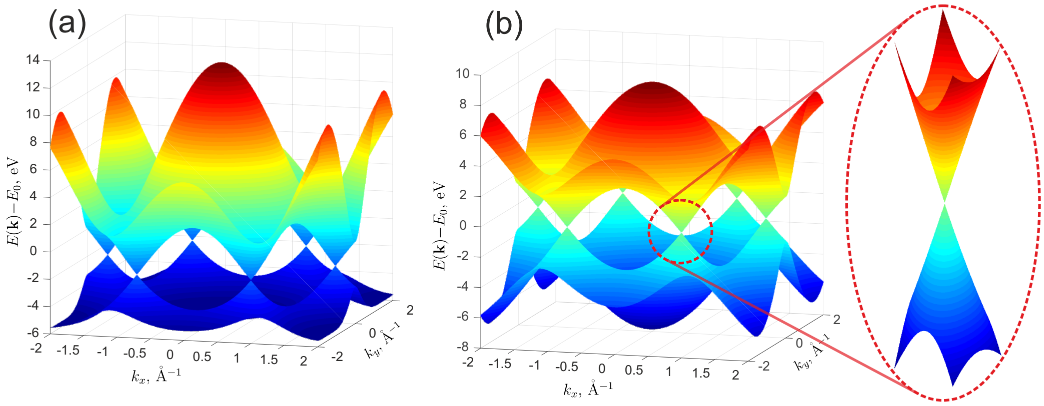

Figure 1.2: Plot of tight binding graphene band structure in nearest-neighbors approximation with a) γ_0 = -3.0 eV, $\gamma_0' = 0.2\gamma_0$, b) γ_0 = -2.7 eV, $\gamma_0' = 0.02\gamma_0$. Zoomed in part displays region around the Dirac point with conical dispersion.

One can immediately see that the two resulting bands are touching at the corners of the BZ and have conical shape around the meeting points, which are called Dirac points for reasons that will be explained below, and this massless feature in the band structure is called a Dirac cone (DC). Another interesting feature of this band structure is the saddle point located in the middle of the BZ edge (M point). The saddle points have to appear in periodic functions for purely mathematical reasons, but in two dimensional systems they are of interest since they lead to a logarithmic divergence in the electronic density of states (DOS), known as Van Hove singularity [21].

As there are two atoms per unit cell, which contribute one p_z electron each, the lower π band is completely filled while the upper π^* band is empty, thus the Fermi level (E_F) in free-standing graphene is located exactly at the touching points of two bands.

Low-energy excitations determine the response of a system to external probes. In the case of graphene we can expand the full band structure (1.17) in the vicinity of the K point of the BZ, using $\vec{\mathbf{k}} = \vec{\mathbf{K}} + \vec{\mathbf{q}}$, where $\vec{\mathbf{K}}$ is the momentum corresponding to the K or K′ point and $|\vec{\mathbf{q}}| \ll |\vec{\mathbf{K}}|$. Then, neglecting the γ_0' contribution, the dispersion of low-energy quasiparticle excitations will be of the following form [7, 22]:

$$E_{\pm}(\vec{\mathbf{q}}) - E_0 = \pm v_F \hbar |\vec{\mathbf{q}}| + O[(q/K)^2], \tag{1.18}$$

where $\hbar$ is the reduced Planck constant, $v_F = -\sqrt{3}\gamma_0 a/(2\hbar) \approx 1 \times 10^6$ m/s is the Fermi velocity. For many metals and doped semiconductors low-energy excitations can be successfully described by nearly free quasiparticles obeying the Schrödinger equation with the Hamiltonian $H_S = \frac{\vec{\mathbf{p}}^2}{2m^*}$, where $\vec{\mathbf{p}}$ is the momentum and m^* is the effective mass. The unusual linear energy dispersion (1.18) resembles rather the dispersion of ultrarelativistic particles, which are quantum mechanically described by the massless Dirac equation [23]. It can be shown that this similarity is not just a coincidence, but low-energy quasiparticles in graphene indeed obey the form of a massless 2D Dirac Hamiltonian (DH). One has to consider a matrix form of the Schrödinger equation with tight-binding Hamiltonian close to the K(K′) point of graphene (we neglect γ_0' terms and introduce $\vec{\mathbf{p}} = \hbar\vec{\mathbf{q}}$):

$$H\Psi = \begin{pmatrix} E_0 & v_F(\tau_z p_x - ip_y) \\ v_F(\tau_z p_x + ip_y) & E_0 \end{pmatrix} \Psi = E\Psi. \tag{1.19}$$

Components of a spinor $\Psi = \begin{pmatrix} \psi_A \\ \psi_B \end{pmatrix}$ correspond to the amplitudes of the wave function on the A and B atoms, respectively, and $\tau_z = 1(-1)$ for K(K′) point of BZ. We can select the origin of the energy axis in a way that $E_0 = 0$, then

$$H = v_F \begin{pmatrix} 0 & (\tau_z p_x - ip_y) \\ (\tau_z p_x + ip_y) & 0 \end{pmatrix}. \tag{1.20}$$

With Pauli matrix notation it can be written in a very compact form (K point, $\tau_z = 1$):

$$H = v_F(\sigma_x p_x + \sigma_y p_y) = v_F \vec{\sigma} \cdot \vec{\mathbf{p}}, \tag{1.21}$$

which is similar to the Dirac Hamiltonian

$$H_D = c\vec{\sigma} \cdot \vec{\mathbf{p}} + mc^2 \sigma_z. \tag{1.22}$$

For graphene the Pauli matrices $\vec{\sigma} = (\sigma_x, \sigma_y)$ and σ_z are acting in the A-B sublattice (so-called "pseudospin") space instead of real spin space for DH and the effective "speed of light" instead of c is given by the Fermi velocity v_F [24].[*] In the case of free-standing graphene the mass term m is zero which allows perfectly linear dispersion in the vicinity of the Dirac point, but in real graphene a term proportional to σ_z may appear due to various reasons, such as A-B sublattice symmetry breaking (SSB) or spin-orbit interactions, causing a band gap opening at the Dirac point.

---

[*] The analogy between low-energy excitations in monolayer graphite and massless Dirac particles in 2D was suggested by different authors already in 1984 [25, 26]

1.2.3 Effect of sublattice asymmetry

Let us discuss the mechanism of band gap opening due to sublattice asymmetry in more detail. The most sizeable SSB effects appear in epitaxial graphene on strongly interacting substrates, such as transition metals (Ni, Co, Ru, Rh, etc.). In epitaxial graphene atoms in A and B sublattices could be located on differing adsorption sites of the substrate, in this case they will experience different electric potential and therefore matrix elements H_{11} and H_{22} in general will not be equal anymore, thus we cannot completely eliminate the main diagonal terms of the Hamiltonian (1.19). If one defines the asymmetry as $\Delta = H_{11} - H_{22}$ and $E_1 = (H_{11} + H_{22})/2$, then the Hamiltonian can be written as:

$$\begin{aligned} H &= \begin{pmatrix} E_1 + \Delta/2 & v_F(\tau_z p_x - i p_y) \\ v_F(\tau_z p_x + i p_y) & E_1 - \Delta/2 \end{pmatrix} = \\ &= E_1 + v_F(\tau_z \sigma_x p_x + \sigma_y p_y) + \frac{\Delta}{2}\sigma_z \end{aligned} \tag{1.23}$$

Here, the mass term proportional to σ_z appears naturally. Let us write down the energy dispersion (equation (1.8) normalized by the number of unit cells):

$$E(\vec{\mathbf{k}}) = E_1 \pm \sqrt{(\Delta/2)^2 + |H_{12}(\vec{\mathbf{k}})|^2} \tag{1.24}$$

One can immediately see that the square root cannot be equal to zero anymore and where we had a touching point now will be a band gap of width Δ. A similar result can be expected for any other mass term in the Hamiltonian, proportional to σ_z.

1.2.4 Bychkov-Rashba and intrinsic spin-orbit interactions in graphene

Spin-orbit interaction (SOI) has been in the focus of intense interest due to its possible applications in modern information technology, in particular for storage and manipulation of data encoded in the electron spin-degrees of freedom in solid state systems. This is a central topic of a new multidisciplinary field of science, *spintronics*, dealing with problems important for fundamental physics and at the same time perspective for applications [27, 28].

Spin-orbit (SO) effects in graphite have been theoretically described as early as 1965 [29], however, they were predicted to be small compared to the effects of coupling between the graphene planes and have largely been ignored. Unlike graphite, graphene is in a critical electronic state and even small perturbations can strongly affect its band structure at low energies [5].

Kane and Mele [5] on the basis of symmetry considerations derived expressions for two allowed terms in the Hamiltonian describing spin-orbit interaction for graphene. They also showed that SOI can open an energy gap at the Dirac point and convert graphene from a zero gap semiconductor to an insulator with a quantum spin Hall effect [5]. Their conclusions were soon supported by more detailed calculations of Min et al. [30], who started from a microscopic tight-binding model and using second-order perturbation theory achieved similar expressions for spin-orbit terms and gave numerical estimations for the size of the gaps in pure graphene.

In general there are only two kinds of symmetry-allowed spin-dependent terms in the Hamiltonian. The first one has the following form:

$$H_i = \lambda_i \sigma_z \tau_z s_z, \tag{1.25}$$

it is called intrinsic SOI. Here the real spin of the electron is represented by a vector of Pauli matrices $\vec{\mathbf{s}} = (s_x, s_y, s_z)$ and λ_i is a coupling constant that shows the strength of the intrinsic SOI. If the mirror symmetry about the graphene plane is preserved, this term is the only spin-dependent term allowed at $\vec{\mathbf{q}} = 0$. If the mirror symmetry is broken (for example by interaction with the substrate or external electric field perpendicular to the plane) then another term is allowed:

$$H_R = \lambda_R(\sigma_x \tau_z s_y - \sigma_y s_x), \tag{1.26}$$

where the coupling constant λ_R shows the strength of SOI. This term is called extrinsic as well as Bychkov-Rashba or just Rashba SOI due to its similarity to the Bychkov-Rashba Hamiltonian $\alpha_R(\vec{\mathbf{k}} \times \vec{\mathbf{s}}) \cdot \hat{z}$ (α_R is a material dependent prefactor known as Rashba-parameter, $\hat{z}$ - unit vector in z direction). This Hamiltonian was first analyzed by Bychkov and Rashba to explain the lifting of the spin-degeneracy in the two-dimensional electron gas (2DEG) in semiconductor heterostructures [31, 32].

The original Rashba Hamiltonian contains the momentum $\vec{\mathbf{k}}$ instead of $\vec{\sigma}$, however, it can be seen from the Hamiltonian (1.21) that $\vec{\sigma}$ indeed transforms as momentum $\vec{\mathbf{k}}$ [33]. And this explains why the SO term can be considered as a modified Rashba term with $\vec{\mathbf{k}} \rightarrow \vec{\sigma}$. The conventional Rashba term proportional to $(\vec{\mathbf{k}} \times \vec{\mathbf{s}}) \cdot \hat{z}$ for graphene is small and can be neglected.

Before discussing the effect of Rashba SOI in graphene we would like to give a short introduction into conventional Rashba SOI.

The spin-orbit interaction term of the Hamiltonian can be derived from the expansion of the relativistic Dirac equation up to terms of order $(\frac{v}{c})^2$ [*]:

$$H_{SOI} = -\frac{\mu_B}{2mc} \vec{\mathbf{s}} \cdot (\vec{\boldsymbol{\nabla}} V(\vec{\mathbf{r}}) \times \vec{\mathbf{p}}) = -\frac{\mu_B}{2} \vec{\mathbf{s}} \cdot (\frac{1}{c} \vec{\mathbf{E}}(\vec{\mathbf{r}}) \times \vec{\mathbf{v}}) = -\frac{\mu_B}{2} \vec{\mathbf{s}} \cdot \vec{\mathbf{B}}_{\mathbf{0}}, \tag{1.27}$$

where the Bohr magneton $\mu_B = \frac{e\hbar}{2mc}$ is used as a unit of magnetic moment. One can see that it has the same form as the Zeeman term $(-\mu_B \vec{\mathbf{s}} \cdot \vec{\mathbf{B}})$ except for a factor of $1/2$ (called Thomas factor [35]). The effective magnetic field $\vec{\mathbf{B}}_0$ can be interpreted as follows: electron moving in an electric field produces magnetic field $\vec{\mathbf{B}}_0$ in its local frame

---

[*] This can be done by Foldy-Wouthuysen transformation [34]. Gaussian system of units is used.

of reference (by Lorentz transformations), which interacts with the spin of this electron. If we consider an electron orbiting the nucleus of an atom, this term couples its orbital motion to its spin, hence the name.

The largest potential gradient in the crystal is close to the nucleus, so one should expect major contribution to the SOI from the vicinity of the nucleus, where $V(r) \approx -\frac{Z}{r}$ and its gradient is proportional to Z, atomic number. Hence the general trend is that SOI should be higher for heavy elements than for light ones. However, it should be pointed out that the SOI strength does not change linearly with Z, since it also depends on the asymmetry of the wavefunction, which changes with Z and as a result the SOI strength grows roughly as the square of Z.

If both time-reversal and inversion symmetry are not broken then each eigenstate is two-fold degenerate for spin-up and spin-down electrons: $E_\uparrow(\vec{\mathbf{k}}) = E_\uparrow(-\vec{\mathbf{k}}) = E_\downarrow(\vec{\mathbf{k}})$. However, due to the presence of a surface dipole, at any surface appears an electric field directed perpendicular to the surface that is proportional to the workfunction [36]. This field breaks the inversion symmetry and allows the spin-degeneracy to be lifted. Thus, on the surface in the absence of a magnetic field, only the time-reversal symmetry $[E_\uparrow(-\vec{\mathbf{k}}) = E_\downarrow(\vec{\mathbf{k}})]$ is present. For a 2DEG in the (x, y) plane with electric field oriented in z direction, the Hamiltonian takes the form

$$H = H_K + H_R = \frac{(\hbar\vec{\mathbf{k}}_\parallel)^2}{2m^*} + \frac{\alpha_R}{\hbar}(s_x p_y - s_y p_x), \tag{1.28}$$

where $\vec{\mathbf{k}}_\parallel = (k_x, k_y, 0) = k_\parallel(\cos(\phi), \sin(\phi), 0)$. Eigenstates can be found analytically:

$$\psi_{\pm\vec{\mathbf{k}}_\parallel}(\vec{\mathbf{r}}_\parallel) = \frac{e^{i\vec{\mathbf{k}}_\parallel\vec{\mathbf{r}}_\parallel}}{2\pi}\frac{1}{\sqrt{2}}\begin{pmatrix} ie^{-i\phi/2} \\ \pm e^{i\phi/2} \end{pmatrix} \tag{1.29}$$

with eigenenergies

$$\begin{aligned} E_\pm(\vec{\mathbf{k}}_\parallel) &= \frac{\vec{\mathbf{k}}_\parallel^2}{2m^*} \pm \alpha_R|\vec{\mathbf{k}}_\parallel| = \\ &= \frac{1}{2m^*}(|\vec{\mathbf{k}}_\parallel| \pm k_{SO})^2 - \Delta_{SO}, \end{aligned} \tag{1.30}$$

where + and − signs denote two spin-split branches.
The most important properties of this solution are:

- spin-degeneracy is preserved only at high-symmetry point $\vec{\mathbf{k}}_\parallel = 0$,
- dispersion $E(\vec{\mathbf{k}})$ appears as figure of rotation formed by two parabolas shifted in k-space by k_{SO} [see Fig. 1.3 (a)],
- energy splitting is linear in $|\vec{\mathbf{k}}_\parallel|$,

- The spins in both branches are oriented opposite to each other and perpendicular to $\vec{\mathbf{k}}_{\|}$, which forms a specific spin-texture (so-called "spin-momentum locking") [Fig. 1.3 (a), arrows].

All these features were observed directly in angle resolved photoemission spectroscopy (ARPES)[*] experiments from surface states of metals (which are a particular realisation of a 2DEG): starting from the pioneering work of LaShell et al. that showed an unexpectedly large splitting of the surface state at the Au(111) surface [37] that was later proven to have a Rashba-type spin-texture in a spin-resolved ARPES experiment [38], to the discovery of a giant Rashba-splitting in the Bi/Ag(111) surface alloy [39] and to the detection of splitting in the Ir(111) [40] and even Cu(111) surface states, the latter was achieved by laser-ARPES experiment with ultimately high energy resolution [41]. Another important class of systems, where the Rashba-effect in 2DEG can be studied is doped semiconductor heterostructures that support an electron gas at the interface. These states are not accessible for ARPES, but they can be studied indirectly, for example by analysis of Shubnikov-de Haas oscillations and spin precession [42, 43].

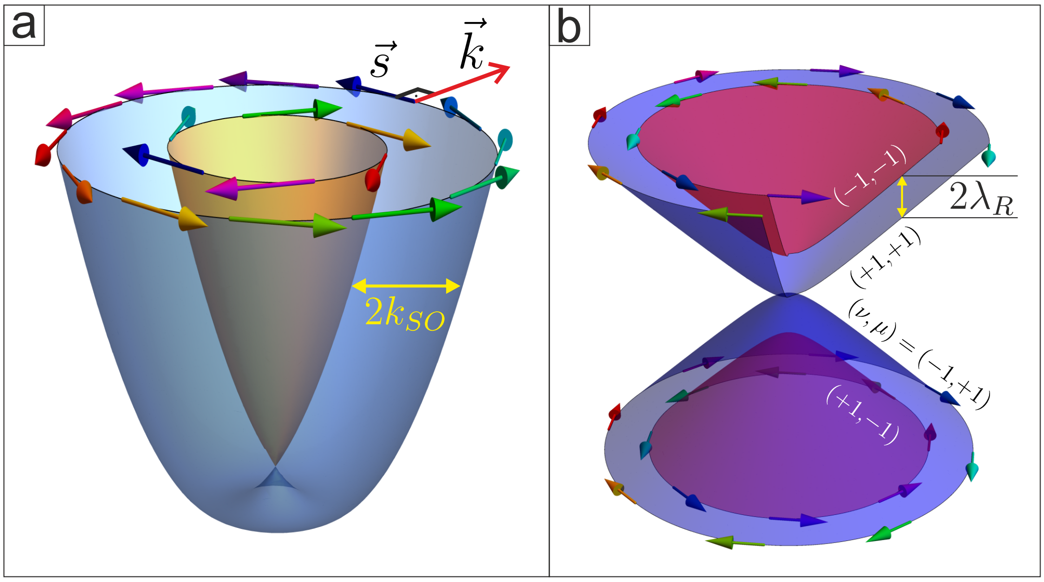

Figure 1.3: Illustration of the spin-degeneracy lifting by Rashba-effect in the (a) typical parabolic band of a semiconductor and (b) Dirac cone of graphene. In both cases spins are in-plane polarized perpendicular to the momentum $\vec{\mathbf{k}}$, orientations of spin polarization are depicted with arrows. Here we assume the electric field oriented in positive direction of z axis (a) and $\lambda_R > 0$ (b), in the opposite cases the directions of spin polarization vectors should be reversed.

One should be careful applying the free electron model described above to real systems because it drastically underestimates the SOI strength, e.g. for the Au(111) surface

---

[*] A detailed description of ARPES method will be given in the "Methodical background" section.

state the estimated spin-splitting is 5 orders of magnitude lower than the experimental value [44]. The reason for this is that it does not take into account the potential gradients *in the atoms*, which are much larger than the field at the surface [36, 44]. In a tight-binding model Petersen and Hedegård demonstrated that the size of Rashba-type splitting is actually proportional to atomic spin-orbit coupling parameter and a specific measure of the wave function asymmetry [44].

If we go back to graphene, one can calculate the eigenenergies of its Hamiltonian with the special kind of Rashba-term (1.26) included. The details of the calculation are lengthy and available in the original paper by Rashba [33], here we just present the result:

$$E_{\nu\mu}(\vec{\mathbf{q}}) = \frac{\nu\mu}{2}(\sqrt{\lambda^2 + 4\gamma^2 q^2} - \mu\lambda), \quad \nu = \pm 1, \mu = \pm 1, \tag{1.31}$$

where $\gamma = \hbar v_F$, $q = |\vec{\mathbf{q}}|$ and $\lambda = 2\lambda_R$. The resulting spectrum contains two zero-gap branches and two gapped (gap is $2|\lambda|$) branches of the same shape. The separation between gapped and ungapped branches is constant and equals λ*. It can be verified that in each branch the spins are oriented in-plane (expectation value for z-component of spin polarization is zero). The mean expectation values of in-plane spin polarizations $\vec{\mathbf{S}}_{\nu\mu}$ will be given by

$$\vec{\mathbf{S}}_{\nu\mu}(\vec{\mathbf{q}}) = \frac{2\mu\gamma(\vec{\mathbf{q}} \times \vec{\mathbf{z}})}{\sqrt{\lambda^2 + 4\gamma^2 q^2}}. \tag{1.32}$$

This vector is oriented normal to the momentum $\vec{\mathbf{q}}$ and the direction of spin-texture alternates between gapped and non-gapped branches [Fig. 1.3 (b)]. The value of spin polarization saturates to 1 for large q, but vanishes close to the Dirac points [33].

If $\lambda_R = 0$ and the intrinsic SOI is finite, an energy gap of $2|\lambda_i|$ opens at the Dirac points and dispersion in the vicinity of the Dirac point [5] is

$$E(\vec{\mathbf{q}}) = \pm\sqrt{{\lambda_i}^2 + \gamma^2 q^2}. \tag{1.33}$$

When Rashba and intrinsic terms are included together, the band structure depends on their relative strength. The dispersion equation can be written in a general form as†

$$E_{\nu\mu}(\vec{\mathbf{q}}) = \nu\sqrt{(\lambda_R - \mu\lambda_i)^2 + \gamma^2 q^2} + \mu\lambda_R, \quad \nu = \pm 1, \mu = \pm 1. \tag{1.34}$$

If $|\lambda_i| > |\lambda_R|$, a gap with a magnitude of $2(|\lambda_i| - |\lambda_R|)$ appears at the graphene Dirac point, and if $|\lambda_i| < |\lambda_R|$, the gap closes, but bands touching at the Dirac point disperse quadratically. At the transition point $|\lambda_i| = |\lambda_R|$ three branches are crossing at the Dirac point and two of them form a cone structure of massless fermions (Fig. 1.4).

---

* In the future discussions of experimental results we will also use $\lambda = 2\lambda_R$ for the coupling strength of Rashba SOI, since it equals the separation between the two dispersion branches that can be measured directly in the ARPES experiment and thus serves as a convenient measure of the coupling strength.

† One can easily evaluate that this equation gives 4 dispersion branches, which are equivalent to the result of Eq. (1.31) for $\lambda_i = 0$ and Eq. (1.33) for $\lambda_R = 0$.

Spin-texture is qualitatively similar to the case of purely Rashba SOI described above [45]. The above-mentioned gaps, arising from the term (1.25), have opposite sign at K and K′ points, hence the topological order of this phase is nontrivial, giving rise to topologically protected spin-polarized edge states in the case of a finite graphene sheet.

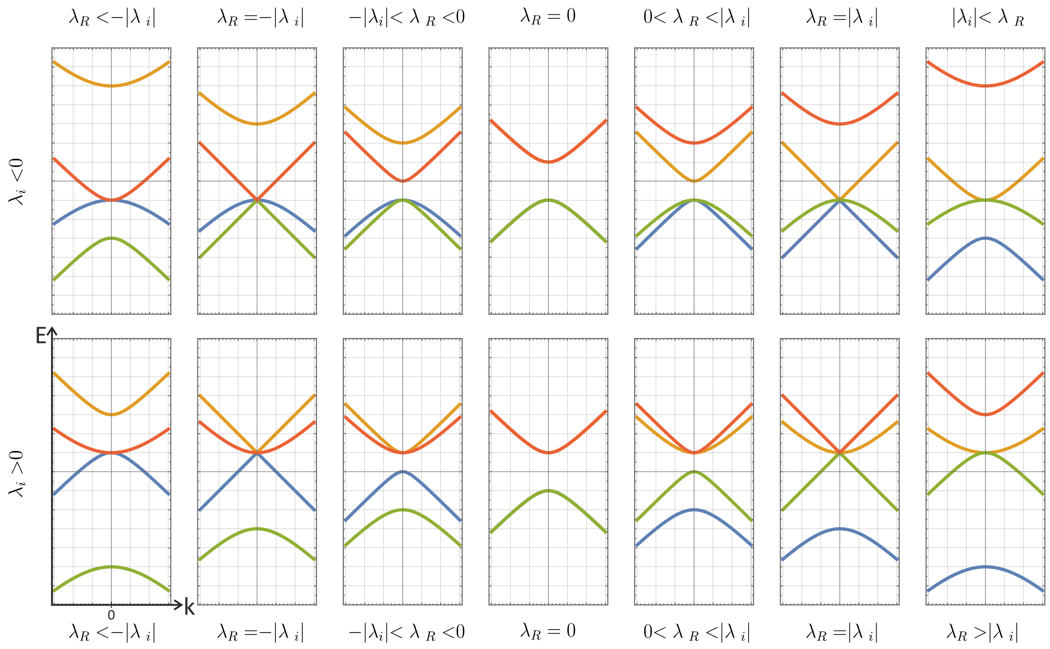

Figure 1.4: Influence of the combined Rashba and intrinsic SOI on the energy spectrum in the Dirac cone region. Schematic E(k) dispersions. From left to right λ_R is gradually increasing from negative to positive values while λ_i has a constant negative or positive value in the upper and lower rows, respectively. One can see linearly dispersing bands when $|\lambda_R| = |\lambda_i|$, gap opening in the region $|\lambda_R| < |\lambda_i|$ and degenerate gapped bands at $|\lambda_R| = 0$.

Min et al. [30] estimated that the SO gap for free-standing graphene is $2\lambda_i \approx$ k$_B \times 0.01$ K ≈ 1 μeV, a very small value, hard to observe by common experimental techniques. From symmetry considerations discussed above it is clear that a Rashba splitting in free-standing graphene will appear only in an external electric field and for typical values of E ~ 50 V/300 nm it was estimated that $\lambda_R \approx$ k$_B \times 0.13$ K ≈ 11 μeV, also extremely weak [30]. The numerical estimates for the SOI strengths are rather controversial, for $2\lambda_i$ they are ranging from ~ 1 μeV [30] to ~ 200 μeV [5], the values obtained in fully first principles calculations also vary $\sim 24 - 50$ μeV [45, 46]. However, even the largest estimates are remarkably small. It makes the realization of many interesting phenomena in graphene, such as topological/quantum spin Hall states or the spin Hall effect (SHE) excessively difficult.

Nevertheless, over the years scientists invented a variety of ways to enhance the SOI in graphene. It was predicted that one can induce stronger SOI in graphene by hydrogenation, fluorination [47] or introduction of other impurities converting sp^2 bonds to sp^3 [48]. The enhanced SOI strength in this case can be on the order of few meV (e.g. 2.5 meV was achieved by controlled hydrogenation [49]), but this approach introduces disorder in the graphene lattice.

Luckily, both intrinsic and Rashba SOI in graphene can be enhanced even stronger with less damage to the graphene lattice by bringing it in contact with high-SOI materials. This proximity induced SOI was first predicted theoretically [6, 50–52] and then demonstrated in multiple experiments.

Two main routes to achieve high SOI by proximity were theoretically proposed. The first one is based on hybridization of valence *d*-states of high-SOI material with carbon $2p_z$ orbitals. In this scope Li et al. predicted a ~ 100 meV SO gap for graphene intercalated with Re [52] and suggested that Mn and Tc should provide similar effect. At the same time they argue and prove by calculation that for *sp*-metal Bi SO gap will not appear due to lack of *d*-component in the outer shell of its atomic wave function. As a variation of this idea it was demonstrated by Hu et al. [51] that adatoms with partially filled *d*-shells (such as Os and Ir) on graphene produce a SO split impurity state that hybridizes with the Dirac cone leading to a large SO gap of ~ 0.2 eV. Ma et al. [50] have studied the influence of Au adatoms on graphene π states around Γ point and they predicted a considerable (~ 200 meV) Rashba type splitting there as well.

The second route is exploiting the process suggested by Weeks et al. [6], consisting of electron hopping from graphene to a heavy adatom, where it is "exposed" to high SOI, and then hopping back to the graphene sheet. Such hopping processes in effect *locally* enhance graphene's spin-orbit strength. An important difference of the second route is that it does not require electrons in the *d*-shells of the adatom and a sizeable SOI is expected with *sp*-metals as well. Moreover, for such sp-adatoms (in particular, In and Tl) the induced SOI is claimed to be predominantly of intrinsic type, which is desirable for the realization of a topological phase in graphene.

Most experiments with epitaxial graphene on metals demonstrated spin textures of Rashba-type, which can be reasoned by breaking of mirror symmetry in combination with hybridization of graphene π and metal d states. However, there are exceptions, as in the case of graphene on Pt(111) intercalated with Pb, where a gap in the Dirac cone near the Fermi level was observed in ARPES experiments and is claimed to be of spin-orbit nature [53]. Another evidence for Pb-enhanced SOI in graphene can be found in a scanning tunneling microscopy (STM) and spectroscopy (STS) study reported by Calleja et al. for graphene on Ir(111) intercalated with islands of Pb [54]. The effect of Pb adsorbates has been theoretically studied by Brey in the framework suggested by Weeks (electron hopping to and from a heavy adatom) [55] and it was discovered that Pb adatoms can induce both intrinsic and Rashba SOI in graphene, depending on how they are distributed: in hollow-sites of graphene (intrinsic) or randomly (Rashba).

Recently an effect of proximity-enhanced SOI was demonstrated in graphene transferred onto WS_2 [56], the obtained strength of the SOI was 17 meV. This effect was explained by hybridization of the Dirac cone with SO split midgap states localized on W. These states are formed by dangling bonds at the sulfur vacancies in WS_2 and have an unusually large spin splitting of about ~ 0.2 eV.

There is also a range of experimental systems realizing the induced *Rashba-type* SOI [4, 57–62]. One of the prominent examples is graphene on Ni(111) intercalated with gold that showed in spin-resolved ARPES experiments a surprisingly large spin splitting of the Dirac cone ($\sim$ 100 meV), exceeding by far the theoretical predictions [4]. The Chapter 2 of the current Thesis is devoted to this topic.

1.3 Methodical background

This section describes the experimental techniques which have been used in this thesis to prepare and study the samples.

1.3.1 Technique of spin- and angle-resolved photoemission spectroscopy

One of the most powerful and direct methods to experimentally explore momentum-resolved electronic band structures of solids is angle resolved photoemission spectroscopy (ARPES). The basis of this method lies in the phenomenon of photoelectric effect, which was discovered in experiments of Hertz in 1887 [63] by observation that electric sparks occur easier when the electrodes are exposed to ultraviolet light. Surprisingly, experiments showed that only light with high enough frequency will cause such effect no matter how intense the beam is. This result was in conflict with the existing physics and the theoretical explanation was given only in 1905 by Einstein [64], who adapted Max Planck's idea of energy quantization and proposed the quantized nature of light, assuming that it is composed of discrete quanta — *photons* — with fixed energies corresponding to certain frequencies. This idea was very fruitful for the physics and the explanation of the photoelectric effect earned Einstein the Nobel Prize in Physics.[*]

If we expose a solid surface to a beam of monochromatic light with wavelength $\lambda = 2\pi c/\omega$, a single photon can get absorbed transferring its energy $\hbar\omega$ to an electron inside the material. If the resulting kinetic energy of the excited electron is sufficient to overcome a surface potential barrier then this electron can escape from the material.[†]

---

[*] "for his services to Theoretical Physics, and especially for his discovery of the law of the photoelectric effect." (1921)

[†] In this case we are talking about the component of kinetic energy related to the movement normal to the surface $E_z^{kin} = m_e v_z^2/2$, where m_e is the electron mass and v_z is the component of velocity perpendicular to the surface. An electron may obtain large total kinetic energy and small E_z^{kin}, then it will travel almost parallel to the surface and get reflected from the surface potential barrier. This is an aspect that will be important for Chapter 4 of the present Thesis.

The magnitude of this potential barrier Φ is called the work function, defined as the minimum energy required to remove an electron from the interior of a solid to a position just outside of it [65]. The work function is material dependent and it varies even for different crystallographic faces of the same crystalline solid. Typical values of Φ are on the scale of several eV.

From Einstein's theory of the photoelectric effect follows that the energy of the photon is used to ionize an atom of the material and overcome the surface potential barrier, the rest can be transferred to the electron's kinetic energy. The extended equation of the photoelectric effect provides the relation between the photon energy, kinetic energy of the photoelectron E_{kin} and its binding energy E_B referred to the Fermi level of the solid:

$$\hbar\omega = |E_B| + \Phi + E_{kin}. \tag{1.35}$$

From this equation it follows that if we fix the photon energy and measure the intensity of outgoing electrons as a function of their kinetic energies then we can figure out what the distribution of their binding energies inside the solid was. This is the general idea of photoelectron spectroscopy (PES) and very first spectra were captured on a photographic plate already in 1907 by P. D. Innes, he used an electromagnet to separate electron energies [66]. In 1914 Robinson and Rawlinson developed the method of Innes and were able to achieve first PES spectra for lead and iron [67]. The experimental techniques were gradually progressing and throughout 1950s – 1960s Kai Siegbahn developed both the instrumentation and theory of the modern electron spectroscopy. The exact value of E_B of core electrons of a given element may differ in different compounds and it depends on the chemical environment of the atoms. PES is a powerful method to detect such chemical shifts of energy levels and hence the first name of this method — electron spectroscopy for chemical analysis (ESCA). However, nowadays it is more often called X-ray photoemission spectroscopy (XPS).

1.3.1.1 Three-step model of photoemission. Step one.

The photoemission process is usually assumed to occur in three independent steps (so-called *three-step model* [65, 68, 69]): excitation of the electron into a bulk final state, travel of the excited electron to the surface and its transmission through the surface potential barrier to the vacuum where it can be captured by the detector. This is a simplified description, however, it gives rather good similarity to the experiment in most cases and it is transparent and intuitive.[*]

---

[*] A more advanced approach is the *one-step model*, where photoemission is described as a single coherent process expressed in terms of optical transition between the initial and final states described by many-body wave functions that satisfy certain boundary conditions at the surface of the material. As "true" final states in this model so-called *time-reversed* or *inverse LEED states* were used very successfully [65]. The one-step model requires more complex calculations, but this is the cost of a higher accuracy in predicting the experimental spectra.

In the first step an electron in the specimen absorbs a photon from the incoming beam, this process can be described as excitation of the N-electron system from initial state i with wave function Ψ_i into a final state f with wave function Ψ_f at the location of absorption.

If we consider the interaction with electromagnetic field of a photon a small perturbation (with perturbing Hamiltonian H'), the transition probability per unit time can be calculated using Fermi's Golden Rule [70, 71] as follows:

$$\omega_{i,f} = \frac{2\pi}{\hbar} | \langle \Psi_f | H' | \Psi_i \rangle |^2 \delta(E_f - E_i - \hbar\omega). \tag{1.36}$$

The delta function term here represents the conservation of energy, the Hamiltonian should include the electromagnetic field of the photon (Gaussian system of units):

$$\begin{aligned} H &= \frac{1}{2m}(\vec{\mathbf{p}} - \frac{e}{c}\vec{\mathbf{A}})^2 + e\phi + V(\vec{\mathbf{r}}) = \\ &= \underbrace{[\frac{|\vec{\mathbf{p}}|^2}{2m} + V(\vec{\mathbf{r}})]}_{H_0} + \underbrace{[-\frac{e}{2mc}(\vec{\mathbf{A}} \cdot \vec{\mathbf{p}} + \vec{\mathbf{p}} \cdot \vec{\mathbf{A}}) + \frac{e^2}{2mc^2}|\vec{\mathbf{A}}|^2 + e\phi]}_{H'}, \end{aligned} \tag{1.37}$$

where $\vec{\mathbf{p}} = -i\hbar\vec{\boldsymbol{\nabla}}$ is the momentum operator, $\vec{\mathbf{A}} = \vec{\mathbf{A}}(\vec{\mathbf{r}}, t)$ and $\phi = \phi(\vec{\mathbf{r}}, t)$ are vector and scalar potentials associated with the photon.

The expression for the H' could be significantly simplified by neglecting two-photon processes (term proportional to $|\vec{\mathbf{A}}|^2$) and using a gauge $\phi = 0$ (known as Hamiltonian gauge). Moreover, typical wavelengths are large compared to atomic distances (for 10–100 eV photon energy $\lambda \approx 1240$–124 Å), thus we can consider the variation of $\vec{\mathbf{A}}(\vec{\mathbf{r}})$ small in the spatial region in which the matrix element is not negligible. Then in the dipole approximation $\vec{\mathbf{A}}(\vec{\mathbf{r}}) = \vec{\mathbf{A}}_0$, where $\vec{\mathbf{A}}_0$ is a constant vector in space, $\vec{\boldsymbol{\nabla}} \cdot \vec{\mathbf{A}} = \vec{\boldsymbol{\nabla}} \cdot \vec{\mathbf{A}}_0 = 0$, which leads to a zero commutator $[\vec{\mathbf{A}}, \vec{\mathbf{p}}] = i\hbar\vec{\boldsymbol{\nabla}} \cdot \vec{\mathbf{A}} = 0$. Although these assumptions may not hold at the surface of the material, where the electromagnetic fields may have a strong spatial dependence [72, 73], such phenomenological description works well for most experiments.*

Furthermore, we can use the commutation relations $[p, H_0] = -i\hbar\vec{\boldsymbol{\nabla}}V(\vec{\mathbf{r}})$ and $[r, H_0] = i\hbar\vec{\mathbf{p}}/m$ to finally write the transition matrix element in two useful forms:

$$M_{i,f} \equiv \langle \Psi_f | H' | \Psi_i \rangle \approx -\frac{e}{mc} \langle \Psi_f | \vec{\mathbf{A}} \cdot \vec{\mathbf{p}} | \Psi_i \rangle = \tag{1.38}$$

$$= \vec{\mathbf{A}}_0 \frac{e}{ic} \frac{(E_f - E_i)}{\hbar} \langle \Psi_f | \vec{\mathbf{r}} | \Psi_i \rangle = \tag{1.39}$$

$$= \vec{\mathbf{A}}_0 \frac{e}{imc} \frac{\hbar}{(E_f - E_i)} \langle \Psi_f | \vec{\boldsymbol{\nabla}} V(\vec{\mathbf{r}}) | \Psi_i \rangle \,. \tag{1.40}$$

---

[*] The above mentioned effect leads to a peculiar surface contribution to photoemission, which is proportional to $(\varepsilon - 1)$ where ε is the dielectric function of the material. By interfering with the bulk contribution it may result in asymmetric lineshapes of the photoemission peaks [74].

One can see that after insertion into Eq. (1.36) terms $(E_f - E_i)/\hbar$ together with delta function will transform to simply ω.

In the form of Eq. (1.39) the matrix element of coordinate operator $\vec{\mathbf{r}}$ is used. This so-called length form is useful for derivation of the selection rules based on the symmetry of the initial and final states. The second form described by Eq. 1.40 is known as acceleration form. One can see that in the case of a free electron gas photoemission is not possible, as $\vec{\boldsymbol{\nabla}} V(\vec{\mathbf{r}}) = 0$ for $V(\vec{\mathbf{r}}) = const$. In general lattice potential is a crucial component in the photoemission from crystals, since it also defines the low-energy final states.*

In ARPES the excited electron generally possesses sufficiently high energy to be able to escape into the vacuum faster than the system response time, thus we can make use of *sudden approximation*, i.e. we assume that an electron is instantaneously removed from the system without any interaction and leaving the (N-1)-electron system behind. Then we can construct the initial and final N-electron states as a product of a photoelectron and (N-1)-electron terms:

$$\Psi_f^N = \mathcal{A}\phi_f^{\vec{\mathbf{k}}}\Psi_f^{N-1}, \tag{1.41}$$

$$\Psi_i^N = \mathcal{A}\phi_i^{\vec{\mathbf{k}}}\Psi_i^{N-1}, \tag{1.42}$$

where $\mathcal{A}$ is an operator antisymmetrizing the N-electron wave function, $\phi_{i,f}^{\vec{\mathbf{k}}}$ are the wave functions representing the initial (orbital) and final state of photoelectron with momentum $\vec{\mathbf{k}}$ and $\Psi_{i,f}^{N-1}$ are the initial and final state wave functions of the (N-1)-electron system. Ψ_f^{N-1} can be one of the excited states, e.g. with eigenfunction Ψ_m^{N-1} and energy E_m^{N-1}, for the calculation of the total transition probability we will sum over all possible excited states m. In a more general way one can write $\Psi_i^{N-1} = c_{\vec{\mathbf{k}}}\Psi_i^N$, where $c_{\vec{\mathbf{k}}}$ is the annihilation operator for an electron with momentum $\vec{\mathbf{k}}$. Note that Ψ_i^{N-1} is generally *not* an eigenstate of the (N-1)-particle Hamiltonian.

In this form we can write the transition matrix element as the following product:

$$M_{i,f} \equiv \langle \Psi_f | H' | \Psi_i \rangle = \left\langle \phi_f^{\vec{\mathbf{k}}} \middle| H' \middle| \phi_i^{\vec{\mathbf{k}}} \right\rangle \left\langle \Psi_m^{N-1} \middle| \Psi_i^{N-1} \right\rangle, \tag{1.43}$$

where the first term is the one-electron transition matrix element, and $\left\langle \Psi_m^{N-1} \middle| \Psi_i^{N-1} \right\rangle$ is the (N-1)-electron overlap integral. If we want to calculate the total photoemission

---

*Moreover, in the case of free-electron gas without translational symmetry of the lattice potential it will not be possible to make a transition due to momentum conservation. Photon momentum for typical ARPES energies (∼ 10–100 eV) is small, hence all the transitions are "vertical" on the $E(k)$ diagram. However, if one imagines the free-electron parabola $E(k) = (\hbar k)^2/2m$, there are obviously no states that could be connected with a vertical line. In a crystal the electron can exchange momentum with the lattice, thus allowing such transitions (they will be represented by vertical lines in the reduced zone scheme representation).

current of electrons with energy E_{kin} and momentum $\vec{\mathbf{k}}$, we need to sum $\omega_{i,f}$ over all possible combinations of initial and final states that give such values:

$$\begin{aligned} I(\vec{\mathbf{k}}, E_{kin}) = \sum_{i,f} \omega_{i,f} \propto \\ \propto \sum_{i,f} \left| m_{i,f}(\vec{\mathbf{k}}) \right|^2 \sum_m |c_{i,f}|^2 \delta(E_{kin} + E_m^{N-1} - E_i^N - \hbar\omega), \end{aligned} \tag{1.44}$$

where

$$m_{i,f}(\vec{\mathbf{k}}) \equiv \left\langle \phi_f^{\vec{\mathbf{k}}} \middle| H' \middle| \phi_i^{\vec{\mathbf{k}}} \right\rangle, \quad c_{i,m} \equiv \left\langle \Psi_m^{N-1} \middle| \Psi_i^{N-1} \right\rangle. \tag{1.45}$$

Here we substituted $E_f = E_{kin} + E_m^{N-1}$ and $E_i^N = E_i$ is the initial energy of the N-electron system. In the first approximation one can assume that the remaining system did not change after excitation, then the overlap integral is unity and the measured energy of the intensity peak will be equal just to the negative of the initial orbital energy of the electron $-\epsilon(\vec{\mathbf{k}})$ (known as Koopman's binding energy). Thus, in the simplest picture the resulting spectrum will reflect the density of electronic states of the sample weighted by transition matrix elements $m_{i,f}$. However, in general the remaining system of (N-1) electrons has to rearrange to minimize its energy after one electron was ejected, and Ψ_i^{N-1} may have an overlap with many of the eigenstates Ψ_m^{N-1}. This will result in satellite peaks next to the main peak in the ARPES spectra.

1.3.1.2 Three-step model of photoemission. Step two.

In the second step of the three step model the excited electrons travel to the surface and the majority of them will suffer inelastic collisions before escaping the material. Hence the photoemission spectrum will have two main components: primary electrons, leaving the material without inelastic scattering, and secondary electrons, which lost part of their kinetic energy in such scattering events [75]. These two components appear superimposed in the resulting spectra: primary electrons form distinct features, reproducing roughly the DOS of the sample, while secondary electrons exhibit a broad, continuous energy spectrum starting from zero kinetic energy (Fig. 1.5).

The probability that an electron excited at the depth z under the surface will escape to vacuum without undergoing inelastic scattering is well approximated by an exponential decay with z [68, 76]:

$$P(z) \propto e^{-\frac{z}{\lambda(E)}}. \tag{1.46}$$

It means that 63% of all the primary electrons originate not deeper that $\lambda(E)$ from the surface and 95% — not deeper than $3\lambda(E)$. The parameter $\lambda(E)$ is the inelastic mean free path (IMFP) — the average distance that an electron of given energy E can travel between successive inelastic collisions. Both aggregated experimental data [77]

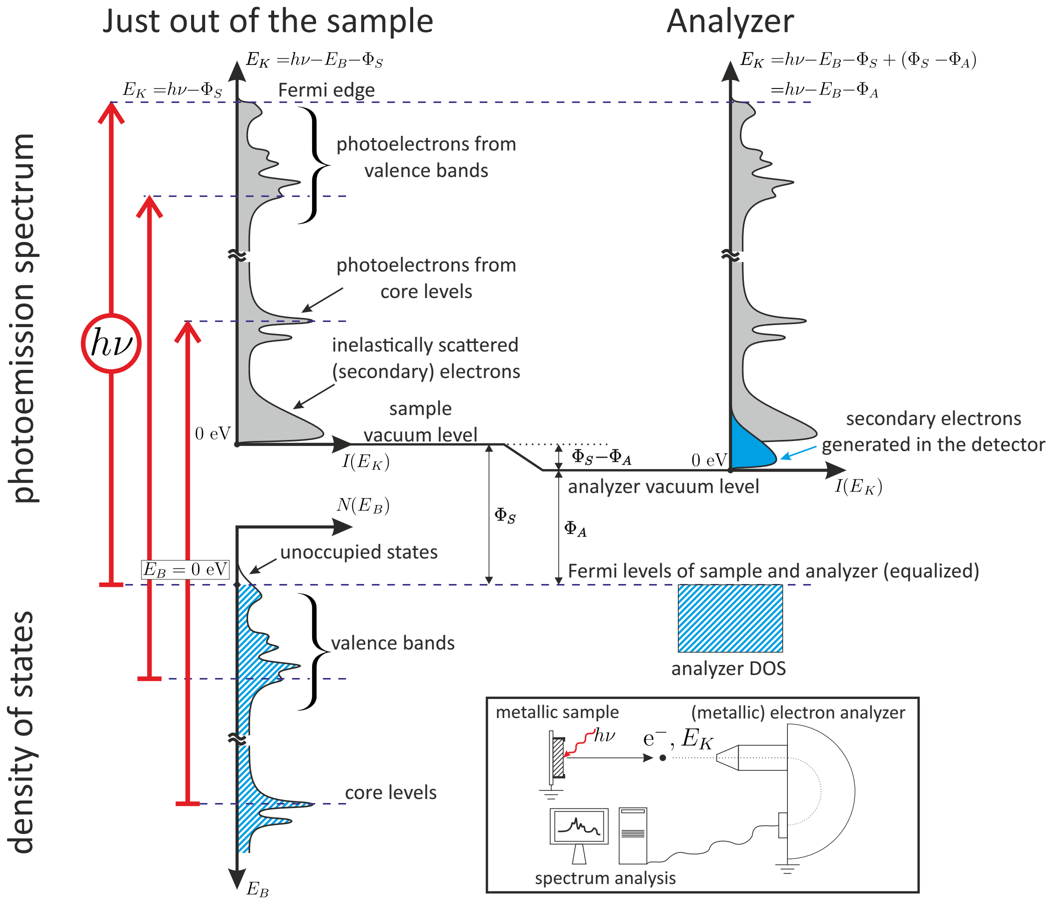

Figure 1.5: Schematic representation of photoemission process. Electrons are excited by the incoming radiation with energy $h\nu$, the spectrum of emitted electrons (top left) reflects the occupied region of the sample DOS (bottom left). Φ_S and Φ_A are work functions of sample and analyzer, respectively. Kinetic energies of the spectrum in the analyzer (top right) are measured relative to its vacuum level. Adapted from Ref. [75]. Inset schematically shows the process of measurement (see Fig. 1.7 for details).

[Fig. 1.6(a)] and calculations [78] show that energy dependence of electron IMFP is very similar for a large variety of solids [Fig. 1.6(b)]: $\lambda(E)$ has a minimum around 50 – 100 eV, exhibits a $\sim \sqrt{E}$ growth for electron kinetic energies above 100 eV and $\sim 1/E^2$ decay in the low-energy region (below 10 eV). This dependence is known as "universal curve" because of the general description that it provides.

From this curve one can see that for typical energies in ARPES experiments (10–200 eV) the majority of the escaping photoelectrons originate from the top few atomic layers, hence the method yields information on the composition of the surface [79] and the peak surface sensitivity is achieved for electrons with kinetic energy of 50–100 eV.

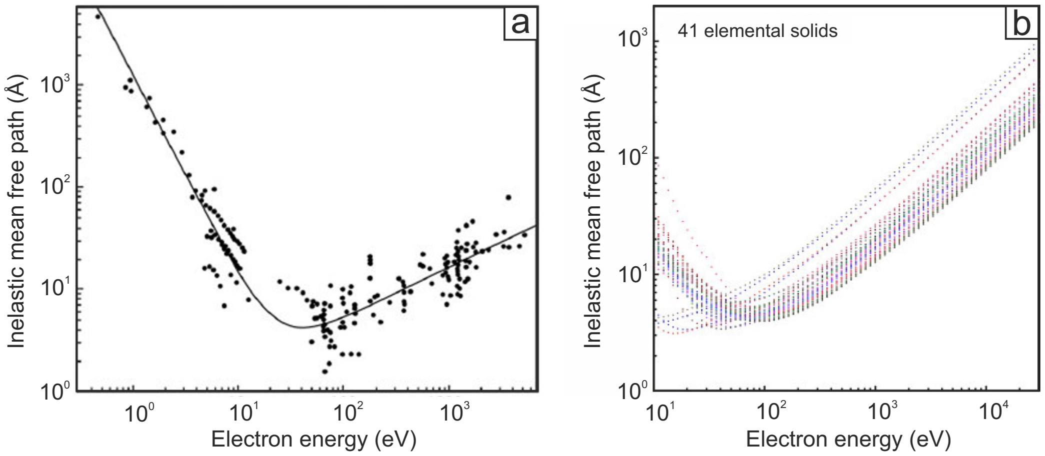

Figure 1.6: "Universal curve". (a) Compilation of experimental IMFP as a function of energy relative to Fermi level for electrons in different materials, adapted from [77]. The full curve is the empirical least squares fit with a function of the form $a/E^2 + b\sqrt{E}$; (b) Calculated IMFP for 41 different elemental materials, reproduced from [78].

1.3.1.3 Three-step model of photoemission. Step three.

The third step of the model is transmission of an electron through the surface potential barrier to the vacuum. By capturing photoemitted electrons and analyzing their energy and momentum *in vacuum* it is possible to deduce the dispersion relation $E(\vec{\mathbf{k}})$ of the electrons as it was *in the solid*. To do that one can measure the kinetic energy E_{kin} of photoelectrons emitted in a given direction by collecting them with an electron energy analyzer with a finite acceptance angle. This way not only the kinetic energy, but also the wave vector or momentum $\vec{\mathbf{K}} = \vec{\mathbf{p}}/\hbar$ of the photoelectrons in vacuum is determined, as its modulus is given by $K = \sqrt{2mE_{kin}}/\hbar$ and its components parallel (K_x, K_y) and perpendicular (K_z) to the sample surface can be obtained in terms of the polar (ϑ) and azimuthal (φ) emission angles defined by the experimental geometry:

$$\begin{aligned} K_x &= \frac{1}{\hbar}\sqrt{2mE_{kin}}\sin\vartheta\cos\varphi, \\ K_y &= \frac{1}{\hbar}\sqrt{2mE_{kin}}\sin\vartheta\sin\varphi, \\ K_z &= \frac{1}{\hbar}\sqrt{2mE_{kin}}\cos\vartheta. \end{aligned} \tag{1.47}$$

In the non-interacting electron picture we can exploit the conservation of energy in the form of Eq. (1.35) to find $E_{kin} = \hbar\omega - |E_B| - \Phi_S$, where Φ_S is the sample work function. To relate electron momentum in the solid $\vec{\mathbf{k}}$ to its momentum in vacuum $\vec{\mathbf{K}}$ one has to take into account that the photon momentum for typical ARPES energies (10–100 eV) is small compared to the typical sizes of the BZ, hence it could be neglected. To find how the momentum is changing at the surface one has to match the bulk Bloch eigenstates inside the sample to free-electron plane waves in the vacuum. Due to the lateral translational symmetry (which is preserved across the the surface) the component of the momentum parallel to the surface is conserved:

$$E_{kin} = \frac{\hbar^2 K^2}{2m}, \quad \left|\vec{\mathbf{K}}_{||}\right| = \left|\vec{\mathbf{K}}\right| \sin\vartheta, \quad \left|\vec{\mathbf{K}}_{\perp}\right| = \left|\vec{\mathbf{K}}\right| \cos\vartheta \tag{1.48}$$

$$\left|\vec{\mathbf{k}}_{||}\right| = \left|\vec{\mathbf{K}}_{||}\right| = \sqrt{\frac{2mE_{kin}}{\hbar^2}} \sin\vartheta, \tag{1.49}$$

$$\left|\vec{\mathbf{K}}_{\perp}\right| = \sqrt{\frac{2mE_{kin}}{\hbar^2}} \cos\vartheta. \tag{1.50}$$

From now on indices $||$ and $\perp$ stand for the components of the momenta parallel and perpendicular to the surface, respectively. The wave vector $\vec{\mathbf{k}}_{||}$ is given in the *extended zone scheme*, the value in the *reduced zone-scheme* can be obtained by subtracting a corresponding reciprocal-lattice vector $\vec{\mathbf{G}}_{||}$. Using experimental data and Eq. (1.49) we already can obtain $E(\vec{\mathbf{k}}_{||})$, however, determination of the perpendicular component of the momentum $\vec{\mathbf{k}}_{\perp}$, which is not conserved, is not so straightforward. One has to determine the dispersion of the final state (e.g. from theoretical calculations) or, in the simple approximation, one can assume nearly-free-electron character of the final state, i.e. parabolic dispersion starting from the bottom of the valence band E_0 (energy is determined relative to E_F):

$$E_f(\vec{\mathbf{k}}) = \frac{\hbar^2}{2m}(\vec{\mathbf{k}}_{||}^2 + \vec{\mathbf{k}}_{\perp}^2) - |E_0|, \tag{1.51}$$

$$\Rightarrow k_{\perp} = \sqrt{\frac{2m}{\hbar^2}(E_{kin}\cos^2\vartheta + V_0)} = \sqrt{K_{\perp}^2 + \frac{2m}{\hbar^2}V_0}, \tag{1.52}$$

$$\text{where we used} \qquad E_f = E_{kin} + \Phi_S, \quad V_0 = |E_0| + \Phi_S. \tag{1.53}$$

V_0 is called the inner potential of the solid and its value is usually considered an adjustable parameter. The most common and convenient method to determine V_0 in synchrotron-based ARPES experiments is by measuring the valence bands spectra in the normal to the surface direction and observation of the periodicity in the dependence of the bands' binding energies over the photon energy $\hbar\omega$. In the case of low-dimensional systems confined in the surface region (such as 2D-materials and, for instance, graphene), the $k_{\perp}$ variation is negligible and the electronic dispersion is well determined by $E(\vec{\mathbf{k}}_{||})$ [80].

1.3.1.4 Many-body interactions.

In ARPES the excited electron generally possesses sufficiently high energy to be able to escape into the vacuum faster than the system response time, thus we can make use of the *sudden approximation*, i.e. we assume that an electron is instantaneously removed from the system leaving an excited hole behind.

Up to this moment we were considering only the excited electron ignoring its interaction with the remaining electrons and other quasiparticles (such as holes, phonons and magnons) and impurities, however, since the sample is always a many-body system, a proper understanding of the observed band structures requires taking into account many-body interactions.

The usual approach to describe the average behavior of one particle in a many-body system is to use the time-ordered one-particle Green's function $G(t-t')$ [81], that can be interpreted as the probability amplitude that a particle added to the system in a Bloch state with momentum $\vec{\mathbf{k}}$ will remain in that state after a time $|t-t'|$. Usually it is more convenient to work with Green's function in energy-momentum representation $G(\vec{\mathbf{k}},\omega)$ by taking its Fourier transform.

In the sudden approximation we can consider removing of an electron with momentum $\vec{\mathbf{k}}$ as addition of a photohole with momentum $-\vec{\mathbf{k}}$ and the same energy. Then the Green's function can be interpreted as the probability amplitude that a hole added to the system will remain in the same state at a later time. It means that the ARPES spectra can be interpreted as describing behavior of the photohole instead of a photoelectron. In particular, the linewidth of the observed spectra reflects the properties of the photohole associated with the photoemission process: linewidths in the energy and momentum directions will reflect the inverse scattering time and length, respectively. In the absence of interactions the photohole has infinite lifetime and linewidth should be infinitely small (i.e. determined by the resolution of the experimental setup), however in the real-life interacting system the photohole will eventually decay through interactions leading to a finite lifetime and finite linewidth in the spectrum. Moreover, the many-body interactions manifest themselves in the shift (*renormalization*) of the photoholes' energy levels.

In the Green's function approach to the condensed matter problems [81] one introduces the many-body interactions as a correction to the Green's function, so-called *proper (irreducible) self-energy* $\Sigma(\vec{\mathbf{k}},\omega)=\operatorname{Re}\Sigma(\vec{\mathbf{k}},\omega)+i\operatorname{Im}\Sigma(\vec{\mathbf{k}},\omega)$, where ω is the electron energy with respect to the Fermi level. This is a complex function of particle momentum and energy and its real and imaginary parts account for energy renormalization and finite lifetime, respectively.* The self-energy corrected Green's function is given by

$$G(\vec{\mathbf{k}},\omega)=\frac{1}{\omega-\epsilon(\vec{\mathbf{k}})-\Sigma(\vec{\mathbf{k}},\omega)}, \tag{1.54}$$

where $\epsilon(\vec{\mathbf{k}})$ is the band energy of the electron, reflecting the "bare" band structure in the absence of the many-body interactions. Using Green's function formalism one can

---

[*] In general self energy contains all the information about the many-body interactions in the system even when the quasiparticle picture is no longer valid.

write the total photoemission intensity as

$$I(\vec{\mathbf{k}},\omega) \propto \sum_{i,f} \left| m_{i,f}(\vec{\mathbf{k}}) \right|^2 A(\vec{\mathbf{k}},\omega) f(\omega,T), \tag{1.55}$$

where we include the Fermi-Dirac distribution $f(\omega,T) = (1 + e^{\omega/k_B T})^{-1}$, reflecting that we can probe only the occupied states, and the one-particle spectral function [69, 81] $A(\vec{\mathbf{k}},\omega) = -(1/\pi)\,\mathrm{Im}\,G(\vec{\mathbf{k}},\omega)$, which can be expressed in terms of self-energy,

$$A(\vec{\mathbf{k}},\omega) = -\frac{1}{\pi} \frac{\mathrm{Im}\,\Sigma(\vec{\mathbf{k}},\omega)}{(\omega - \epsilon(\vec{\mathbf{k}}) - \mathrm{Re}\,\Sigma(\vec{\mathbf{k}},\omega))^2 + (\mathrm{Im}\,\Sigma(\vec{\mathbf{k}},\omega))^2}. \tag{1.56}$$

This function provides information about the allowed electronic states after removal (or addition) of electron and can be considered as a generalization of the density of states in case of many-body systems. The one-particle spectral function in the simplest case will have a Lorentzian shape with maximum shifted to $\epsilon(\vec{\mathbf{k}}) + \mathrm{Re}\,\Sigma(\vec{\mathbf{k}},\omega)$ and full width at half maximum $\Gamma(\vec{\mathbf{k}}) = 2\left|\mathrm{Im}\,\Sigma(\vec{\mathbf{k}},\omega)\right|$. Speaking more generally, the spectrum can be divided into a main coherent quasiparticle peak that includes the pole and an incoherent smooth part without poles leading to satellite peaks, as discussed above.

The full knowledge of $A(\vec{\mathbf{k}},\omega)$ would give us the imaginary part of Green's function $\mathrm{Im}\,G(\vec{\mathbf{k}},\omega) = -\pi A(\vec{\mathbf{k}},\omega)$. Since $G(\vec{\mathbf{k}},\omega)$ is constructed as a Fourier transform of a response function, it satisfies causality and therefore Kramers-Kronig relations connect its real and imaginary parts [82]. Thus, one can reconstruct full $G(\vec{\mathbf{k}},\omega)$ and finally obtain the self-energy from Eq. (1.54). However, in the ARPES experiment one is probing only the occupied states [see Eq. (1.55)] and to gain full information about the spectral function one has to perform high quality inverse photoemission spectroscopy (IPES) experiments or use certain approximations [83].

In the ARPES measurements the spectra $I(\vec{\mathbf{k}} = const, \omega)$ with a fixed momentum value are called the energy distribution curves (EDC) and the spectra with a constant energy $I(\vec{\mathbf{k}}, \omega = const)$ are called the momentum distribution curves (MDC).

1.3.1.5 ARPES spectrometer.

As of today there are two dominating spectrometer types used for measuring angle resolved photoemission spectra: combination of an advanced electron optical lens with a hemispherical deflection analyzer (HDA) and the time-of-flight (ToF) analyzer, the detailed comparison of both types can be found in Ref. [84]. The most basic difference is in the approach to energy analysis — in HDA electrons with different energies passing through the analyzer are separated in space, whether in the case of ToF they are separated by the time it takes them to reach the detector. In the latter case the lens system itself plays a role of energy analyzer and to achieve a competitive to HDA energy resolution one requires a very high time resolution not only of the electron detector but also of the excitation source.

HDA is an established workhorse of photoemission spectroscopy that combines high energy and angular resolution with flexibility in operation modes. The experimental setups used to prepare this thesis were equipped with this type of analyzer. A conventional HDA consists of an electrostatic input lens, a hemispherical deflector with entrance and exit slits, and an electron detector, that can be a channeltron or a microchannel plate (MCP). MCP is an array of miniature channels oriented parallel to one another that act as electron multipliers and form the first element of a two-dimensional positional electron detector [85]. Usually the full detector assembly consists of two microchannel plates stacked together,* a fast phosphor plate and a charge-coupled device (CCD) camera that captures the image of the phosphor screen. Nowadays detectors in HDA systems are generally based on MCP type electron multipliers [84].

The deflector consists of two concentric hemispheres of radii R_1 and R_2 that are kept at potentials V_1 and V_2. The resulting magnitude of central electrostatic field inside this hemispherical capacitor will be given by

$$E(r) = -\frac{V_2 - V_1}{R_2 - R_1}\frac{R_1 R_2}{r^2}. \tag{1.57}$$

It is easy to see that an electron entering the analyzer tangentially to an imaginary concentric sphere with radius r_e will have its trajectory constantly on this sphere if its kinetic energy T_{kin} satisfies $2T_{kin}/r_e = eE(r_e)$. Such kinetic energy is usually referred to as *pass energy* (E_p), because only those electrons that have kinetic energies close to this value will be able to pass through the hemispherical deflector and reach the detector. The pass energy also determines the energy resolution of the analyzer and in the measurements it is usually kept constant. The entrance slit of the analyzer is typically located at the distance of central radius $R_0 = (R_1 + R_2)/2$, so we will assume $r_e = R_0$ from now on. The pass energy can be predefined by selecting V_1 and V_2, for R_0 the relation is $E_p = e(V_2 - V_1)/(\frac{R_1}{R_2} - \frac{R_2}{R_1})$.

All electrons that enter the analyzer with energy E_p in different directions tangential to the above mentioned imaginary sphere will follow big circles of this sphere and will be effectively focused on its opposite side (see Fig. 1.7), at the location of the detector. If some electrons have equal kinetic energy larger than E_p they will follow elongated elliptic trajectories and focus further away from the center (and vice-versa).† Moreover,

---

[*] In the so-called "chevron" MCP design the channels in each of the separate plates are parallel to each other, but inclined at a small angle to the axis of MCPs. The two plates have opposite inclination angles, forming together V-shaped channels that provide higher amplification efficiency.

[†] The central field inside the analyzer has a $\propto 1/r$ potential, so one can imagine electron trajectories in the HDA as well-known Kepler trajectories of point masses in the gravitational field, i.e. conical sections with a focus in the center of the analyzer. This analogy helps to make many properties of the electron trajectories a bit more intuitive. The detailed analysis of electron trajectories in the ideal HDA can be found in [86].

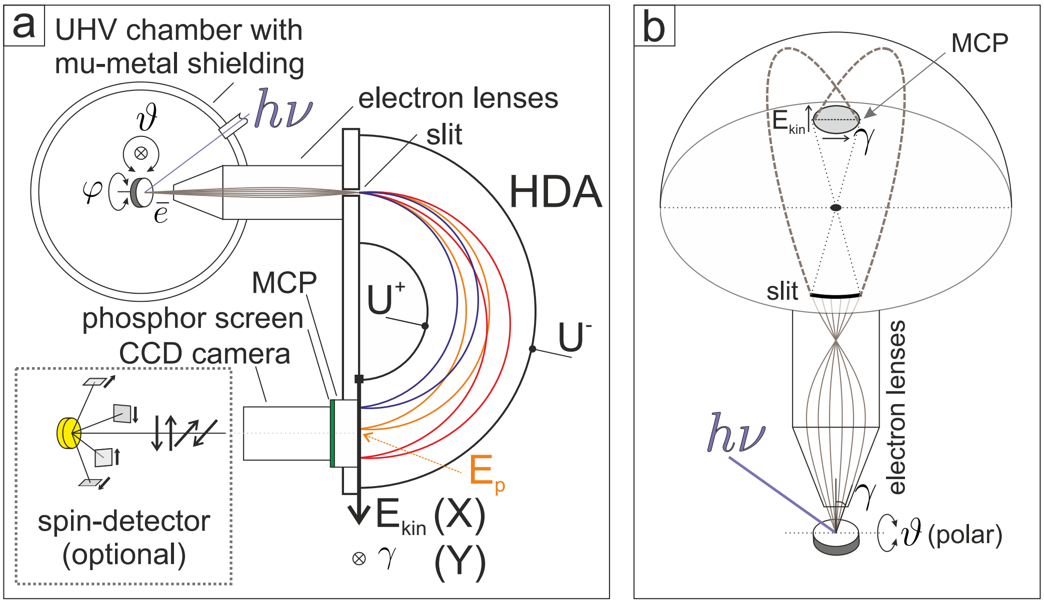

Figure 1.7: ARPES setup and trajectories of electrons in the HDA. (a) Top-view, sample inside the UHV chamber is illuminated by light with energy $h\nu$. Photoemitted electrons collected by electron lenses are separated in HDA by their E_{kin} and focussed on the MCP (E_{kin} is reflected by colours of trajectories, increasing from blue to orange to red, orange corresponds to pass energy). Optionally, the monochromatic beam of electrons after HDA can be transmitted or deflected to the spin-detector (see Section 1.3.1.6). (b) Side-view in perpendicular direction to (a). One can see how electrons with different $\vec{\mathbf{k}}$ emitted at angles γ are projected at different points of MCP. Only projection of $\vec{\mathbf{k}}$ parallel to the slit is measured at the same time, to vary the perpendicular component one can rotate the sample around the axis parallel to the slit (polar angle ϑ).

in the first approximation, the shift of the electron position on the detector will be linear with energy [84]. The image formed by monochromatic electrons passing through a narrow entrance slit represents a line of constant kinetic energy on the detector and electrons with different take-off angles will be projected in different points along this line [Fig. 1.7(b)]. However, for a straight slit this line will not be straight. The electrons entering the analyzer at the edge of such slit will be further away from the center than electrons entering the middle of the slit, as a result the electrons from the edge will end up on the detector in points closer to the center of the analyzer. Because of this effect straight entrance slit will be imaged as an arc with curvature radius $R_0/2$. To achieve a straight constant energy line on the detector (which is more convenient for further analysis) one can apply the reversibility of trajectories and use a curved entrance slit with radius $R_0/2$ instead of a straight one.[*]

---

[*] The preferential choice of a curved slit is actually not so straightforward, since a straight slit has an advantage that the electrons transmitted through the slit have initial directions distributed in one plane, i.e. only one component of surface parallel momentum is changing along the slit. A curved entrance slit will deviate from the lens mirror plane and lead to a curved cut in the momentum space.

Electrostatic lenses are used not only to collect the electrons emitted from the sample and distribute them onto the entrance slit in accordance to their take-off direction, but also to decelerate or accelerate the electrons to reach kinetic energy E_p, thus allowing to measure spectra in wide energy ranges by varying the lens retarding potential. The resulting image in the detector XY plane reflects the photoemission intensity with respect to two orthogonal coordinates — X (the radial one) can be converted to the kinetic energy (E_{kin}) and Y reflects the coordinate along the entrance slit (Fig. 1.7), which can be calibrated to directly show take-off angles of electrons (γ).

The energy resolution of HDA is determined mainly by its mean radius R_0, the slit width w and angular acceptance α in direction perpendicular to the slit. The slit width can be treated as an error in the radius r_e at which the electron enters the analyzer and, as was discussed above, electrons with the same energy but starting from different r_e will have different X coordinates on the detector, i.e. will be interpreted as electrons with different kinetic energies. The overall energy resolution will be given by:

$$\Delta E = E_p\left(\frac{w}{2R_0} + \frac{\alpha^2}{4}\right). \tag{1.58}$$

The angular resolution mainly depends on the density of channels on the detector and finite beam spot size of the excitation radiation. In both cases there is a trade-off between the resolution and intensity of the informative signal, i.e. the time needed for acquisition of the spectrum. A narrower entrance slit and lower pass energy will provide better energy resolution and a small aperture will reduce the size of the beam improving angular resolution, but all of these optimizations will significantly reduce the intensity. Hence a compromise combination of tunable parameters has to be selected in every specific experimental case to achieve a reasonable analyzer resolution.

Another purely experimental aspect that was not mentioned in the section 1.3.1.2 is related to the work function. In experiment the kinetic energy of the electron is measured by an analyzer that has its own work function, generally different from that of the sample. Even though analyzer and the sample are in electric contact during the measurements, only their Fermi levels are equilibrated, but not the vacuum levels, leading to a contact potential equal to $(\Phi_S - \Phi_A)$ — the difference in the work functions of sample and analyzer, respectively (Fig. 1.5). It means that all measured kinetic energies E_{kin}^{meas} will be shifted by this value and equation (1.35) can be transformed as

$$E_{kin}^{meas} = \hbar\omega - |E_B| - \Phi_S + (\Phi_S - \Phi_A) = \hbar\omega - |E_B| - \Phi_A. \tag{1.59}$$

The ultimate solution here is to use a straight slit and digitally rectify the detector image by applying an image transformation with precalibrated parameters. The computational possibilities of modern computers allow to perform such transformations in real time. [84] However, for HDA with large R_0 and room temperature measurements the effect of straight slit might be smeared out by temperature broadening of the spectrum.

It means that, surprisingly, the experimentally measured kinetic energy E_{kin}^{meas} does not depend on the value of Φ_S, that is different for each sample, but instead depends only on Φ_A that can be determined prior to the experiments and can stay technically constant for a long time.

1.3.1.6 Spin-resolved ARPES.

Conventional ARPES allows to determine the momenta and energies of electronic states, however, to fully describe the electronic state in the solid a third parameter is required — the spin. The spin state is described by Pauli spin-operator $\vec{\sigma}$ and since we will mainly speak about the averaged result of measurements of a large number of spins, we will use the expectation value of $\vec{\sigma}$ called spin polarization ($\vec{\mathbf{P}} = \langle\vec{\sigma}\rangle$).[*]

Generally speaking, the spin polarization of the photoemitted electrons reflects the spin polarization of the initial photoemission state.[†] This allows to experimentally determine the spin state of electrons in solid systems, giving access to a plethora of physical phenomena manifesting themselves in spin-polarized electronic states. This includes magnetism, spin–orbit interaction and related spin-textures in low-dimensional systems (see section 1.2.4, where spin-textures induced by the Rashba effect are discussed), moreover, in the non-trivial surface states of topological insulators the spin is locked to the electron momenta, forming a chiral spin-texture [90].

Unfortunately, electrons cannot be separated according to their spin projection in a simple way, as was done with neutral atoms in the Stern-Gerlach experiment [91–93]. Therefore many kinds of detectors have been developed to solve the task of experimental determination of the spin polarization of photoelectrons, most of them utilizing the effect of spin-dependent scattering of relativistic electrons on heavy atoms with high SOI, known as Mott scattering [94]. Other spin-detector designs utilize exchange scattering from a magnetic surface [95, 96] and spin-polarised low-energy electron diffraction (SPLEED) [97], in particular, a very efficient SPLEED spin-filter was recently designed for application in photoemission microscopy (PEEM) [98]. Compared to Mott-type

---

[*] Actually, this value depends on the reference frame due to relativistic effects [87], to remove this ambiguity we will refer to the polarization value measured in the rest frame of the electron in the following.

[†] The photon field that excites the electron does not couple to the spin degree of freedom directly, so in the first approximation one can consider the spin to be conserved in the process of photoemission. However, there is a variety of mechanisms that can introduce or change the spin polarization of photoelectrons, e.g. selection rules, spin-orbit effects and spin-polarized photoelectron diffraction in the final state of photoemission, or spin-dependent scattering processes during electron transport to the surface [87]. It is well known that circularly polarized light can often influence spin-polarized photoemission due to dipole selection rules [88, 89], therefore the observed spin polarizations may depend strongly on the final state of photoemission, i.e. on the photon energy. Relative importance of all these various effects may be difficult to predict, but interpretation of experimental results should be done keeping in mind that such effects exist.

these detectors work at much lower energies (typically around 100 eV compared to 20–120 keV in the case of Mott detectors [99]) and hence are more compact, however they are also more sensitive to surface contamination of the spin-selective element [87].

In the experiments presented in this thesis Mott type spin-detectors were used. The underlying theory describing elastic scattering of relativistic electrons on heavy atoms was developed by Sir N.F. Mott in 1929 [94]. The earliest reliable successful observation of this effect dates back to 1942 [100] and in 1969 the first spin-polarized *photoemission* measurements were performed by Busch et al. [101] with a Mott-type detector.

The basic physics of Mott-scattering can be described as following. When an electron with spin $\vec{\mathbf{s}}$ scatters in the radial potential $V(r)$ of a nucleus with atomic number Z, there is a term in the overall scattering potential which depends on the relative orientation of the incident electron spin $\vec{\mathbf{s}}$ and its orbital angular momentum $\vec{\mathbf{L}}$. This term is called spin-orbit potential V_{SO}, and it is given by

$$V_{SO} = \frac{1}{2m^2c^2}\frac{1}{r}\frac{\mathrm{d}V(r)}{\mathrm{d}r}\vec{\mathbf{L}}\cdot\vec{\mathbf{s}}. \tag{1.60}$$

By the origin this is the same spin-orbit interaction term from the expansion of the Dirac equation for relativistic electron that appeared in Eq. (1.27) along the discussion of SOI effects in section 1.2.4. In the same way the SOI effect can be explained by the magnetic field that the electron experiences in its rest frame [92]. It was shown by Mott [94] that V_{SO} should have a sizeable effect on scattering in the case of high-energy electrons and scattering atoms with large Z. Because of this Mott detectors operate at high voltages (20–120 kV) to accelerate electrons to relativistic velocities and the usual targets for Mott detectors are films of heavy elements, such as thorium, tungsten or gold owing to their large SOI.

As a result of the finite V_{SO} term, the differential scattering cross-section for electrons with non-zero polarization $\vec{\mathbf{P}}$ is not symmetric anymore and is given by [92]

$$\sigma(\theta) = \sigma_0(\theta)[1 + S(\theta)\vec{\mathbf{P}}\cdot\vec{\mathbf{n}}], \tag{1.61}$$

where θ is the scattering angle, $\sigma_0(\theta)$ — differential scattering cross-section for a non-polarized electron beam and $S(\theta)$ is called the analyzing power or Sherman function [92, 99]. The parameter $S(\theta)$ has to be calibrated experimentally, it depends on the target material and thickness (multiple scattering is more likely in thick targets) as well as on the electron kinetic energy and scattering angle. The unit vector $\vec{\mathbf{n}}$ is perpendicular to the scattering plane and its direction depends on the direction of scattering, $\vec{\mathbf{n}}$ can be defined as

$$\vec{\mathbf{n}} = \frac{\vec{\mathbf{k}}_1 \times \vec{\mathbf{k}}_2}{\left|\vec{\mathbf{k}}_1 \times \vec{\mathbf{k}}_2\right|}, \tag{1.62}$$

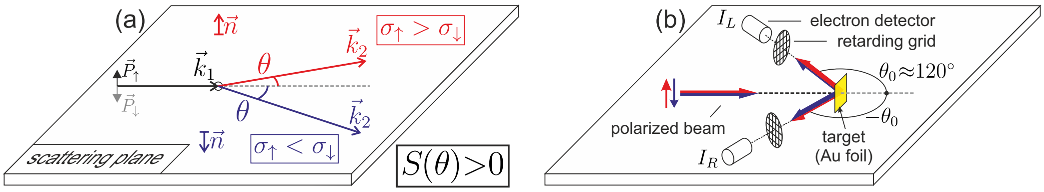

Figure 1.8: Schematic representation of Mott scattering for positive Sherman function. (a) Scattering of two beams with opposite polarizations. From Eq. (1.61) follows that the scattering cross-section in certain direction $\sigma(\theta)$ is larger for the beam with $\vec{\mathbf{P}} \parallel \vec{\mathbf{n}}$. (b) Working principle of Mott-detector: polarized electron beam is scattered from a heavy-element foil, the elastic electrons intensity is measured by two symmetrically placed detectors (I_L and I_R), while the inelastic background is suppressed by retarding grids.

where $\vec{\mathbf{k}}_1$ is the initial electron momentum and $\vec{\mathbf{k}}_2$ is the momentum after elastic scattering [see Fig. 1.8(a)]. Note that $\vec{\mathbf{n}}$ has *opposite orientations* for electrons that were scattered in the same plane, but to different sides.

The scalar product $\vec{\mathbf{P}} \cdot \vec{\mathbf{n}}$ in Eq. (1.61) reflects two important aspects: there is an asymmetry in the scattering cross-section for a spin-polarized beam, and this asymmetry depends only on the transversal (i.e. perpendicular to the beam) component of polarization [92].

In the experiment a selected beam of electrons with a certain kinetic energy and momentum is extracted from the analyzer and directed to the target [Fig. 1.8(b), see also Fig. 1.7(a)] (dependence of intensities on $E, \vec{\mathbf{k}}$ will be omitted for brevity). Two detectors placed symmetrically with respect to the electron beam axis (at angles $\pm\theta_0$) will measure the intensities of electrons scattered in the opposite directions (see Fig. 1.8(b)], let us call them left ($I_L = I(\theta_0)$) and right ($I_R = I(-\theta_0)$).*

The polarization component P_z along the direction perpendicular to the scattering plane (here z) can be calculated directly from the relative difference in the intensities. To see this one can use Eq. 1.61 (intensity is proportional to the scattering cross-section):

$$\begin{aligned} I_L &= I_0(\theta_0)(1 + S\vec{\mathbf{P}} \cdot \vec{\mathbf{n}}) = I_0(1 + SP_z), \\ I_R &= I_0(-\theta_0)(1 + S\vec{\mathbf{P}} \cdot \vec{\mathbf{n}}) = I_0(1 - SP_z), \end{aligned} \tag{1.63}$$

where I_0 is the intensity in the case of an unpolarized beam, which is equal for both directions and $S = S(\theta_0) = S(-\theta_0)$. It immediately follows that

$$I_0 = \frac{1}{2}(I_L + I_R), \tag{1.64}$$

$$P_z = \frac{1}{S}\frac{I_L - I_R}{2I_0} = \frac{A_z}{S}, \tag{1.65}$$

---

[*] The optimal angle θ_0 depends on the energy and the target material. For Au targets in a wide range of energies (from tens to hundreds keV) $|S|$ as a function of the scattering angle exhibits a broad maximum around $\theta_0 \approx 120°$ [102, 103] and this angle is often used in experimental setups. The actual value of the Sherman function for Au at 120° is negative (typically from -0.2 to -0.4 depending on the energy).

where A_z is the asymmetry in z direction defined as

$$A_z = \frac{I_L - I_R}{I_L + I_R}. \tag{1.66}$$

The polarization along one axis can be derived from the directly measurable intensities in two channels using Eq. 1.65. For an unpolarized beam the asymmetry is zero and for a 100% polarized beam it is equal to the Sherman function, thus a larger Sherman function means a higher spin-sensitivity of the detector.

For each electron in the beam there are only two possible values of spin projections on the z axis equal to $\pm\frac{\hbar}{2}$, corresponding to eigenvalues of σ_z $+1$ and -1. Let $N_\uparrow$ and $N_\downarrow$ be the numbers of electrons in the respective eigenstates, then the polarization of the beam is

$$P_z \equiv \langle \sigma_z \rangle = \frac{(+1)N_\uparrow + (-1)N_\downarrow}{N_\uparrow + N_\downarrow} = \frac{I_\uparrow - I_\downarrow}{I_\uparrow + I_\downarrow}. \tag{1.67}$$

$I_{\uparrow,\downarrow}$ are the components of intensity related to electrons with corresponding spin-projections along the z axis. Given that the spin-integrated intensity is $I_{tot} = I_\uparrow + I_\downarrow$, the two components can be extracted as

$$I_{\uparrow,\downarrow} = \frac{1 \pm P_z}{2} I_{tot}. \tag{1.68}$$

In a single device one can place two pairs of detectors in orthogonal scattering planes to be able to measure both spin components transverse to the beam direction at the same time. Even though the modulus of the electron spin vector is constant, the length of the vector $\vec{\mathbf{P}}$ is not necessary unity (for example, for a completely unpolarized beam it is zero), thus the remaining third polarization component cannot be simply calculated from the first two. However, by combining two of such 2-axis polarimeters in an orthogonal geometry a full three-dimensional picture of spin polarization can be achieved. The electron beam can be navigated to one of the polarimeters by electrostatic deflector lenses, conserving the spin orientation. One axis will be shared between both analyzers, which is useful for mutual calibration of detectors.

1.3.2 Technique of scanning tunneling microscopy

The development of the first scanning tunneling microscope (STM) by Binnig and Rohrer in early 1980-s [104–106] allowed to study local properties of surfaces with very high resolution, down to single atoms. Today STM is one of the most powerful methods of visualization and analysis of surfaces on the nanoscale, suitable for the investigation of surface topography, reconstructions of crystalline surfaces, adsorbate superstructures, overlayer growth mechanisms, surface dynamics and chemistry. At the same time STM can be used for visualization of local electronic structure and chemical- and spin-selective imaging, manipulation of individual atoms or molecules for nanofabrication and many other very delicate procedures requiring atomic precision [107].

The physical basis of the STM technique is quantum tunneling of electrons between the atoms of a sample surface and a sharp conductive tip positioned very close to each other. The probability of such tunneling has an abrupt exponential dependence on the distance between the tip and the surface, meaning that small changes in the distance between the tip and the sample result in strong changes in the tunneling current, providing very high sensitivity and resolution in the direction perpendicular to the surface. To achieve a microscopic image of the surface topography one can move the tip in a raster grid with small steps and measure the tunneling current. These high accuracy movements are usually done by a piezo-ceramic element, which allows to position the tip along the x-, y-, and z-axes with precision of tenths of angstroms.

If a bias voltage V is applied between the sample and the tip, which are separated by only several interatomic distances, electrons can tunnel from the occupied electronic states of the sample to the empty states of the tip or vice versa (Fig. 1.9).

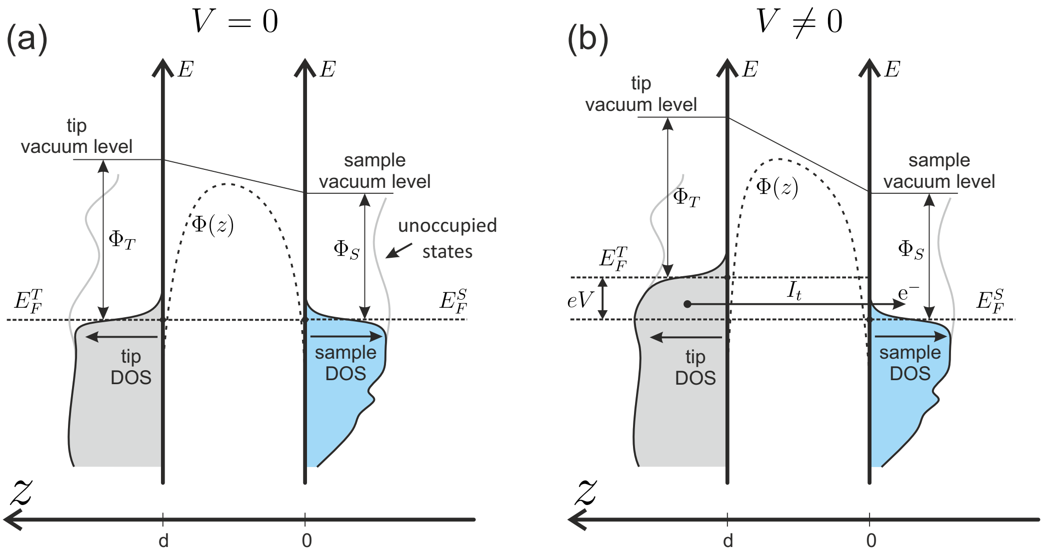

Figure 1.9: Tunneling between sample and tip located at distance d in the STM experiment. Dashed line schematically depicts the potential barrier in the tunneling gap. (a) Equilibrium situation, Fermi levels (E_F) of sample and tip are equalized, bias voltage is zero, no net tunneling current. (b) Bias voltage V applied, net tunneling current appears.

A net tunneling current I_t results from the difference of the numbers of electrons tunneling from sample to tip and in the opposite direction. Therefore it depends on the electron densities of states of the tip $\rho_t(E)$ and the sample surface $\rho_s(E)$ and can be derived as the following integral over energy (ε) [108]:

$$\begin{aligned} I_t = G_0 \frac{4\pi^2}{e} \int_{-\infty}^{\infty} [f(E_F - eV + \varepsilon) - f(E_F + \varepsilon)] \rho_t(E_F - eV + \varepsilon) \rho_s(E_F + \varepsilon) |M|^2 d\varepsilon \approx \\ \approx G_0 \frac{4\pi^2}{e} \int_{0}^{eV} \rho_t(E_F - eV + \varepsilon) \rho_s(E_F + \varepsilon) |M|^2 d\varepsilon, \end{aligned} \tag{1.69}$$

where $G_0 = 2e^2/h$ is the conductance quantum and $f(E) = (1 + e^{E-E_F/k_BT})^{-1}$ is the Fermi-Dirac distribution for temperature T. In the second line we assume that T is low enough to approximate $f(E)$ with a step-function (i.e. k_BT is much lower than the required energy resolution). M is the tunneling matrix element reflecting transition between the states of the tip and the sample, it can be evaluated in the formalism of Bardeen [109]. In general, the tunneling probability $|M|^2$ decays exponentially with the distance between the electrodes. This behavior is well known from the text-book solution for an electron with kinetic energy E tunneling through a 1D rectangular potential barrier of height $U_0 > E$ and width s. The probability for an electron to pass through the barrier is given by the barrier transmission coefficient T [110]:

$$T \propto e^{-2ks}, \quad k = \frac{1}{\hbar}\sqrt{2m(U_0 - E)}, \tag{1.70}$$

where k is the inverse decay length of the electron wave function. This is the simplest case, but a similar exponential dependence on the barrier width appears in the general case as well independently of the exact barrier shape [110]. Using typical values of the work function in metals for U_0 one can estimate that the tunneling current changes by one order of magnitude when the tip-sample separation is changed by only ~ 1 Å.

Another important property of STM experiment can be obtained under the assumption that $|M|$ does not change significantly in the energy region of integration in Eq. 1.69, in this case

$$I_t \propto \int_0^{eV} \rho_t(E_F - eV + \varepsilon)\rho_s(E_F + \varepsilon)d\varepsilon. \tag{1.71}$$

The measured signal is directly proportional not to the DOS of the sample, but to a convolution of the DOS of the sample and that of the tip, which contribute equally and, moreover, enter the equation in a symmetric form. This is the basis of the so-called STM reciprocity principle introduced by C. J. Chen [111] — probing the sample electron orbitals by the tip orbitals is equivalent to probing the tip orbitals by the sample orbitals. This fact also means that the electronic structure of the tip is always present in the experimental data, to probe the DOS of the sample with minimal influence of the tip states one has to use a tip with a constant or well-known DOS, for example made of a nearly-free-electron metal.

One of the first theoretical studies of the STM resolution taking into account the finite size of the tip was conducted by Tersoff and Hamann [112, 113]. They exploited a model of a spherical tip with s-like wave functions to simulate the STM experiment[*] and estimated the best lateral resolution achievable in this model as $r = \sqrt{2(d + R_t)k^{-1}}$, where d is the distance between the interacting tip and surface atoms, R_t is the curvature

---

[*] One has to be aware that Tersoff and Hamann used tip wave functions in a form of solutions of the Schrödinger equation in a macroscopic spherical potential well and not atomic s-like orbitals [113].

radius of the tip apex and the parameter $k^{-1} \approx 1$ Å. From this formula it is clear that even for the sharpest tip and $d = 4.5$ Å the resolution has a lower boundary of $r \geq 3$ Å.

The simulations produced in the framework of the Tersoff-Hamann model agree in many cases with experimental STM images, however, the resolutions achieved in experiments on metal surfaces are significantly *better* than the model estimations. This effect was explained later in theoretical works of C. J. Chen [111, 114], where the atomic resolution was attributed to d_{z^2} and p_z tip electron states. The origin of the resolution enhancement for these tip states lies in the so-called *derivative rule* introduced by Chen [114]: in the case of s-wave tip states the tunneling matrix element M is proportional to the sample wave function at the center of the tip apex atom, while for $l \neq 0$ tip states M is proportional to the *derivative* of the sample wave function. This rule can be formulated in a general way [108] and it is in a very good agreement with high-resolution STM experiments (see e.g. [115]). Therefore, d-band metals (such as Ir, Pt, W) and semiconductors with p_z dangling bonds are expected to be good materials for high resolution STM tips.

There are two main imaging modes used in STM: constant height mode (CHM) and constant current mode (CCM). In the first one the tip is moved only along x- and y- directions in a raster grid ($z = z_0 = const$) [Fig. 1.10(b)], the value of the tunneling current $I(x, y, z_0)$ is measured at each point and plotted as an image (values of I are displayed by color). In the CCM [Fig. 1.10(c)] one defines a desired value of the tunneling current I_0 (usually on the scale from pA to few nA) and while the raster is scanned the height of the tip is adjusted at every new point to maintain $I(x, y, z) = I_0$, then the values of the height $z(x, y)$ are plotted. The adjustment is done by passing the current difference to a feedback loop that controls the z-piezodrive.

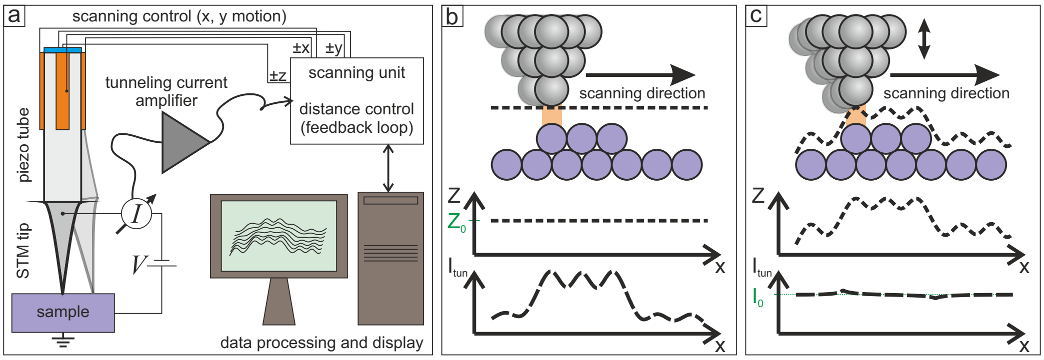

Figure 1.10: STM working principle (a) and two main modes of operation: constant height mode (b) and constant current mode (c).

The CCM is especially useful for surfaces with complicated atomic structures, large corrugations or adsorbed atoms and molecules, while CHM is suitable for flat samples. In both modes the resulting plot reflects simultaneously the surface topography and the convolution of the local density of electronic states (LDOS) tip and the sample. For the STM measurements presented in the current thesis only CCM was used, however both $z(x, y)$ ("Z channel") and $I(x, y)$ ("I channel") were measured at the same time. Since adjustment of the tip height does not happen instantaneously, image in the I channel is not completely "flat", but has positive and negative peaks in the areas where height was changing abruptly, e.g. borders of the atomic terraces [Fig. 1.10(c), bottom]. This makes I channel image similar to the derivative of $z(x, y)$ in the direction of scanning, which often helps to see the details of surface topography better.

Due to nanoscopic length scales in the STM measurements even small external mechanical vibrations may cause noise in the data or even lead to tip damage. For stable and reliable STM operation both passive and active damping systems are used to isolate the setup on multiple levels: the whole STM chamber is mechanically isolated from the laboratory and the scanner itself can be damped mechanically (by spring suspension) and magnetically. Moreover, working with room temperature STM, one has to stabilize the ambient conditions, such as temperature, electromagnetic noise and even sunlight.

The major part of the tunneling current flows only through the very end of the tip due to the abrupt distance dependence of the tunneling current. Basically, the actual probing zone of the tip is limited to a few or even one front atom at the apex. Because of this even a relatively blunt tip that still has natural nanoscale surface roughness can provide atomic resolution for some samples, since most of the current will be collected by a single front nano-protrusion on the surface. However, this will work only for samples with atomically flat surfaces without defects, and for the vast majority of experiments the sharpness of the apex of the tip is of great importance. As we discussed above, the ultimate lateral resolution is achieved when the surface is probed by specific orbitals of a single atom on the apex, thus the best tip has to be terminated by a single atom with a well-known orientation — this can be achieved in single crystalline tips. Reproducible and reliable preparation of sharp tips is possible only under UHV conditions. The description of the tip preparation procedure will be given in the experimental part.

In the majority of STM experiments tips made of chemically etched polycrystalline tungsten wire are used, since tungsten is a d-metal with very high stiffness.

1.3.3 Technique of low energy electron diffraction

Low energy electron diffraction (LEED) is a powerful method of surface characterization giving information about the characteristic periodicities of the surface structures.

In the very basic description of this technique a primary beam of electrons with certain kinetic energy E_p is incident on a crystal surface and the elastically scattered electrons, that carry information about the surface structure, are detected. The low kinetic energy of the primary beam electrons (typical values are from 20 to 200 eV) guarantees low penetration depth and high surface sensitivity (see Fig. 1.6 and discussion in section 1.3.1.2).

The incident and reflected beams can be considered plane waves and the reflected wave is formed as a result of elastic scattering (diffraction) of the incident wave on the surface atoms. In the elastic scattering process the absolute value of the incident electron's wavevector $\vec{\mathbf{k}}_0$ is conserved ($|\vec{\mathbf{k}}_0| = |\vec{\mathbf{k}}|$, where $\vec{\mathbf{k}}$ is the wavevector of the reflected electron), but the direction may change and the set of possible new directions will be determined by the condition for constructive interference. In the form of the Laue condition it is given by $\vec{\mathbf{k}} - \vec{\mathbf{k}}_0 = \vec{\mathbf{G}}_{hk}$, where $\vec{\mathbf{G}}_{hk} = h\vec{\mathbf{a}} + k\vec{\mathbf{b}}$ is a reciprocal vector of the surface lattice with basic lattice vectors $\vec{\mathbf{a}}$ and $\vec{\mathbf{b}}$. Here we exploited that in the case of low penetration depth only the component of the wavevector parallel to the surface will be changed. One has to note that in this assumption we deal with a 2D system and its lattice in the reciprocal space will be represented by rods perpendicular to the surface plane rather than points. The wavevectors that satisfy the above stated conditions can be constructed by the Ewald's sphere method. A diffracted beam related to parallel-momentum transfer $\hbar\vec{\mathbf{G}}_{hk}$ is conventionally indexed as (hk) [116].

In the pattern of diffracted peaks one can find information about the structure of the surface reconstructions and adsorbate superstructures that may have different translational symmetry from the bulk of the crystal. To describe such structures the following convention is used. If the ideal substrate surface has translational symmetry with unit translation vectors $(\vec{\mathbf{a}}_1, \vec{\mathbf{a}}_2)$ (lattice a) and the surface has unit translations $(\vec{\mathbf{b}}_1, \vec{\mathbf{b}}_2)$ (lattice b), each of the vectors rotated by the same angle α relative to $(\vec{\mathbf{a}}_1, \vec{\mathbf{a}}_2)$, then the surface periodicity is designated by $[(b_1/a_1) \times (b_2/a_2)]R\alpha$. If $\alpha = 0$ the angle designation is omitted. Conventionally, instead of $(\sqrt{2} \times \sqrt{2})R45°$ one can use $c(2{\times}2)$, where c stands for "centered", and $p(2{\times}2)$ ("primitive") is usually used instead of just (2×2). As an example in this notation W(110)$p(2{\times}2)$O means (110) face of W substrate crystal with p(2×2) superstructure of O atoms adsorbed on the surface. For atomically clean non-reconstructed surfaces the designation (1×1) is usually omitted so that, e.g. W(110) means W(110)(1×1).

Many of the observed structures can be described in this notation, however, in the most general case vectors $\vec{\mathbf{b}}_1$, $\vec{\mathbf{b}}_2$ are expressed as linear combinations of $\vec{\mathbf{a}}_1$, $\vec{\mathbf{a}}_2$, i.e. $(\vec{\mathbf{b}}_1, \vec{\mathbf{b}}_2)^T = M(\vec{\mathbf{a}}_1, \vec{\mathbf{a}}_2)^T$, and the matrix of coefficients M is used to designate the surface structure [117]. If the determinant $\det(M)$ is an integer, the surface lattice b is called *simple*. If $\det(M)$ is a rational fraction then the two lattices a and b come in coincidence at regular intervals and such lattice b is called *coincident*. In the last case of irrational $\det(M)$ the surface lattice b is *incommensurate*, i.e. for every two points related by translational symmetry of the lattice b their local surrounding in the lattice a will be different.

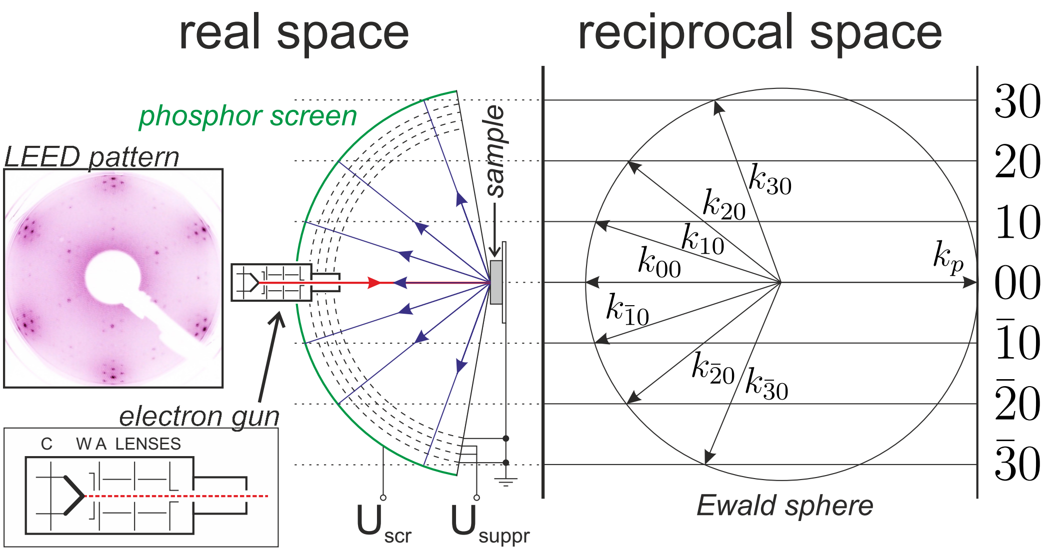

Figure 1.11: Principle scheme of LEED setup and formation of the diffraction pattern. In the middle is a scheme of a standard LEED setup with 4 grids. Parts of the electron gun are: C – cathode with hot filament (thick line); W – Wehnelt cylinder; A – anode; LENSES – system of adjustable electrostatic lenses*. On the right is a scheme of the Ewald construction used for determination of the possible diffraction directions for primary electrons with momentum k_p and reciprocal rods with different (hk) indices (labelled on the right). An example of a LEED pattern is shown in the inset on the left.

The typical LEED setup is shown schematically in Fig. 1.11. The electron gun produces a monochromatic beam of electrons with defined energy E_p ("primary" beam). The electrons diffracted from the sample surface are detected by a hemispherical fluorescent screen (or other position-sensitive detector). To provide enough energy for the excitation of fluorescent material low-energy electrons have to be accelerated by a high voltage U_{scr} applied between the screen and the last grid (typically 5–7 kV). The inelastic background can be suppressed by the retarding grids (2 middle grids in Fig. 1.11) kept at voltage $U_{suppr} = -(E_p - \Delta E)/e$, thus letting only the electrons with energy E_p through. The resulting angular distribution of intensity on the spherical surface of the screen $I(\phi, \theta)$ can be recorded and further analysed.

LEED is very useful in combination with STM, since it provides averaged structural information in reciprocal space from a large sample area (as opposed to local information in direct space in STM), thus it allows to conclude about the local or non-local nature of the structures observed in STM.

---

*The whole device can be considered as an electron optical scheme, where the sample acts as a mirror. A hot filament produces electrons that are accelerated towards the anode, the Wehnelt cylinder shapes the beam and focuses it to a so-called "cross-over" point and the lens system is adjusted in a way to project this cross-over point on the phosphor screen.

1.3.4 Graphene preparation

The characterization of basic physical properties of graphene was a breakthrough result first achieved by Novoselov and Geim [1], who were able to isolate a monolayer of graphite by using an adhesive tape to separate progressively thinner layers of highly oriented pyrolytic graphite (HOPG). This technique, called *mechanical exfoliation*, allows to achieve a flake of graphene with typically low defect concentrations and high electron mobility (see for example Ref. [118]). Other types of exfoliation exist that are able to produce larger amounts of graphene, such as *liquid-phase* exfoliation: a process, where interaction between the graphite layers is reduced by dispersing it in a solvent and ultrasonication helps to effectively separate the individual layers [119]. Both types of exfoliation provide rather small graphene flakes. However, for practical applications, such as fabrication of electronic devices, it is more convenient to use large-area single-crystalline graphene sheets that can be implemented in the existing technological cycle.

Multiple approaches to large-scale production of graphene are developed, the two most widely used among them are graphitization of semiconducting SiC crystals [120] and chemical vapour deposition synthesis on metals [121]. Both methods were first developed in the surface science community to grow monolayers of graphite on crystalline surfaces *long before* the works of Geim and Novoselov [122–125], but with increased interest in this topic these methods were refined and re-investigated in greater detail.

The basic idea of the first method is to anneal a single-crystal of SiC at certain temperature and pressure to cause thermal decomposition with sublimation of Si from the surface that leads to formation of graphene on a specific face of the crystal [120]. This method of graphene growth is popular in the scientific community, since it gives relatively high quality of graphene that comes already on a semiconducting substrate which is convenient for transport measurements. However, at the moment the chemical varoup deposition (CVD) approach is considered to give the best balance of quality, size and cost for mass production of graphene [121].

Chemical vapour deposition of graphene can be described as cracking of molecules of a gas (which is a source of carbon) at elevated temperature on a surface of a metallic substrate that acts both as a catalyst and as a structural precursor [Fig. 1.12(a)]. Typical choice for a source of carbon is a light hydrocarbon gas, such as methane or propylene. The exact mechanism of graphene formation in the CVD process depends on the catalytic activity of the metal and solubility of carbon in the substrate material both at the cracking and room temperatures [121].

The difference of the two major routes was well illustrated in the work of Li et al. [126], who used carbon isotopes ^{12}C and ^{13}C to investigate the mechanism of CVD graphene growth on Cu and Ni — two substrates with significantly different carbon solubilities. In both cases the first step was surface adsorption and catalytic decomposition of hydrocarbons with formation of carbon radicals. The results of Li et al. evidenced

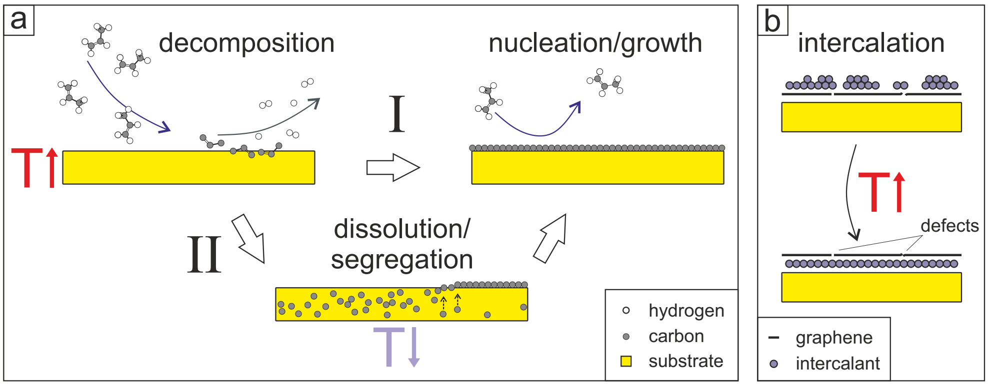

Figure 1.12: Schemes of (a) graphene preparation by CVD process and (b) its intercalation. (a) CVD growth of graphene. Hydrocarbon gas is decomposed on the hot substrate surface forming carbon radicals which either directly form a graphene sheet (route I) or dissolve in the substrate and graphene is formed by segregation of carbon after cooling (route II). A complete graphene layer passivates the substrate and prevents further hydrocarbon decomposition. (b) Typical scheme of intercalation process: material is deposited on top of graphene and by thermal diffusion during annealing it passes through nanoscale defects and occupies the graphene-substrate interface.

that for Cu (low C solubility) the subsequent formation of graphene is predominantly due to thermal diffusion of the carbon radicals on the surface rearranging to form a honeycomb graphene lattice. The graphene layer occupying part of the surface area is catalytically inactive and as it grows the area where catalytic decomposition is still possible constantly reduces, therefore, the growth process slows down and practically stops after the formation of the full graphene layer, making this process "self-limiting" [127]. In contrast, for the Ni substrate due to high carbon solubility a large part of carbon radicals can migrate to the *subsurface region* of the substrate by thermal diffusion. The amount of dissolved carbon is limited by the carbon solubility at the growth temperature or by the time of exposition to the carbon source. During cooling the solubility of carbon reduces and at a certain temperature supersaturation is reached leading to a segregation of carbon on the surface in the form of graphite with thickness depending on the growth conditions [128]. By careful control over the cooling rate and the amount of dissolved carbon one can achieve precisely a monolayer of graphene [129].

The segregation growth is expected to happen also on other substrates with high carbon solubility [125, 130, 131], whereas surface adsorption occurs on other substrates with low carbon solubility. However, in the intermediate cases both regimes can coexist (for example in Cu-Ni alloys [132]).

CVD synthesis of graphene has been achieved and investigated on a variety of transition metals, including Ni [133–136], Co [137–139], Cu [127], Ir [57, 140, 141], Pt [142, 143], Ru [144, 145], Rh [146, 147], Re [148, 149] and more recently Fe [150, 151]. In some cases graphene can be grown by the CVD process on transition metal *carbides*, such as TiC, TaC, HfC [152, 153] and a small number of other more exotic substrates [124, 125, 154].

The list of available substrates is not very long and direct CVD growth of single-crystalline epitaxial graphene on some metals is problematic, this is especially true for weakly interacting substrates, such as Au, Ag, Pt. However, one can overcome this issue and prepare many more epitaxial interfaces with graphene by growing graphene on a strongly interacting substrate and *intercalating* the material of interest in the interface between graphene and the substrate [Fig. 1.12(b)]. The list of interfaces already realized by this method is rather large and is constantly expanding, some of the prominent examples that have to be mentioned are: weakly interacting noble metals Au, Ag and Cu [134, 155–159]; elements realizing magnetic order (Mn, Fe) [160, 161]; rare earth metals [162]; semiconductors (Si, Ge) [163–165]; alkali metals (Cs, K, Na, Li) [136, 166–168]. Moreover, even intercalation of large fullerene molecules is possible [169]. This variety of materials with different properties makes it possible to control multiple aspects of the graphene-metal interfaces, including charge transfer, A-B sublattice asymmetry, spin-orbit and exchange interactions, etc., all of these parameters are reflected in the band structure and properties of the Dirac fermions in graphene.

The exact mechanism of intercalation is not fully established, generally it is attributed to diffusion through defects in the graphene sheet, such as holes and domain borders, because direct penetration of metal atoms through graphene hexagons is energetically unlikely. However, in some cases alternative mechanisms are possible, for example with local destruction and restoration of the graphene sheet in the case of Ni intercalation [154].

All of the described graphene-metal interfaces can be roughly divided into two large classes based on the strength of interaction between graphene and the substrate. The first is strongly interacting chemisorbed graphene that has significantly modified Dirac cone dispersion and electronic properties (prominent examples of substrates are Ni(111), Co(0001), Re(0001), etc.). The second class is weakly bound, physisorbed graphene, with dispersion resembling free-standing graphene (e.g. Ir(111), SiC(0001) and graphene supported by noble metals).

1.3.5 Moiré patterns

If two periodic patterns with slightly different reciprocal lattice vectors $\vec{\mathbf{k}}_1$ and $\vec{\mathbf{k}}_2$ are overlaid, they produce an apparent spatial beating pattern with a larger-scale periodicity, which is called a *moiré pattern* and has a reciprocal lattice vector

$$\vec{\mathbf{k}}_m = \vec{\mathbf{k}}_1 - \vec{\mathbf{k}}_2. \tag{1.72}$$

Moiré patterns are a very common feature of epitaxially grown layers due to a lattice mismatch between the overlayer and the substrate, which is in most cases small but

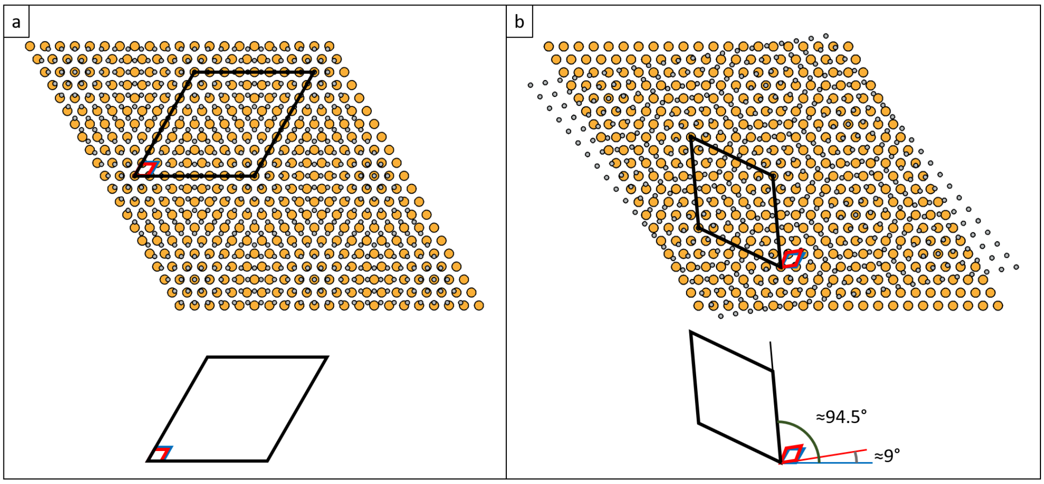

Figure 1.13: Mechanism of formation of moiré patterns due to: (a) lattice mismatch, in this case 9 periods of the overlayer match with 8 periods of the substrate; (b) rotation of two equivalent lattices by a small angle (in this case $\alpha \approx 9°$). One can prove using (1.72) that the resulting moiré pattern supercell will be rotated by $(\pi + \alpha)/2$ (here $\approx 94.5°$).

finite. Such pattern appears not only if one lattice is expanded relative to another, but also if two lattices are rotated by a small angle [Figs. 1.13 (a,b)].

It seems not that obvious that the "visual" effect of overlapping lattices could be detected by direct observation with STM. However, there is always some interaction between the substrate and the overlayer material that influences the electronic landscape probed by STM.* This interaction may change the topography of the surface or only the LDOS and its strength depends on the nature of both interacting substrate and overlayer, resulting in different contrast of the moiré pattern. But, independently of how pronounced it is, the moiré pattern has to obey the geometric rules stated above and the possibility of its detection depends mostly on the sensitivity of the probe. Even in the case of weakly-interacting graphene on Ir(111) or Pt(111) such moiré patterns are clearly observed in STM [170, 171]. Moreover, moiré patterns can be detected indirectly as superstructural effects in reciprocal space, which are commonly observed in LEED (as superstructural spots) and in ARPES (as band replicas, see e.g. Refs. [59, 172]) and very recently moiré patterns were detected in *transmission* of low energy electrons through twisted bilayer graphene both in diffraction (reciprocal space) and in-line holography (real space) modes [173].

---

*Even in the hypothetical case of completely non-interacting materials, there is still a possibility that the substrate has electronic states that extend far above the surface and it is possible to probe them "through" the overlayer, this way both lattices can be visualized simultaneously producing the moiré pattern.

1.3.6 Density functional theory

Many theoretical approaches were developed to predict and analyze the electronic band structures of the molecules and solids. One of the most widely used, robust and efficient for many-electron systems is the density-functional theory (DFT).

The determination of a band structure for a many-body system is not simple. One can start with the Schrödinger equation in the Born-Oppenheimer approximation:

$$H\Psi = \left(T^e + V^{n-n} + V^{e-n} + V^{e-e}\right)\Psi = E\Psi, \tag{1.73}$$

where T^e is the operator of kinetic energy for all N electrons, V^{n-n} reflects the electrostatic interaction between all nuclei, V^{e-n} is the interaction between electrons and nuclei and finally V^{e-e} stands for electron-electron interaction energy. We are interested in the ground-state energy of the system, E_0. However, since this is a many-body problem, it is impossible to solve it exactly in any practical case. The main difficulty comes from the term V^{e-e} that depends on 3N coordinates of electrons. To overcome this issue, the DFT approach works with the ground state *electron density distribution* $n_0(\vec{\mathbf{r}})$ instead of the many-body wavefunction. This reduces the number of variables to only 3 spatial coordinates. The solid theoretical basis of DFT was developed by Hohenberg and Kohn in 1964 [174]. They proved that the many-body ground state and its observables are unique functionals of $n = n(\vec{\mathbf{r}})$. Moreover, the ground state electronic energy functional $E^e = E^e[n]$ realizes its minimum on the ground state density $n_0 = n_0(\vec{\mathbf{r}})$ and this minimum provides the ground state energy, i.e.,

$$E_0^e = E_0^e[n_0] = \min_{n(\vec{\mathbf{r}})} \left\langle \Psi[n] \middle| T^e + V^{e-n} + V^{e-e} \middle| \Psi[n] \right\rangle . \tag{1.74}$$

For a sufficiently simple functional $E^e[n]$ determination of the energy would be an easy variational problem. Unfortunately, direct evaluation of the kinetic energy functional for the system of interacting electrons is not possible. One can write the electron-nuclei interaction in terms of electronic density as

$$V^{e-n}[n] = \int V(\vec{\mathbf{r}}) n(\vec{\mathbf{r}})\, \mathrm{d}^3\vec{\mathbf{r}}, \tag{1.75}$$

and also separate from electron-electron interaction the Coulomb term $E^C[n]$ as

$$E^C[n] = \frac{e^2}{2} \iint \frac{n(\vec{\mathbf{r}})n(\vec{\mathbf{r}}')}{|\vec{\mathbf{r}} - \vec{\mathbf{r}}'|}\, \mathrm{d}^3\vec{\mathbf{r}}\, \mathrm{d}^3\vec{\mathbf{r}}' . \tag{1.76}$$

Approximating T^e with the kinetic energy of a system of non-interacting electrons T_s^e:

$$E^e[n] = T_s^e[n] + \int V(\vec{\mathbf{r}}) n(\vec{\mathbf{r}})\, \mathrm{d}^3\vec{\mathbf{r}} + \frac{e^2}{2} \iint \frac{n(\vec{\mathbf{r}})n(\vec{\mathbf{r}}')}{|\vec{\mathbf{r}} - \vec{\mathbf{r}}'|}\, \mathrm{d}^3\vec{\mathbf{r}}\, \mathrm{d}^3\vec{\mathbf{r}}' + E^{xc}[n], \tag{1.77}$$

where E^{xc} describes the exchange and correlation effects.

Kohn and Sham [175] have shown that using the stationary property of Eq. 1.77 and applying variational method one gets exactly the same equations as in the case of non-interacting electrons moving in the potential V^{eff},

$$\begin{aligned} V^{eff}(\vec{\mathbf{r}}) &= \frac{\delta\big(\int V(\vec{\mathbf{r}})n(\vec{\mathbf{r}})\,\mathrm{d}^3\vec{\mathbf{r}} + E^C[n] + E^{xc}[n]\big)}{\delta n(\vec{\mathbf{r}})} = \\ &= V(\vec{\mathbf{r}}) + e^2 \int \frac{n(\vec{\mathbf{r}}')}{|\vec{\mathbf{r}} - \vec{\mathbf{r}}'|}\,\mathrm{d}^3\vec{\mathbf{r}}' + \frac{\delta E^{xc}[n]}{\delta n(\vec{\mathbf{r}})}. \end{aligned} \tag{1.78}$$

Inserting this effective potential in the single-particle Schrödinger equation and solving it one can get the eigenvectors $\phi_i(\vec{\mathbf{r}})$ that reproduce the initial electron density

$$n(\vec{\mathbf{r}}) = \sum_{i=1}^{N} |\phi_i(\vec{\mathbf{r}})|^2. \tag{1.79}$$

The Eqs. 1.78–1.79 (Kohn-Sham equations) are all interconnected and should be treated in a self-consistent way. One can start with an initial guess of $n(\vec{\mathbf{r}})$, calculate V^{eff}, find ϕ_i and finally calculate the new density $n_1(\vec{\mathbf{r}})$ using the Eq. 1.79. The whole process can be repeated with $n_1(\vec{\mathbf{r}})$ producing $n_2(\vec{\mathbf{r}})$ and so on until it converges.

The main difficulty (and an area of intense research) is the form of the exchange and correlation functional $E^{xc}[n]$. Due to the complexity of the underlying physical effects this term has to be approximated and there are many different ways to do it. The simplest one is the *local-density approximation* that assumes that the exchange-correlation energy per particle is a known function of n. The more advanced "semi-local" functionals take into account also the *gradient* of electron density (*generalised gradient approximation* or GGA). One of the most widely used exchange-correlation functionals developed by Perdew, Burke and Ernzerhof (PBE) [176] belongs to the latter class. A more detailed introduction to DFT can be found in Ref. [177] and references therein.

1.4 Experimental aspects

1.4.1 UHV

Surface purity is a paramount concern in experiments on crystal surfaces. Therefore, all experiments are performed in ultra-high vacuum (UHV), starting with the preparation of atomically clean sample surfaces by special techniques such as cleaving, ion sputtering, deposition of chemically pure materials etc. During the experiments the surface condition has to be monitored (for example, the surface purity can be verified by XPS and the surface order by LEED).

Contamination of the surface by adsorbates will happen at any finite pressure, however, the *time* τ before one full monolayer of adsorbate will be formed on the surface is inversely proportional to the pressure in the experimental chamber. Of course, τ

depends on the nature of the adsorbate and the surface, but in general one can estimate that at a pressure $p \approx 10^{-6}$ mbar τ is on the scale of few seconds, while for typical UHV conditions $p \approx 10^{-10}$ mbar, therefore τ is four orders of magnitude larger — on the scale of many *hours*. This makes UHV a prerequisite for all surface science experiments.

In our experiments base pressure was below 3×10^{-10} mbar. The prepared samples have been transferred between ARPES and STM chambers in a UHV suitcase.

1.4.2 ARPES

ARPES measurements were mainly conducted at the beamline UE112-PGM2 at the BESSY II synchrotron facility. The heart of the beamline is the APPLE II undulator UE112 that produces intense radiation in a range of photon energies well suited for ARPES experiments (9 – 250 eV). Moreover, the design of APPLE II undulators allows to control the polarization of the radiation, in the case of UE112 it can be selected to be linear (arbitrary orientation) or circular (positive or negative). In the experiments presented in this thesis linear p-polarized (i.e. parallel to the plane of incidence) light was used if not stated differently.

The endstation ARPES 1^2 [178] is equipped with a Scienta R8000 HDA and a 6-axis sample manipulator (3 translational and 3 rotational independent axes). The emission angle of a photoelectron carries important momentum information and to ensure high momentum resolution one has to avoid any fields in the vacuum chamber disturbing the paths of photoelectrons. For this reason ARPES vacuum chambers are protected from external magnetic fields by an internal shielding made of mu-metal — a special alloy with very high permeability mainly composed of nickel and iron. The overall resolutions of the experiment were 0.3° (angular) and 10 meV (energy).

Spectra have been measured in a parallel angular detection mode, the sample was illuminated by light with constant photon energy while the energies of the emitted electrons were scanned by the electrostatic lenses of the analyzer. ARPES mapping was performed by stepwise polar rotation of the sample and acquisition of ARPES spectra for each value of the polar angle. The data was further converted from angular to momentum space using the formulas described above (Eq. 1.47).

Spin-resolved ARPES experiments have been performed at the Russian-German beamline 2 (RGBL2) at BESSY II which is based on the U125-2 undulator. The RGBL2 endstation is similar to ARPES 1^2 in most aspects except that its Scienta R4000 HDA is additionally coupled to two Rice University Mott-type spin polarimeters operated at 25 kV. They allow to detect the spin-polarization of electrons along all three axes of quantization. Linear p-polarized light has been used for the excitation. Overall energy and angular resolution of the spin-resolved spectra is defined by the apertures and was 46 meV and 0.75°. Despite the fact that the energy resolution is relatively low in spin-resolved mode, it does not limit the ability to detect spin-splittings in the band structure that are smaller than 46 meV [179]. The reason is that the spectral peaks from opposite spin-channels are measured independently and the energy shift between them can be determined with high precision. The detection limit depends on the statistics and in this case estimated as ~ 5 meV.

1.4.3 STM

STM measurements were performed at room temperature with VT STM (Omicron). The whole setup including the STM and a preparation chamber was isolated from the mechanical vibrations by active pneumatic supports (Newport).

The STM tips were prepared from a polycrystalline tungsten wire (99.995% purity) that was cut and electrochemically etched in a solution of NaOH (20% by weight). During the procedure the wire is partially submerged in the solution and etching is happening mainly in the meniscus region, forming a "neck" that gets narrower and at some point the bottom part of wire falls down under its own weight, leaving a sharp tip on the top part of the wire. The etching current is constantly monitored: if it drops below a certain limit, this is a signal that the bottom part fell down, at this point the power supply is automatically switched off to avoid further etching that will lead to blunting. The as-etched tip is rinsed in distilled water and dried. It is known that after such preparation the tip still has a 5–10 nm insulating oxide layer on the surface [180, 181] and probably some residuals of the etching solution. The contamination is removed by electron-beam heating of the tip in vacuum before its installation in the STM [180, 182].

The base pressure in the vacuum chambers of the STM setup was better than $3{\times}10^{-10}$ mbar. All STM images were acquired in constant current mode and with a positive bias voltage on the tip (i.e. the *occupied* states of the sample were probed).

1.4.4 Software used for data analysis

The (spin-)ARPES spectra were analyzed using custom scripts developed in our group for IGOR Pro software (WaveMetrics, Inc.). Visualization of the atomic structures was performed with VESTA [183]. STM data was analyzed with help of the software SCALA Pro (Omicron NanoTechnology GmbH) and Gwyddion (open-source [184]).

Other software products that were significant for writing and preparation of visual materials of the current thesis include CorelDRAW, TeXstudio, JabRef, MATLAB and Mathematica.

Chapter 2

Giant Rashba effect in graphene intercalated with gold nanoclusters

Structural and electronic properties of graphene can be modified in intriguing ways by contact to metals. In particular, epitaxial graphene on certain substrates intercalated with heavy noble metals, such as gold or iridium, display an overall band structure similar to that of a free-standing graphene, but its Dirac cone exhibits a Rashba-type spin-texture with a relatively strong spin splitting. This effect was discovered experimentally in 2008, however a quantitative explanation is yet missing and the exact mechanism leading to the spin splitting of a large magnitude is still a matter of debate.

The following Chapter is devoted to the investigation of the possible origin of this Rashba-effect in the graphene/Au/Ni(111) system in connection with its peculiar surface structure observed in STM. An overview of existing up to date experimental and theoretical work on this topic will be given as a starting point. We will present the available results for Rashba-effect studied by ARPES and spin-ARPES techniques. To explain those results the surface structure of the prepared samples will be extensively studied by means of STM and various types of observed structures will be listed and analyzed. Among them we describe a new structure that is attributed to ordered arrays of intercalated Au nanoclusters, which is further modelled theoretically and tested as a possible source of the Rashba-effect under investigation. For that we exploit density functional theory (DFT) to first identify the energetically favourable atomic configurations and then to perform band structure calculations for the obtained model structures and compare the results with the experiment.

2.1 Introduction

Introducing the beautiful theoretical picture of Dirac fermions in graphene one usually considers an idealized sheet of *free-standing* graphene isolated from other bodies. However, in a more realistic picture, for any practical purpose graphene has to be in contact with other materials — it could be either electrical contacts or at least some supporting frame or grid. Moreover, for application in electronics, large areas of high-quality single-crystalline graphene have to be manufactured and at the moment one of the most successful approaches to do that is CVD synthesis of epitaxial graphene on metallic substrates. But the presence of a substrate is not just an inevitable shortcoming of the real world, on the contrary, it gives unique possibilities to *tune* the properties of graphene in a great variety of ways.

In Section 1.2.4 we already discussed some particular cases of how interaction with the substrate can influence the properties of graphene. In general, epitaxial contact with metallic substrates can induce a large variety of effects in graphene, affecting its structural, electronic and magnetic properties [154, 185, 186]. Ideally, by studying the nature of these effects, one can learn how to achieve the desired set of properties in graphene by preparing a specific substrate. For example, one can control the charge doping and band gap [155, 156, 187–189], turn graphene into a spin-filter [190] or induce certain spin-textures in the Dirac cone [4, 138, 191, 192]. On the other hand, the substrate can induce stress or superstructural periodicity shaping graphene on the nanoscale and resulting in moiré patterns and quantum size effects [140, 141, 193, 194].

The fruitful field of studying epitaxial graphene on various substrates has an obvious shortcoming — not every desired substrate supports direct growth of graphene. As we discussed in Section 1.3.4, the choice of substrates suitable for CVD growth is limited mainly to d-metals, however, the list of graphene-metal interfaces that one can achieve is significantly extended by the possibility of intercalation.

This chapter is devoted to a special case of such interfaces — graphene on Ni(111) intercalated with gold (further denoted as Gr/Au/Ni(111)): a system that displays in experiments a surprisingly large Rashba-effect induced in graphene by proximity to gold, a metal with high SOI.

The Rashba-effect [31] lifts spin degeneracy due to spin-orbit interaction in combination with the inversion symmetry breaking at the surface.[*] It manifests itself in the band structure of materials by formation of a chiral spin-texture of the spin-split bands in momentum space. The theory of the Rashba-effect and its application to graphene were discussed in detail in the Section 1.2.4.

An important point is that the intrinsic spin-orbit interaction in pure graphene is very small [5, 195]. The proximity-induced *extrinsic* spin-orbit interaction of significant

---

[*] In general, the definition of Rashba-effect is wider and not limited by the surface, here we use the usual meaning of this term employed in surface science.

magnitude enables to manipulate spins of electrons passing through graphene without external magnetic field or ferromagnetic materials. Therefore, such effect is important for application of graphene for active elements of spintronic devices, such as the Datta-Das spin field-effect transistor [3].

However, there is a very limited number of systems where the large Rashba-effect in the Dirac cone of epitaxial graphene was experimentally realized: except Gr/Au/Ni(111) important examples are graphene on Ir(111) and gold-intercalated graphene on SiC(0001) or Fe(110) [4, 57–62].

2.2 Historical overview

From the early experiments with graphene on metal surfaces it is well-known that some intercalants, including noble metals, can electronically decouple graphene from strongly-interacting substrates that is reflected in "stiffening" of the phonon modes [196, 197]. The first high-resolution ARPES experiments with Gr/Au/Ni(111) [157] confirmed the decoupling of graphene from Ni(111) after intercalation of gold, moreover, they revealed a quasi-free-standing character of graphene band structure: linearly dispersing π-band and a gapless Dirac cone with its Dirac point almost at the Fermi level (with only slight p-doping) in agreement with the earlier theoretical prediction for graphene/Au(111) [187]. Spin-ARPES data showed (13 ± 3) meV spin splitting of the Dirac cone. Optimization of sample preparation technique allowed later to achieve a much larger spin splitting of ~ 100 meV, furthermore, the directions of spin-polarization were in a good agreement with a Rashba-like spin-texture. This result was attributed to a proximity-induced Rashba-effect [4]. The origin of this effect lies in hybridization between the out-of-plane p_z-orbitals of graphene and $5d$ orbitals of Au [4, 58], this hybridization can be clearly observed in the ARPES spectra (see e.g. Fig. 2(c) from Ref. [4]).

The leading role of π–d hybridization with a high-Z element for spin splitting of the Dirac cone was later confirmed by a specially designed experiment [58]: instead of gold graphene was intercalated by bismuth — a heavy element that lacks d-states in the valence band, and in this case only spin splitting values ≤ 10 meV were detected (close to the detection limit). Moreover, in further experiments intercalation of both 0.5 ML Bi and 0.5 ML Au at the same time resulted in intermediate spin splitting values of $\sim 40 - 50$ meV [60].

Ab initio calculations performed for Gr/Au/Ni(111) system with a complete monolayer of intercalated gold [4] also predict a Rashba-type spin-structure in qualitative agreement with the experiment. However, the theoretically estimated value of spin splitting is only around ~ 10 meV. The reason is that gold acts as a weakly interacting substrate and, even though it has strong SOI, the equilibrium distance between the graphene and the Au layer of 3.3 Å (which is in agreement with the result for graphene/Au(111) [187]) is too large for the experimentally observed spin splitting to be produced. Artificially reducing the graphene-Au separation in calculations [4, 198] one can figure out that the splitting starts to increase rapidly at smaller distances, but it reaches 100 meV only at 2.3 Å, which is unrealistically far from equilibrium (Fig. 2.1). The result of such artificial "pressing" of graphene depends strongly on the exact configuration of the graphene-Au interface. In an "on-top" configuration carbon atoms of one sublattice are located directly above the Au atoms, in this case the different potentials on A and B graphene sites lead to a sublattice asymmetry that enhances even more when the graphene-Au separation is reduced. The effect of this is opening of a band-gap in the Dirac cone (see Section 1.2.3), thus only a configuration that keeps the A-B sublattice symmetry perfectly intact can display a gapless Dirac cone after "pressing". This is possible only in a "hollow-site" geometry, i.e. when Au atoms are located below the centers of graphene hexagons [Fig. 2.1 (a)].

It seems that in the model of a full monolayer of intercalated gold it is impossible to satisfy both experimentally observed properties — quasi-free-standing character of graphene and strong SO-splitting in the Dirac cone. Attempts were made to model the intercalated gold as a $p(2 \times 2)$ overlayer on Ni(111), such assumption leads to a 2.3 Å equilibrium distance and 60 meV spin splitting in the Dirac cone, but such structure was neither supported by STM nor by LEED data [4].

Even though the Au $p(2 \times 2)$ overlayer was not confirmed, the general theoretical result is interesting: the layer of gold with only 0.25 ML coverage can induce 6 times *stronger* spin-orbit interaction in graphene than a full monolayer of gold. This surprising effect is achieved by attraction of graphene to the gold-free areas that effectively press it closer to gold atoms, increasing the proximity-induced spin-orbit effects. A similar idea will be exploited further to explain the experimental results obtained in this work.

To date, the details of the mechanism leading to a giant ($\sim$ 100 meV) spin splitting of the Dirac cone in Au-intercalated graphene on Ni(111) have remained a topic of discussion and in this chapter we propose a new possible structural explanation.

2.3 Experimental details

The unexplained giant Rashba spin splitting could be determined by the structural details of the Gr/Au/Ni(111), as in the hypothetical example of a Au(2×2) interlayer discussed above. To explore this possibility we conducted an extensive STM study of Gr/Au/Ni(111).

First of all, we had to compare two types of substrates typically used in experiments: the Ni(111) surface was prepared either as a clean face of bulk single crystalline Ni or as a surface of a thin (15–20 ML) film of Ni deposited on a W(110) single crystal.

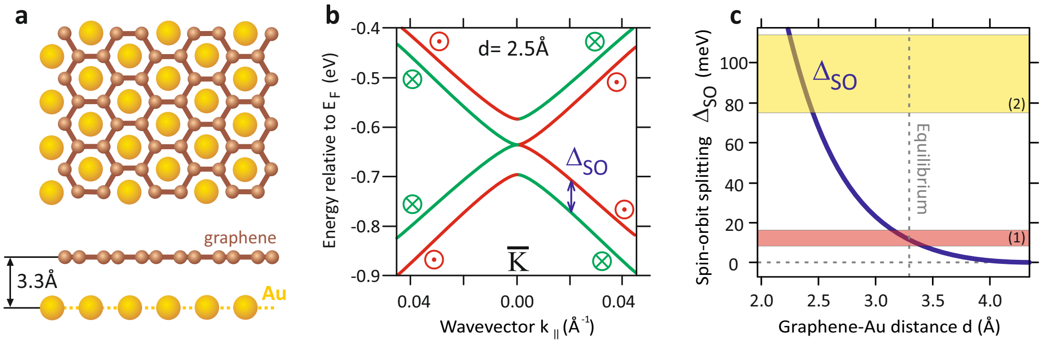

Figure 2.1: Rashba spin-orbit splitting in Gr/Au/Ni(111) and its dependence on graphene-Au separation (reproduced from Ref. [198]). (a) Structural model of Gr/Au(111), gold atoms are located symmetrically with respect to both graphene sublattices — in the centres of hexagons (hollow-site configuration). Equilibrium graphene-Au distance is 3.3 Å. (b) Band structure around $\overline{K}$ point of graphene, Graphene-Au separation was artificially reduced to 2.5 Å. SO splitting in the DC of graphene Δ_{SO} increased to 70 meV. Spin directions are marked by red and green colors. (c) General theoretical dependence of SO splitting in the DC on the graphene-Au separation. The variety of experimental values of Δ_{SO} acquired for different wavevectors $\mathbf{k}_{||}$ extracted from Refs. [4, 157] is presented on the graph as two ranges: (1) for single crystalline Ni(111) substrate and (2) thin film Ni(111) substrate. Average values of Δ_{SO} are determined as 13 and 96 meV, respectively.

The comparison revealed that a surface of single crystal Ni(111) typically displays a higher concentration of structural defects, such as screw-dislocations (see Fig. 2.2(a), left) and atomic step edges. All samples were prepared multiple times on different types of substrates and on average graphene grown on single-crystalline Ni(111) displayed lower structural coherence with the substrate, as can be seen from the arcs in the LEED images. These arcs have the same diffraction angle as the (01) spots of the $p(1 \times 1)$ pattern of graphene/Ni(111) and correspond to rotationally misoriented graphene domains (Fig. 2.2(a), right). Another important difference observed in STM is related to unidirectional compressive strain that appears in the thin film of Ni(111) grown on W(110) due to the film-substrate lattice mismatch. This results in a "wavy" one-dimensional stress-relief pattern with amplitude of $\Delta z \approx 0.2$ Å seen in Fig. 2.2(b), left. Surprisingly, after preparation of graphene this corrugation pattern is not observed in STM anymore, but another feature arises in the form of large-scale elevated regions with smooth profile ("bubbles"), especially pronounced in the regions of domain borders (Fig. 2.2(b), middle) and absent in the case of graphene on single-crystal Ni(111).

Even though there is a number of substrate-type specific features for Gr/Ni(111), the types of structures formed by the intercalated gold observed in our experiments were qualitatively the same.

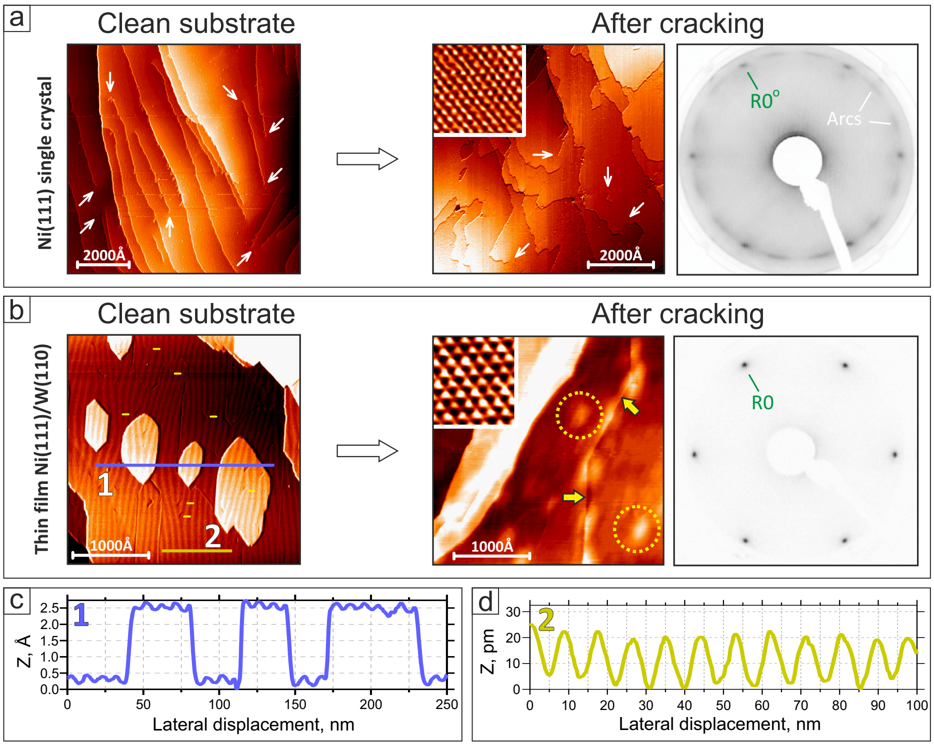

Figure 2.2: Comparison of two types of Ni(111) substrates: single crystal (a) and thin film Ni(111)/W(110) (b). Left column contains STM images of clean substrates and right two columns contain STM images after CVD cracking of graphene and corresponding LEED patterns. Insets present STM images of graphene with atomic resolution. White arrows mark the screw dislocations. The thin film Ni surface has a 1D periodic corrugation pattern that is present all across the film with an average period of ∼ 90–100 Å and amplitude $\Delta z \approx 0.2$Å, height profiles along lines 1 and 2 are displayed in (c) and (d), respectively. Yellow dashes mark dislocations in this pattern. After CVD cracking this stress-relief pattern disappears, however a large-scale unevenness remains in a form of "bubbles" (marked with yellow dotted circles), especially pronounced in the regions of domain borders (marked with yellow arrows).

2.3.1 Sample preparation and experimental details

2.3.1.1 Sample preparation procedure

Two common approaches of Ni(111) surface preparation were used: cleaning of a (111) terminated single crystal Ni or deposition of a thin film of Ni on a W(110) crystal. Single crystal Ni(111) was cleaned by repeated cycles of Ar^+ sputtering at 2 kV followed by annealing at T=1000 K. Thin (15–20 ML) Ni(111) film was prepared by e-beam deposition of Ni on W(110) and subsequent annealing at T=800 K.

Graphene was prepared on the Ni(111) surface according to procedures described in the literature ([133, 196]) in a CVD process using propylene gas as source of carbon. Partial pressure of propylene in the reaction chamber was 1×10^{-6} mbar and the Ni substrate was kept at T=800 K. Intercalation of Au under graphene was performed by deposition of Au on top of graphene and subsequent annealing at 750 K. Nominal gold coverage was uniform 1 ML in one type of experiments or spatially varied from 0 to 1 ML in a systematic way, the latter was achieved by shadowing parts of the crystal with a moving shutter (creating a "wedge").

Thickness of Ni film and Au coverage were estimated from deposition times and rates calibrated by a quartz microbalance. Deposition rates of both Au and Ni evaporators were typically 0.2 ML per minute.

The surface condition was monitored at each step of preparation by LEED.

2.3.1.2 Details of DFT calculations

The atomic structures and electronic band structures in this chapter were modelled and studied theoretically using DFT calculations as implemented in the Vienna Ab initio Simulation Package (VASP) [199].

The model structures under consideration were Au_1 and Au_3 clusters embedded in a graphene/1 ML Ni slab with lateral dimensions of (6×6) and (10×10) graphene unit cells, respectively. To find the equilibrium shape of the graphene sheet for the studied model supercells we have performed a structural optimization as the first step. This relaxation started from several different initial configurations of graphene, in each case C atoms were allowed to move in order to minimize the total energy of the system (Au and Ni atoms were fixed). The calculations employed the projector-augmented wave (PAW) [200] method with a semi-local exchange-correlation functional introduced by Perdew, Burke and Ernzerhof (PBE) [176]. The iterative optimization process was repeated until the total energy difference between two consecutive energy minimization steps did not fall below 10^{-4} eV. The basis for the expansion of the electronic orbitals was formed by plane waves with kinetic energies up to 500 eV. Reciprocal space was sampled by $3\times3\times1$ $\overline{\Gamma}$-centered k-point mesh and the $\overline{\Gamma}$-point for (6×6) and (10×10) supercells, respectively. As DFT approach with usual exchange-correlation functionals has difficulties to account for the non-local dispersive van-der-Waals forces, the latter requires a special treatment. Here the DFT-D2 methodology of Grimme [201] was used for this purpose. The spin-orbit interaction was included only in the band structure calculation of the most stable of Au_1 configurations.

2.4 Results and discussion

2.4.1 Structure of the graphene/Au/Ni(111) interface

It was observed that after annealing at 800 K, gold intercalates under graphene and stays trapped in the interface region between graphene and Ni(111), i.e. it neither deintercalates, nor dissolves in the bulk of the substrate. The reason is the immiscibility of

Au in Ni in the bulk [202], even the gold initially dissolved in the bulk tends to segregate at elevated temperatures and stays on the surface, as it was shown in experiments [203].

The STM experiments conducted in the course of this work showed a variety of structures that are formed by gold trapped between graphene and the Ni(111) surface that will be discussed in the following subsections.

2.4.1.1 Phase I. Continuous monolayer of intercalated Au with triangular pattern

First LEED and STM studies of Gr/Au/Ni(111) suggested that intercalation of gold underneath graphene happens in the form of a close-packed monolayer and a roughly $p(9 \times 9)$ superstructure attributed to a trivial moiré pattern due to lattice mismatch between the layers of gold and graphene [4, 157]. The characteristic LEED pattern obtained from a sample prepared on a thin film Ni(111) substrate is presented in Fig. 2.3. The LEED pattern and the explanation above are consistent with the fact that the lattice constant of a close-packed Au monolayer on Ni(111) amounts to $a_{Au} \approx 2.8$Å [204][*], thus $a_{Au}/(a_{Au} - a_{Gr}) \approx 9$, where a_{Gr} is the lattice constant of graphene. (See section 1.3.5 for details about the formation of moiré patterns.)

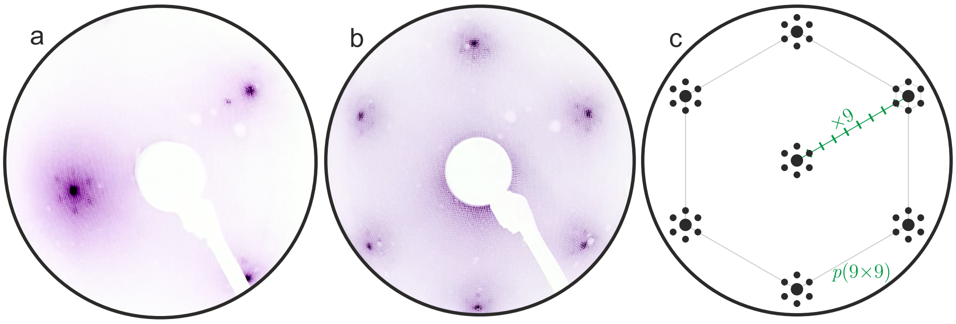

Figure 2.3: LEED images of graphene prepared on 40 ML Ni film on W(110) and intercalated with gold. The primary beam energies are $E_p = 28$ eV (a) and 76 eV (b), colours are inverted for better contrast. The extra reflections are related to a periodic superstructure. (c) A schematic $p(9 \times 9)$ LEED pattern with 1 order of superstructural spots.

However, our detailed STM examination revealed that the superstructure is actually significantly more complex than a lattice-mismatch induced moiré pattern with a sinusoidal-like height-profile. The actual superstructure is formed by isolated triangular loops of depressed Au atoms in the layer underneath the graphene (we will call it further "triangular pattern", see Fig. 2.4). This interesting pattern was discovered in earlier STM studies of Au deposited on Ni(111) (without graphene overlayer), where

---

[*] This value is slightly reduced compared to the Au-Au distance of 2.88 Å in the (111) plane of a bulk gold crystal, meaning that the Au layer experiences compressive strain.

it appeared for coverages from 0.3 to 0.8 ML[*], extensively studied and explained by Jacobsen et al. and Nielsen (PhD Thesis) [204, 205].

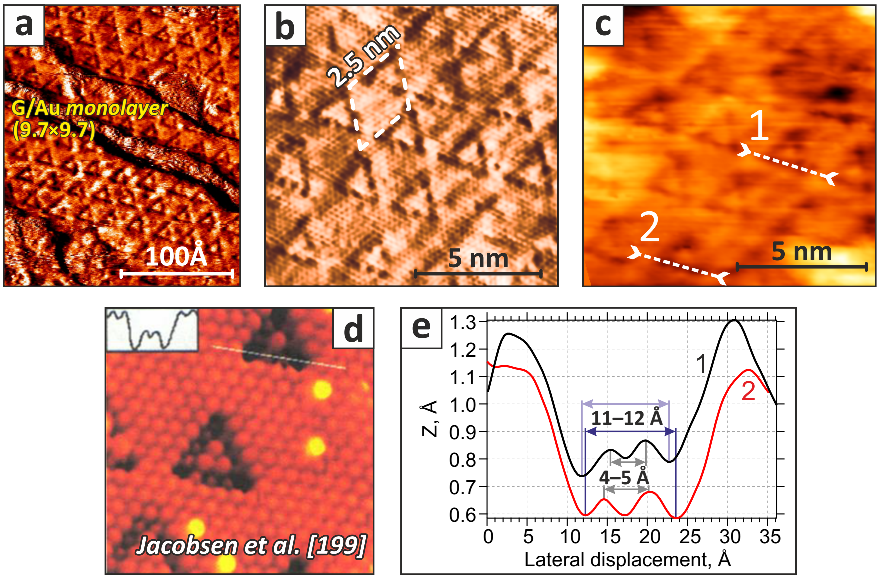

Figure 2.4: Triangular superstructural pattern in Gr/Au/Ni(111). Current channel STM image (a) shows well-ordered triangular pattern on multiple atomic terraces. Zoom-in is presented in image (b), specific tunneling parameters allow to see both the graphene lattice and triangular pattern below simultaneously (I channel). One can see periodic height variation along the edges of triangular depressions. Supercell is denoted by a white dashed line. (c) Z-channel image corresponding to (b). (d) Atomically resolved STM image of the triangular pattern in Au/Ni(111) (reproduced from Ref. [205]). Bright protrusions are attributed to Ni atoms ejected to the surface. Inset shows a Z-profile along the white line, image dimensions are (4.5×5) nm^2. (e) Height profiles extracted along the edges of triangles [white lines in (c)]. Tunneling currents I_t and bias voltages U_b were: 0.78 nA, 100 mV (a); 0.65 nA, 20 mV (b,c). Graphene in (a-c,e) was prepared on single-crystal Ni(111).

In these works using STM and molecular dynamics calculations the authors were able to suggest a formation mechanism of the triangular pattern. If one first imagines a (9×9) supercell of a flat Au monolayer on (10×10) Ni(111), it becomes clear that a large portion of Au atoms are close to energetically less-favourable on-top position [Fig. 2.5(b)]. The surface energy can be minimized by the following reconstruction that involves both Au and Ni top-most layers: a row of few adjacent Ni atoms is ejected from the substrate allowing the nearby Ni atoms to shift in-plane from fcc to hcp-sites [Figs. 2.5(a,c)]. As a result, the group of Au atoms that were in the positions almost on top of Ni atoms now appear close to the most energetically favourable positions with 3 Ni neighbors [205, 206][Figs. 2.5(a,c)]. This process continues until the whole adjacent triangular block of Ni atoms is shifted to hcp sites and a triangular dislocation loop

---

[*] Coverages are presented as a ratio of numbers of Au and Ni atoms on the same area, due to a difference in the interatomic distances 0.8 ML Au coverage stands for a full monolayer of gold.

is formed around it. Triangles in the gold overlayer reflect the underlying structure, as Au atoms directly above the triangular dislocation loops minimize their energy by shifting closer to the Ni layer forming triangular depression lines. One notable feature of this reconstruction observed also in experiments is a larger depth of Au depression in the corners of triangles that can be expected from the empirical argument of larger available space in the corners of the dislocation loops [see Fig. 2.5 (d)] and this effect was confirmed by calculations [205]. Ni atoms that were removed from the top-most Ni layer presumably remain on the surface alloyed in the Au layer [204, 205]

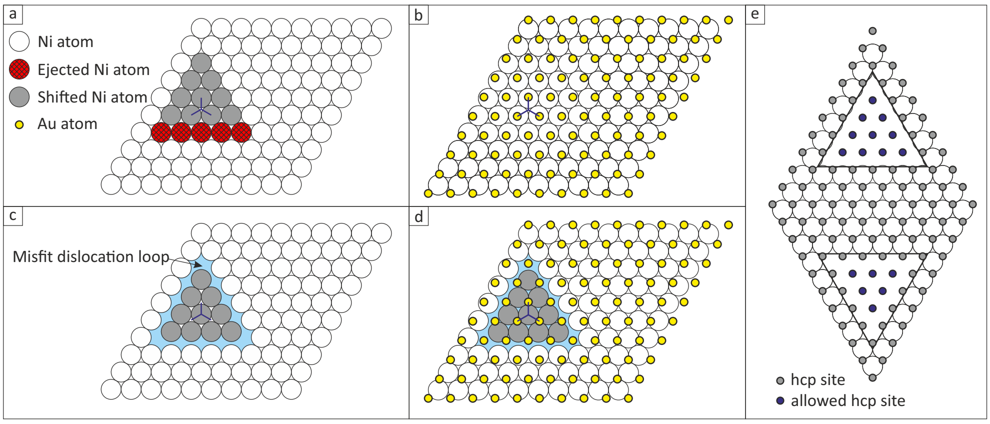

Figure 2.5: A hardball model of atomic structure of triangular pattern in (9×9) Au on (10×10) Ni(111). Blue reference mark in (a–d) is fixed relative to the Ni bulk. (a) a (10×10) supercell of the topmost Ni layer before reconstruction, a row of 5 Ni atoms (marked with red and hatching) will be ejected from the layer, the atoms adjacent to it (marked grey) will shift and occupy hcp sites. (b) Same as (a), but (9×9) Au layer is overlaid. Au atoms nearby the reference point are almost on-top of the Ni atoms, while on the opposite side of the supercell they are close to three-fold coordinated positions. (c) After the reconstruction the triangular block of Ni atoms shifts to hcp sites and a triangular misfit dislocation loop is formed. (d) Au atoms around the reference mark are now close to three-fold coordinated positions as well and Au atoms that appear above the misfit dislocation loop form a triangular dip visible in STM. (e) Comparison of two possible orientations of triangular pattern in Au/Ni(111). Number of hcp sites that can be occupied by shifted Ni atoms is different in two cases.

STM data shows that all the triangles are oriented in the same direction, this preferential orientation can be also justified in the framework of dislocation loop mechanism. If one considers two triangular loops of the same size, but opposite orientations, in one case the number of available hcp sites will be larger ["up" orientation in the Figure 2.5(e)], thus its formation requires a lower number of vacancies*.

---

*The reason for this asymmetry is the ABC stacking of layers in fcc-Ni(111) (let the topmost layer be C). There are actually two possible shifts that result in higher Au-Ni coordination numbers. First one changes A-B-C to A-B-A, locally reproducing hcp type of stacking — this is what we call a shift to hcp-sites. The other possibility would realize exactly the same structure described in the text for the opposite orientation of triangle, but it also leads to A-**B-B** stacking, thus energetically very unfavorable and does not realize in practice.

A monolayer of gold on Ni(111) without triangular pattern was observed to form only when Au was deposited at low temperatures (170 K) realizing a metastable structure with a moiré pattern, this possibility is excluded in our case by the necessity of annealing to enable intercalation.

In the reference [204] it was described as well that characteristic size of triangles and periodicity of the pattern depend on the Au coverage θ, and for $\theta = 0.3$ ML coverage the average size of the superstructure is close to (20×20), roughly double of the one at the maximum coverage, which is (9.7×9.7). In our experiments we observe a rather uniform distribution of periodicities and sizes of triangles in good agreement with the (9.7×9.7) pattern (see Fig. 2.4(a)), meaning that gold underneath graphene forms a uniform single layer film with coverage close to maximum. For lower coverage one would expect larger average sizes of triangles and in the case of multiple layers of gold it was found that the triangular pattern smooths out quickly with thickness and the second Au layer is already almost uniform and displays no strong corrugation across the depression lines [205].

Another important observation is that in our experiments with *submonolayer* Au coverages the triangular pattern was still observed even on small intercalated Au islands (Fig. 2.6). Moreover, the periodicity and size of triangles on small islands is similar to that of a full monolayer, as can be seen in Fig. 2.6(d). Together with the arguments stated above it means that the behavior of gold islands intercalated under graphene slightly differs from that in the pure Au/Ni(111) system. This can be attributed to the extra compressive strain induced by the graphene overlayer on gold islands.

At specific tunneling conditions we can observe details of the triangular pattern underneath graphene [Fig. 2.4(b)], line profiles along the edge of triangles [Fig. 2.4(e)] display apparent protrusions (typically 2 or 3, depending on the size of triangle). It is tempting to associate those features with Au atoms submerged in the triangular dislocation loop and compare the line profiles directly with the profile obtained in [205] for pure Au/Ni(111) system [Fig. 2.4(d)]. However, the situation is more complex due to the graphene overlayer and interplay between topography of graphene and gold states extending above the surface of graphene. The distance between the deepest points varies in the range from 11 to 12 Å, which is in agreement with $4 \times a_{Au} = 4 \times 2.8\text{Å} = 11.2\text{Å}$, meaning that the size of our triangles is similar to the central one in Fig. 2.4(d). In this case there should be 3 protrusions along the edge, however we see only two with distance between them around 4–5 Å. The detailed study of this effect is a matter of future research.

The reconstruction discussed in this section is rather unique because it happens mainly in the *subsurface* region, a similar pattern formation was observed only in the interfaces of a few other immiscible and largely strained systems, a prominent example is Ag/Cu(111) [207–210]. Another system realizing a subsurface reconstruction is Ag

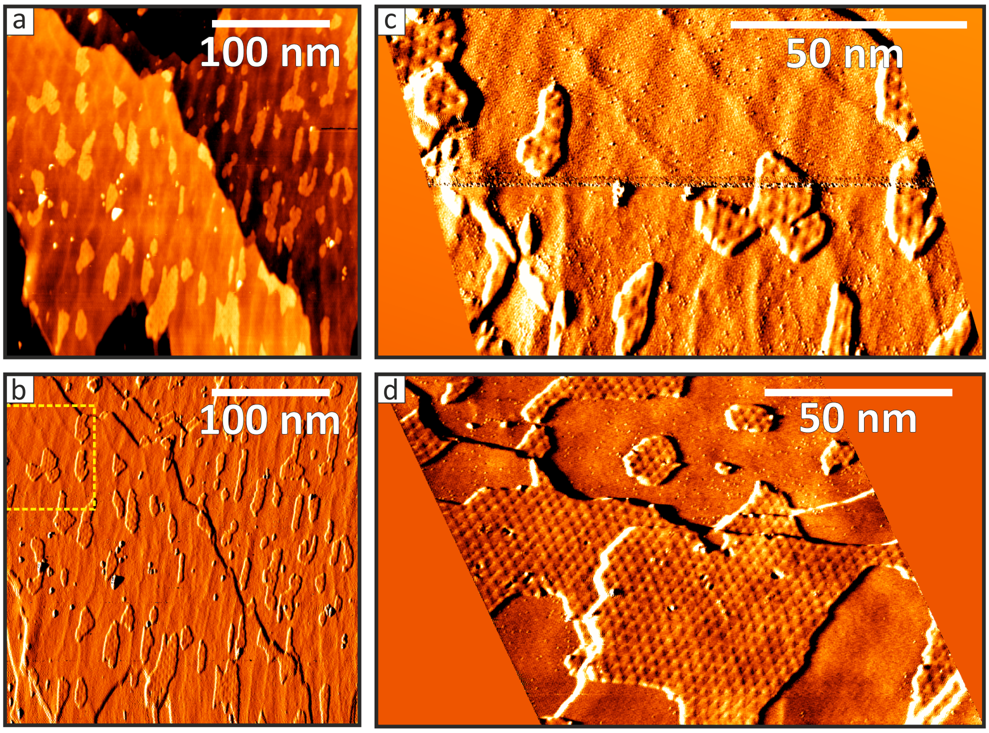

Figure 2.6: STM of triangular pattern in Gr/Au/Ni(111) for submonolayer Au coverages. (a,b) STM of a sample with low (~ 0.3 ML) Au coverage, Z (a) and current (b) channels. One can see periodic corrugation on islands of intercalated Au. (c) A close-up of the area marked by a yellow frame in (b), triangular shape of protrusions is visible (current channel image). (d) Sample prepared with an intermediate Au coverage [0.5 ML], triangular pattern can be observed and it looks identical both on large and small islands.
Graphene was prepared on thin film Ni(111), tunneling currents I_t and bias voltages U_b were: 1.14 nA, 1.23 V (a,b,c); 0.65 nA, 1.05 V (d).

bilayer on Pt(111) [211, 212]. It produces an even more complex reconstruction pattern [212] resembling a distorted kagome lattice. Moreover, it was demonstrated that it can support highly ordered self-organized arrays of Ag nanoclusters [211]. A similar pattern was observed for a sputtered and annealed $Pt_{25}Ni_{75}(111)$ crystal, where it was also attributed to appearance of subsurface dislocations [213] (and recently the same pattern was observed for 2 ML of Pt deposited on $Pt_{25}Ni_{75}(111)$ [214], although the latter system was not studied in detail). Regarding the case *with graphene overlayer* most recently a triangular pattern analogous to the one discussed above was discovered for Gr/Co(0001) intercalated with gold [215].

2.4.1.2 Phase II. Ordered arrays of intercalated Au nanoclusters

In all STM experiments with various Gr/Au/Ni(111) samples the major part of intercalated gold was in form of Phase I described above. However, it was observed that this phase coexists with another intriguing structure: intercalated *Au nanocluster arrays* (see Fig. 2.7). In the large-scale STM image 2.7(a) one can see different intercalated structures coexisting in the same area: monolayer gold and periodic arrays of protrusions (large and small ones) which we interpret as intercalated nanoclusters (for reasons explained below). These nanoclusters can form a well-periodic lattice structurally coherent to the triangular $p(9.7 \times 9.7)$ pattern. The size of the areas occupied by these arrays vary from 20 to 200 nm. Nanoclusters formation is observed systematically for samples prepared both on single-crystalline and on thin film Ni(111) substrates.

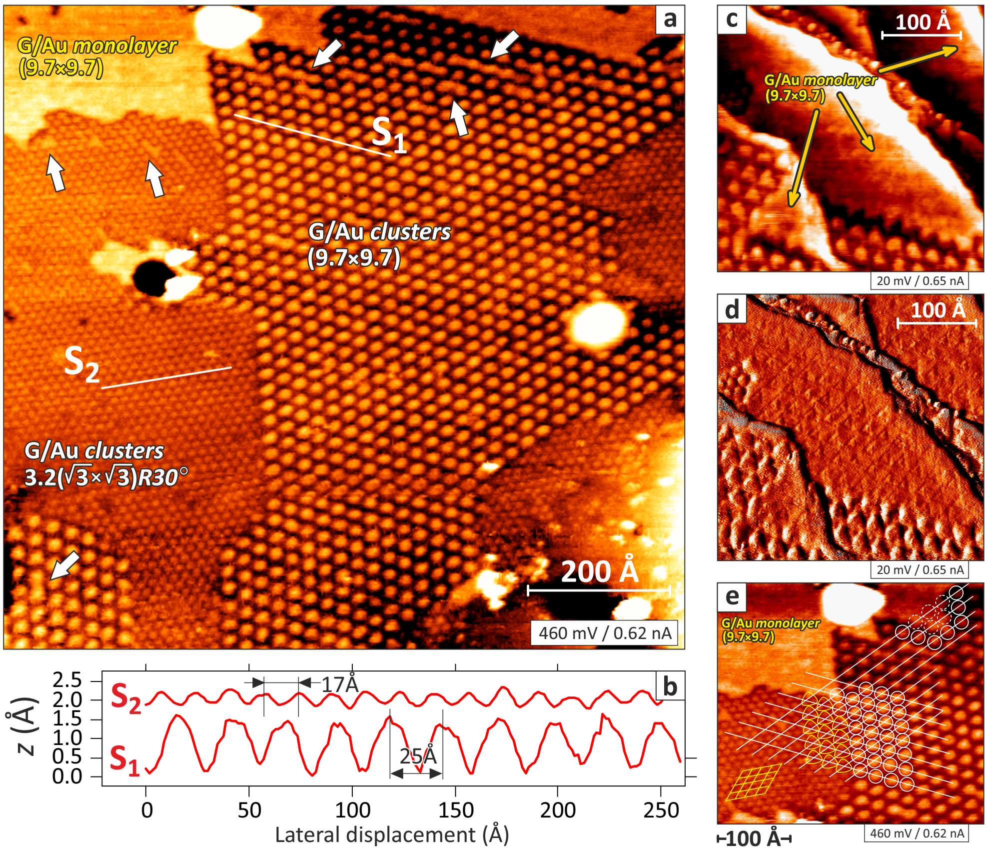

Figure 2.7: STM of arrays of intercalated clusters. (a) Large scale STM image depicting different intercalated phases coexisting in the same area: continuous monolayer, lattice of large clusters (coherent with (9.7×9.7) triangular pattern) and lattice of smaller clusters (identified relative to the large one as $(3.2\sqrt{3} \times 3.2\sqrt{3})$ R30°, see main text). The areas where coalescence of clusters happens are marked with white arrows. Height profiles along the lines S1 and S2 are presented in (b). A close-up STM image of the border between the large cluster array and the monolayer Au phase is shown in (c) and (d) (Z and I channels, respectively). One can see the coherence and the peculiar relationship between the typical (9.7×9.7) triangular pattern in the monolayer Au phase and the nanocluster array. Panel (e) is a close up of the upper left corner of (a), lines are guides to the eye to show the coherence between all three types of structures formed by intercalated Au: white lattice corresponds to large clusters and yellow to small ones. Graphene was prepared on Ni single crystals. Tunneling currents I_t and bias voltages U_b are presented directly in the figures.

Unlike the triangular pattern that was observed in pure Au/Ni(111) [205], nanocluster arrays are a unique feature of the Gr/Au/Ni(111) system and were never reported to occur without graphene overlayer to the best of our knowledge. On the other hand, intercalation of gold under graphene in form of small clusters was reported in the literature [216–218]. Those authors intercalated Au between graphene and carbon-rich interface layer (buffer layer) on SiC(0001) that resulted in the formation of few-atom clusters arranged in a rather irregular lattice without long-range order. This superstructure was described as disordered (9×9) relative to the graphene lattice, and the average distance between the nearest-neighbouring clusters was 2.2 nm.

In our case intercalated arrays of clusters are well periodic (Figure 2.7). We distinguish two phases: with larger and smaller clusters. For the first one the periodicity is ~ 25 Å this value is close to the periodicity of the triangular pattern, and the apparent height of the protrusions is ~ 1.5 Å [see line profile along S_1 in Figure 2.7(b)]. Similar orientation and periodicity of this phase and the triangular pattern indicates that their formation mechanisms are probably related to each other and stem from the large lattice mismatch between Ni and Au. In the second phase the smaller clusters are arranged in a lattice with smaller periodicity of ~ 17 Å and rotated by 30° relative to the lattice of larger clusters (and triangular pattern). Apparent height of the protrusions is only ~ 0.5 Å [see line profile along S_2 in Figure 2.7(b)]. A detailed characterisation of the superstructure formed by small clusters will be given further based on its relation to the superstructure of larger clusters.

Figures 2.7(c,d) present a close-up STM image of the border between the monolayer Au phase and the array of large clusters. The edge of the monolayer region has a peculiar sawtooth shape that forms the transition region to individual clusters that form a lattice coherent with the (9.7×9.7) triangular pattern of the ML Au phase. The triangular pattern itself here is much more pronounced than in Fig. 2.7(a), where it was not well resolved due to different tunneling parameters.

One has to note that the observed patterns that we describe as intercalated Au nanoclusters share an apparent similarity with the structures observed in Ref. [219], where Au was not involved at all. Those authors studied the growth of graphene on a Ni(111) single crystal and suggested that under specific conditions a transformation of surface nickel carbide (Ni_2C) into graphene may occur. Such transformation results in a graphene sheet rotated by $\sim 3°$ relative to the Ni(111) substrate (for geometrical reasons) and this small misorientation leads to a moiré pattern with periodicity of 2.7–3.0 nm. However, despite the visual similarity, there are multiple experimental evidences that the periodic arrays of protrusions that we observe in the gold intercalated samples cannot be explained by a simple moiré pattern without Au.

First of all, both cluster phases are observed together with a continuous Au monolayer phase, assuming the moiré pattern mechanism this would require graphene domains with different possible orientations providing different types of apparent structures. As we see from Fig. 2.7(a), even in disconnected regions of the same phase protrusions form exactly the same lattices. Taking into account that a moiré pattern is very sensitive to small changes in angle, it means that graphene domains in disconnected regions should be oriented precisely the same, which is unlikely, as we see a uniform distribution of misorientation angles in the LEED pattern [see for example 2.2(a), right]. The second argument is the same apparent height measured in STM at different bias voltages from regions with the large cluster phase and the continuous monolayer phase. Moreover, large islands of the continuous ML Au phase and clusters show similar behavior of their Z-contrast with bias voltage (Fig. 2.7). This indicates that the nanoclusters are electronically similar to the monolayer Au phase. The third argument supporting the intercalated clusters is observation of merging of individual protrusions together [marked by white arrows in Fig. 2.7(a)]. This coalescence happens for both types of periodic arrays observed. Similar effects of cluster intercalation and coalescence have been reported for Si intercalated under graphene on Ru [220]. Among other arguments one can mention the not perfectly uniform shape of individual protrusions and a few visible vacancies in the small cluster lattice.

All these observations indicate that the periodic arrays of protrusions are indeed composed of individual nanoclusters under graphene and cannot be explained solely by conventional moiré superstructures. The possibility remains that gold intercalates in the form of clusters under a moiré pattern of graphene on Ni rotated by $\sim 3°$, however, the periodicity observed in [219] was significantly larger and we have never detected any sign of a square Ni_2C lattice in LEED. With this argumentation we can conclude that the observed periodic protrusions are intercalated individual nanoclusters arranged in periodic arrays under graphene.

To analyze the relationship between all three structures and prove their coherence we overlaid a (9.7×9.7) superstructural mesh in the area where all three phases meet [see Fig. 2.7(e), white mesh]. Large clusters precisely fit in this (9.7×9.7) mesh proving their coherence with triangular pattern. However, the lattice of smaller clusters is *also* closely related to (9.7×9.7). To see that, one needs to join nearest small clusters in groups of three [Fig. 2.7(e), yellow rounded triangles], the resulting lattice perfectly extrapolates the positions of the larger clusters and thus matches the (9.7×9.7). This relationship allows to identify the superstructure formed by smaller clusters as $(3.2\sqrt{3} \times 3.2\sqrt{3})$ R30° [yellow mesh in Fig. 2.7(e)].

All three structures are closely related to each other and it indicates that there is the same driving force of their formation. Taking into account a coalescence effect one

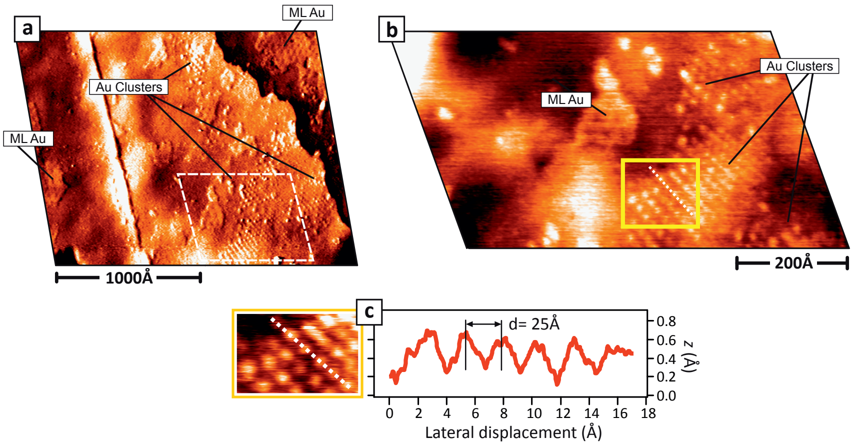

Figure 2.8: Au nanocluster structure in Gr/Au/Ni(111) on a thin film Ni substrate prepared on W(110) with low nominal Au coverage (~ 0.2 ML). Two types of intercalated Au structures are visible simultaneously: triangular patter on Au monolayer phase (labelled "ML Au") and arrays of Au clusters ("Au clusters"). (a) Large scale STM image. Close-up of the marked area is presented in (b). (c) Height profile over cluster arrays extracted from (b). Tunneling currents I_t and bias voltages U_b: (a) 26.1 nA, 1575 mV; (b) 5.7 nA, 1049 mV; (c) 11.4 nA, 1544 mV.

can consider cluster phases as incomplete versions of the full monolayer phase in regions of reduced Au coverage.

Figure 2.7 presents a very good example of the cluster phase formation on a Ni(111) single crystal, however, as we stated above, this phase is observed equally well on the thin-film Ni(111) substrate prepared on W(110) (see Fig. 2.8). One can see that the periodicity of cluster lattice is the same as in the case of the single-crystal substrate.

The ratio between areas occupied by cluster array structures and by monolayer Au phase was in the range 10-30% for different sample preparations. These estimated values are based on STM data obtained from 3-4 macroscopically distinct areas on the surface of each sample. Still, information obtained by STM has a local nature and might not represent the average condition of the whole sample surface. For example, in large-scale STM images presented in Figures 2.9(a,b) we observed that roughly 50% of the Au-intercalated surface area is occupied by cluster structures.

Regarding surface-averaging techniques, due to similar $\sim(9.7 \times 9.7)$ superstructures the large cluster arrays and triangular pattern cannot be distinguished by LEED in a simple way, especially taking into account that superstructural reflections are relatively weak in this system (typically only the first order is visible). The reflections that could be attributed to a $(3.2\sqrt{3} \times 3.2\sqrt{3})$ R30° structure of smaller clusters were not observed in the LEED data.

To test whether the observed nanocluster arrays can cause the enhanced Rashba effect observed in spin-ARPES experiments we have conducted a series of theoretical simulations to model the atomic structure corresponding to the cluster arrays and performed spinful band structure calculations.

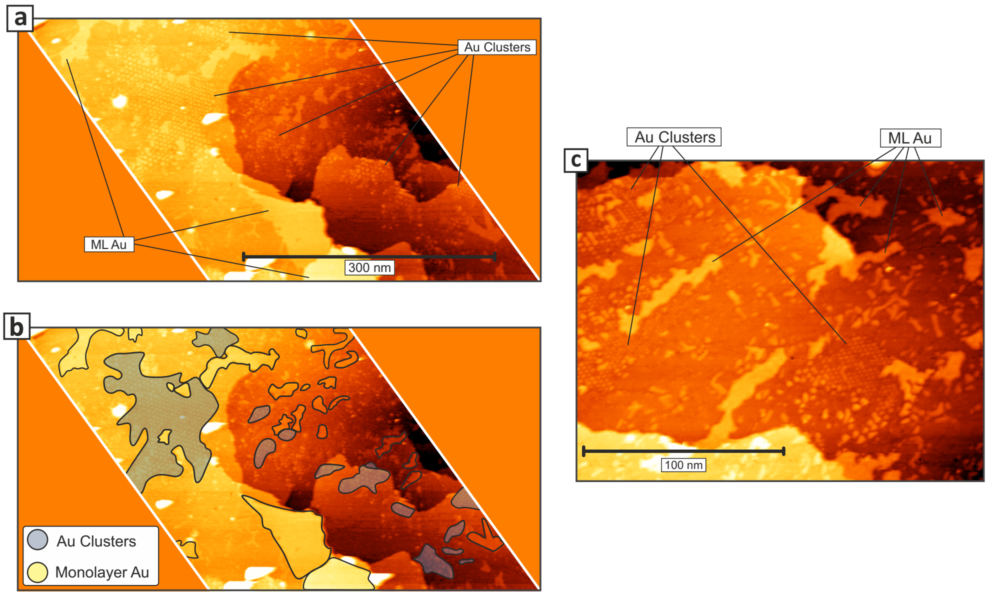

Figure 2.9: Au nanocluster array structure in Gr/Au/Ni(111) on single-crystal Ni(111). (a) Large-scale STM image displays areas of full monolayer of gold (marked as "ML Au") and areas with nanocluster arrays ("Au clusters"). (b) Same image as (a), but areas with intercalated clusters and monolayer Au are highlighted. In this region total areas occupied by clusters and gold monolayer are approximately equal. (c) Smaller scale STM image from a nearby region that reveals arrays of small clusters.
Tunneling currents I_t and bias voltages U_b: (a,b) 0.7 nA, 337 mV; (c) 0.5 nA, 619 mV.

2.4.2 DFT modelling of the cluster structures

As it was discussed in Section 2.2 a diluted $p(2 \times 2)$ gold intercalated superstructure can induce *stronger* spin-orbit effects in graphene than a full monolayer of gold due to an effective attraction of graphene towards the bare Ni areas that significantly reduces the graphene-Au separation. A qualitatively similar effect can be expected in the case of the even more diluted structure of few-atom Au clusters. In this section we apply DFT calculations to quantify this effect and figure out whether it is strong enough to explain the giant Rashba effect observed experimentally.

Two different cluster models were used to represent smaller and larger clusters: a single gold atom (Au_1) and a cluster of three atoms (Au_3) [see Figs. 2.10(a,b)], which were introduced in the interface of a Gr/Ni slab in the hollow-site positions. Supercell sizes were selected (6×6) and (10×10) graphene hexagons, respectively, to approximate the periodicities observed experimentally. For brevity we will call these two configurations by the size of incorporated clusters: Au_1 and Au_3. The Ni(111) substrate was modelled by one atomic layer of Ni atoms.

To obtain an equilibrium shape, the structures were allowed to relax from the initial configuration. The choice of the latter is important, since in some cases after relaxation the system might reach a local minimum and end up in a metastable configuration that is not realized in practice. To avoid this situation we performed relaxation from two opposing starting points. In the first case graphene was initially flat and placed relatively far from the Ni substrate (3 Å above the clusters), and in the second case graphene was initially placed close to the Ni substrate and artificially buckled around the clusters.

For both Au_1 and Au_3 structures relaxation from different initial configurations did not result in the same structures, however they all display a common feature — a buckled shape of graphene around the cluster region [see Figs. 2.10(c–f)]. The difference is that initially flat graphene remained at large (≥3.0 Å) distance from the Ni substrate [Figs. 2.10(c,e)] while in the opposite case [Fig. 2.10(d)] graphene did not decouple from the substrate and equilibrated at $\sim$ 2.0 Å from the Ni surface in the areas between the clusters (close to the equilibrium distance for Gr/Ni(111) that is d_{Ni}=2.05 Å as calculated in Refs. [187, 188]). However, the total energies of relaxed configurations were different and we discuss the stability of these structures further in detail.

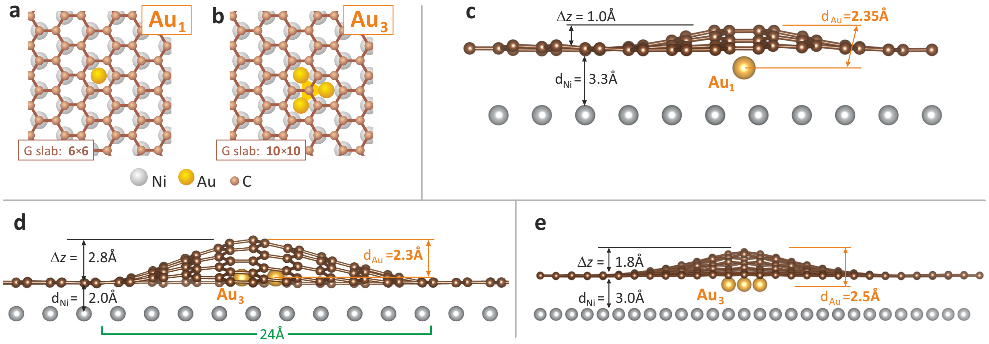

Figure 2.10: DFT modelling of graphene supported by nanocluster arrays. Structural models of Au_1 (a) and Au_3 (b) structures (with 1 and 3 Au atoms in the intercalated cluster, respectively). Dimensions of the slab used in calculations were (6×6) for Au_1 and (10×10) for Au_3. (c) Calculated relaxed atomic structure for Au_1 case. Distance between graphene and Ni(111) substrate is d_{Ni}=3.3 Å, suggesting reduced interaction with the Ni substrate. On the other hand, the graphene-Au distance (d_{Au}=2.35 Å) is much smaller than 3.3 Å for graphene on bulk Au, thus one can expect enhancement of the locally induced SOI in graphene. Two relaxed configurations obtained for Au_3 (d,e) differ in the behavior of the graphene in the areas between the clusters: in (d) it is strongly bonded to Ni(111) (d_{Ni}=2.0 Å) and has a giant amplitude of corrugation (Δ_z=2.8 Å), while in (e) it is quasi-free-standing with large distance to the substrate (d_{Ni}=3.0 Å) and smaller corrugation amplitude (Δ_z=1.8 Å). Distances to gold are d_{Au}=2.3 Å and 2.5 Å, respectively.

2.4.2.1 Au_1 relaxed structures

In the case of the Au_1 structure the lowest energy configuration [Fig. 2.10(c)] was achieved from initially flat graphene, while relaxation of the bent configuration resulted in a more deformed graphene with higher corrugation height Δz and higher total energy that even exceeded slightly the energy of flat graphene (< 8 meV per C atom).

The most stable of Au_1 configurations is presented in [Fig. 2.10(c)]. The corrugation height is $\Delta z \approx 1$ Å and the distance between graphene sheet and Ni substrate is d_{Ni}=3.3 Å (minimal value taken in the area between the clusters), which is much larger than the 2.05 Å separation in Gr/Ni(111) and similar to values obtained for substrates weakly interacting with graphene [187, 188]. It means that not only a monolayer of gold, but even its diluted superstructures can effectively decouple graphene from the strongly interacting substrate, even when gold is present at very low concentrations (1 Au atom per 36 graphene hexagons in this case). This decoupling should reduce the effect of Ni on the sublattice asymmetry and electron doping making graphene quasi-free-standing.

The second important feature of this structure is the small minimal distance between graphene and gold atom, that is only d_{Au}=2.35 Å [Fig. 2.10(c)], significantly reduced compared to the equilibrium distance of 3.3 Å for graphene on a monolayer of gold [4]. If one could achieve such proximity to a monolayer Au, the spin-orbit splitting would be around 100 meV, as estimated from the graph in Figure 2.1(c). This result gives a strong motivation to study this system further, since it is not intuitively clear what would be the effect in case of a superstructure of individual atoms, moreover, the relatively strong buckling of graphene might significantly influence its band structure. To answer these questions all at once, fully-relativistic spinful band structure calculations were performed.

2.4.2.2 Au_1 band structure calculations

For these calculations the most stable relaxed Au_1 configuration was used [Fig. 2.10(c)]. Only the smaller cluster structure was modelled because of the computational limitations*, for the same reason the Ni layer had to be removed. The latter can be justified by the large graphene-Ni separation and thus expectedly weak interaction. Moreover, the main focus of this study is on the details of the graphene-Au interaction, which should not be affected.

The resulting band structure around the Dirac point of graphene is presented in Figure 2.11. The results obtained for three spatial projections of spin (S_x, S_y and S_z) are presented in three separate panels with corresponding labels. The z axis is oriented perpendicular to the in-plane translation vectors of the supercell, while x and y axes are in-plane and their orientation is shown in the top of S_z panel. The magnitudes of spin-projections are presented by color of the dispersion graph on the scale from red (negative) to green (positive) [see the color bar in Fig. 2.11]. Due to backfolding the bands from $\overline{K}$ and $\overline{K'}$ are superimposed at the $\overline{\Gamma}$ point of the superstructural BZ. This happens for all superlattices of size $(3k \times 3k)$, where $k \in \mathbb{N}$, including our case of (6×6) [see Fig. 2.12].

---

*The time required for the DFT band structure calculations scales non-linearly with the number of electrons in the system n. The scaling law depends on the used implementation of the DFT approach and the system under study, but as a rough estimate the number of operations is $\propto n^3$ and it can be optimized to be $\propto n^2$ [221].

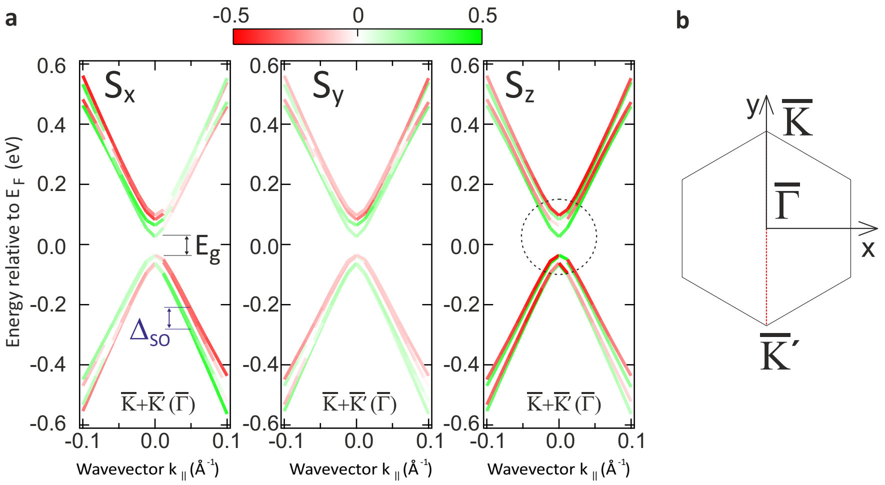

Figure 2.11: (a) Results of fully-relativistic band structure calculations for the atomic configuration Au_1 presented in Figure 2.10(c) (excluding Ni atoms). Spin structure of the Dirac cone agrees well with the one expected for a Rashba effect (S_x and S_y projections). There is a band gap (dashed circle, E_g=60 meV) and a component of spin in the out-of-plane direction (S_z projection). (b) Reference frame axes in the reciprocal space.

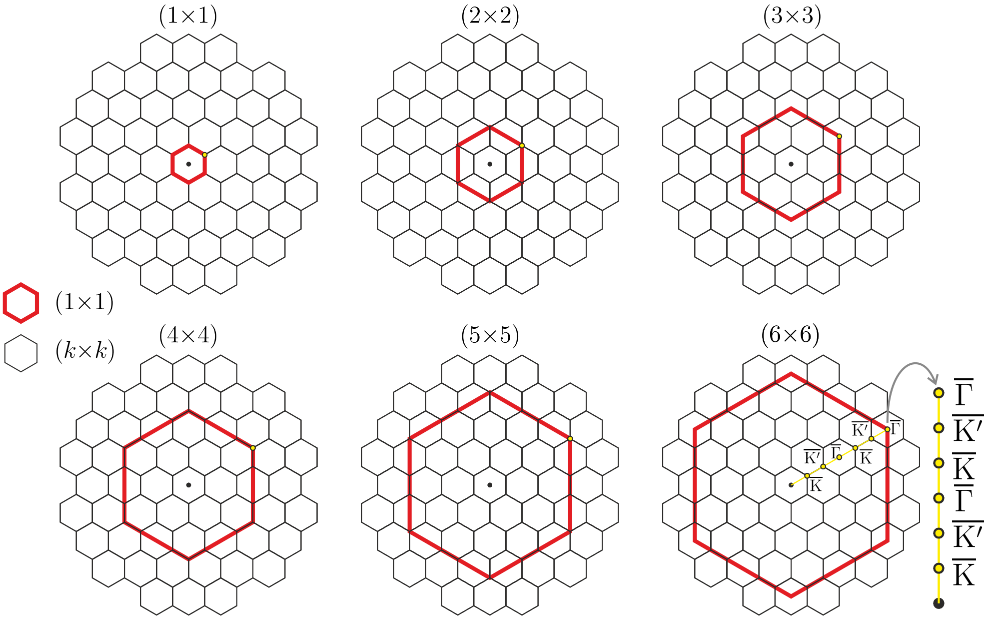

Figure 2.12: Backfolding in Brillouin zones of $(k \times k)$ hexagonal supercells. Red hexagons represent a (1×1) BZ and black hexagons are k times smaller mini-BZs of the $(k \times k)$ supercell (scale is increasing proportionally to k to keep small features visible). One can see that the $\overline{\mathrm{K}}$ point of (1×1) matches $\overline{\mathrm{K}}$, $\overline{\mathrm{K}'}$ and $\overline{\Gamma}$ points of mini-BZs when $k = 1, 2$ and 3, respectively. This sequence continues periodically, thus for (3×3), (6×6), ... , $(3k \times 3k)$ the $\overline{\mathrm{K}}$ and $\overline{\mathrm{K}'}$ points of the (1×1) BZ will match with the $\overline{\Gamma}$ point of the mini-BZ.

The Dirac cone in Figure 2.11 is formed by spin-split bands with nearly constant splitting of ∼ 60 meV. Both the uniform splitting in the vicinity of the Dirac point and the specific distribution of the spin-polarization (as seen from plots S_x and S_y) are characteristic of a Rashba-type spin-texture [see Fig. 1.3(b) in Section 1.2.4]. The strength of Rashba SOI ($\lambda = 2\lambda_R \approx 60$ meV) is surprisingly large for such a diluted Au layer. It seems that the small concentration of gold is counterbalanced by shorter graphene-Au distance. This effect has been recently verified theoretically [222].

Among other interesting features of this band structure are the band gap ($E_g = 60$ meV) and non-zero values of S_z components of spin. Both these effects can be attributed mainly to the buckling of the graphene layer around the Au clusters. Such buckling breaks the sublattice symmetry in graphene and thus forms a band gap [see Section 1.2.3]. Together with a strong SOI this can lead to a "hedgehog" spin-texture in the vicinity of the Dirac point, i.e. a non-zero z component of spin and inclination of spins towards an out-of-plane orientation when approaching the band gap region [59, 223].

The band gap itself [marked by a dashed circle in panel S_z of Fig. 2.11] can appear for a variety of reasons in addition to the suggested buckling-induced sublattice asymmetry, for example, one can assume an influence of Au on the sublattice asymmetry or lateral confinement of electrons in the buckled parts of graphene. To distinguish the effects of buckling and Au cluster on the band gap another band structure calculation was conducted for the same system but with Au removed. The resulting band gap width was determined to be 54 meV, only slightly less than 60 meV in presence of gold. This leads to the conclusion that the small band gap in the Dirac cone of graphene is inevitable in such system because it appears as a result of buckling over the Au clusters.

2.4.2.3 Au_3 relaxed structures

The Au_3 structure models the larger cluster arrays. It was not possible to perform the band structure calculations for such a large system because of the computational limitations as explained above, but the obtained structural data is still very informative.

Similar to the Au_1 case, structures were allowed to relax from different initial conditions [Figs. 2.10(d,e)]. The first one, obtained from a buckled initial configuration [Fig. 2.10(d)], has graphene-Ni separation of only d_{Ni}=2.0 Å that leads to a large corrugation height $\Delta z \sim 2.8$ Å and small graphene-Au distance d_{Au}=2.3 Å. On the contrary, in case of the structure obtained from the initially flat configuration [Fig. 2.10(e)] graphene can be considered quasi-free-standing (d_{Ni}=3.0 Å), it is less corrugated ($\Delta z \sim 1.8$ Å) and appears just slightly further away from the Au_3 cluster (d_{Au}=2.5 Å).

Comparing these two structures one can expect stronger induced SOI in the first one due to slightly lower d_{Au}, however, due to a strong interaction with the Ni substrate the Dirac cone of graphene should be energetically shifted and distorted by hybridization with Ni 3d states, as it happens in the Gr/Ni(111) system [135], such band structure cannot reproduce the previously obtained ARPES data of Refs. [4, 157]. Moreover, the extreme corrugation value $\Delta z \sim 2.8$ Å is in conflict with the apparent height of structures in STM data: $\Delta z \sim 1.5$ Å. In contrast, corrugation of the second structure ($\Delta z \sim 1.8$ Å) agrees with our STM data well, and large graphene-Ni distance significantly reduces the influence of the interaction with Ni on the graphene bands.

Calculations reveal that the total energy for the second structure is lower as well, although the obtained energy difference is rather small: 7 meV per carbon atom, lower than the room temperature thermal energy $k_B T \approx 26$ meV. Altogether it means that the first relaxed structure is actually metastable and less probable to be realized than the other one.

The important question is whether this structure can also produce large spin-orbit splitting in the Dirac cone of graphene. Unfortunately, it was not possible to check it directly by calculation, but the estimation using the distance dependence of the SO splitting for a full ML of Au [Fig. 2.1(c)] was rather successful for the Au_1 structure: the estimated splitting was ~ 100 meV and the calculation resulted in a value of 60 meV. The concentration of Au atoms for Au_1 and Au_3 structures is also similar: $1/36 \approx 0.0278$ and $3/100 = 0.03$ Au atoms per graphene hexagon, respectively. Applying this estimation to the Au_3 structure one can expect a spin-orbit splitting of $\Delta_{SO} \lesssim 70$ meV for $d_{Au}=2.5$ Å.

To summarize, the obtained structures for small Au nanoclusters under graphene Au_1 [Fig. 2.10(c)] and Au_3 [Fig. 2.10(e)] form buckled graphene surfaces that are in good agreement with the two nanocluster array structures observed in our STM data. Moreover, calculations revealed that even small concentrations of gold can decouple graphene from the strongly interacting substrate and keep the Dirac cone band structure of graphene intact with only a small band gap due to buckling and, most importantly, a giant Rashba-type spin splitting induced by gold.

2.4.3 Origin of the giant Rashba-effect

The question remains if these areas covered by nanocluster arrays are the actual origin of the spin splitting observed in the previously reported ARPES experiments. As mentioned above, areas occupied by these structures constitute not more than 30% of all the Au-intercalated surface area of the sample and the rest is formed by a ML Au phase that can provide only ~ 10 meV spin splitting. Due to the non-local character of the ARPES experiment the signals from both types of areas will be averaged in the spectra. This effect was indeed observed: the detailed analysis of spin-ARPES spectra in Ref. [4] revealed asymmetric shapes of the photoemission peaks, which were attributed to averaging of signals from areas with large and small spin splitting magnitudes. However, in Ref. [4] the *prevailing* contribution to the spectral weight was from the signal with the large magnitude of splitting.

We demonstrated that the nanocluster mechanism presented in this chapter can act as a plausible structural origin of the giant spin splitting in graphene on Ni(111) intercalated with gold, but is it the only possible structural explanation? This system is very rich and one can think of several other scenarios, some of them were studied in the literature, but mostly did not succeed in explaining the giant Rashba-effect.

First of all, one could suspect the complicated triangular pattern discussed in detail in Section 2.4.1.1. The effect of this reconstruction[*] on the band structure of graphene was recently studied theoretically in Ref. [224] (see Appendix C) and it was concluded that, even though there is a small enhancement of the *intrinsic* SOI, the overall influence of the triangular pattern on the band structure of graphene is weak and cannot explain the giant Rashba-type splitting.

Another possibility is related to single atoms of Au in direct contact with graphene: remaining on the surface of graphene after intercalation or located in-between graphene and intercalated Au monolayer. Even though there is no strong experimental evidence for realization of the scenario with Au adatoms on top of graphene, both possibilities were very recently tested by calculations in Ref. [225]. Two systems with quasi-free-standing graphene were studied: Gr/Au/Ni(111) and Gr/Pt(111). In the case of Gr/Pt(111) it was demonstrated that single Pt atoms intercalated in between graphene and Pt substrate result in a buckled graphene structure and indeed may induce almost constant giant spin splitting of ~ 100 meV in the Dirac cone of graphene. However, for the Gr/Au/Ni(111) system the same mechanism (intercalation of extra Au atom between graphene and ML Au) did not result in an enhancement of the SOI. The obtained relaxed structure with 1 extra Au atom per (9×9) graphene supercell was also *buckled* (with corrugation of $\Delta z \sim 0.8$ Å), but it is also not a suitable model for the structures observed in our STM data. The reason is that it cannot explain the same apparent height of graphene supported by nanocluster arrays and ML Au. Considering the case of Au adatoms on top of graphene, only an out-of-plane spin-polarization was detected [225], which also cannot explain the ARPES results.

Finally, one has to consider the interaction between graphene and *Ni atoms* ejected from the top-most Ni layer to form the triangular reconstruction pattern. In the pure Au/Ni(111) system these Ni atoms are mixed in the Au layer outside the triangular loops [205], thus they can interact with graphene directly, leading to reduced graphene-Au distance. This possibility, to the best of our knowledge, was not yet investigated in the published research. Moreover, these atoms of ferromagnetic material can transfer the exchange field from the substrate to graphene causing a strong exchange-type splitting in the Dirac cone while keeping its linear band structure intact. This effect was demonstrated in the recent paper by Rybkin et al. [215] for Gr/Au/Co(0001) — a system very similar to Gr/Au/Ni(111) in its physical properties and realizing the same triangular reconstruction pattern. Further investigations are required in this fruitful direction, since the structural model used in this paper for band structure calculations

---

[*] The results were obtained for only one size of reconstruction: Au(8×8)/Ni(9×9) with triangular block of 10 Ni atoms shifted to the hcp position.

was significantly simplified due to computational constraints (a (2×2) supercell relative to graphene was used). The study of the interplay between the multiple physical effects in this system (enhancement of SOI, transfer of the exchange field and distortion of the Dirac cone in graphene due to interaction with Ni adatoms) requires state-of-the-art band structure calculations of a realistic structural model, similar to those applied for example in Ref. [224].

2.5 Summary of conclusions

In this chapter we have explored possible structural explanations of how the Au intercalation in Gr/Ni(111) can result in a Rashba effect with a giant ~ 100 meV spin splitting magnitude.

The extensive STM study demonstrated that gold can be intercalated under graphene not only as a dense monolayer, observed in earlier works, but also in the form of well-periodic arrays of small nanoclusters, a structure previously not reported. These structures were observed in Gr/Au/Ni samples prepared on both thin film and single crystalline Ni substrates. The monolayer phase has a triangular reconstruction pattern similar to that observed earlier for pure Au/Ni(111), i.e. the presence of the graphene overlayer did not induce any observable change in it. Nanocluster arrays, on the contrary, were not reported to appear without graphene. Two types of nanocluster lattices were observed: the first one consists of larger clusters arranged in a (9.7×9.7) superstructure, while the second one is formed by smaller clusters in a lattice determined as $(3.2\sqrt{3} \times 3.2\sqrt{3})$ R30° by its relation to the first one. Both of these cluster structures are very diluted, but still able to decouple graphene from the strongly interacting Ni substrate and render it quasi-free-standing, as demonstrated by our DFT study. At the same time calculations confirm the initial concept of "pinning": large areas of Ni(111) surface free from Au attract graphene and effectively press it towards the Au clusters, strongly enhancing the proximity-induced SOI in graphene. This mechanism provides a large Rashba-type spin splitting of ~ 60 meV in the model corresponding to the smaller clusters. Graphene supported by intercalated clusters will be inevitably buckled and we demonstrate that such buckling can lead to a small band gap and an out-of-plane reorientation of spins in the gap.

The enhancement of induced spin-orbit interactions in graphene due to the pinning effect presented in this chapter can be generalized for graphene on other strongly interacting substrates intercalated by nanostructures of heavy noble *d* metals.

The main results of this chapter were published in the journal 2D Materials (Ref. [198]).

Chapter 3

Origin of the band gap in Bi-intercalated graphene on Ir(111)

3.1 Introduction

In Chapter 2 we have discussed the intercalation of the heavy noble metal Au under graphene on Ni(111). Proximity to gold induces a *Rashba-type* spin splitting in the Dirac cone of graphene by hybridization of its p_z orbitals with Au d-states. We also demonstrated how structural details can give important insights into the SOI enhancement mechanism in graphene. Even more intriguing is the proximity of graphene to heavy *sp*-metals that were predicted to induce an *intrinsic* SOI [6]. This type of SOI results in band gaps of opposite signs at K and K′ points and allows to realize a long-sought quantum spin Hall effect in graphene [5].

This Chapter is devoted to our study of the electronic band structure of graphene on Ir(111) intercalated by the heavy *sp*-metal Bi. We present ARPES results that show a nearly ideal dispersion of graphene bands in Bi-intercalated samples. Lack of superstructural band replicas or hybridization with the substrate states reflects the weak interaction between graphene and Bi. However, the main focus of the study is a band gap at the $\overline{\mathrm{K}}$ point of graphene and its possible origin. Extensive structural study by means of STM and analysis of the ARPES intensity distribution in the Dirac cones allow us to conclude that the major contribution to the band gap is due to A-B sublattice asymmetry. We start this chapter with a theoretical introduction essential for our analysis and an overview of existing literature about Bi-intercalated graphene.

3.1.1 ARPES intensity distribution in the Dirac cone of graphene

A prominent feature of a typical graphene ARPES map is the peculiar intensity distribution pattern observed in the constant energy surfaces (CESs) (Fig. 3.1). Since the band structure is periodic in reciprocal space and has certain symmetries one would expect to see the same symmetry in the CESs extracted from ARPES maps. However, in the vicinity of the Dirac point one can see that intensity of the π-band gradually disappears towards one side of the cone, which is not consistent with the three-fold symmetry of the $\overline{\mathrm{K}}$ point of the BZ.

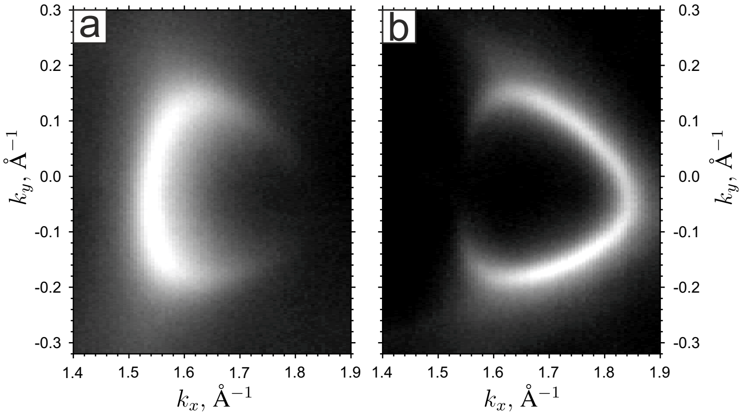

Figure 3.1: Typical experimental CESs extracted from ARPES mapping of the Dirac cone in graphene display the peculiar non-threefold-symmetric intensity distribution. Sample is graphene on Ir(111) intercalated by Gd. CESs are taken for energies (a) 1 eV *below* the Dirac point, i.e. in the π-band; (b) 1 eV *above* the Dirac point, i.e. π^*-band.

The photoemission intensity along the Dirac cone (DC) changes from maximum closer to the $\overline{\Gamma}$ point of the first BZ to minimum on the opposite side in the $\overline{\Gamma\mathrm{K}}$ direction. Since for ideal graphene minimal intensity drops to the level of background, this area is sometimes referred to as "dark corridor" of graphene photoemission intensity. This effect was observed already in early photoemission experiments with graphite and its detailed theoretical explanation was given first by Shirley et al. [226].

In very general terms one can explain this intensity modulation as interference between electrons photoemitted with the same kinetic energy and momentum reaching the same point on the detector at the same time. The result of interference between those electrons will depend not only on their path length difference but also on the initial phase difference of their wavefunctions in graphene. As was briefly discussed in the Introduction, the electronic eigenstates of the graphene Hamiltonian in the vicinity of the $\overline{\mathrm{K}}$ point [Eq. (1.19)] can be written as spinors with two components that show complex amplitudes of the wavefunction located at different sublattices. Their phases are generally not equal and also vary with momentum $\vec{\mathbf{k}}$, which results in a complex $\vec{\mathbf{k}}$-dependent interference pattern observed in photoemission.

To theoretically describe how such interference pattern should look like one has to determine the wavefunction phase difference for electrons with momentum $\vec{\mathbf{k}}$ that originate from different sublattices. There are two ways to approach this problem:

- to use "honest" tight-binding calculations for graphene as was done in the beginning of the Introduction (Section 1.2.2). This is a simple and powerful method providing an analytical solution for the whole momentum space using some reasonable assumptions that simplify calculations. This approach is perfect for the simple case of an idealized graphene sheet.
- to use a Dirac-like Hamiltonian [Eq. (1.19)] for the region around the $\overline{\mathrm{K}}$ points. Although this Hamiltonian is valid only as approximation for the low-energy excitations and this approach cannot be used for the whole momentum-space, it allows one to directly discuss the results in graphene-specific terms, such as pseudospin and chirality. Moreover, it seems easier to use this approach as a starting point for more complex calculations, e.g. with several graphene layers, with included A-B sublattice symmetry breaking, etc.

We will exploit the first approach and follow Shirley et al. [226] to calculate the interference-related ARPES intensity modulation in the π-band. We can use the system of secular equations that was already derived in the Introduction (see Eq. (1.5)):

$$\begin{cases} c_1 H_{11}(\vec{\mathbf{k}}) + c_2 H_{12}(\vec{\mathbf{k}}) & = c_1 E, \\ c_1 H_{21}(\vec{\mathbf{k}}) + c_2 H_{22}(\vec{\mathbf{k}}) & = c_2 E. \end{cases} \tag{3.1}$$

Next step is to find the relative phase of the coefficients c_1 and c_2. Using that $H_{11}(\vec{\mathbf{k}}) = H_{22}(\vec{\mathbf{k}}) = E_0$ and $(E_0 - E)^2 = |H_{12}|^2$ we get

$$\frac{c_1}{c_2} = \mp \frac{H_{12}(\vec{\mathbf{k}})}{\left|H_{12}(\vec{\mathbf{k}})\right|}, \tag{3.2}$$

where "$-$" corresponds to occupied π and "$+$" – to unoccupied π^* bands, respectively. Now from Eq. (1.14) we obtain[*]:

$$H_{12}(\vec{\mathbf{k}}) = -\gamma_0 \left[e^{ik_y b} + e^{i(\sqrt{3}/2k_x - 1/2k_y)b} + e^{i(-\sqrt{3}/2k_x - 1/2k_y)b} \right], \tag{3.3}$$

where $b = 1.42$ Å is the nearest-neighbour distance in graphene. Now we need to determine the photoemission intensity $I(\vec{\mathbf{k}})$, that is proportional to the squared modulus of the transition matrix element $M_{i,f}(\vec{\mathbf{k}})$. The first approximation would be to make the assumption of a plane-wave final state, which actually gives a good overall agreement

---

[*] Reference frame is rotated by 90° relative to the description in the introduction for convenience of calculations.

with experiment for p-polarized radiation with photon energies above 60 eV (ARPES experiments performed in this Chapter satisfy those conditions) [227]. Then the matrix element in the dipole approximation can be written as

$$M(\vec{\mathbf{k}}) \propto (\vec{\mathbf{k}} \cdot \vec{\lambda}) \sum_{j=1,2} c_j e^{-i\vec{\mathbf{k}}\cdot\vec{\tau}_j} \psi_j(\vec{\mathbf{k}}). \tag{3.4}$$

Here, $(\vec{\mathbf{k}} \cdot \vec{\lambda})$ is a polarization factor, where $\vec{\lambda}$ is the polarization vector of the incident radiation. In the following we assume that p-polarized light is used (for more details on the influence of light polarization see Ref. [227]). Vector $\vec{\tau}_j$ describes the position of the atom that emits the electron. Since p_z atomic orbitals are rotationally symmetric the $\psi_j(\vec{\mathbf{k}})$ factor does not influence the resulting angular distribution of intensity. The modulation of intensity due to interference then can be described by a simple analytical formula using Eq. (3.2) and taking into account that $\vec{\tau}_2 - \vec{\tau}_1 = b\vec{\mathbf{e}}_y$:

$$I(\vec{\mathbf{k}}) \propto \left| c_1 e^{-i\vec{\mathbf{k}}\cdot\vec{\tau}_1} + c_2 e^{-i\vec{\mathbf{k}}\cdot\vec{\tau}_2} \right|^2 \propto \left| 1 \pm e^{ibk_y} \frac{H_{12}^*}{|H_{12}|} \right|^2 \equiv |\xi_\pm(k_x, k_y)|^2. \tag{3.5}$$

The intensity modulating function $|\xi_+(k_x, k_y)|^2$ for the π band ("+" sign) is plotted in Figs. 3.2(a,b). One can see that it has almost constant profile inside the first BZ and abrupt slopes around the zone corners. The modelled intensity of CESs is presented in Fig. 3.2(e) as a contour plot of graphene π-band dispersion (same model as in Fig. 1.2(b) of the Introduction) for binding energies starting close to E_F and with steps of 1 eV, black colour corresponds to high intensity. In case of π^* band ("$-$" sign in Eq. (3.5)) intensity distribution around the zone corners reverses (see Fig. 3.3).

Results for the model agree very well with the experimental observations of the "dark corridor". And this agreement is not only qualitative: the profile of the modulation function tracked along a circle centered at $\overline{\mathrm{K}}$ (similar to a Dirac cone CES taken close to E_F) has a typical $\cos^2(\theta/2)$ dependence* [Fig. 3.2(d)] and the same shape can be extracted from the experimental data [228]. Important to note that in one direction the modulation function becomes zero and intensity is expected to vanish completely.

One of the idealizations of the model was perfect A-B symmetry of graphene. As was discussed in Section 1.2.3, breaking of this symmetry can occur for graphene on a substrate and result in a band gap in the Dirac cone. At the same time, this symmetry is responsible for the effect of perfect intensity cancellation in electron interference. Disturbance of the sublattice symmetry will influence the phases of the electronic wavefunctions on A and B sites and cause a non-zero intensity in the area of the "dark corridor". This effect was quantified and studied in detail by Bostwick et al. [228] and

---

*This formula can be proved analytically by expansion of the $|\xi_+(k_x, k_y)|^2$ function around $\overline{\mathrm{K}}$. However, this approximation of the intensity profile is good only in the vicinity of the $\overline{\mathrm{K}}$ point and it starts to deviate significantly from the real curve for distances larger than 0.1 Å^{-1}.

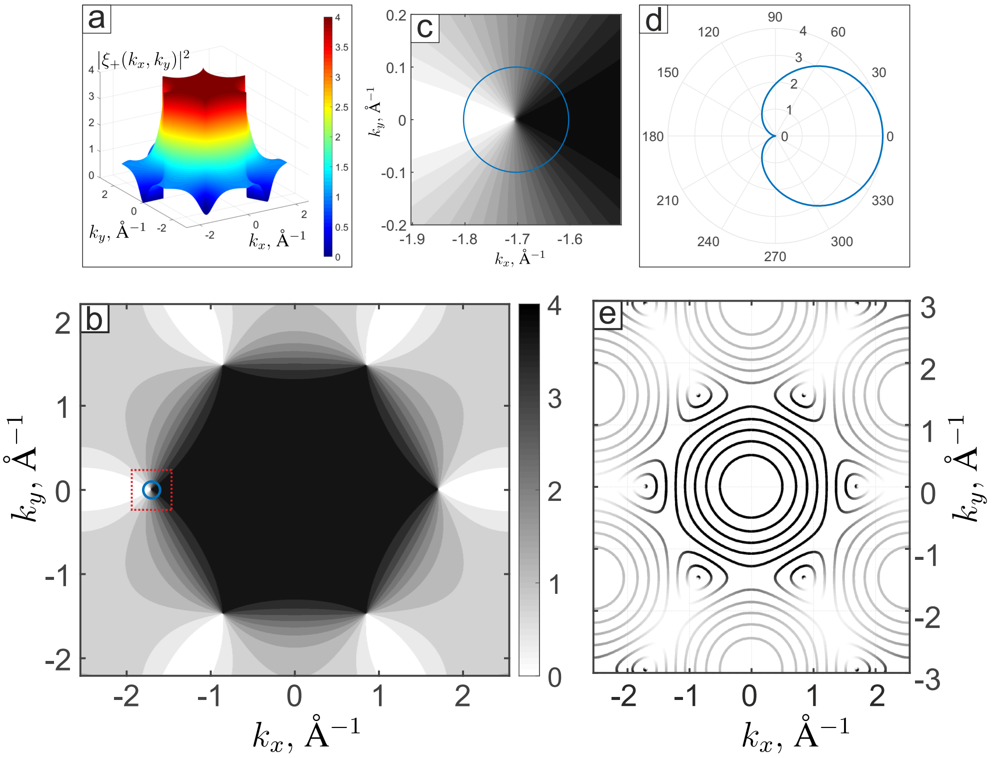

Figure 3.2: PES intensity modulation due to the interference effect in graphene. (a) 3D plot of the modulation function $|\xi_+(k_x, k_y)|^2$ (for the π-band). Remarkable feature is an abrupt slope at the corners of the high hexagonal region ($\overline{\mathrm{K}}$ and $\overline{\mathrm{K}}$' points). Contour plot of the same function is displayed in (b). One can see the area of maximal intensity (black) inside the first BZ and a complicated behavior around its corners. Close-up of the area around $\overline{\mathrm{K}}$' point marked by a red dashed box is presented in (c). Values of the modulation function tracked along the $\overline{\mathrm{K}}$-centered blue circle with radius 0.1 Å^{-1} are displayed as a polar plot in (d). (e) Contour plot of π-band dispersion for binding energies $E_B = \{0.1, 1.1, 2.1, ..., 7.1\}$ eV. Color corresponds to the value of $|\xi_+(k_x, k_y)|^2$.

in the follow-up studies [227, 229]. The calculations show that relative intensity in the "dark corridor" region increases as a function of Δ [Fig. 3.4]. This means that one can use experimental ARPES maps to extract the ratio of minimal and maximal intensities from a CES and estimate Δ from it. A useful analytical expression for intensity can be elaborated from Ref. [223] (assuming negligible Rashba SOI, i.e. $\lambda_R \approx 0$):

$$I_\mu(q) \propto 1 - \mu \frac{2v_F \hbar q_y}{\sqrt{(2v_F \hbar q)^2 + \Delta^2}}, \tag{3.6}$$

where $\mu = 1(-1)$ for $\pi^*(\pi)$ band, q is momentum relative to $\overline{\mathrm{K}}$.

For systems where the asymmetry is not very strong, minimal intensities can be very low, down to the noise level of the experimental setup. This way the noise level puts a physical limit on the minimal Δ that can be measured by this method.

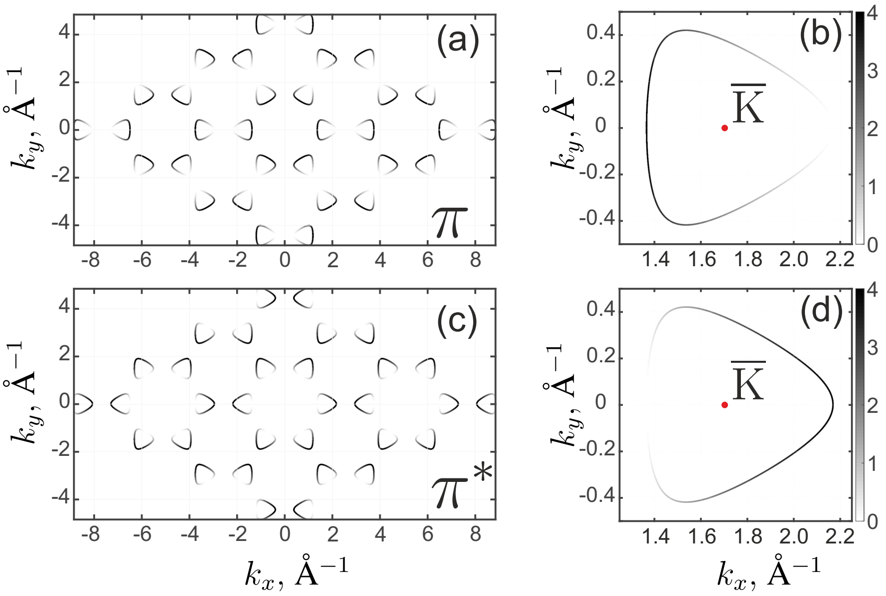

Figure 3.3: Comparison of interference effects in the modelled CESs for π (a,b) and π^* (c,d) bands. Contour plots are presented for binding energies of 2.1 eV and -2.1 eV, respectively. (a,c) Large-scale view of the interference pattern, area of (4×4) Brillouin zones is visualized (corners of the figures are empty). (b,d) Close-up of the area around the $\overline{\mathrm{K}}$ points. One can clearly see the reversal of intensity between π and π^* bands.

3.1.2 Overview of Gr/Ir(111) and Gr/Bi interfaces

Iridium (111) is a widely used substrate that allows direct CVD-growth of graphene, consequently graphene/Ir(111) [Gr/Ir(111)] is a well studied system by now. The popularity of the Ir(111) substrate is explained not only by the relative simplicity of preparation and good quality of graphene, but also by a large number of structural and electronic effects that can be observed and successfully studied in this system. First of all, one should note that depending on the growth conditions Gr/Ir(111) may appear in a variety of phases that differ by the rotation angle relative to the substrate [230–232]. The two most common among them are the so-called R0 phase, aligned with the Ir(111) surface lattice, and R30 phase where the graphene lattice is rotated by 30° relative to the substrate. A ~ 10% lattice mismatch between graphene and Ir(111) leads to a characteristic ~ (10 × 10) moiré pattern of the R0 phase* that is observed in LEED [Fig. 3.8(a)] and STM [Figs. 3.10(a–c)]. This moiré pattern produces a corrugation of the graphene sheet with an amplitude of 0.3–0.4 Å observed not only in STM, but also in Surface X-ray Diffraction (SXRD) experiments [233]. This allows to exclude the possibility of a pure LDOS effect in STM and proves that the apparent corrugation reflects the actual geometry of the surface. The periodicity of the pattern is ~ 25 Å and can be approximated by a higher order coincidence between the (10 × 10) graphene

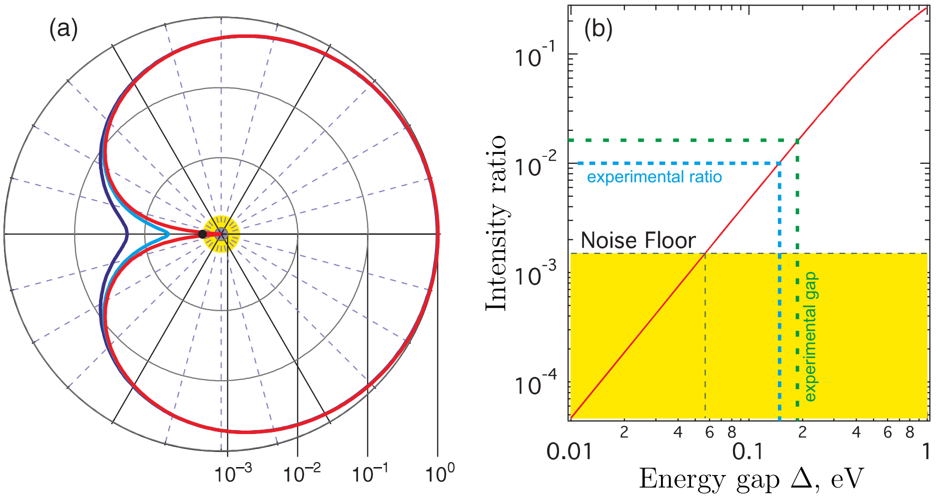

Figure 3.4: Intensity distribution pattern in graphene with broken A-B sublattice symmetry (adapted from [228]). (a) Polar plot of the theoretical intensity distributions along the circular CES for monolayer graphene (logarithmic intensity scale) for three different asymmetry parameters $\Delta = 0.0$, 0.1 and 0.2 eV (red, blue and dark blue lines, respectively). The minimal value of intensity increases with Δ. (b) Dependence of the minimal to maximal intensities ratio as a function of asymmetry parameter Δ. The area where minimal intensity is smaller than the noise level of the experimental setup is filled with yellow, the minimal gap value that can be determined is 55 meV. Blue and green dashed lines denote the values obtained in this work for intensity ratio and band gap, respectively (see the main text).

supercell and the (9×9) Ir(111) surface supercell. This large-scale superstructure inflicts a periodic variation of the potential and results in umklapp-derived replicas of the Dirac cone that are observed in ARPES (Fig. 3.5).

In the view of a superstructural Brillouin zone (so-called "mini-BZ", see Fig. 3.5), the crossing of replicated cones will happen at the mini-zone boundary and one can observe the "minigaps": narrow band gaps that appear in the crossing region [140, 141, 194] [marked with arrows in Fig. 3.9, and with red arrows in Fig. 3.9(a)].

The second prominent feature of Gr/Ir(111) is a sharp and nearly charge-neutral Dirac cone with only a slight p-doping (Dirac point is located above E_F, but its position can be estimated as $E_B = (-0.10 \pm 0.02)$ eV [140]). Nevertheless, one can hardly treat Gr/Ir(111) as quasi-free-standing due to the superpotential effects mentioned above and hybridization between π-band of graphene and $5d$-states of iridium that is clearly seen in ARPES as avoided crossings [57] [marked with green circles in Fig. 3.8(b)].

In a large number of experiments, desired properties of graphene on Ir(111) are achieved by intercalation of foreign atoms or molecules. A wide variety of substances

---

[*] One can calculate this using Eq. 1.72. Since lattice vectors are collinear, moiré vector also has the same direction and its period a_m satisfies $a_m^{-1} = \left|a_{Ir}^{-1} - a_{Gr}^{-1}\right|$. Thus $a_m = \left|2.452^{-1} - 2.715^{-1}\right|^{-1}$ Å $\approx$ 25.3 Å. This value depends strongly on the lattice parameters, here we used the value a_{Gr} of free-standing graphene assuming that it was not changed by interaction with the substrate.

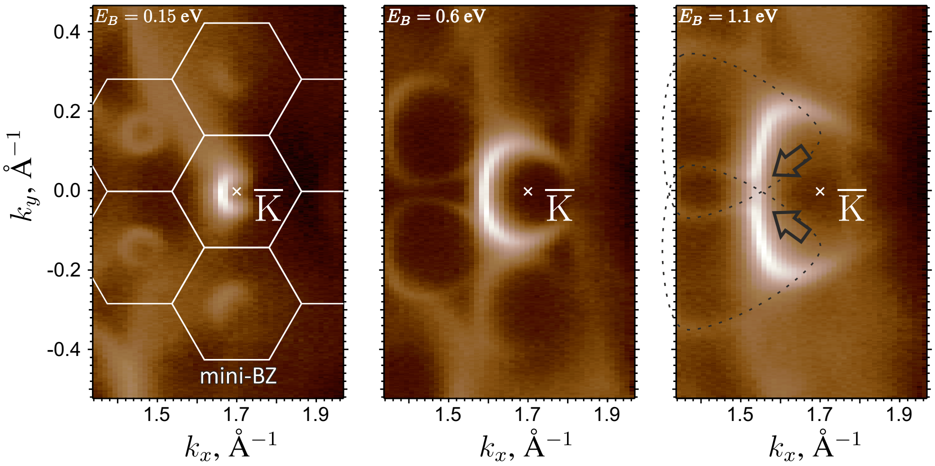

Figure 3.5: Replica cones and mini-Brillouin zones of Gr/Ir(111) in ARPES mapping. Three CESs extracted at increasing E_B (0.15, 0.6 and 1.1 eV) are presented in logarithmic intensity scale. The high intensity (white) feature centered exactly at the $\overline{\mathrm{K}}$ point is the main DC CES, its size increases towards higher binding energies and its shape changes from a circle to a rounded triangle. In the first panel one can see several faint replicas of the main cone CES symmetrically located around $\overline{\mathrm{K}}$, at the centers of the mini-BZs (white hexagons). The intensity distribution and size of the replicas' CESs reproduce the ones of the main cone. At high E_B replica cones intersect the main cone and minigaps appear at the crossing points (marked by arrows in the last panel).

has been tested, including noble metals (Au [234], Cu [235]), rare-earth metals (Gd [236], Eu [162], Hf [237]), atoms of magnetic (Co [238, 239]) and semiconducting (Si [240]) materials as well as some gases (oxygen [241] and CO [242]). Nevertheless, the published literature regarding **bismuth**-intercalated graphene is relatively scarce, especially for the Ir(111) substrate, for which to the best of our knowledge up to date it was studied only once [243, 244]. But this is only a part of motivation to study this system and another large part comes from the fact that bismuth itself is a fascinating material from many points of view [245]. It is the heaviest stable element in group V and its 3D and 2D compounds demonstrate a variety of interesting physical phenomena, such as quantum Hall effects, and realize topological phases [246]. Pure bulk Bi was shown to be a higher order topological insulator as well [247], while its 2D honeycomb phase on SiC(0001) is a candidate for a room temperature quantum spin Hall insulator [248].

A single layer of graphene on SiC(0001) intercalated by 1 ML of the *sp*-metal Bi was predicted to exhibit a nearly ideal Dirac cone dispersion except for n-doping and a minor extrinsic spin-orbit splitting of 5 meV [249]. Moreover, it was shown that 2/3 ML of intercalated Bi can form the above-mentioned honeycomb structure underneath graphene. The first prediction was partially experimentally verified in 2016 by Stöhr et al. [250, 251], the authors succeeded to intercalate Bi atoms under a "zero-layer" graphene on SiC(0001) [ZLG/SiC(0001)] — a strongly bonded graphene layer at the surface (also known as "buffer layer"). This was achieved by a complicated procedure consisting of Bi ion implantation in a hot ZLG/SiC(0001) and post-annealing in argon atmosphere. The following ARPES measurements indeed revealed a graphene band structure with intact Dirac cone in the π-band and n-doping of 0.35 eV. However, no spin splitting of the Dirac cone was observed above the resolution limit of the experiment [250].

Absence of spin splitting was observed as well in earlier series of experiments with Bi-intercalated Gr/Ni(111) [58, 60] and this effect allowed to pinpoint the π-d hybridization as the main mechanism responsible for the induced spin-orbit interaction observed in the Dirac cones of graphene on heavy d-metals [4, 57].

To the best of our knowledge the only data available up to date for Gr/Ir(111) intercalated with Bi [Gr/Bi/Ir(111)] was obtained by Warmuth et al. [243, 244]. The authors have experimentally determined that for the Ir(111) substrate intercalation of Bi was possible by simple deposition on the hot substrate with post-annealing. The resulting Dirac cones of graphene demonstrated n-doping of 0.39 eV and a large band gap at the Dirac point of ~ 0.42 eV. Moreover, a thorough STM structural study was conducted that revealed a $(\sqrt{3} \times \sqrt{3})$ $R30^\circ$ superstructure formed by 1/3 ML of Bi on Ir(111) together with an unusual double-line dislocation network (this phase is further referred to as low-density or LD phase). This dislocation network was proposed as a possible origin of the observed large band gap. Unfortunately, the details of electronic bands measured by ARPES in this study are smeared out due to relatively large spectral broadening. In present Chapter we try to extend the knowledge about both the possible atomic and electronic band structures of Bi-intercalated Gr/Ir(111). The band gap in the DC observed for this system in our study is much smaller — only 190 meV, moreover combination of STM and ARPES data reveal unambiguously that we achieve an intercalation phase that is different from the $(\sqrt{3} \times \sqrt{3})$ $R30^\circ$ phase reported by Warmuth et al. We attribute the differences to higher surface coverages of intercalated Bi and refer to this phase as high-density (HD) phase. Finally, carefully analyzing the photoemission intensities we are able to identify that the main contribution to the band gap arises from A-B sublattice symmetry breaking.

3.2 Experimental details

Sample preparation and all STM and ARPES experiments have been performed in UHV at a base pressure below 2×10^{-10} mbar. Spin-resolved PES has been performed using a Rice University Mott-type spin polarimeter [252] with Au target.

Preparation of graphene on Ir(111) [Gr/Ir(111)] has been conducted following the recipe from Ref. [57]. Several iridium single crystals cut and oriented in the (111) direction with $<0.1^\circ$ accuracy were purchased from MaTecK GmbH. For sample manipulation in the UHV experimental setups all crystals were mechanically fixed on molybdenum Omicron-type sample plates by spot-welded tantalum stripes.

Clean and atomically flat (111) surfaces of iridium single crystals were prepared by repeated cycles consisting of ion sputtering (Ar^+) and subsequent annealing at T=1600 K. To prepare graphene a CVD process was used: the clean Ir(111) substrate was heated up to T=1200 K and a hydrocarbon gas (propene) was introduced in the chamber at a partial pressure of 5×10^{-8} mbar. These conditions allow to achieve graphene with large domains of predominantly R0 phase, with only minor inclusion of R30.

The typical LEED pattern of the prepared sample is presented in Fig. 3.8(a) and does not contain any visible traces of the R30 phase. Moreover, proper identification of rotational domains is possible both in microscopic studies (by the difference in the moiré patterns) and in ARPES band structure measurements due to the large momentum space displacement of $\overline{\mathrm{K}}$ points of corresponding rotated Brillouin zones.

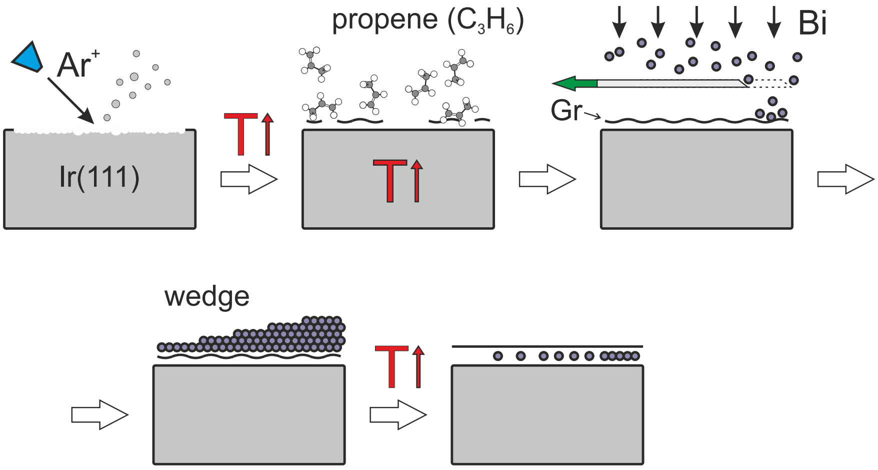

Figure 3.6: Schematic sample preparation procedure for Gr/Bi/Ir(111). Step by step: Ar^+ ion sputtering and annealing of the substrate; CVD cracking of propene on clean and flat Ir(111) surface; deposition of Bi on top of Gr/Ir(111) using a moving shutter technique; Bi wedge deposited on graphene with maximum thickness of several ML (method I); result of intercalation: local coverage gradually increases from no Bi to a full monolayer.

Many metals can be intercalated under graphene by deposition of the required amount of material on the sample surface (e.g. 1 ML) at room temperature and subsequent annealing. However, we have observed that for Bi this method is very ineffective and only small amounts of the material can be intercalated in one step, most likely this happens due to the low sublimation temperature of Bi (∼ 520°C [250]). To actually achieve intercalation three different methods were used:

I. deposition of several times larger amounts of Bi than required (∼ 5–6 ML as calibrated by a quartz microbalance) on Gr/Ir(111) held at room temperature and subsequent annealing at $T = 800$ K for 10 min;

II. deposition of Bi on a hot Gr/Ir(111) surface maintained at $T = 750$ K for 30 min with subsequent short-time annealing at $T \approx 1300$ K (following Ref. [243, 244]);

III. the same as above but without the short-time high-temperature annealing step.

All of the approaches above proved to be equally successful for intercalation and ARPES results from the obtained samples were qualitatively similar, however, some differences were observed (especially for approach III) and will be discussed below. Most of the experimental results were obtained for samples prepared by method I. To study the effect of different coverages of intercalated Bi this method was extended by the following technique: during Bi deposition a shutter with a sharp straight edge was moved parallel to the surface of the sample shadowing some part of it from the deposited material. The shutter was translated in discrete steps of constant width at equal time intervals producing a stepped profile of Bi thickness ("wedge", Fig. 3.6). The deposition rate was calibrated by a quartz microbalance to be 0.6 Å/min in all cases. At each step of preparation the surface condition was monitored by LEED and reference measurements by LEED, STM, ARPES and XPS were performed.

All STM data was obtained at room temperature with an Omicron VT STM. ARPES measurements including the band structure mapping have been carried out at the end-station ARPES 1^2 [178]. Resolutions of the experiment were 0.3° (angular) and 10 meV (energy). A photon energy of 62 eV and linear p-polarization of light have been used.

The samples have been prepared both in ARPES and STM preparation chambers. To perform a consistency check, some samples have been transferred between ARPES and STM chambers in a vacuum suitcase.

3.3 Experimental results and discussion

3.3.1 Preparation and core-level spectroscopy

In the overview spectrum of a clean Ir(111) crystal measured at a photon energy of 120 eV one can observe peaks of photoelectron intensity corresponding to Ir 4f core-levels (CLs) [Fig. 3.7(a), bottom]. The Ir 4f spectrum consists of *two* overlapping spin-orbit doublets [Fig. 3.7(b)]. They are attributed to electrons emitted from the Ir atoms located in the bulk and at the surface of the crystal, which have higher and lower binding energies, respectively (detailed description of this effect is given e.g. in Ref. [65], section 8.4). Fitting and analysis of CL spectroscopy data shows that the surface component is shifted relative to the bulk one by $\Delta_{surf} = 0.43$ eV. For Gr/Ir(111) the surface (or more precisely, *interface*) component does not disappear in the spectrum and the energy shift increases to 0.53 eV, whereas after Bi intercalation Δ_{surf} decreases to 0.3–0.4 eV (depending on the preparation method, see Table 3.1) and becomes even lower than the value for clean Ir(111).

Only one component can be distinguished in the 5d Bi CLs for all types of intercalation [see Fig. 3.7(c)]. The slightly asymmetric lineshapes are very well described with Doniach-Sunjic profiles, typical for excitation from metallic compounds [253].

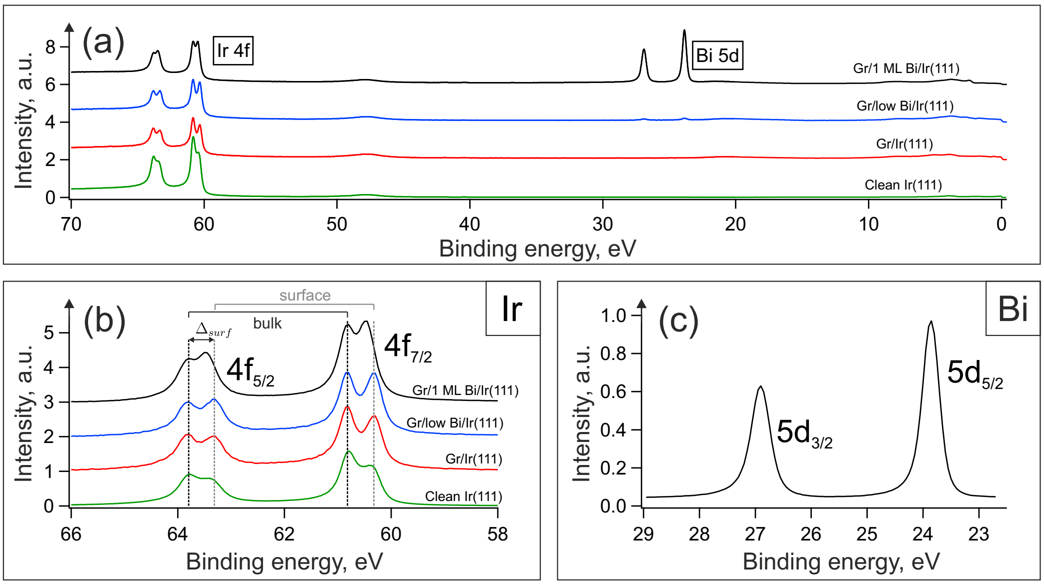

Figure 3.7: Core-level spectroscopy of Gr/Bi/Ir(111) sample at different stages of preparation (method II): clean Ir(111), Gr/Ir(111), sample with low concentration of intercalated Bi and fully intercalated sample (1 ML of Bi). Photon energy $h\nu = 120$ eV was used. (a) Overview spectra. (b) Close-up of Ir 4f CLs with Shirley background subtracted, positions of bulk and surface components are shown with bars on top. Relative intensities are not to scale. (c) Close-up of Bi 5d CLs for fully intercalated sample.

Binding energies for both bulk Ir 4f (63.8 and 60.85 eV) and Bi 5d (26.9 and 23.9 eV) CLs agree well with the tabulated values for bulk elements in their natural forms [254] and show almost no variation with the preparation method. The only exception is deposition on hot substrate without post-annealing (method III), in that case the Bi CL has $E_B = 27.2$ eV, i.e. shifted by 0.25–0.30 eV towards higher binding energies. Moreover, method III results in a different Ir 4f CL surface component energy shift: 0.3 eV instead of the very close values 0.40 and 0.38 eV for methods I and II, respectively. Looking ahead, the Dirac point of graphene in method III is also located at the highest binding energy among the different preparations (0.47 eV, see Table 3.1).

Altogether, we observe very similar spectra for samples prepared by methods I and II and some spectral differences for intercalation on a hot substrate without post-annealing (III). These differences may stem from uneven distribution of Bi under graphene. In the following we will use data obtained from samples prepared by methods I and II.

Surprisingly, the large 0.42 eV band gap in the DC of graphene observed by Warmuth et al. [243] was not reproduced by any of our intercalation methods, even method II that was based on the preparation procedure described in the mentioned reference. However, other parameters, such as DC doping and Ir and Bi CL positions are in relatively good agreement (Table 3.1).

	I	II	III	Refs. [243, 244]
Bi $5d_{3/2}$, eV	26.95	26.9	**27.2**	26.95
Ir 4f Δ_{surf}, eV	0.40	0.38	**0.30**	0.37
DC Doping, eV	0.38	0.43	**0.47**	0.39
DC Gap, eV	0.19	0.18	0.19	0.42

Table 3.1: Reference energies in Gr/Bi/Ir(111) for different Bi intercalation methods: I. deposition of 5–6 ML Bi with post-annealing; II. deposition on hot sample with post-annealing (as in [243]); III. deposition on hot sample, no post-annealing (see main text).

3.3.2 Preparation and characterization by LEED and ARPES

The intercalation of Bi under Gr/Ir(111) leads to significant changes both in the LEED pattern and in ARPES spectra allowing to immediately identify a successful preparation, the direct comparison is presented in Fig. 3.8. The LEED pattern of pristine Gr/Ir(111) [Fig. 3.8(a)] has around the primary reflections multiple superstructural diffraction spots that originate from the moiré pattern discussed above (section 3.1.2). Their formation is the result of electrons scattering by multiples of the moiré reciprocal vector $\vec{\mathbf{G}}_m = \vec{\mathbf{G}}_{Gr} - \vec{\mathbf{G}}_{Ir}$ in the diffraction process, one can also interpret this as multiple scattering of electrons on two lattices (e.g. by vectors $\vec{\mathbf{G}}_{Gr}$ and $-\vec{\mathbf{G}}_{Ir}$) [255]. The sharpness of the moiré LEED pattern and the large number of superstructural reflections evidence good quality of graphene.

In the case of the Gr/Bi/Ir(111) HD phase, moiré pattern spots are still present but strongly suppressed as compared to Gr/Ir(111), indicating a significantly reduced superpotential amplitude [Fig. 3.8(d)]. Moiré pattern spots are visible only up to the first order of diffraction, moreover their intensities are very weak as compared to the primary spots of graphene (gray arrow) and the substrate (yellow arrow), the latter displays a periodicity similar to Ir(111). Such LEED pattern evidences a reduced probability for an electron to undergo multiple scattering from *both* Ir and graphene lattices which could be explained by a dense layer of intercalated Bi decoupling graphene from the Ir(111) substrate. Since we do not observe any extra structural spots to appear after intercalation, the Bi layer has to be structurally coherent either to the Ir(111) or to the graphene (formation of an amorphous layer is unlikely). The overall experimental band structure of Gr/Ir(111) is displayed in Fig. 3.8(b). Spectra were measured along high-symmetry directions $\overline{\Gamma \mathrm{M}}$ and $\overline{\Gamma \mathrm{K}}$ of the SBZ. One can see the intense graphene π-band and σ-bands crossing it between 6 and 7 eV binding energy. Moreover, multiple bands related to the Ir substrate are observed, including the well-known Ir(111) surface resonance state [40] (0.2 eV below E_F at the $\overline{\Gamma}$ point, marked as "Ir-SS") and Ir *5d* bands (at 2–6 eV binding energy). The latter hybridize with the π-band of graphene as seen from the avoided-crossing gaps marked with green dotted circles in Fig. 3.8. This hybridization was proposed earlier as the origin of a 50 meV spin splitting in the DC of

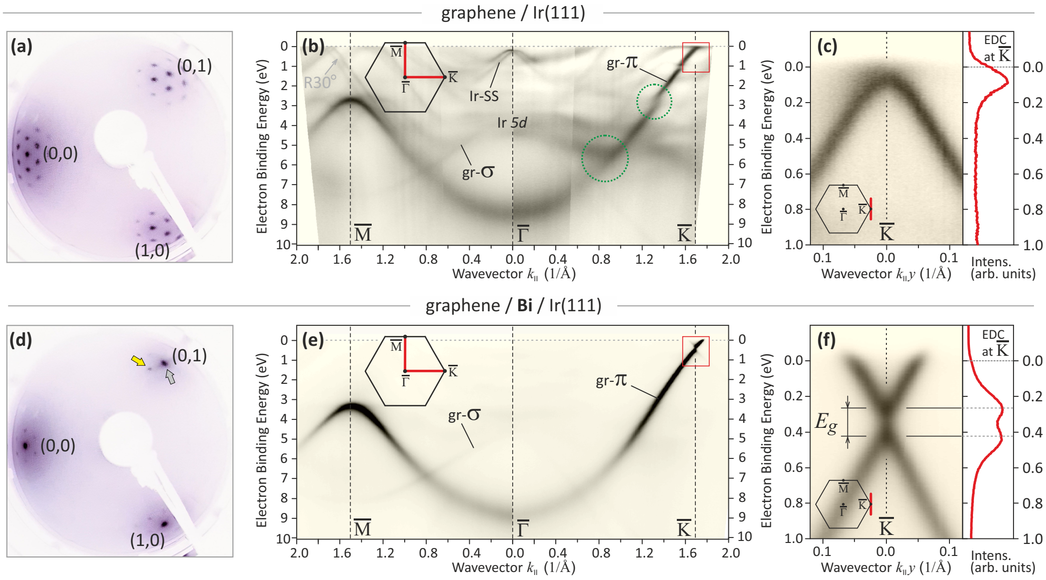

Figure 3.8: Characterization and comparison of Gr/Ir(111) (a–c) and HP phase of Gr/Bi/Ir(111) (d–f) by LEED and ARPES. (a) LEED pattern of pristine Gr/Ir(111) with pronounced $\sim (10 \times 10)$ moiré pattern ($E_p = 53$ eV). (b) Overview ARPES spectra along the $\overline{\Gamma \mathrm{M}}$ and $\overline{\Gamma \mathrm{K}}$ directions of the SBZ (sketched in the inset). Faint band visible at the $\overline{\mathrm{M}}$ point close to E_F is the Dirac cone of the R30 phase that is present in the sample in minor concentrations. (c) Close-up of the Dirac cone measured with high angular resolution along the direction perpendicular to $\overline{\Gamma \mathrm{K}}$ (red line in the inset BZ sketch). (d) LEED pattern of Gr/Bi/Ir(111) HD phase with suppressed moiré pattern ($E_p = 53$ eV). (e) Overview ARPES spectra of Gr/Bi/Ir(111) HD phase. Ir bands, minigap, and hybridization gaps [green circles in (b)] disappear. (f) Close-up of the Dirac cone showing n-doping and band gap of ~ 190 meV.

Gr/Ir(111) [57]. Another, more narrow gap in the DC visible in Fig. 3.8(b) close to the $\overline{\mathrm{K}}$ point of graphene ($E_B \approx 1$ eV) is a "minigap" due to a crossing of the main Dirac cone with its superstructural replica [the latter is not seen in Fig. 3.8(b) due to its low intensity, see the first panel of Fig. 3.9(a)].

Close-up of the Dirac cone at $\overline{\mathrm{K}}$ is displayed in Fig. 3.8(c). The presented dispersion was measured in the direction perpendicular to $\overline{\Gamma \mathrm{K}}$ and thus has symmetric ARPES intensities on both sides of the cone in contrast to the dispersion in Fig. 3.8(b), where one side of the cone falls into the "dark corridor" of photoemission intensity, as discussed in the introduction to this Chapter. The Dirac point (E_D) is located above the Fermi level but from the curvature of the DC apex one can estimate the band gap as ~ 200 meV. This band gap is typically explained to arise from local A-B symmetry breaking [141, 194] and hybridization between the DC and an Ir $5d$ band located close to E_F [256].

Superstructural effects, band gap and hybridization altogether substantially alter the Dirac cone dispersion of Gr/Ir(111). However, after intercalation of Bi most of these effects are eliminated and the observed dispersion becomes closer to a quasi-free-standing case [Figs. 3.8(e,f)].

First obvious change in spectra is that Ir surface resonance and all Ir $5d$ bands visible for pristine Gr/Ir(111) are completely suppressed and there are no hybridization gaps in the π-band of graphene anymore [Fig. 3.8(e)]. Secondly, as suggested by the changes in LEED pattern, the amplitude of the moiré superpotential is significantly reduced, thereafter the superstructural replicas in ARPES also vanish together with the minigaps. As a result the band structure of graphene is nearly ideal with only minor deviations from the free-standing case, such as a relatively small band gap $E_g \approx 0.19$ eV and n-doping ($E_\mathrm{D} \approx E_\mathrm{F} - 0.4$ eV) [red rectangle, zoomed in Fig. 3.8(f)].

The high quality of the resulting graphene is reflected by the narrow photoemission peaks. Analysis by fitting of MDCs with a Lorentzian profile gives full widths at half-maximum (FWHM) of 0.024 Å^{-1} for MDC taken 1 eV below the E_D and 0.017 Å^{-1} close to E_F. This is comparable to the values for pristine Gr/Ir(111) (here and e.g. in Ref. [257]) and much smaller than in Ref. [243], also it is several times smaller than for the ion implanted Gr/Bi/SiC(0001) system (FWHM $\sim (0.11 \pm 0.02)$ Å^{-1}, [250]).

The negligible spectral contribution from the Ir states [Fig. 3.8(e)] can be explained by a dense and homogeneous layer of intercalated Bi together with the surface sensitivity of ARPES. Electrons photoemitted from the buried Ir surface have a reduced probability to escape to vacuum without undergoing inelastic collisions in the Bi layer. As we will show further by STM measurements, the thickness of the Bi interlayer can exceed a single ML, as observed at the intercalation sites (see Fig. 3.11).

To sum up, intercalation of Bi under graphene on Ir(111) results in a Bi interlayer of high density that provides a quasi-free-standing graphene decoupled from the Ir(111) substrate with n-type doping of ~ 0.4 eV and a band gap $E_g < 0.2$ eV. In the following section of this study we show that the width of this band gap can be controlled by variation of the Bi concentration.

3.3.3 Dependence on Bi concentration

To study the influence of the Bi concentration on the band structure of graphene we have prepared a sample with variable amount of Bi along the surface. Intercalation was performed by Method I. Since only a small portion of Bi deposited on the sample surface gets intercalated under graphene ($\sim 1/5$ of the total amount), factual Bi concentrations were estimated *after* the preparation as the ratio between intercalated and non-intercalated sample areas. This value was determined from the intensity ratio of two well separated graphene Dirac cones visible in the ARPES spectra of samples with intermediate Bi concentrations [Figs. 3.9(a,b)] and attributed to Bi-intercalated and pristine Gr/Ir(111). In the following we refer to this value as "local concentration" of Bi on the sample surface.

The most important changes that happen in the band structure with increasing Bi concentration can be monitored in the vicinity of a $\overline{\mathrm{K}}$ point of graphene [Fig. 3.9]. Two sets of DC dispersions were measured: along the intensity-symmetric direction [perpendicular to $\overline{\Gamma\mathrm{K}}$ Fig. 3.9(a)] and along the most intensity-asymmetric direction [$\overline{\Gamma\mathrm{K}}$, Fig. 3.9(b)]. The directions in the SBZ are marked in Fig. 3.9(d) with orange and green lines, respectively.

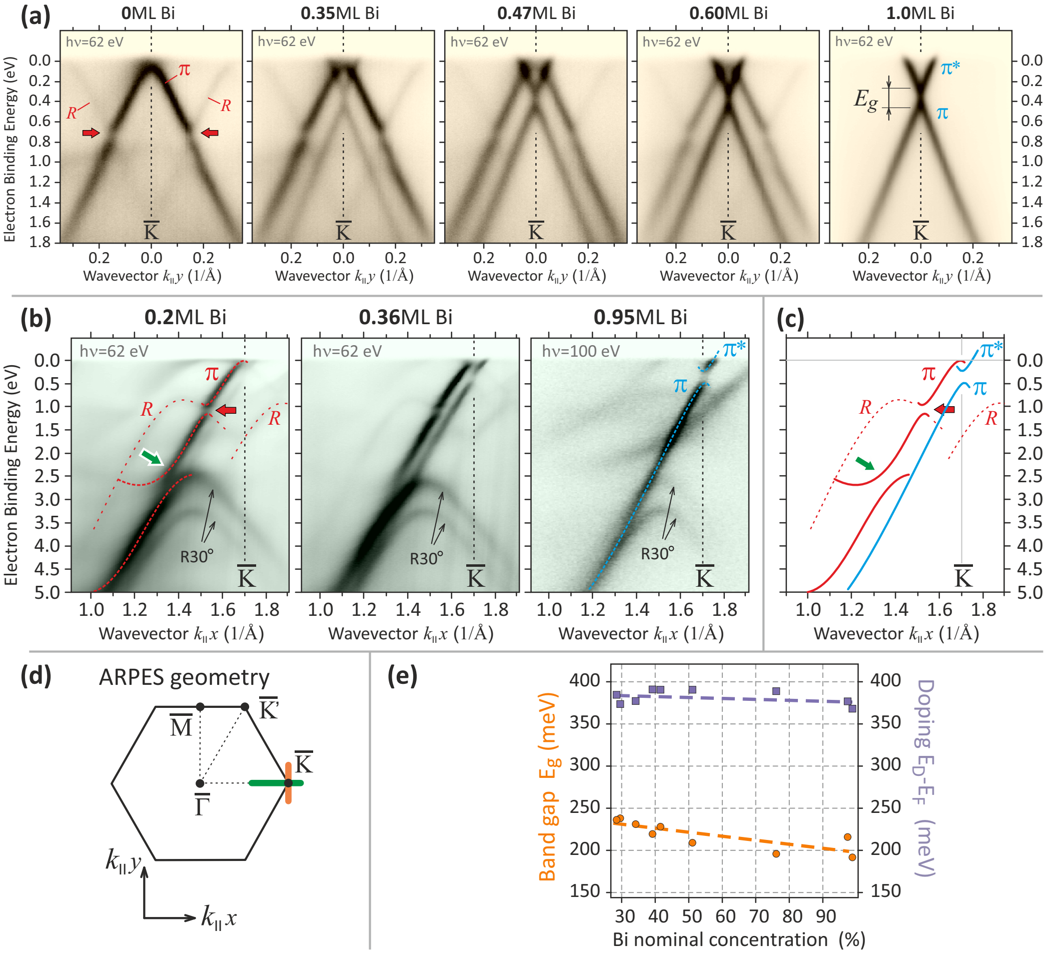

Figure 3.9: Evolution of Gr/Bi/Ir(111) ARPES spectra with increasing Bi concentration. (a) Changes in the DC of graphene from 0 to 1 ML of intercalated Bi. Measurements along the direction perpendicular to $\overline{\Gamma\mathrm{K}}$ [orange line in (d)]. Superstructural replica cones (marked with R) are crossing the main cone forming the minigaps (marked with red arrows). (b) Same as (a), but along the intensity-asymmetric $\overline{\Gamma\mathrm{K}}$ direction [green line in (d)]. The enlarged scale allows to see the evolution not only of replica bands (R, dashed lines), but also of the hybridization gap (green arrow). (c) Sketch of band dispersions extracted from (b). Red corresponds to the π-band of Gr/Ir(111) (and its replicas) and blue — of Gr/Bi/Ir(111). (d) Schematic of the SBZ and ARPES measurement directions. (e) Concentration dependence of doping (magenta) and band gap (orange) of the DC in Gr/Bi/Ir(111).

First of all, from Fig. 3.9(a) one can see that ARPES spectra for the intermediate Bi concentrations look exactly like a linear combination of two limiting cases: spectrum of pristine Gr/Ir(111) (0 ML Bi) and fully intercalated Gr/Bi/Ir(111) (1ML Bi), summed up with different weights. All of the characteristic features of the component associated with Gr/Ir(111), such as charge neutrality, replica bands and minigaps, are clearly visible and display no sizeable change with Bi concentration. Only the intensity of this component is changing, gradually decreasing with higher amounts of Bi, while the intensity of the other component correspondingly increases.

This superposition of signals indicates that intercalated Bi forms compact islands separated by areas of non-intercalated Gr/Ir(111), which was further confirmed by our STM data, and the electronic properties of graphene supported by such islands are not very different from a fully intercalated system. In the ARPES experiment the signal is measured from a finite surface area illuminated by the photon beam, in our case the average dimensions of Bi islands (several 100 nm, according to STM measurements) are much smaller than the beam size ($\sim 400 \times 20$ μm^2), thus it should lead to the superposition of signals from the two phases in proportion of the areas they occupy. Such a sharp transition without any intermediate phases allowed us to use the intensity ratio between the two spectral components to precisely measure the fraction of the intercalated area for each position on the sample (further called "Bi concentration").

To investigate if there are any subtle changes in the band gap or charge doping in the DC of the HD-phase, EDCs through the $\overline{\mathrm{K}}$ point were extracted from ARPES spectra for various Bi concentrations [similar to the ones presented in Fig 3.9(a)]. The values of the band gap (E_g) and charge doping (E_D) obtained by fitting of these EDCs are displayed in Fig. 3.9(e). While E_D remains constant [$E_\mathrm{D} = E_\mathrm{F} - 380$ (± 5) meV] in the whole concentration range, E_g decreases from $E_g = 240$ (± 5) meV for 30% Bi to $E_g = 185$ (± 5) meV for a fully intercalated area. This relatively small change highlights that graphene supported by Bi islands is not fully identical to a graphene on a monolayer of Bi. The reason could be a higher amount of imperfections in the smaller Bi islands, affecting the A-B symmetry of graphene that in turn influences the DC band gap. The details of this effect will be revealed further with the help of microscopy data.

Series of ARPES spectra of the DC region of the HD phase reported in Fig. 3.9(b) were measured along the $\overline{\Gamma\mathrm{K}}$ direction where one branch of the Dirac cone is not visible due to BZ-selection effect. Similarly to Fig. 3.9(a) the spectra display the evolution of the band structure with increasing Bi concentration, but in this case energy and momentum ranges are larger allowing to capture the region of the π-Ir 5d hybridization gap (marked with a green arrow). One can also see a contribution from the $\overline{\mathrm{M}}$ point of rotated graphene domains (R30 phase), however it does not affect our conclusions. The overall behavior of the spectrum is similar to Fig. 3.9(a): the pristine Gr/Ir(111) component vanishes with no significant change in its shape and characteristic features, while the Gr/Bi/Ir(111) component increases in intensity and displays no minigaps and no hybridization gap. A sketch of extracted band dispersions is presented in Fig. 3.9(c), where blue lines correspond to the HD-phase Gr/Bi/Ir(111) and red ones — to pristine Gr/Ir(111).

3.3.4 Structural study with STM

3.3.4.1 Comparison of Gr/Bi/Ir(111) and Gr/Ir(111)

The STM characterization of the sample is presented in Fig. 3.10. The STM data for Bi intercalated samples [Figs. 3.10(d–j)] was analyzed in comparison with the data for pristine Gr/Ir(111) [Figs. 3.10(a–c)]. The prominent feature of the latter is the moiré pattern due to a $\sim 10\%$ lattice mismatch between graphene and Ir(111) [140, 258]. It is observed in STM as a smooth two-dimensional periodic large-scale rippling of the graphene sheet with a period of ~ 25 Å and corrugation amplitude of ~ 0.3 Å [see Figs. 3.10(a–b) and trace I in Fig. 3(k)]. Inset of the Fig. 3.10(b) displays a high-resolution close-up of the graphene sheet showing its structure on atomic scale. A fast Fourier transform (FFT) was used to visualize and determine the periodicities present in the STM data. The FFT of Fig. 3.10(b) is shown in Fig. 3.10(c), it resembles the LEED pattern of Gr/Ir(111) [Fig. 3.8(a)] and reveals two main frequencies*: $f_1 = 4.22$ nm^{-1} and $f_2 = 0.41$ nm^{-1}. They correspond to lateral periodicities $d_1 = 1/f_1 = (2.37 \pm 0.08)$ Å (graphene) and $d_2 = 1/f_1 = (24.4 \pm 0.8)$ Å (moiré pattern).

After intercalation of a sub-monolayer amount of Bi (0.3 ML actual coverage) we observed the formation of islands with polygonal shapes: the borders of the islands were aligned parallel to the [010], [100] and $[\bar{1}\bar{1}0]$ directions of the Ir(111) surface with 120° angles between them [Fig. 3.10(d)]. The islands are separated by areas of pristine Gr/Ir(111) distinguishable by its characteristic moiré pattern [inset of Fig. 3.10(d)], at the same time on the island moiré pattern has a much smaller amplitude. These observations corroborate the intercalation mechanism proposed in the previous section with regard to the evolution of ARPES data with increasing Bi concentration.

In stark contrast to the results of Warmuth et al. [243, 244] for the LD-phase we did not observe a double-line dislocation pattern and a $(\sqrt{3} \times \sqrt{3})$ $R30°$ structure was visible only at some specific very localized areas on the sample (see discussion in Section 3.3.4.4). In general the surface of the HD-phase Gr/Bi/Ir(111) was smooth and maintained a moiré pattern similar to that in Gr/Ir(111) but with significantly reduced amplitude. In figure Fig. 3.10(e) we present STM image of an intercalated sample with high Bi concentration (around 0.9 ML). One can see a uniform graphene lattice all across the image. The signature of a successful intercalation is a smaller amplitude of the moiré pattern in contrast to pristine Gr/Ir(111) as it appears in the upper part of

---

[*] In the context of FFT we will use the term "lateral frequency", for a one-dimensional pattern with period d its lateral frequency is simply $f = 1/d$. Not to be confused with reciprocal lattice vector.

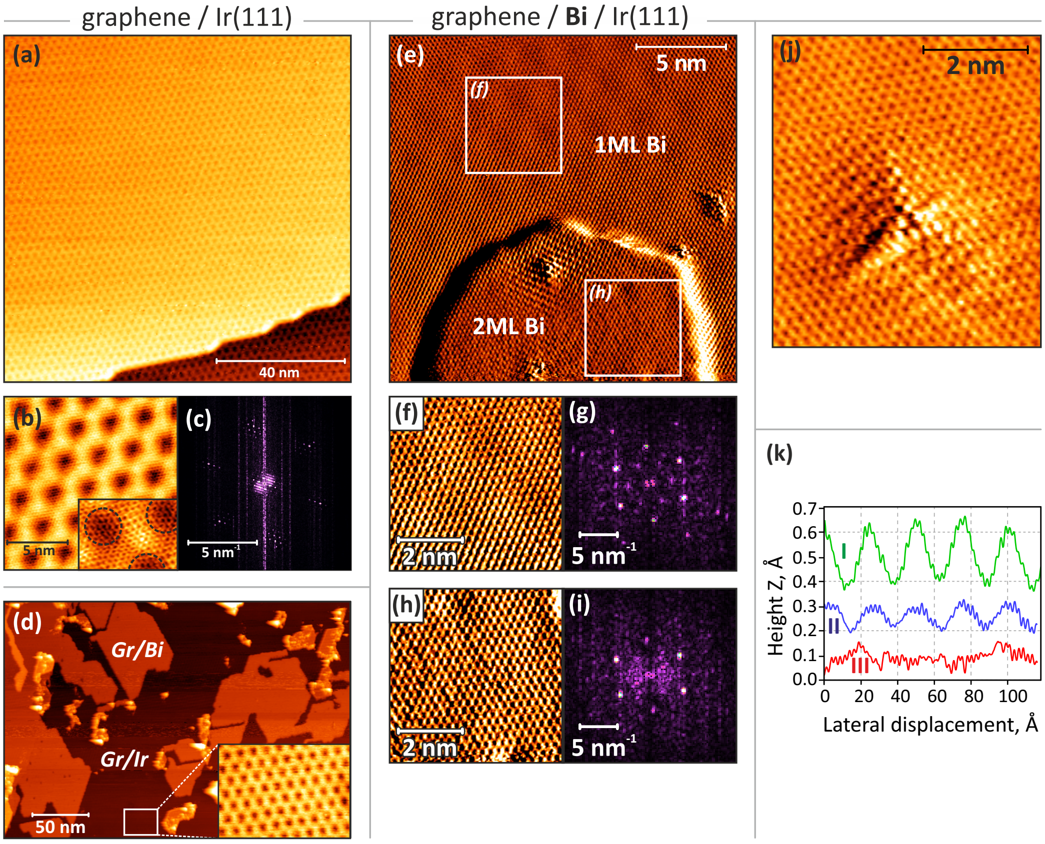

Figure 3.10: STM characterization and comparison of Gr/Ir(111) (a–c) and the HD phase of Gr/Bi/Ir(111) (d–k). (a) Large-scale STM image displaying R0 graphene extending over a step edge of Ir(111). Periodic moiré pattern is observed on both terraces. (b) Zoom-in of the moiré pattern in (a), the honeycomb lattice of graphene is visible in a close-up image in the inset (I channel). (c) Fast Fourier transform (FFT) of image (b). (d) Partially intercalated Gr/Ir(111). Bi forms islands of polygonal shape and between them a characteristic Gr/Ir(111) moiré pattern is observed, as shown in the inset close-up. (e–i) Fully intercalated Gr/Bi/Ir(111) characterized by STM (I channel): (e) displays two graphene-covered areas, with 1 ML (top) and 2 ML (island at the bottom) of intercalated Bi. Close-up images of these areas are (f) and (h), respectively, their FFT images are presented in (g) and (i). Around the atomic-scale defects one can see standing-wave patterns (SWPs) formed by electron scattering. SWPs appear in both areas in (e). STM image of such pattern around a point-defect is presented in (j) (I channel). (k) Comparison of Z profiles traced along the [10] graphene direction: I. Gr/Ir(111); II. Gr/1 ML Bi/Ir(111); III. Gr/2 ML Bi/Ir(111). Profiles are offset along the Z-axis for better visualization. Tunneling parameters (I_t, U_b): (a,b) 0.5 nA, 2 mV; (d) 0.45 nA, 0.8 V; (e,f,h) 2.1 nA, 0.24 V; (j) 0.67 nA, 2 mV.

the Fig. 3.10(e) [see also line profiles II and I in Fig. 3.10(k)]. Moreover, in the lower part we observe an island covered with graphene and attribute it to a second monolayer of intercalated Bi. This is not a rare case and we have systematically observed the formation of similar small areas under the graphene [see Section 3.3.4.3 and Fig. 3.11]. While the moiré pattern on the 1 ML area is clearly visible and well-periodic, on the

2 ML island it is not observed at all [see line profile III in Fig. 3.10(k)]. This effect can be explained both by a more effective decoupling of graphene by a thicker layer of Bi and simply by border corrugation effects on a relatively small island (∼ 10 nm in diameter). The topography of the two areas is presented in atomically resolved close-ups in Figs. 3.10(f,h) corresponding to 1 ML and 2 ML areas, respectively, however on this scale they are very similar. The A and B sublattices are not exactly equally visualized in both areas, but the asymmetry between them is rather weak as compared to graphene on strongly interacting substrates, such as Gr/Ni(111) or Gr/Co(0001) where atoms of one sublattice completely dominate and the visible structure is rather threefold than honeycomb-like [135]. Fourier transforms of 1 ML and 2 ML close-up images are presented in Figs. 3.10(g,i), respectively. They show mainly lateral frequencies corresponding to the graphene lattice, however at a close look one can notice a weak $(\sqrt{3} \times \sqrt{3})\ R30^\circ$ structure in both FFT images, which is attributed to scattering on defects and will be discussed further below. The spots close to the center in Fig. 3.10(g) correspond to moiré periodicity [similar to those in Fig. 3.10(c)]. The scale of the real-space image Fig. 3.10(f) was selected for direct comparison with Fig. 3.10(h) and it covers only a couple of moiré periods, thus it is too small to resolve well the moiré frequencies, but they were confirmed by FFT of a larger part of a 1 ML area (not shown here).

A comparison of moiré line profiles is presented in Fig. 3.10(k), where trace II corresponds to a 1 ML Bi area and displays a periodicity of ∼ 25 Å similar to the pristine Gr/Ir(111) (trace I) and z-corrugation of only ca. 0.1 Å. Trace III shows a similar line profile for 2 ML Bi area, but it has no clear periodic structure.

The presence of moiré in areas of 1 ML Bi with a period similar to that in Gr/Ir(111) is rather surprising, one possible explanation could be a structure of the Bi layer pseudomorphic to Ir(111), this does not contradict LEED data, however, such a dense structure of the Bi layer is unlikely based on the calculations presented in Warmuth et al. [243]. The second possibility is that this moiré is a purely electronic effect arising due to electronic interference with the Ir(111) substrate through Bi layer. The latter is well consistent with the very weak superpotential that we deduce from the vanishing moiré pattern in LEED and the lack of superstructural replicas in ARPES.

3.3.4.2 Standing waves of electronic density due to scattering on defects

Another effect of purely electronic nature can be observed in the areas of structural imperfections in graphene or in the substrate directly under graphene. In Fig. 3.10(j) one can see an example of such area with a defect site and a star-like apparent distortion around it. Such perturbation can be seen even few nm away from the defect and can have a large apparent height, but it does not represent the real geometry of the surface. These patterns are well-known since the 1980s when first high-quality STM images of the graphite surface were obtained. They arise from electrons scattering on point-defects and forming standing waves of electronic density [259–261]. This is a good example of the importance of electronic effects for interpretation of STM data. Similar standing-wave patterns (SWPs) are also present in Fig. 3.10(e) and they have larger apparent height than the 0.1 Å amplitude of the weak moiré, which in turn could also be of electronic instead of structural nature.

3.3.4.3 Multilayer intercalation

The general possibility of multilayer Bi intercalation is supported by our STM data. In Fig. 3.11 we present one of the stepped protrusions that were observed on the surface of the intercalated samples. The step height of 2.2 Å within this protrusion, which is equal to the typical step height of the Bi islands, suggests that the steps are formed by layers of Bi. Moreover, this feature was very stable during the measurement, which allows us to exclude the possibility of a Bi island *on top* of graphene. Presumably, such local enhancement of thickness could be due to a defect in the graphene sheet that made this area a Bi intercalation site.

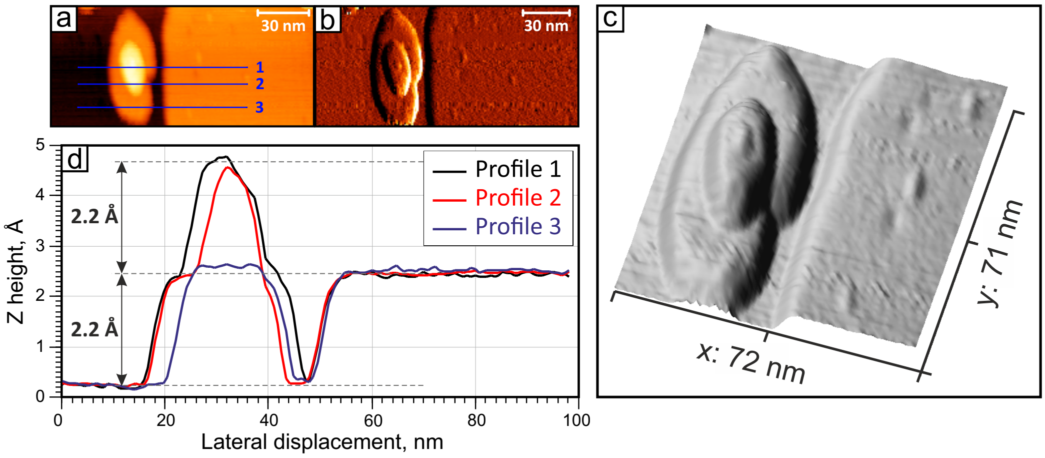

Figure 3.11: STM image of a Bi intercalation site, Z (a) and I (b) channels. Tunneling parameters: $I_t = 0.44$ nA, $U_b = 1.0$ V. (c) Three-dimensional render of the protrusion region in (a). (d) Z-height profiles extracted along the blue lines in (a) that display terraces of different heights.

3.3.4.4 Local observation of $(\sqrt{3} \times \sqrt{3})$ $R30°$ structure

Another important feature observed by STM are smooth areas of graphene with a pronounced $(\sqrt{3} \times \sqrt{3})$ $R30°$ structure. A region with multiple areas of this kind is depicted in Fig. 3.12(a) ($(\sqrt{3} \times \sqrt{3})$ $R30°$ areas are marked with arrows). In the whole region one can see a weak moiré pattern typical for 1 ML Bi areas and a honeycomb lattice of graphene, however in some areas graphene obtains a "hauberk"-like appearance

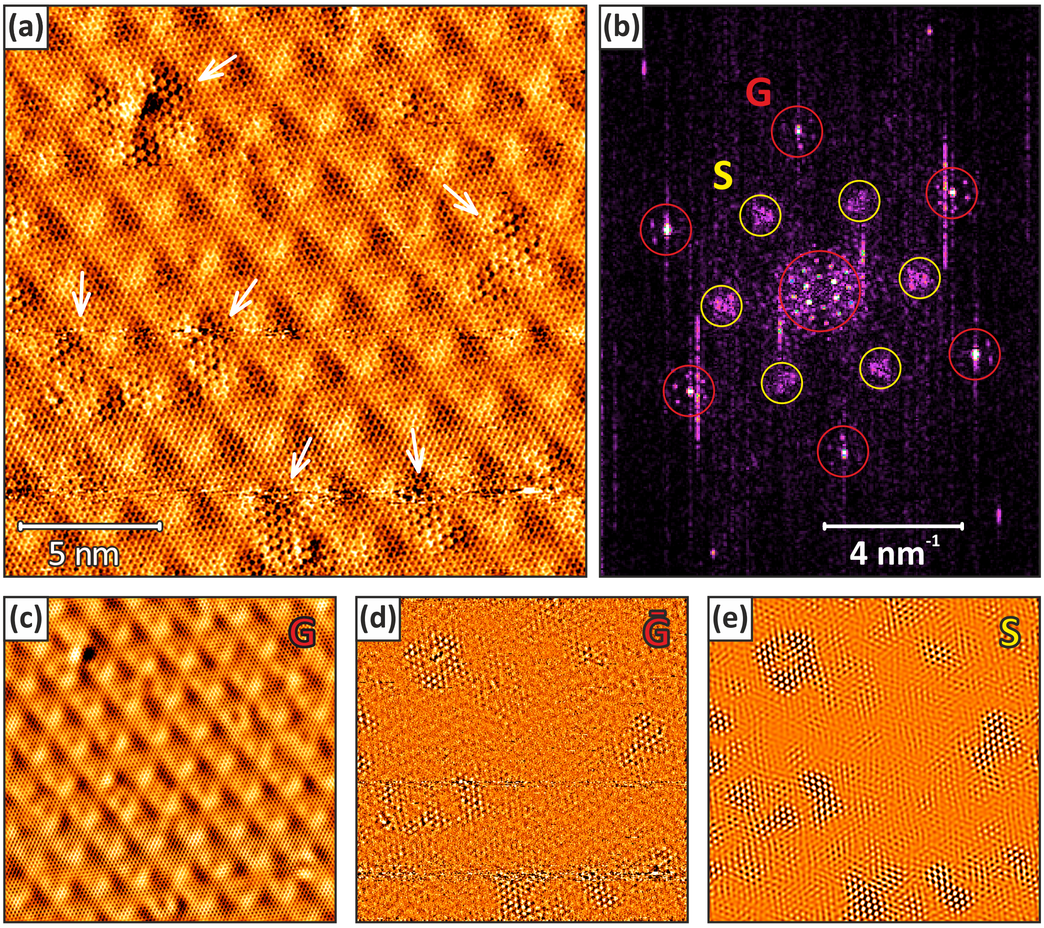

Figure 3.12: Local observation of the LD-phase with a $(\sqrt{3} \times \sqrt{3})$ $R30°$ structure in Gr/Bi/Ir(111). (a) STM image of the Bi-intercalated sample, white arrows mark areas with locally differing topography (I channel, $I_t = 1.6$ nA, $U_b = 2$ mV). (b) FFT image of (a), bright spots correspond to the frequencies of two types of periodic structures: graphene lattice (red circles, G) and a lattice oriented as $(\sqrt{3} \times \sqrt{3})$ $R30°$ relative to graphene (yellow circles, S). To highlight the location of the different periodic patterns in the real-space image (a) we filter out all FFT-frequencies except for: (c) inside G (graphene); (d) *outside* G (everything besides graphene, $\overline{\mathrm{G}}$); (e) inside S [$(\sqrt{3} \times \sqrt{3})$ $R30°$ superstructure].

with electronic density concentrated in certain graphene hexagons. Analysis of the FFT amplitudes [Fig. 3.12(b)] reveals that except for the component related to graphene and its moiré pattern (marked with G and red circles) there is another component with a structure close to $(\sqrt{3} \times \sqrt{3})$ $R30°$ (marked with S and yellow circles). One has to note that spots of the S pattern are diffuse and their shape is rather triangular than round. To distinguish between the two components in *real* space we have applied FFT-filtering: roughly speaking, in this procedure FFT-amplitudes for a certain set of frequencies are kept intact while all other amplitudes are set to zero, after that an inverse Fourier transform is performed to achieve a real-space image. Results of such operation are presented in Figs. 3.12(c–e). Figure 3.12(c) is reconstructed exclusively from frequencies corresponding to the G pattern (inside the red circles), it displays a uniform graphene sheet with a moiré pattern. A complementary image ($\overline{\mathrm{G}}$) that contains all frequencies *except* G is displayed in Fig. 3.12(d). Here one can clearly see the $(\sqrt{3} \times \sqrt{3})$ $R30^\circ$ structure on a noisy featureless background, confirming that there are only two significant periodic signals. Importantly, borders of the textured areas are relatively sharp. Finally, we visualize exclusively frequencies corresponding to the S pattern [Fig. 3.12(e)].

There are two possible explanations for this "hauberk"-like texture. The first one is electronic scattering on subsurface defects, such as vacancies in the dense intercalated layer. Such scattering should lead to $(\sqrt{3} \times \sqrt{3})$ $R30^\circ$ standing wave patterns similar to those discussed in Section 3.3.4.2. This idea seems plausible since we see protrusions in some of the textured areas [e.g. top-left corner of Fig. 3.12(a)]. However, against this explanation is the fact that borders of the "hauberk"-areas are sharp, moreover, there is no strong change in the apparent height for the observed structures.

The second and more suitable explanation can be given comparing our results to Ref. [243], where a LD-phase of intercalated Bi with a $(\sqrt{3} \times \sqrt{3})$ $R30^\circ$ structure was observed. Taking into account the observed sharp borders of the $(\sqrt{3} \times \sqrt{3})$ $R30^\circ$ areas in our samples we conclude that the "hauberk"-texture may correspond to locally emerging small domains of LD-phase. The reason behind this effect could be locally reduced concentration of Bi leading to a less dense Bi phase. Such textures were found in different locations on the sample but the total surface area covered by them is small, and they are unlikely to be observed in LEED or ARPES.

3.4 Origin of the band gap in Gr/Bi/Ir(111)

One of the main results of our ARPES and STM studies is that Bi indeed intercalates under graphene on Ir(111) in the form of a dense layer and decouples graphene from the substrate. The decoupled graphene has a quasi-free-standing band structure that lacks a number of substrate-induced features of Gr/Ir(111). The Dirac cone in Gr/Bi/Ir(111), as compared to truly free-standing case, demonstrates n-type doping and a ~ 190 meV band gap at the Dirac point. The intriguing question is the origin of this band gap and why is it possible to tune its size by Bi concentration.

3.4.1 Spin-resolved ARPES results

There is a large number of effects that can result in the opening of a band gap. First of all we will examine the most interesting option — lifting of degeneracy at the $\overline{\mathrm{K}}$ point due to substrate-enhanced *intrinsic* spin-orbit interaction. In the general case one would expect a combination of both non-zero Rashba and intrinsic SOI of different strengths, but a band gap appears only if $|\lambda_i| > |\lambda_R|$. Examples of possible band structures were displayed in Fig. 1.4. In all cases the spin-texture (i.e. orientations of spin polarization vector in the band) is predicted to be purely in-plane [45] and resemble the one presented in Fig. 1.3(b). To experimentally determine what kind of spin structure, if any, exists in the Dirac cone of Gr/Bi/Ir(111) we have performed spin-resolved ARPES measurements. If the main origin of the gap is SOI then a spin-resolved spectrum measured away from $\overline{\mathrm{K}}$ should show that the DC is split into bands with spin-polarization vector oriented in-plane (tangentially to the cone). It is worth to note that in the hypothetical case of a purely intrinsic SOI ($\lambda_R \approx 0$ and $|\lambda_i| > 0$) a band gap will appear, but upper and lower branches of the DC should remain spin-degenerate and their spin-polarizations will cancel out in the experiment. Thus we cannot completely exclude this possibility, even though it requires a specific combination of large intrinsic and negligible Rashba SOI.

Results of the spin-resolved (SR) ARPES experiments are presented in Fig. 3.13. The spectra display EDCs measured with photon energy 62 eV for three different emission angles, corresponding areas in k-space are marked in the experimental geometry sketch in Fig. 3.13(a). At the same time two components of the spin-polarization were measured: i) out-of-plane and ii) in-plane, in the direction tangential to the DC. The Sherman function of the detector was $S = -0.16$.

The analysis of the spectra revealed that there is no resolvable energy shift between the two spin-components in any part of the DC. The energy splitting of both DC branches does not exceed 5 meV. The asymmetry between the spin channels was below the statistical error in all cases. Important to note that exactly at the $\overline{\mathrm{K}}$ point [point 3, Figs. 3.13(f,g)] no spin-polarization was detected in any direction as well. This allows to exclude the "hedgehog" spin-texture with an out-of-plane spin-polarization in close vicinity of the $\overline{\mathrm{K}}$ point, which is expected to arise when both sublattice asymmetry and Rashba SOI are present [59, 223].

Important comment: one can see that in spin-resolved EDC measured exactly at the $\overline{\mathrm{K}}$ point [displayed in Fig. 3.13(f,g)] the apparent band gap width is significantly larger than the value of 190 meV stated above. This effect does not reflect the properties of the sample but stems from an experimental limitation: the angular resolution in SR ARPES measurements was 0.75° in both k_x and k_y directions. This value, determined by the analyzer apertures, is still small, but for a very steep dispersion of the graphene DC the spectrum averaged in k does not reproduce the band gap precisely. However, this resolution effect does not change the main conclusion about the absence of spin splitting in the DC.

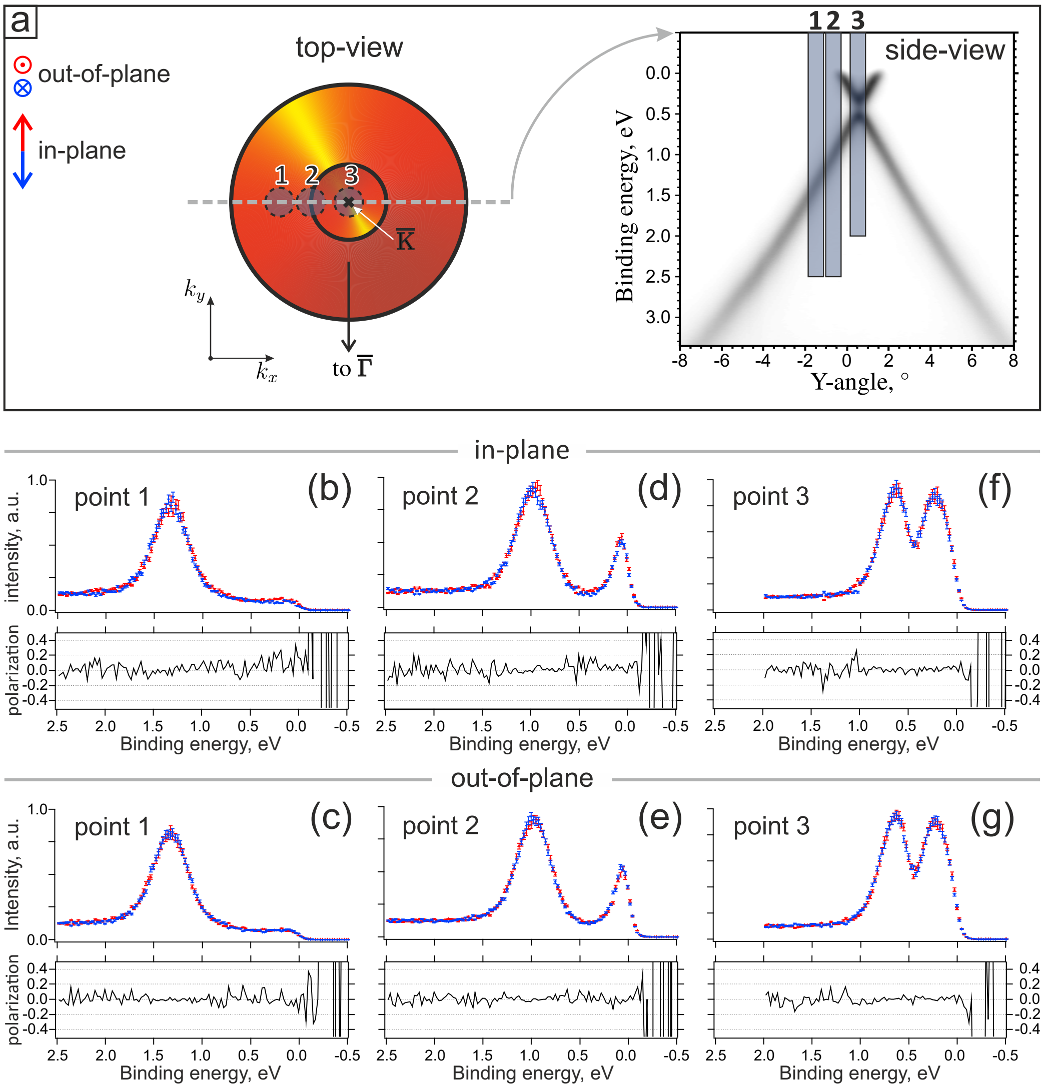

Figure 3.13: Spin-resolved PES of the Dirac cone in Gr/Bi/Ir(111). (a) Sketch of the experimental geometry. Measurement points are marked with filled circles: (1) 2.0° offset; (2) 1.2° offset; (3) exactly at $\overline{\mathrm{K}}$. The diameter of these circles corresponds to the angular resolution of 0.75°. ARPES spectrum (right) is taken along the dashed line (through $\overline{\mathrm{K}}$ in the direction perpendicular to $\overline{\Gamma\mathrm{K}}$). Stripes represent the lines along which spin-resolved EDCs were acquired. (b–g) Reconstructed spectral intensities $I_\uparrow$ (red) and $I_\downarrow$ (blue) with opposite polarization projections along two axes: in-plane (b,d,f) and out-of-plane (c,e,g) for spectra taken at points 1 (b,c), 2 (d,e) and 3 (f,g). Intensity scale varies between different points. Graphs at the bottom of subfigures display the absolute spin polarization.

3.4.2 Corrugation effects and local rehybridization

Another possible explanation is that the observed gap is due to the effect of lattice corrugation. In particular, Warmuth et al. [243] in their study of the Gr/Bi/Ir(111) system attribute the band gap to the lattice distortions they observed in STM. However, in our case of HD-phase graphene, the lattice was observed to be nearly flat and uniform with only an extremely weak moiré pattern: the apparent amplitude of corrugation is only ~ 0.1 Å across a lateral period of 25 Å.

One of the ways how corrugation can induce a band gap in free-standing graphene is through σ–π hybridization. This hybridization vanishes in the case of a flat graphene sheet due to symmetry considerations but increases with a distortion of the lattice in the out-of-plane direction, as demonstrated by Gmitra et al. [45]. However, from their calculations one can see that the spectral gap of free-standing graphene does not exceed 100 μeV even for strong differences in height between A and B sites.

Another insight about the influence of corrugation is given by the study of Rossi et al. [262]. They have calculated structures and electronic bands of a large graphene supercell under various strain/compression conditions. Under small uniform compressions the achieved structures resembled typical moiré patterns, however the band gap did not exceed 50 meV even when the corrugation amplitude reached 1 Å [262]. The interesting observation of that work is that the band gap was in direct relation to the variance of the C-C bond lengths. In highly 2D-corrugated graphene this variance is large and may play a role for the band gap (as we observed in Chapter 2). However, in the case of the HD-phase of Gr/Bi/Ir(111) this variance (estimated from the corrugation of the moiré pattern) is at least 2 orders of magnitude too low to reproduce the observed band gap.

We can also exclude the local rehybridization of graphene from sp^2 to sp^3 as the origin of the band gap. Even small concentrations of such rehybridized sites should be clearly visible in STM due to local deformation of the graphene plane [263], which is not the case. Moreover, in experiments with hydrogenated graphene even small concentrations of sp^3 sites (C_{sp^3}) were leading to a strong broadening of the bands due to electron scattering. The band gap displayed a strong dependence on C_{sp^3} and reached up to 1 eV [264, 265]. In contrast, our ARPES measurements of the HD-phase showed a sharp DC and a much smaller value of the band gap, which was uniform across the sample.

The conclusion can be drawn that the observed corrugations of the graphene sheet were not strong enough to solely produce a gap with $E_g = 190$ meV in the HD-phase.

3.4.3 Hybridization with substrate states

For epitaxial graphene the atoms of A and B sublattices are typically located above non-equivalent atomic sites of the substrate surface. The difference in sublattice potentials and interaction between graphene and the substrate can break the sublattice symmetry [135, 192, 266] and result in a band gap opening at the Dirac point. In the case of intercalated d-metals this can happen through hybridization of graphene p_z with metal d orbitals of different symmetry at A and B sublattices, as it was shown for Cu-intercalated Gr/Ir(111) [235]. In the case of Gr/Bi/Ir(111) we can exclude the p–d

hybridization mechanism due to the lack of Bi d states in the valence band, also no hybridization between the π-band of graphene and Bi states was observed in ARPES [Fig. 3.8].

3.4.4 Sublattice asymmetry

However, even if orbital hybridization does not happen, non-equivalent adsorption sites will result in a difference in electrostatic potentials between A and B sites (Δ). This difference leads to a band gap $E_g = \Delta$ at the Dirac point of graphene (see Section 1.2.3). This effect is very common and relatively small band gaps in graphene on weakly-interacting substrates are often attributed to it. At the same time the difference in potentials influences the photoemission intensity distribution in the DC and leads to a non-zero intensity in the "dark corridor" region which increases as a function of Δ (see Section 3.1.1) . In the following we use this dependence (Fig. 3.4) to estimate the possible magnitude of the sublattice potential difference from our photoemission data.

The analysis of intensity in the "dark corridor" of photoemission requires very precise alignment. This was achieved by a complete ARPES mapping of the DC region with high momentum resolution. Using the ARPES map one can extract constant energy surfaces at different binding energies, such as one displayed in Fig. 3.14(a). This CES was taken at $E_B = 0.8$ eV (~ 0.4 eV below Dirac point) and shows an intensity distribution that is visually similar to the theoretical one for a free-standing graphene [Fig. 3.3(b)]. A dispersion with high statistics was measured along $\overline{\Gamma \mathrm{K}}$ to determine the photoemission intensity ratio precisely. The result is displayed in linear and logarithmic intensity scales in Figs. 3.14(b,c), respectively. One can see that there is a very weak but non-vanishing intensity in the "dark" region, indicating some degree of sublattice asymmetry. For a direct comparison with the theoretical plots in Fig. 3.4 the distribution of intensity along the CESs was extracted from the ARPES map ($E_B = 0.9$ eV*). Taking into account the finite width of the DC in the experiment, the intensity was integrated in the radial momentum direction (with center at the $\overline{\mathrm{K}}$ point) and displayed as a function of the azimuthal angle $I(\varphi)$. The polar intensity plot in logarithmic scale is presented in Fig. 3.14(d). Due to low total intensity (and thus large statistical error) in the "dark corridor" area the $I(\varphi)$ plot was complemented with a point at $\varphi = 0°$ measured separately. This point was extracted from the MDC of a high-statistics spectrum [Fig. 3.14(c)] taken at $E_B = 0.9$ eV (along the red dashed line L). The MDC itself is displayed in logarithmic intensity scale in Fig. 3.14(e). One can quantify the ratio of minimal and maximal intensities as $I_{min}/I_{max} \approx 1/100$ (the exact value depends on the details of analysis). Comparison of both this ratio with Eq. (3.6) and the shape of the $I(\varphi)$ plot [Fig. 3.14(d)] with the theoretical graphs in Fig. 3.4 allows us to estimate the

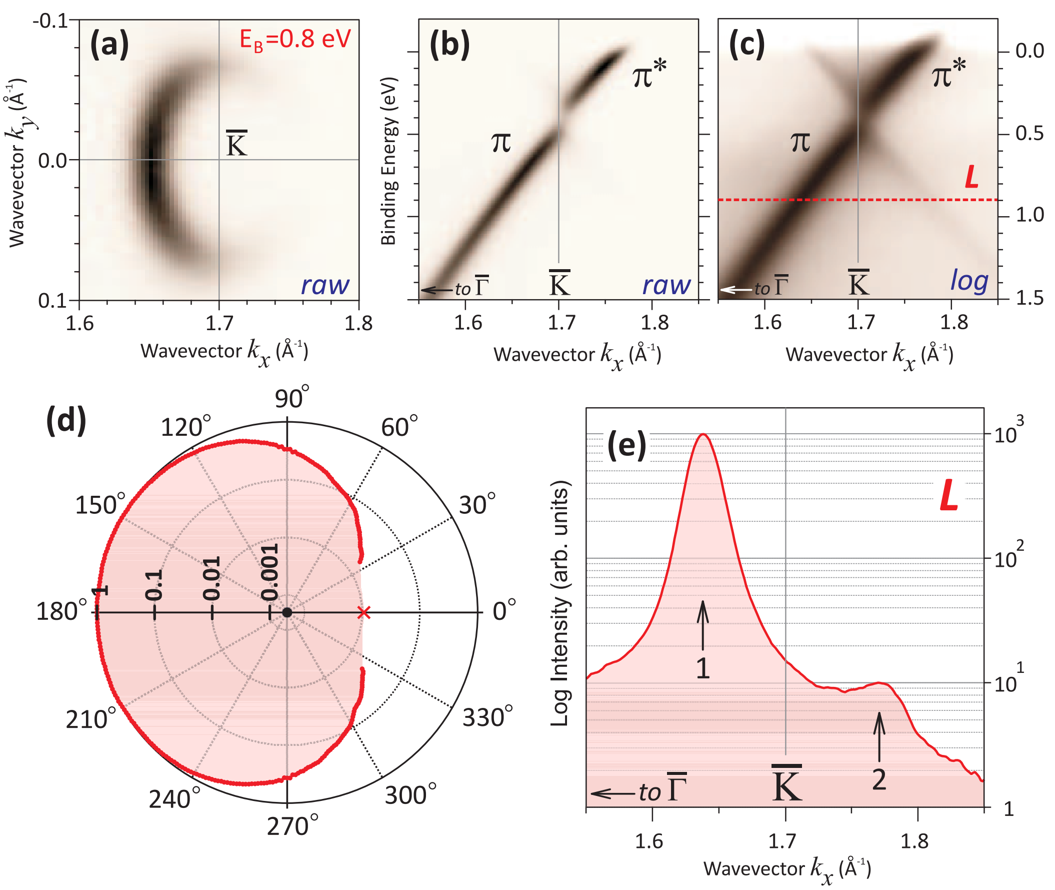

Figure 3.14: PES interference effects in the HD-phase of Gr/Bi/Ir(111). (a) A Dirac cone CES extracted from ARPES map at $E_B = 0.8$ eV with a typical anisotropic intensity distribution. (b) ARPES dispersion through $\overline{\mathrm{K}}$ and along the intensity-asymmetric $\overline{\Gamma\mathrm{K}}$ direction. The same image in logarithmic color scale (c) reveals a non-zero intensity in the dark-corridor region. (d) Polar plot of DC ARPES intensity integrated along the radial traces as a function of the trace orientation angle. Maximal intensity is normalized to 1. (e) MDC taken along the line L in (c) at $E_B = 0.9$ eV (logarithmic scale). Intensity of the DC in 1^{st} (arrow 1) SBZ is much higher than in the 2^{nd} (arrow 2).

value of $\Delta \approx 140$ meV, which is just slightly less than the observed value of $E_g = 190$ meV (see blue and green dashed lines in Fig. 3.4).

The discrepancy of the values can be a result of many factors. First of all the simplifications of the theoretical approach, in particular the calculations were done for a free-standing graphene in approximation of plane-wave final states. Depending on the exact final state the intensity distribution in the DC of graphene can be modified as it was shown by Gierz et al. [227] for Gr/SiC(0001). However, for p-polarized light and photon energy of 62 eV used in our experiments this effect should be minimal. Secondly,

---

[*] This choice of binding energy allows to better separate intensity contributions from the opposite sides of the DC. At the same time the momentum radius of the DC contour in CES is still less than 0.1 Å meaning that the intensity distribution does not deviate significantly from the calculated ones.

the experimental effects of background, band broadening and finite resolution also play a role in the precise determination of the intensity ratio. Finally, the value of the band gap obtained directly from ARPES spectra might also be slightly overestimated due to finite k_y resolution of the experiment defined by the entrance slit of the analyzer.

However, the obtained estimate is still in a good agreement with the directly observed gap value and it means that this effect is by far the strongest among the other gap-opening mechanisms discussed above. Altogether we can conclude that A-B sublattice symmetry breaking is the main candidate for the origin of the small observed band gap in the HD-phase of Gr/Bi/Ir(111). Moreover, this mechanism also provides an explanation for the dependence of the band gap on the local concentration of intercalated Bi [Fig. 3.9(e)]: as the density of Bi layer increases with concentration, its long-range structural order should improve leading to a reduction of the overall sublattice asymmetry.

3.5 Summary of conclusions

In this chapter we have synthesized a previously unreported HD-phase of Bi-intercalated graphene on Ir(111). A combined study by means of LEED, STM and (SR) ARPES reveals its structural and electronic properties. We observe that all spectral signatures of interaction between graphene and Ir(111) substrate disappear after Bi-intercalation and the photoemission signal from Ir(111) nearly vanishes. Moreover, the characteristic moiré pattern observed by LEED and STM in Gr/Ir(111) is strongly suppressed after intercalation. The whole set of experimental data evidences that Bi forms a dense intercalated layer that efficiently decouples graphene from the substrate.

The band structure of HD-phase Gr/Bi/Ir(111) is nearly ideal except for n-type charge doping ($E_{\mathrm{D}} \sim E_{\mathrm{F}} - 0.4$ eV) and a relatively small band gap ($E_g \sim 190$ meV). Furthermore, systematically varying the amount of intercalated Bi we reveal a monotonous decrease of the band gap with Bi concentration. This gives a mechanism of experimental control over the band gap in this system within ±25 meV at the stage of sample preparation. The origin of this effect can be found in the reduction of A-B asymmetry at higher densities of the Bi interlayer.

From the experimental data a wide range of mechanisms responsible for the band gap can be excluded, such as induced intrinsic spin-orbit interaction, hybridization with the substrate states and corrugation of the graphene lattice. All of the possibilities considered above were shown to be orders of magnitude too weak to produce the experimentally observed band gap. The only explanation that remained qualitatively feasible is the A-B symmetry breaking induced by a difference of electrostatic potentials (Δ) at two sublattice sites. The quantitative test of this mechanism was performed by analysis of interference effects in ARPES that allowed to estimate the $\Delta = 140$ meV. This should result in a band gap of equivalent width and, in contrast to estimates made for other mechanisms, it is on the same scale with the observed value of E_g. This allows to attribute the main origin of the band gap in the HD-phase of Gr/Bi/Ir(111) to the A-B sublattice symmetry breaking.

The main results of this chapter were submitted as an article to the journal "2D Materials", which is currently under review ("Origin of the band gap in Bi-intercalated graphene on Ir(111)", submission ID: 2DM-105632).

Chapter 4

Electronic scattering resonances in photoemission from monolayer graphene

4.1 Introduction

The previous Chapters are mainly focused on tuning the properties of graphene by proximity to heavy metals in the form of monolayers or nanostructures. However, graphene itself is a great model system to study various physical effects at crystal surfaces.

This Chapter is devoted to a specific phenomenon related exclusively to the surface — so-called "scattering resonances". They manifest themselves in ARPES in the form of strongly dispersing lines of intensity modulation in the low kinetic energy region. Despite their abundance, such features are most often overlooked, since they are typically weak and appear in the area of secondary electron background that is rarely studied with angular resolution in detail. However, their behavior can provide important information about the surface potential barrier and structure of the sample. Beyond that, understanding of these resonant states is relevant to optoelectronic properties of the materials. The two-dimensional nature of graphene and its nearly ideal surface make it a perfect sample for this study.

In the following we will discuss the origin of the features named with the common term "scattering resonances" and present examples of their experimental observation by ARPES in graphene supported by various substrates. In the final part the possibilities of tuning, modification and suppression of the scattering resonances in graphene will be investigated.

4.1.1 Surface states and surface related effects in ARPES

In the picture of an ideal three-dimensional crystal, the surface acts as a large-scale defect that breaks the translation symmetry of the lattice, reducing it to only two directions parallel to the surface. This causes changes in the electronic states in the surface region: due to the symmetry lowering, the 3D wave vector $\vec{\mathbf{k}}$ is not a constant of motion anymore, and only its component parallel to the surface remains a good quantum number. This way the presence of the surface allows extra solutions of the Schrödinger equation that are described by 2D wave vectors. These surface electronic states play a crucial role in the chemical interaction of a material with its environment, for example in the mediation of adsorbate lateral interactions [267]. Moreover, surface states represent an interesting physical phenomenon in its own right, as example of a 2D electronic system. Nowadays they can be routinely observed in experiments, specifically with ARPES [65] or modern STM, where they can be studied via electron scattering interference patterns around surface defects or adsorbates [259].

Another important surface property is the behavior of the electrostatic potential that acts on the emitted electrons close to the surfaces of metals. This potential does not change abruptly at the border of the crystal, but decays smoothly with distance (z) due to the interaction of the electron just above the surface with those in the bulk of the metal. This interaction can be described in terms of the potential created by an "image charge" from classic electrodynamics, which has a long-range Coulomb "tail" ($\propto 1/z$). The overall surface potential comprises this Coulomb-like potential on the vacuum side far from the crystal surface and the transition region to the inner potential of the crystal [Fig. 4.1(a)]. Electrons trapped in this Coulombic potential form a Rydberg-like series of "image potential states" (IPS) converging to E_{vac} (vacuum energy level) from below [268, 269].

Due to the phenomena described above, the surface leads to [Fig. 4.1(b)]:

- *Surface-localized states* that lie in the projected bulk band gap of the crystal (common examples are surface states on Au(111), Ag(111), Cu(111), etc.);
- *Surface resonances*, states with enhanced amplitude close to the surface, but extending into the bulk of the crystal due to mixing with bulk states (typical example is surface resonance of Ir(111) [40, 270]);
- *Image potential states (IPS)* — a series of states below E_{vac} that arise due to the interaction of the electron above the metal surface with those remaining in the bulk;

In this chapter we will discuss yet another surface-related electronic effect that we refer to as *"surface scattering resonances" (ScR)*. These *scattering* resonances are different from the surface resonances mentioned above and closely related to the image potential states, as their formation strongly relies on the properties of the surface potential barrier.

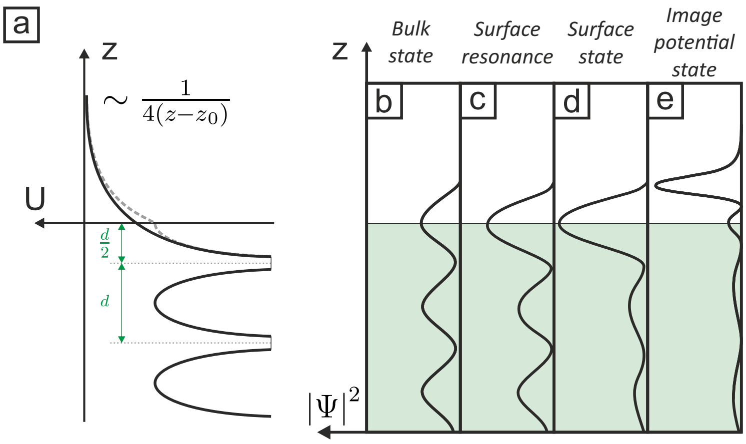

Figure 4.1: (a) Schematic picture of a laterally averaged potential $U(z)$ at a crystal surface, z is the coordinate along the surface normal, d is the minimal distance between the atomic planes parallel to the surface. Dashed lines stand for the model approximations of the potential inside the crystal and image potential far from the surface (z_0 is a fitting parameter). Adapted from Refs. [271, 272]. (b–e) Schematic drawing of electron density distributions in different types of states in vicinity of crystal surface: bulk state (b), surface resonance (c), surface state (d) and image potential state (e). Adapted from Ref. [177].

4.1.2 Electronic surface scattering resonances

There are several different models of the "electronic surface scattering resonances", but they share a similar idea used to explain their origin. Imagine an electron leaving the crystal surface at a grazing angle. It may have a large momentum *parallel* to the surface but at the same time a momentum *perpendicular* to the surface that is not sufficient to overcome the surface potential barrier (SPB). This would lead to a situation when the escaping electron will be deflected by the SPB back to the crystal surface. After that the electron might get diffracted at the surface of the crystal, obtain higher perpendicular momentum and escape to vacuum or it might undergo reflection without change of parallel momentum and return to the initial situation. Theoretically, under certain conditions this electron can be reflected back and forth a large number of times, forming a quasi-bound state [272] and traveling along the surface like in a waveguide — such implied states were named "electronic surface resonances" [272]. This effect was widely discussed in the 1970s in relation to fine structure of very low energy electron diffraction (VLEED) spectra observed experimentally (so-called "threshold" or "pre-emergent beam" effects) [272–274]. However, later it was noted that despite the rather strict conditions under which such resonances can exist, VLEED fine structures are very commonly observed. An alternative explanation was found that does not require infinite reflections and existence of quasi-bound electronic states: the electrons that participated in the under-barrier scattering before leaving the crystal will have an energy-dependent phase shift relative to those that were transmitted through the SPB directly (Fig. 4.2).

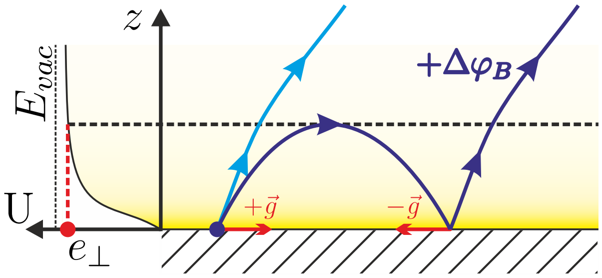

Figure 4.2: Scheme of the interference model. Electron reflected by or emitted from the crystal (hatched area) may escape to vacuum directly (light blue arrow) or get diffracted at the surface (dark blue arrow) acquiring extra $k_\parallel$ equal to the surface reciprocal lattice vector $\vec{\mathbf{g}}$. In the last case, the $e_\perp = \frac{\hbar^2}{2m_e}k_\perp^2$ (energy corresponding to electron motion normal to the surface) may become less than E_{vac}, then the electron gets reflected by the SPB. After reflection from the surface a second diffraction event ($-\vec{\mathbf{g}}$) returns the electron to the initial direction allowing it to escape. The experimental (VLEED or ARPES) signal from electrons with the corresponding $(E, k_\parallel)$ will be affected by the interference and depend on the phase shift $\Delta\varphi_B$ between the two paths.

The interference produces the energy-dependent intensity modulations that explain well the experimentally observed "threshold effects" [273, 275]. Similar mechanism should also produce fine structures in ARPES spectra, however until recently they were very rarely observed and recognized. In this work we investigate the unusual features present in ARPES spectra and provide arguments that they are analogous to the threshold effects observed in VLEED. Figure 4.3 presents an example of an ARPES spectrum that has such features. Panel (a) shows a spectrum of Gr/Ir(111) measured in $\overline{\Gamma\mathrm{M}}$ direction. In the low kinetic energy region one can see bright wide lines (WL) of enhanced intensity and darker narrow lines (NL) of reduced intensity above them*. To provide a sharper picture the derivative of intensity is presented in panel (b). The WL and NL features are not independent but represent parts of one complex structure that we will call "surface scattering resonances" (ScR) — the topic of discussion in this Chapter.

One of the particularly interesting points in studying electronic surface scattering resonances is that based on their structure one can get information on the shape of the surface potential barrier, which is essential for the interpretation of data from electron spectroscopies such as photoemission, inverse photoemission and low-energy electron diffraction (LEED). Scattering resonances were proposed to provide experimentalists a valuable method for observation of the spin-dependent surface potential barrier [276]. Moreover, scattering resonances can be observed also in transmission of low-energy electrons through two-dimensional materials [277], which is important for implementation of those materials in optoelectronic devices.

---

*At the higher kinetic energy side of the dark lines NL there are also narrow *bright* lines, which are expected from the model, but often too weak to be observed.

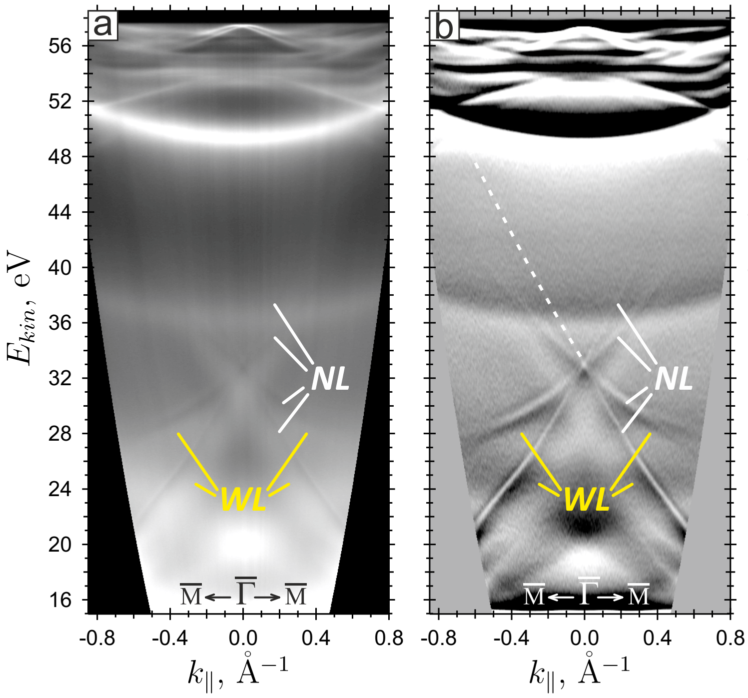

Figure 4.3: (a) ARPES spectrum of Gr/Ir(111) measured in $\overline{\Gamma M}$ direction of the surface Brillouin zone (SBZ) across a wide range of kinetic energies. The features observed in the low kinetic energy region are an example of surface scattering resonances. (b) Same spectrum as (a), but presented as a derivative of intensity ($\frac{dI}{dE}$). This provides a sharp and clear picture of the resonant state ScR incorporating a set of strongly dispersing narrow (NL) and wide (WL) features. Dispersion of NL can be traced almost up to the valence band (white dashed line).

In the following we will give a short overview about the nature of this effect, its past experimental observations and theoretical description. After that we will provide a detailed description of the features that we observe in ARPES to prove their equivalence with the features reported by other methods.

We would like to start with a short review of some of the experimental and theoretical studies of scattering resonances found in the literature over the last five decades.

4.1.3 Historical overview

Historically first observations of surface resonances were made in the 1930s in the *atom* diffraction experiments [278]. Estermann and Stern studied scattering of He atoms from a LiF(001) surface and observed narrow minima in the intensity of the specularly reflected beam at specific incidence conditions. These features were explained later by a process in which an incident atom is temporarily trapped in a surface state [279, 280].

In the following years the resonant scattering of *electrons* at the crystal surfaces was also observed. Kikuchi and Nakagawa studied high-energy (40–100 keV) electron diffraction from the (110) face of a zinc blende crystal and observed anomalously high intensity of the specularly reflected beam under certain conditions [281]. Later, an analysis of their data by Miyake et al. [282, 283] showed that the conditions of anomalous intensity enhancement are close to the threshold conditions for diffracted beams. This effect was explained in terms of surface resonance scattering.

Significant advances in understanding of the resonance scattering were achieved in VLEED (very low energy electron diffraction) experiments, in which a fine structure appears in intensity over energy curves $I(E)$ of elastically reflected electrons. McRae and Caldwell in 1964 were the first to observe such a fine structure for LiF(100) [284]. This work started a long scientific discussion about the nature and precise details of the observed fine structure. Similar features were later discovered in the data obtained from crystalline samples by other methods, such as electron energy-loss spectroscopy, target-current spectroscopy and photoemission techniques [272]. Moreover, since the main component defining the existence of electron surface resonances is the image-like surface potential barrier, they can be observed even above some liquid surfaces (provided that there is a repulsive potential barrier at the surface). In particular, quasi-stationary states of electrons above the surface of liquid helium have been extensively investigated in the 1970s [285].

The phenomenon of scattering resonances was a topic of active experimental and theoretical research for more than 20 years from 1960s to late 1980s [268, 272–275, 284, 286–295] and now it starts to gain attention again due to the new experimental possibilities of spectroscopic methods. It was proposed [276] that a modern VLEED experiment with a state-of-the-art energy and angular resolution should make it possible to observe such delicate effects as spin dependence of the surface potential barrier at the ferromagnetic surfaces.

Recent experimental reports include observations of similar fine-structures not only in VLEED [296, 297], but also in photoelectron emission spectroscopy experiments with angular resolution. The latter includes not only conventional ARPES [298, 299], but also PEEM (photoemission electron microscopy) [300, 301] and SPELEEM (spectroscopic photoemission and low energy electron microscopy) [302] experiments. Another study reports observation of similar features in electron transmission experiments (using a low energy electron point source [LEEPS] microscope) [277]. The same fine structures were theoretically predicted to appear in inverse photoemission spectroscopy (IPES) data [303], however to the best of our knowledge the resolution of modern IPES is not sufficient to resolve the narrow peaks. Nevertheless, the lowest lying peaks of the Rydberg series recognized as image potential states are commonly observed at the $\overline{\Gamma}$ point of the 1^{st} BZ both in IPES [304, 305] and two-photon photoemission spectroscopy [306–308]. These methods allow to probe the energy range directly below E_{vac}, which is unavailable for ARPES and VLEED.

It is especially interesting to investigate the existence and behavior of surface scattering resonances in 2D materials, such as graphene, that became a topic of extensive research in the last two decades. However, only a few experimental reports are available at the moment [277, 298, 301, 302].

To better explain the concept of scattering resonances we will follow the approach of McRae [272] but taking into consideration the important critical comments that appeared in the later years.

4.2 General theoretical picture of surface scattering resonances

In this chapter a comprehensive review of theoretical models of scattering resonances will be provided and, where useful and possible, will be illustrated with our own ARPES photoemission data acquired from various samples of epitaxial graphene.

4.2.1 Two-layer scattering model

As it was shortly explained above, electrons traveling near the surface of a solid can be temporarily trapped between the image potential on one side and the crystal surface on the other side. In a simplified theoretical picture one can imagine a one-dimensional surface potential $U(z)$ and describe the elastic scattering of an individual electron at the crystal surface as a sequence of reflection, diffraction or transmission events happening between two parallel planes that correspond to the crystal surface* and a constant energy surface of the SPB [272, 288, 309].

The probability of reflection from the crystal surface should be larger than zero, otherwise electrons deflected by the SPB towards the surface will be simply absorbed in the crystal. High crystal surface reflectivity r_C is expected for energies corresponding to an energy-momentum gap in the band structure of the crystal. However, it was shown that even for some metals with no band gap close to the vacuum level the reflectivity is still larger than zero, $r_C \approx 0.1$, and this is enough for resonances to appear [310].

The position of the surface plane can be selected arbitrarily, but for the convenience of calculations it is often considered to be located $\frac{d}{2}$ away from the center of the outermost atomic layer, where d is the spacing between the atomic layers parallel to the surface (in Fig. 4.1 the surface plane is at the origin of the z axis). The potential should smoothly change from the periodic function in the bulk of the crystal to the image-like asymptotic behavior far above the surface. Correct modeling of this transition can be challenging [311–313], but in many cases good results can be achieved even with simple idealized models approximating the barrier piecewise by a number of specific

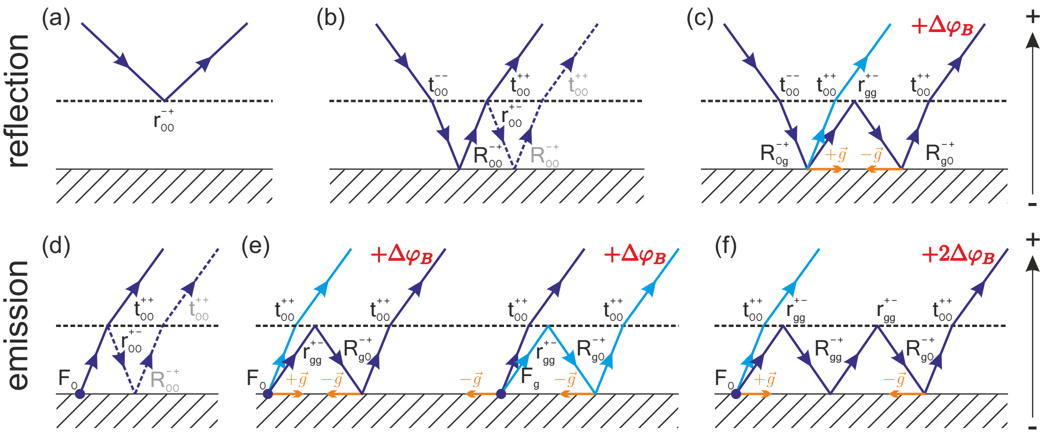

Figure 4.4: Schematic illustration of different electron scattering pathways in reflection (a–c, adapted from Ref. [276]) and emission (d–f). Dashed black line marks a constant energy surface of the SPB. Detailed description see in the text.

one-dimensional functions that are joined in a continuous and differentiable way (e.g. SPB shape proposed by Jones and Jennings [314]).

The basic elastic scattering processes that are possible in the two-layer description are shown in Fig. 4.4. In all cases the outgoing electron's momentum $\vec{\mathbf{k}}$ is fixed to be the same and all momentum indices are given with respect to this $\vec{\mathbf{k}} = \vec{\mathbf{k}}_0$. This model was widely used to explain the fine-structure in the VLEED data, in this case the electron is initially moving towards the surface ["reflection", Figs. 4.4(a–c)], however, with minor modifications the same model can be applied to the electrons *emitted* from the crystal as well ["emission", Figs. 4.4(d–f)]. The simplest processes are e.g. reflection from the barrier[*](a), reflection from the surface (b, full line) and transmission of the photoemitted electron through the barrier (d, full line). The last two processes in the case of a semi-reflective barrier can lead to backscattered beams (dashed lines) or even series of them if this process repeats. For electrons with energy $e_\perp = \frac{\hbar^2}{2m_e}k_\perp^2$ corresponding to electron motion normal to the surface such that $e_\perp > E_{vac}$ the probability of barrier reflection is generally very low [275], however such reflection may happen if initially $e_\perp < E_{vac}$ or if it was reduced in some process below the barrier and this is exactly what happens in the more complicated cases depicted in (c,e,f).

To discuss more complex diagrams first we need to introduce some notation. Sequences of such scattering events (and the resulting amplitudes) can be described as a composition of operators that can change the phase, amplitude, direction of motion along z axis and parallel momentum of the electron. Operators r and t stand for *reflection from* and *transmission through* the potential barrier, respectively; R denotes reflection from the crystal surface. F is the amplitude of emission of an electron. The

---

[*] Crystal surface plane in this case is not well-defined, see text below.

[*] For energies 20 – 250 eV its probability is usually small and can be neglected [275, 315].

subscript indices show the momentum before (left) and after (right) the action of the operator, the superscript indices show the direction along the z axis before (left) and after (right). For example, R_{0g}^{-+} means that an electron that was initially travelling towards the crystal $(-)$ is reflected from the surface (R) and travels away from the crystal $(+)$ at the same time its $\vec{\mathbf{k}}$ was changed from $\vec{\mathbf{k}}_0$ to $\vec{\mathbf{k}}_0+\vec{\mathbf{g}}$ by diffraction at the surface[*]. This process happens in Fig. 4.4(c) and it is crucial for the VLEED fine-structures. The reason is that the change in momentum direction of the diffracted electron may reduce the part of its kinetic energy related to the motion in the z direction $e_\perp$, in certain cases making it impossible for the electron to surmount the SPB, so that it will be reflected back to the surface. If this electron gets reflected from the surface without a change in its parallel momentum, the whole process of back-and-forth reflection may repeat multiple times resulting in a channel-like motion of the electron trapped under the barrier. In the original theory of McRae [272] the intensity dips in the VLEED fine-structures were attributed to the conditions when this channelling was possible (they can be found by summation of infinite series of scattering sequences). In this case an interpretation of the phenomenon of VLEED fine-structure can be given in terms of electronic *states* corresponding to the channelling conditions. For an image potential these states are similar to those of an electron in a Coulomb potential well, i.e. they form a Rydberg series converging towards E_{vac} at $\overline{\Gamma}$ and have a free-electron-like dispersion [272]. The total kinetic energy of electrons in these states can be above E_{vac} away from the $\overline{\Gamma}$ point (see Fig. 4.5). Thus there is a non-zero probability that a channelling electron may escape into vacuum by a diffraction event at the surface [Fig. 4.5, purple arrow]. This means that the states of trapped electrons above E_{vac} have limited lifetimes and therefore they are named "scattering *resonances*".

However, already Dietz et al. [290] noted that the best fit of the fine structure in their high resolution VLEED data on Cu(001) was achieved in assumption of a *single* under-barrier reflection[†]. In this scenario the rapid intensity oscillations result from the interference of two contributions in the wavefunction of the outgoing electron: one from direct reflection from the surface and another after experiencing a single under-barrier reflection, therefore accumulating some phase shift $\Delta\varphi_B$ (Fig. 4.4, see also discussion in Section 4.2.2). Further theoretical studies [273, 275] insisted on this interpretation, arguing that the channelling conditions are too strict and that in most real-life crystals the lifetime of proposed states would be very short. Later work by Read and Christopoulos [295] attempted to model VLEED data for a W(001) surface and they have demonstrated that up to seven internal scattering events may occur between

---

[*] Diffraction is possible because the electron interacts with the 2D periodic potential at the surface and can exchange momentum (equal to some reciprocal lattice vector) with the crystal lattice.

[†] However, in the later studies the full multiple-reflection approach was implemented to fit VLEED curves for Cu(001) rather successfully [316].

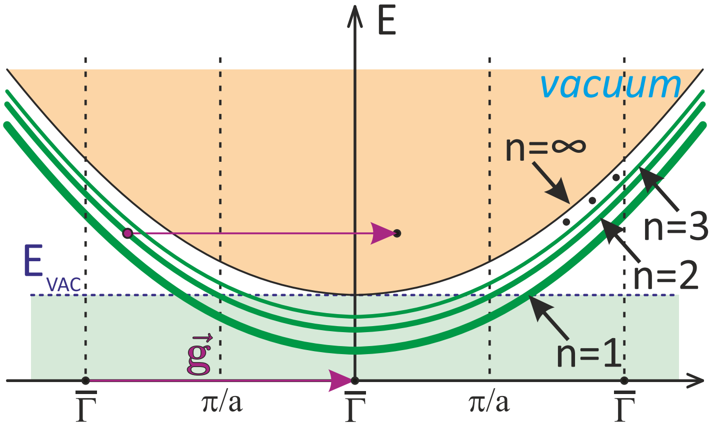

Figure 4.5: Rydberg series of electronic scattering resonance states converging towards E_{vac} at the $\overline{\Gamma}$ point of the 1^{st} SBZ. Scattering by a surface reciprocal lattice vector $\vec{\mathbf{g}}$ (purple arrow) allows an electron (purple dot) to escape into the free-electron continuum.

surface barrier and metal substrate, thus in certain cases the resonance mechanism is important (in particular, at small angles of the beam incidence).

In the case of *emission* of electrons the simplest interfering processes [Fig. 4.4(e)] are very similar to those discussed for *reflection* [Fig. 4.4(c)]. The acquired phase shift $\Delta\varphi_B$ is exactly the same, thus the intensity modulations produced by interference in emission should also be similar to those that appear in VLEED. In both cases it is possible to take into account paths with higher number of under-barrier reflections, an example of double reflection for emission is shown in Fig. 4.4(f).

Putting aside the existence of short-living states and the number of reflections that should be considered to fit the experiment, the fundamental principle of threshold effects remains the same both for interference and resonant states model, and it is based on surface diffraction processes like the ones depicted in Figs. 4.4(c,e,f).

Different interpretations and experimental methodologies resulted in a variety of names that are used for the same concept: scattering resonances, threshold effects, pre-emergent beam effects and many others. We will use them interchangeably, but keeping in mind that "surface resonances" presumes the existence of temporary, but long-lived (quasi-bound) states and that is not always the case. "Threshold" refers to the fact that the intensity oscillations (or Rydberg series of states) are abruptly bounded from above by a certain energy, at which the electron can finally escape the SPB. In VLEED the electron beam with $e_{\perp}$ close to this threshold is called "pre-emergent", as it is formed by electrons travelling nearly parallel to the surface and one can force this beam to "emerge" into vacuum by increasing the energy of the primary electron beam. We will use this terminology also for ARPES.

Appearance of scattering resonances is sensitive to the precise spatial dependence of the surface potential barrier. Thus, comparing the ScR observed in the experiment with those calculated for different models of the SPB we can determine the shape of the latter, which is important for the interpretation of the results of surface-sensitive electron spectroscopies, such as photoemission and inverse photoemission. Recently it was shown by U. Burgbacher et al. that in modern VLEED experiments with high energy and angular resolution one can derive the shape of the surface barrier from fine-structure measurements [276]. Moreover, in the same work it was claimed possible to distinguish the spin-dependence of the surface barrier in experiments with spin-polarized electrons.

4.2.1.1 How does it apply to ARPES?

To project the ideas of the VLEED "beams" to the ARPES picture we can focus on a single point of the ARPES spectrum $I(E_{kin}, k_{\|})$. It corresponds to the intensity of electrons that have emerged from the sample with certain kinetic energy and parallel momentum. Fixing these two parameters is equivalent to selecting an outgoing VLEED beam with a certain energy and escape direction.

Since threshold effects described above only *modulate* the intensity of the outgoing beams, one can see fine-structures only in the areas of high ARPES intensity (e.g. on top of the spectrum of occupied bands). Therefore, to study the threshold effects in a wide range of energies and momenta, we need some broad uniform spectrum of initially photoemitted electrons $I(E_{kin}, k_{\|}) \approx const.$ Fortunately, secondary electrons (SE) provide a broad background of high intensity in the low kinetic energy region of ARPES spectra. The downside is that the intensity of this background is energy-dependent and changes by orders of magnitude across the low kinetic energy region making it harder to extract the features of interest. Moreover, it is known that the spectrum of SE may also have some structure. This broad background originates from the photoexcited electrons that undergo a series of *inelastic* scattering events producing a cascade of secondary electrons. In this process information about the initial state is lost and the energies and momenta of SE are "randomized" producing a broad spectrum. However, the probability of their transmission to vacuum is not completely uniform, but depends on the electronic states that exist there. It was demonstrated that the details of the SE background measured in ARPES directly reflect the unoccupied band structure of the sample and provide information equivalent to VLEED [299]. This is important in two aspects: first, it gives another link between the fine-structures observed in VLEED experiments and features visible in the spectrum of ScR; second, one has to carefully distinguish in the experimental data the features related to ScR from those that stem from the unoccupied band structure of the sample.

4.2.2 Phase accumulation (interference) model

4.2.2.1 Phase shift due to underbarrier scattering

To obtain a better understanding how features described above should appear in ARPES one can model the interference intensity profile in the phase accumulation model [268]. As a first approximation of the surface potential barrier we will use a classical image potential for a metallic surface $U(z) = -\frac{e^2}{4z}$*[317]. This approximation describes the asymptotic behavior of the potential far from the surface. One can obtain the analytical solution for the phase φ_B that the electron acquires while being deflected in this potential barrier, in the Wentzel–Kramers–Brillouin approximation [271, 292]:

$$\varphi_B = \pi(\sqrt{E_0/(E^S_{vac} - e_\perp)} - 1), \quad \text{where} \quad e_\perp = E - \frac{\hbar^2}{2m_e}\vec{\mathbf{k}}^2_\parallel \tag{4.1}$$

Here $E_0 = Ry/4 = 3.4$ eV, E is the energy measured from the bottom of the inner potential well and $e_\perp$ is a quantity of kinetic energy corresponding to the motion in the direction perpendicular to the surface. One can immediately see that for $k_\parallel = 0$ as $e_\perp = E$ is getting closer to the sample vacuum level (E^S_{vac}), the phase of the reflected electron starts to change increasingly fast. Due to the interference with the process in which the electron is emitted in the same direction *without* under-barrier reflection the measured intensity will be modulated as $I(E) \propto \left|1 + r_B e^{i\varphi_B} r_C e^{i\varphi_C}\right|^2$, where $r_B e^{i\varphi_B}$ and $r_C e^{i\varphi_C}$ are the barrier and crystal complex reflection amplitudes, respectively. For energies just below the threshold, the modulus of barrier reflection $r_B \approx 1$ and the phase φ_C acquired after reflection at the crystal surface is assumed to be a slowly varying function of energy compared to φ_B (phase acquired by reflection from the surface potential barrier), thus can be considered constant. The interference results in an intensity profile with increasingly fast oscillations converging towards E^S_{vac}. The energies E_i of the intensity maxima form a Rydberg series, similar to that predicted in the resonant scattering model [272]. At other $\vec{\mathbf{k}}_\parallel$ exactly the same intensity profile should appear, but shifted in energy towards the corresponding threshold position $E_{thr} = E^S_{vac} + \frac{\hbar^2}{2m_e}\vec{\mathbf{k}}^2_\parallel$: a free-electron-like parabola (or, in 2D, a paraboloid of revolution) originating at the $\overline{\Gamma}$ point of the first SBZ and having the minimum at E^S_{vac} (Fig. 4.6).

Unfortunately, the fine-structure of intensity close to this threshold cannot be observed in the ARPES experiment. The reason is that the energy-momentum region below the threshold is not observable by photoemission in principle: electrons with

---

*More generally $U(z) = -\frac{e^2}{4z}(\frac{\epsilon-1}{\epsilon+1})$ (see e.g. the Ref. [318], p.154), where ϵ is the static relative permittivity (dielectric constant) of the material. In case of bulk metals ϵ is effectively infinite leading to the formula in the text. However, one has to be careful applying it to graphene on dielectric substrates and even to graphene in general due to its reduced dimensionality and semimetallic nature. Detailed analysis of how the image potential in graphene depends on its doping and the permittivity of the substrate can be found in Refs. [319, 320].

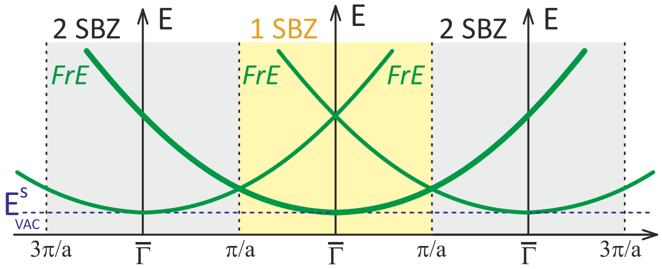

Figure 4.6: Fine-structure thresholds in extended zone scheme. Free-electron-like threshold parabola (FrE) of the first SBZ (yellow) is not visible in ARPES data because it coincides with the border of the region reachable by photoemission. In contrast, parabolas centered at the $\overline{\Gamma}$ points of the neighbouring SBZs (gray) are seen in the first SBZ and cross at its $\overline{\Gamma}$ point.

kinetic energies below the threshold at a given surface-parallel momentum cannot overcome the SPB and thus cannot escape to vacuum to be measured. Surprisingly, this does not mean that fine-structures are not observable by ARPES at all, to see this one has to consider the electrons that were scattered by surface reciprocal lattice vectors $\vec{\mathbf{G}}_i$ before escaping in the direction of the analyzer. These electrons can be accounted for by simply replacing in the Eq. 4.1 $\vec{\mathbf{k}}_{\|}$ by $(\vec{\mathbf{k}}_{\|} - \vec{\mathbf{G}}_i)$, which leads us to new threshold free-electron-like paraboloids originating at the $\overline{\Gamma}_i$ points of the neighboring SBZs (Fig. 4.7). Such paraboloids cross at the $\overline{\Gamma}$ point of 1^{st} SBZ due to general symmetry. This makes them observable by ARPES, moreover, similar crossings of the paraboloids from *next*-nearest SBZs should appear.

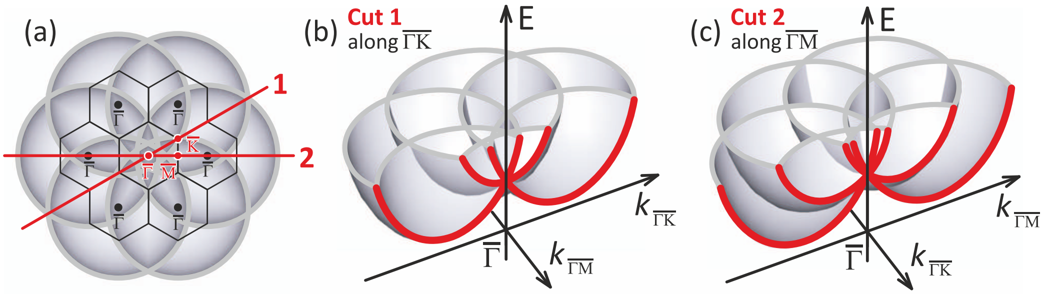

Figure 4.7: Fine-structure thresholds for a hexagonal lattice in the 2D extended zone scheme. (a) Free-electron-like paraboloids of revolution originating at six neighbouring Brillouin zones (the central one is hidden for clarity); (b,c) Slices along (b) $\overline{\Gamma K}$ (Cut 1) and (c) $\overline{\Gamma M}$ (Cut2) show different number of branches in the high-symmetry directions due to pairwise crossings of paraboloids along the planes of the cuts.

Summing up all the contributions from different $\vec{\mathbf{G}}_i$ and using formulae given above the electron transmission spectrum is calculated. The result is presented in Fig. 4.8(a). This picture shows how the interference due to surface barrier reflection would modulate the initially uniform electron background ($I_0(E, k) = const$). The four main sharp features crossing at the center are following free-electron paraboloids originating at different $\vec{\mathbf{G}}_i$. The main parameters of the model are the 2D geometry of the surface layer (given by $\vec{\mathbf{G}}_i$) and the function $\varphi_B(e_\perp)$ that is determined by the shape of the surface potential barrier. In our proof-of-principle calculation only the 6 shortest $\vec{\mathbf{G}}_i$ of the graphene lattice were taken into account. The value of the reflection modulus $r_B r_C \approx r_C = 0.05$ was selected empirically, however this small value is in line with the studies of Le Bosse et al. where the reflection modulus was estimated to be from 0.07 to 0.17 for several metallic surfaces [273, 275] and with the value 0.1 calculated for an Al(111) surface far from the band gap [310]. To mimic the finite energy resolution the image was convolved with the instrument function — a Gaussian curve with HWHM = 50 meV, a value realistically reflecting the experimental resolution. The result of such convolution on the fast-oscillating intensity profile is depicted in Figs. 4.8(g,h): the original spiky profile with multiple peaks in panel (h) is transformed to only three distinguishable peaks in panel (g) (see insets for zoom-in of the threshold region).

Simulation results presented in Fig. 4.8(a) reveal complex structure of ScR features formed by multiple peaks of intensity with various linewidths and shows that both narrow (NL) and wide (WL) lines observed in photoemission experiments belong to the same threshold-bound resonance structure (ScR) emerging as a Rydberg series.

Comparison of the Fig. 4.8(a) with the experimental spectrum of Gr/Ir(111) [Fig. 4.8(b)] reveals a general similarity in the positions and dispersion of the features confirming that the surface geometry is indeed a decisive factor for the shape of ScR. However, the behavior of intensity at kinetic energies lower than the threshold is somewhat different, as in the experiment we clearly observe a wide line of enhanced intensity (WL) parallel to the threshold that is bordered by a dark region (i.e. reduced intensity) from lower kinetic energy side. This line of intensity WL has a large, but finite width. On the contrary, at lower kinetic energies in the model image Fig. 4.8(a) there is a slow decay of intensity instead of a sharp drop [see also the red profile in Fig. 4.8(g)].

The reason for this discrepancy is in the non-physical behavior of the image potential $U(z) = -\frac{e^2}{4z}$ that goes to negative infinity in the vicinity of the surface. A more realistic approximation of the surface potential should saturate to the value of the inner potential V_{int} inside the crystal (Fig. 4.9). In this case the function $\varphi_B(e_\perp)$ will be also modified and will saturate to $-\pi$ at some finite value of $e_\perp$, say $e_\perp^0$. In Fig. 4.8(i) the graph of $\varphi_B(e_\perp)$ for the image potential is shown as a red dashed line and of the more realistic artificial phase as a black full line. The value of $e_\perp^0$ is determined by the depth of the surface potential barrier and defines the width of the WL. In our case $e_\perp^0$ is selected to be -6 eV as this value reproduces the experimental data reasonably well.

The model spectrum based on this simple phase accumulation model with the artificially constructed phase function [Fig. 4.8(c)] provides a surprisingly good overall

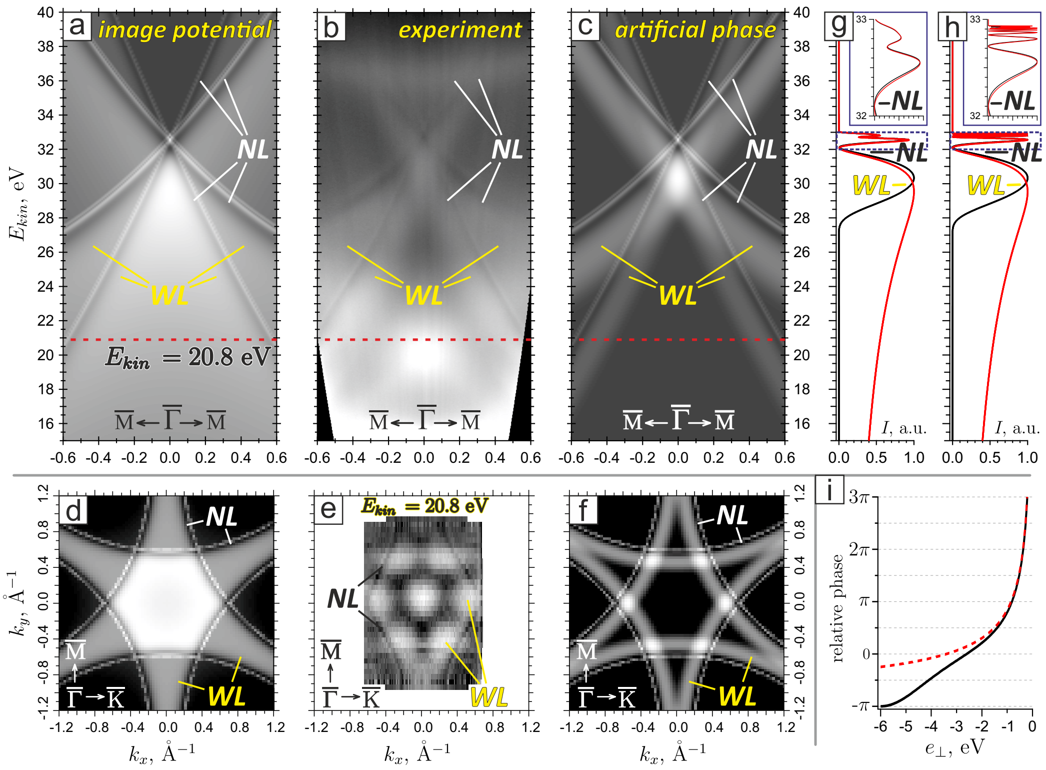

Figure 4.8: Results of calculations in the phase accumulation model and comparison with experimental ARPES data. Brighter colors correspond to higher intensity. (a) Intensity modulation of the initially uniform ARPES signal due to threshold effects as calculated for image potential. The image is convolved with Gaussian instrument function (HWHM = 50 meV); (b) Experimental ARPES spectrum for Gr/Ir(111) with wide intensity lines (WL); (c) Same as (a), but for the modified phase (see text for details). (d–f) Constant energy surfaces (CESs) corresponding to (a–c) taken at E_{kin} = 20.8 eV. (g) The line profiles at $\mathbf{k}_{\parallel}$=0 from (a) and (c) (red and black, respectively). (h) Same as (g), but before convolution with the instrument function. The insets in (g,h) show zoomed-in threshold region (between 32 and 33 eV). (i) The $\varphi_B(e_\perp)$ curve for image potential (red) and the artificial phase (black). Results of the simulation in (g,h) reveal narrow NL and wide WL features as belonging to the same quasi-bound resonance state (ScR).

agreement with the experimental spectrum [Fig. 4.8(b)]. The only feature that is completely missing in the model is the area of high intensity visible around E_{kin} = 20 eV in the experimental spectrum, which is most probably related to the unoccupied band structure of the sample. Another minor discrepancy is observed in the shape of the line profile close to the threshold. Based on our model and experimental resolution, we should be able to see a double peak feature in vicinity of the threshold [see inset of Fig. 4.8(g)], unfortunately, it is not clearly resolved, however the total width is in agreement with the model.

The constant energy surfaces (CESs) from model calculations compared with experimental ARPES mapping of graphene on Ir(111) at E_{kin} = 20.8 eV are presented

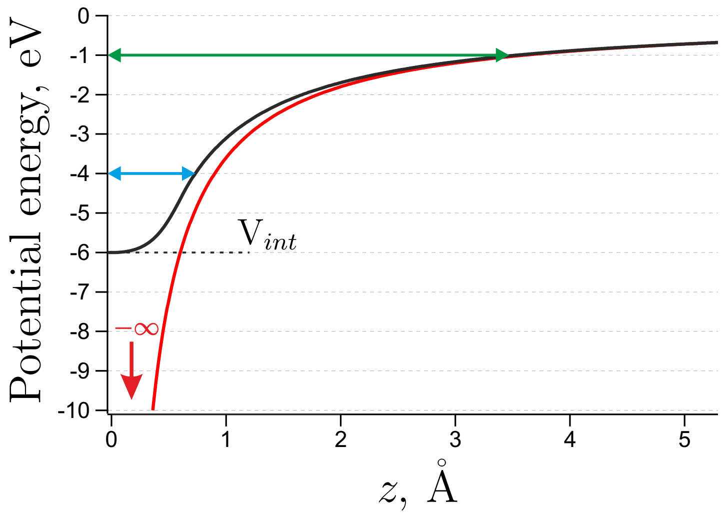

Figure 4.9: Sketch of the image potential (red) and a more realistic surface potential (black) dependence on the distance from the sample surface (z), energy is given relative to E_{vac}. While pure image potential is infinitely deep, a realistic one saturates at the surface to a constant value V_{int}. Blue and green arrows correspond to electrons with certain values of $e_\perp$ moving in the underbarrier region. The electron with higher value of $e_\perp$ (green arrow), travels a longer distance before being reflected by the barrier and acquires a larger phase.

in Fig. 4.8(d–f). The hexagonal shape and position of the features observed in the experiment are well reproduced. The intensity distribution in the (k_x, k_y) plane of the experimental CES [Fig. 4.8(e)] has brighter areas in the corners of the hexagon, this feature is reproduced in both models, but not very accurately. The experimental shape is somewhere "in between" the two model results, however the anisotropy is stronger than in the models. Both phase functions used for the calculations were just rough approximations and there has to be a function that provides a better fit of the experimental data. This function can be calculated directly from the SPB shape, but the latter is unknown. In principle, by fitting the experimental data one can estimate the parameters defining the shape of the surface potential barrier (as it was successfully done for VLEED experimental curves [274, 290]). Unfortunately, in the simple model it was not possible to completely reproduce the anisotropy in the CES of the WL that appears at low kinetic energies.

All of the above shows that the simplest interference model that accounts only for the paths with a *single* reflection at the SPB is already able to qualitatively explain the main intensity features observed in ARPES (as well as in VLEED [273, 275]). Nevertheless, a closer look at the experimental spectra reveals that dispersion of the WL deviates from parabolic at kinetic energies below 18 eV [Figs. 4.10(a,b)]. Moreover, as mentioned above, from the CESs [Fig. 4.8(e)] it is clear that the behavior of the WL at low kinetic energies is different from the behavior of the rest of fine structure. Indications for such discrepancies were also observed in secondary electron emission patterns from graphene in Ref. [302]. In the recent ARPES study [298] both fine and wide spectral features were measured in a very low kinetic energy range (down to ca. 3 eV) revealing strong deviations of the WL dispersion from free-electron-like. The authors distinguish the fine and wide features by their physical origin and attribute them to pre-emergent beam effects and quasi-bound states, respectively. However, our modeling results indicate that it is very likely that the nature of WL and the rest of fine structure is the same, only the deviations at the very low kinetic energies require a separate explanation.

By modifying the parameters of the interference model and including the paths with *multiple* underbarrier scattering events [thus obtaining phase shift of multiple φ_B, see Fig. 4.4(f)] one can approximate the experimental intensity profile better, but it seems unlikely that the model with 1D surface potential can adequately explain the shape of CES at very low kinetic energies. This means that the interference model gives a good general description but is, however, insufficient to carefully explain the experimental data.

4.2.2.2 Possible origins of deviations from interference model

Up to now we have neglected almost all the details of the sample and exploited only the 1D approximation of the SPB and the geometry of the surface, where beam emergence threshold energies were defined by free-electron parabola starting from the $\overline{\Gamma}$ point of the SBZ. Most importantly, the electronic band structure of the sample was not included in the discussion. It is known that the unoccupied states should influence the transmission of secondary electrons to vacuum [299] and therefore along with the scattering resonances we should observe features related to the unoccupied band structure of the sample.

Moreover, in some cases special discrete states can exist close to the border of the continuum of delocalized states (i.e. close to the threshold) and even above it along certain high-symmetry lines, as it was shown for 2D metallic films [321, 322] as well as for graphene [323]. The latter states should have finite lifetime due to non-zero probability of electrons to tunnel into the vacuum and thus referred to as *resonances*. Photoexcitation of electrons to energies in the vicinity of such quasi-bound states should produce a Fano-shape intensity profile due to quantum-mechanical interference [321, 324, 325]. Such spectral features in the region close to the emission threshold would overlap with the pre-emergent beam effects discussed above.

To test if the manifestations of the unoccupied band structure are present in the low-kinetic-energy region in ARPES we have measured a spectrum in a wide range of angles and energies [due to limited acceptance angle of the analyzer several spectra

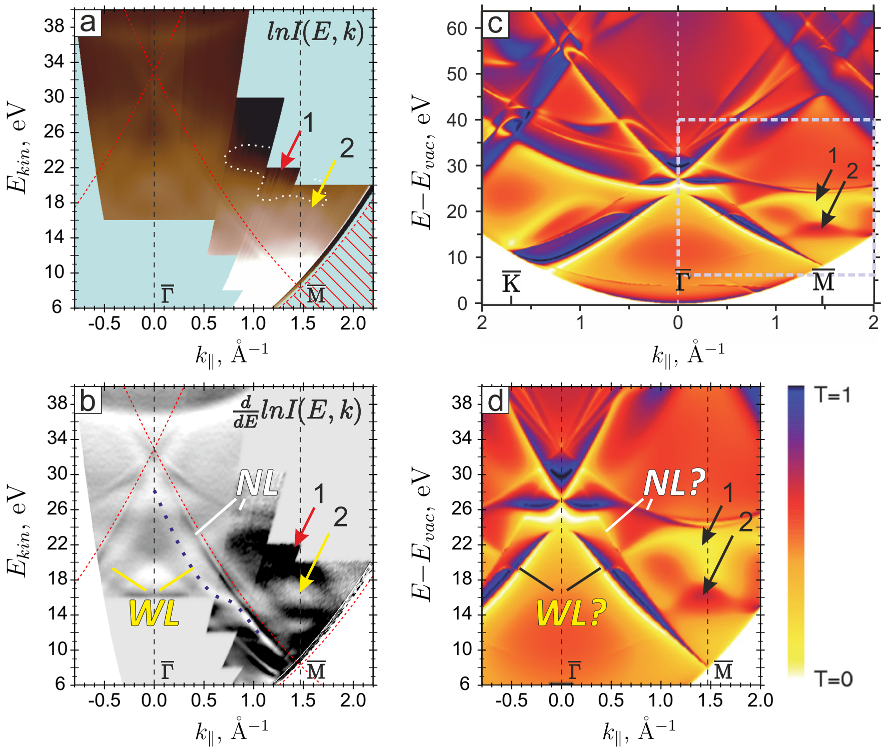

Figure 4.10: Spectral features observed at low kinetic energies far from normal emission. (a) ARPES spectrum of Gr/Ir(111) combined of several spectra measured with different tilt angles, logarithmic intensity scale. Red dashed lines are free-electron parabolas originating at the $\overline{\Gamma}$ points of 2^{nd} SBZ. Hatched area is principally unreachable by ARPES, blue areas were not measured in the experiment. (b) Derivative $\frac{\mathrm{d}}{\mathrm{d}E}ln(I)$ of (a), narrow (NL) and wide (WL) ScR features are visible. The dispersion of WL (sketched by a blue dotted line) deviates from parabolic. (c) Electron transmission probability through free-standing graphene, adapted from Nazarov et al. [323]. (d) Zoom-in of the dashed rectangle in (c), to scale with panels (a,b). Features 1 and 2 (low and high transmission, respectively) are clearly visible in (a,b). One can also see some features at the position of NL and WL from (b), however their intensity profile is significantly different.

were combined together, covering angles up to 75 degrees from normal emission[*], Figures 4.10(a,b)] and compared it with the theoretical transmission function of graphene calculated by Nazarov et al. [323] presented in Fig. 4.10(c,d).

As the secondary electron background drastically increases at low kinetic energies, the raw ARPES data is difficult to present in a comprehensible way. The spectrum in Fig. 4.10(a) is presented in a logarithmic intensity scale, red dashed lines mark the theoretical threshold positions for different SBZs. One can see that data is available

---

[*] This was achieved by tilting the sample. Linear p-polarization of light was used, meaning that the angle between the polarization vector and sample surface remained the same for each spectrum (Fig. 4.11). For experimental geometries of ARPES endstations at BESSY II (Figure 4.10) such large tilt angles are unreachable with any commercially available manipulator used for ARPES, the experiment was only possible with the use of manipulator S6.Cryo of a new design developed by Dr. A. Varykhalov.

almost to the threshold of the 1^{st} SBZ (hatched area is physically unreachable in ARPES experiments, blue areas correspond to lack of photoemission data). The pre-emergent beam effects (NL and WL) are visible at the lower kinetic energy side of the threshold lines, additionally, close to $\overline{\mathrm{M}}$ point, there are areas with reduced (1) and increased (2) intensity. To see the details better we present in Fig. 4.10(b) a derivative of Fig. 4.10(a) along the energy axis. Since this is a derivative of a logarithm, the result is scaled inversely to the intensity of the original data, effectively flattening the background, while keeping the important details intact:

$$\frac{\mathrm{d}}{\mathrm{d}E}(\ln I(E,k)) = \frac{1}{I(E,k)}\frac{\mathrm{d}I(E,k)}{\mathrm{d}E}. \tag{4.2}$$

Fig. 4.10(b) uncovers the deviations from parabolic dispersion of the WL at kinetic energies below 18 eV (see the blue dotted line as a guide to the eye) – it displays a pronounced "kink" at kinetic energy around 16 eV. Comparison of experimental data with the transmission spectrum calculated for free-standing graphene [Fig. 4.10(d)] reveals a decent agreement between the two, bearing in mind that Fig. 4.10(d) is a 1^{st} derivative image. This allows to attribute the features 1, 2 to the details of the unoccupied band structure. The interference with the unoccupied states could also be one of the reasons for the detour of the WL from parabolic behavior and formation of the "kink".

Unfortunately, despite the partial agreement, Fig. 4.10(d) does not reproduce exactly the details of the fine-structure near the threshold (marked as "NL?"). The reason could be that typical DFT approaches with local or semilocal exchange-correlation potential normally produce non-image asymptotic behavior of the potential far away from the surface (e.g. decaying exponentially instead of $\propto 1/z$ [311–313]). This may also affect the broader features in Fig. 4.10(d) (marked as "WL?"), which are located at the same position as WL in the experimental spectra, but have a sharp intensity border that is not observed in the experiment.

Regarding the unoccupied band structure of graphene, in Ref. [298] the authors claim to observe the manifestation of π^* and σ^* bands at kinetic energies around 3–7 eV. Unfortunately, this energy range was out of reach in our experiments.

Another simplification that may lead to discrepancy between the model and the experiment is the assumption of a 1D surface potential. On the atomic scale variations of the potential in the (x, y) plane could significantly modify the results of the interference model discussed above, resulting in anisotropy. The importance of the 3D nature of the SPB was demonstrated for LEED in Ref. [326]. The corrugation of the potential should smooth out far from the surface and be the strongest close to it. It means that in the first place WL feature will be affected, as it is formed by electrons that are deep in the surface potential well and thus localized closer to the surface. All the above makes up for another possible explanation of the anisotropic and non-parabolic behavior of the WL at low kinetic energies.

One more assumption was that the phase change related to the reflection at the crystal surface, φ_C, can be neglected as a slowly varying function of energy compared to φ_B. However, this reasoning works well only in the region close to the threshold, where the phase φ_B is indeed changing increasingly rapidly, and in the region of WL this may not hold true. It means that in general a variation of φ_C should be also taken into account, especially in case of a narrow band gap in the band structure, as φ_C varies by π when the energy sweeps across the band gap [268, 271].

To sum up, the complicated structure of the low kinetic energy region of ARPES spectra is affected not only by pre-emergent beam effects, but also by the unoccupied band structure including Fano-shaped excitations to quasi-bound resonant states. Now we proceed with systematic presentation of the experimental results.

4.3 Experimental details

ARPES measurements were carried out at the endstation ARPES 1[2] at room temperature, photon energies ranging from 30 to 100 eV and linear polarization of light (mixed s and p) were used (see Fig. 4.11 for experimental geometry). The electrons emitted in the detection plane L at angles ϕ ($-15° < \phi < 15°$) are transmitted to the analyzer and form a single 2D ARPES spectrum $I(E, \phi)$ along a certain line in momentum space. To acquire a full ARPES intensity map samples were rotated along the polar axis (θ) with steps of 0.5° and 2D spectra were acquired at each step.

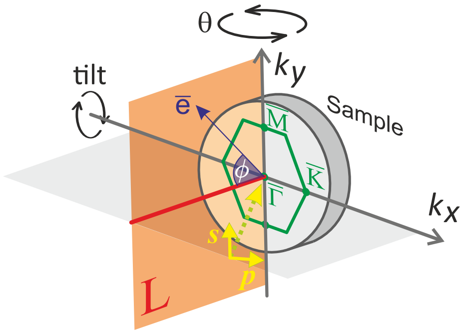

Figure 4.11: Geometry of ARPES experiment. The electrons (e^-) emitted in the plane L at various photoemission angles ϕ are detected by the analyzer. The synchrotron beam (yellow dashed line) was incident at an angle of 45° to the spectrometer axis (red line). Linearly polarized light was used (yellow arrows depict s- and p-polarization directions). ARPES mapping was achieved by scanning polar angle θ. The example orientation of graphene BZ is shown with green.

All samples of graphene on various substrates were prepared *in situ* [the only exception is graphene on SiC(0001)]. Preparation procedures for Gr/Ni(111), Gr/Ir(111) and Gr/Bi/Ir(111) were the same as described in previous chapters (see sections 2.3.1.1 and 3.2). Gadolinium intercalated Gr/Ir(111) [Gr/Gd/Ir(111)] and graphene on TiC(111)

[Gr/TiC(111)] were prepared according to Refs. [236] and [153], respectively. Samples of monolayer graphene on a SiC(0001) substrate [MLG/SiC(0001)] were prepared by the scientific group of Prof. Thomas Seyller (Technical University of Chemnitz). The preparation procedure is described in Ref. [120] and results in samples of high quality, nevertheless they may contain a minor amount of bilayer graphene in addition to monolayer one. Samples of MLG/SiC(0001) were transferred to the ARPES experimental chamber in air and annealed in UHV up to 300°C in order to remove water and other adsorbates from the surface.

In experiments devoted to control of scattering resonances by superlattices of quantum dots, a nanocluster decoration of Gr/Ir(111) was achieved by depositing iridium from a e^--beam heated 1 mm thick rod at slow rate (~ 0.1 ML in 10 min). The rate and total amount of deposited material were controlled by a quartz microbalance. At room temperature Ir atoms self-organize into nanoclusters at the valleys of the moiré pattern of Gr/Ir(111) thus forming stable well-periodic arrays without any additional treatment [258]. STM experiments were conducted as described in Section 1.4.3. The quality of the synthesized epitaxial graphene (crystallinity and orientation) was monitored by LEED. The base pressure in the experimental chamber was below 3×10^{-10} mbar.

Trace amounts of Te adatoms were used in some of the ARPES experiments as a source of an additional energy reference – sharp Te $4d$ core levels. This was useful in cases when it was not possible to measure features of interest and the Fermi level at the same time. The photoionization cross section of Te is very high in the range of photon energies used in this work (below 100 eV) and the intensity of Te $4d$ peaks (visible mainly in derivative) indicates very low quantities of adatoms that do not influence the results of this study.

Hydrogenation of Gr/Ir(111) was performed by exposing the sample to atomic hydrogen obtained by thermal dissociation of H_2 (an established method, see e.g. [264]). Gas was introduced in the UHV chamber at partial pressure of 5×10^{-7} mbar and cracked on a hot tantalum filament ($\sim$ 1800°C, [327]) in the vicinity of the sample surface.

4.4 Results and discussion

4.4.1 Occurrence and general properties of scattering resonances in ARPES

The spectral features discussed in this chapter have several unique properties that distinguish them from any other effect and allow to unequivocally identify them as scattering resonances ScR described in the introduction.

First of all, it is the characteristic picture of wide (WL) and narrow (NL) lines of intensity modulation with a pronounced crossing exactly at the $\overline{\Gamma}$ point (Fig. 4.3). The dispersion of the lines is very steep and even small errors in angular sample positioning will result in an obviously asymmetric picture. These lines can be well approximated in a certain energy range by free-electron-like parabolas originating at $\overline{\Gamma}$ points of neighbouring SBZs of graphene (see Fig. 4.15 and text therein for details). In this model the energy position of the crossing at the $\overline{\Gamma}$ point is very sensitive to the *surface* lattice constant making it possible to distinguish for example between graphene and Ir(111) lattices, as was demonstrated in Ref. [301], where similar effects were observed in ARPES from Gr/Ir(111). It proves that the observed features are directly related to the structure of the *topmost* surface atomic layer and not the substrate.

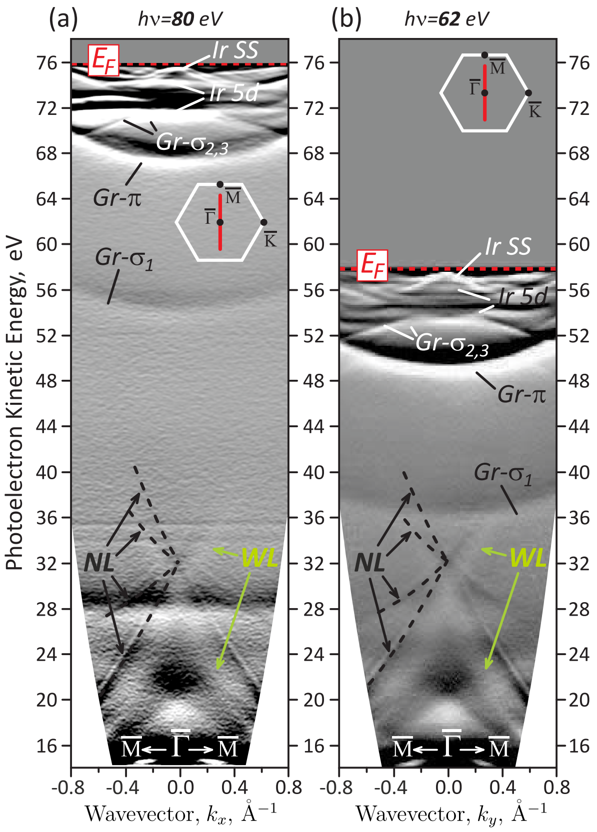

Figure 4.12: First derivative ($\frac{\mathrm{dI(E,k)}}{\mathrm{d}E}$) of Gr/Ir(111) ARPES spectra measured along $\overline{\Gamma \mathrm{M}}$ with (a) $h\nu$=80 eV and (b) $h\nu$=62 eV. Approximate dispersions of narrow lines are marked with dashed lines. The measurement geometry relative to the BZ of graphene is sketched in the insets (spectrum is measured along the red line). Both narrow (NL) and wide (WL) intensity lines do not move in kinetic energy scale with changing photon energy, while Fermi level E_{F} and occupied bands of Gr/Ir(111) do.

Second, independently of the excitation energy the positions of these features on the *kinetic* energy scale remain the same (Fig. 4.12). Such behavior is unusual for conventional photoemission features, which are related to the occupied band structure of the sample and thus described by a certain *binding* energy. One can clearly see the different behavior in Fig. 4.12, where two spectra of Gr/Ir(111) measured with photon energies $h\nu = 80$ eV (a) and $h\nu = 62$ eV (b) are displayed. Both types of features are present in these spectra: scattering resonances and occupied bands of graphene and Ir(111). One can see that the positions of Fermi level E_F and all valence bands are shifted by the difference in photon energies (18 eV), while the characteristic crossings of scattering resonance features NL and WL appear at the same kinetic energies. This is in good agreement with the model described earlier, as the energy position of resonances is bound not to E_F, but to the vacuum level of the sample E^S_{vac}.

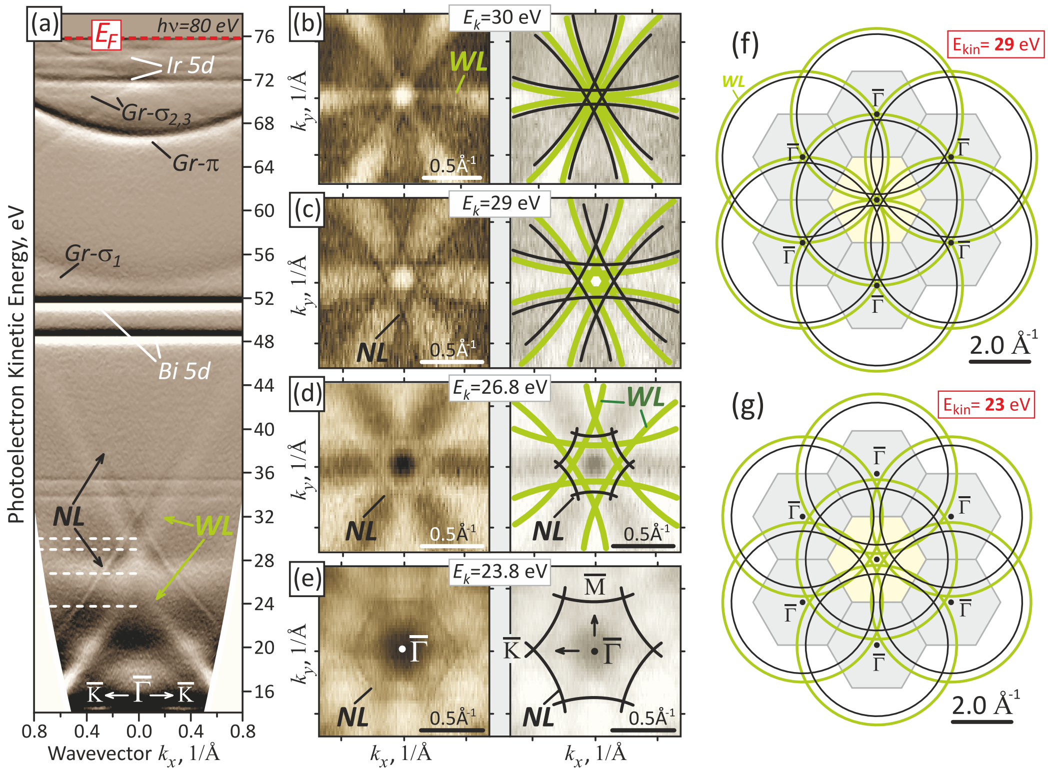

Figure 4.13: Results of ARPES mapping of scattering resonances ScR (NL + WL features). (a) ARPES spectrum of Gr/Bi/Ir(111) taken at normal emission along $\overline{\Gamma \mathrm{K}}$ ($\frac{\mathrm{dI(E,k)}}{\mathrm{d}E}$). Crossing of narrow features NL is observed around 32 eV. (b–e) Sequence of CESs extracted for different kinetic energies from ARPES map (left) and model circular contours of ScR features (right). (f, g) Larger-scale simulation of ScR constant-energy surfaces (same colour scheme as in b–e) in the approximation of free-electron-like paraboloids. CESs are constructed for the kinetic energies of 29 eV (f) and 23 eV (g). Circular contours are centered at the $\overline{\Gamma}$ points of the 2^{nd} BZs (shaded gray) and their intersection in the 1^{st} BZ (shaded yellow) forms a symmetric pattern.

The branching of the sharp NL features in Fig. 4.12 is also consistent with the geometric model of resonances as crossing free-electron-like threshold paraboloids [Fig. 4.7(c)]. This statement is further confirmed in the constant energy surfaces extracted from full photoemission mapping of the scattering resonances [Figs. 4.13(b–e)]. The shape of the central area formed by intersecting narrow ScR features is changing from a "star of David" at higher kinetic energies (b, c) to nearly hexagonal at lower ones (d, e). This is in perfect agreement with the geometric model, where CESs of ScR paraboloids* are circles of a diameter that varies with kinetic energy [Figs. 4.13(f, g)]. Similar patterns were observed for free-standing graphene in the electron transmission experiments [277] and in secondary electron emission from graphene on SiC(0001) [302]. Right panels in Figs. 4.13(b–e) display the simulated contours of both narrow (NL, black lines) and wide (WL, green lines) ScR features superimposed on the ARPES data.

We already know from the experimental evidences discussed above that ScR features are present in the spectrum of secondary electrons and that their global structure is determined by the geometry of graphene. Up to now the importance of the SPB was not obvious (except that it gives a good prediction of the intensity profile) and one can hypothesise that the *graphene sheet* acts as a "filter" for the photoemitted secondary electrons of the substrate, and the SPB can be removed from the consideration. In the framework of this hypothesis the electrons emitted from *graphene* itself should not be affected by the ScR spectrum.

Fortunately, this idea can be tested experimentally: the different photon-energy dependence of scattering resonances and the valence bands in ARPES makes it possible to overlap the two in one spectrum by selecting a certain excitation energy. Such experiments were conducted and the results for the Gr/Bi/Ir(111) system are displayed in Fig. 4.14. The displayed spectral region contains the dispersions of $\sigma_{2,3}$ and π states of graphene measured with photon energies 62 eV (a) and 35 eV (b). In the second panel we see pronounced intensity modulations of σ and π bands along the narrow lines of scattering resonances. This means that ScR affect not only the secondary electrons from the substrate, but also the electrons that are emitted from graphene itself. This result is hardly compatible with the "graphene as a filter" hypothesis. If we assume the existence of some "filtering" process, it should happen *above* graphene and the surface potential barrier region is the only candidate. To sum up, this simple observation leads to deep insights about the nature of the observed features and proves that the SPB plays a major role in their formation.

All our experimental observations confirm the equivalence of the discussed features with the scattering resonances observed by VLEED and support the SPB scattering as the main mechanism of their formation.

---

[*] Dispersions of narrow and wide ScR features follow the same paraboloids of rotation as thresholds, only shifted in kinetic energy by a constant value.

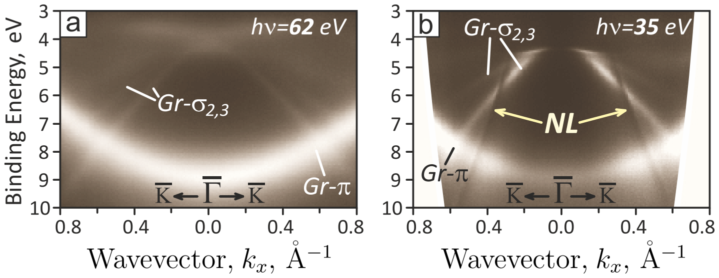

Figure 4.14: ARPES spectra of Gr/Bi/Ir(111) (raw intensity data) measured along $\overline{\Gamma\mathrm{K}}$ with different photon energies: (a) $h\nu = 62$ eV and (b) $h\nu = 35$ eV. The region of $\sigma_{2,3}$ and π bands of graphene is shown, in panel (b) the intensity of the bands is modulated by narrow lines NL of ScR.

4.4.2 Crossing positions and the effect of doping

From the previous section we know that the global structure of the scattering resonances, i.e. their position in energy-momentum space, is defined mainly by the geometry of the upper-most layer. Indeed, studying graphene on a large number of different substrates we were always able to observe very similar ScR features NL and WL (this also proves their stability against the chemical interaction between graphene and the substrate). However, their position was not *exactly* the same and varied stronger than can be explained by the small possible changes of the lattice constant of graphene.

A quantitative study of this effect requires a reliable reference for the energy position of the scattering resonances, such as the energy E_{thr} at which threshold lines from second SBZs cross at the $\overline{\Gamma}$ point. At the same k-point, but higher in energy, one can also observe crossings of parabolas originating from further SBZs – they appear at energies scaling as squared distances $\left|\vec{\mathbf{G}}_i\right|$ to the corresponding $\overline{\Gamma}_i$ points: $E^i_{thr} = \frac{\hbar^2}{2m_e}\vec{\mathbf{G}}^2_i + E^S_{vac}$. Then for hexagonal SBZ: $E^i_{thr} - E^S_{vac} = \{E_0,\, 3E_0,\, 4E_0,\, \ldots\}$, where $E_0 \equiv (E^1_{thr} - E^S_{vac}) = \frac{\hbar^2}{2m_e}\vec{\mathbf{G}}^2_1$ is the first crossing [see Fig. 4.15(a,b) for a geometric view]. Here E^S_{vac} denotes the vacuum level of sample.

Unfortunately, the exact threshold position is not directly observed in the experiment [see e.g. Fig. 4.8(b,g,h)], instead we use the most well-defined feature of ScR – the narrow intensity dip of NL (seen as a sharp black line in the spectra). Its position relative to the threshold E_{dip} may vary from sample to sample depending on the details of the SPB. However, such variations should be relatively small, values estimated from our interference model for different SPB depths varied by less than 0.4 eV*. Using the position of the minimum of the intensity in the NL (at $k_{\parallel} = 0$) as a reference mark we track the energy position E_{cr} of scattering resonances in graphene on a variety of substrates (see Table 4.1 and Fig. 4.16).

---

*In Ref. [276] changes in the fine-structure profile were analyzed with regard to the position of the image plane (which influences the shape of the model SPB). Based on the obtained fine-structure profiles one can see that in this case the variation of E_{dip} was also ≤ 0.5 eV.

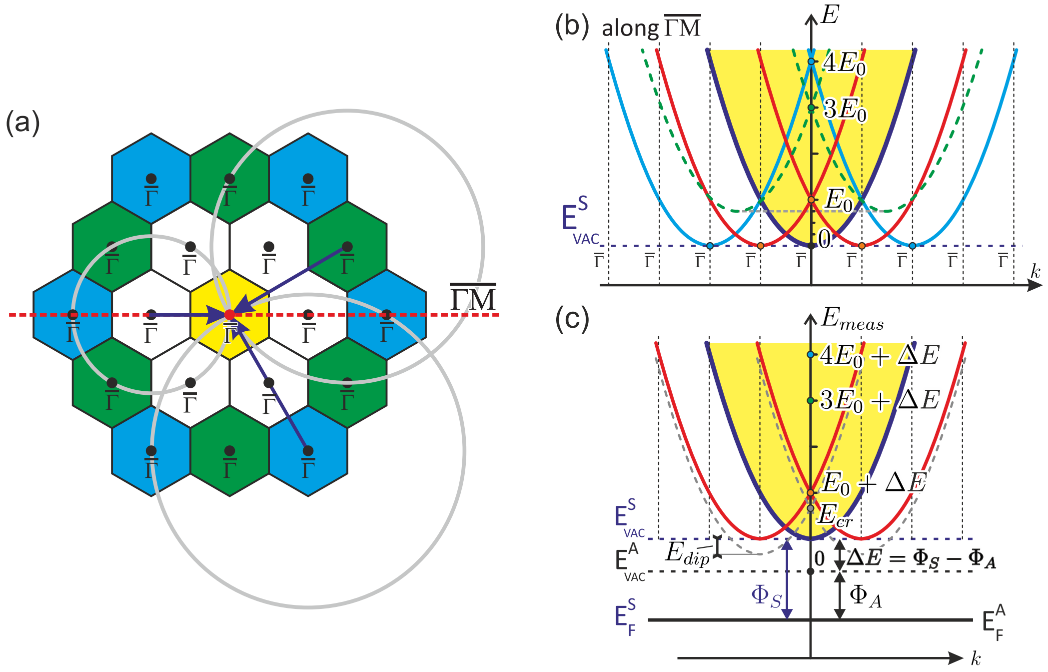

Figure 4.15: (a) 2D scheme (k_x, k_y) of repeated BZs. Zones are coloured based on the distance $\left|\vec{\mathbf{G}}_i\right|$ from their $\overline{\Gamma}$ point to the $\overline{\Gamma}$ of the 1^{st} BZ ($\left|\vec{\mathbf{G}}_i\right| = \left|\vec{\mathbf{G}}_1\right| * \{0, 1, \sqrt{3}, 2\}$ in this order are yellow, white, green and blue). Circular ScR contours (gray, only one of each kind is shown for clarity) coming from BZs of the same colour by symmetry should all cross at the $\overline{\Gamma}$ of the 1^{st} BZ, different colours at different energies. (b) The threshold parabolas along the $\overline{\Gamma\mathrm{M}}$ direction [red dashed line in (a)]. One can see the lowest crossing at E_0 (crossing of parabolas centered at white BZs) and other crossings at $3E_0$ and $4E_0$ (from green and blue zones, respectively). (c) The origin of the experimental kinetic energy axis (E_{meas}) is E^A_{vac}, which is generally not equal to E^S_{vac} (bottom of the threshold parabola). In the experiment not E_0, but $E_{cr} = E_0 + (\Phi_S - \Phi_A) - E_{dip}$ is measured. Here E^S_{vac} and Φ_S denote vacuum level and work function of sample, E^A_{vac} and Φ_A – vacuum level and work function of analyzer. E_{dip} is a sample-specific energy correction (see text for details).

The selected substrates have distinct chemical properties and have different effect on graphene. All substrates can be divided into two groups: strongly interacting with graphene [Ni(111), TiC(111)], placed at the bottom of the table, and those where graphene is considered quasi-free-standing [Ir(111), Bi/Ir(111), SiC(0001), Gd/Ir(111)]. Those in the second group differ by the amount of charge-transfer between graphene and the substrate and as a result the energy position of its Dirac point E_B^{DP} is also different. The latter varies from small negative value for Ir(111) to large positive for Gd/Ir(111) [1 ML of Gd intercalated under Gr/Ir(111)]. The strongly interacting substrates produce an even larger shift of the Dirac point, which is defined both by charge-transfer and hybridization of the DC with the substrate electronic bands. In Figure 4.17 ARPES spectra of DC (a–c) and ScR (d–f) regions are presented for three characteristic samples from the list: weakly interacting Gr/Bi/Ir(111) and Gr/Ir(111), both introduced in the

Substrate	a_{gr}, Å	$\frac{\hbar^2\lvert\vec{\mathbf{G}}\rvert^2}{2m_e}$, eV	E_B^{DP}, eV	E_{cr}^{th}, eV	E_{cr}, eV
Ir(111)	2.46	33.1	-0.1	32.6	32.7
1 ML Bi/Ir(111)	2.46	33.1	0.4	32.1	32.0
SiC(0001)	2.46	33.1	0.42	32.1	32.0
1 ML Gd/Ir(111)	2.46	33.1	1.1	31.4	31.7
Ni(111)	2.49	32.3	2.84	28.9	30.5
TiC(111)	2.47	32.9	2.35	29.1	30.5

Table 4.1: Kinetic energies of ScR crossings in graphene on various substrates (E_{cr}). Based on the graphene lattice parameter a_{gr}, binding energy of the Dirac point (E_B^{DP}) and constant shift of 0.6 eV (see text) the estimate of the threshold crossing kinetic energy is calculated as $E_{cr}^{th} = \frac{\hbar^2|\vec{\mathbf{G}}|^2}{2m_e} - E_B^{DP} - 0.6$ eV. For weakly interacting substrates (top) a_{gr} is that of free-standing graphene, for strongly interacting substrates (bottom) – see text.

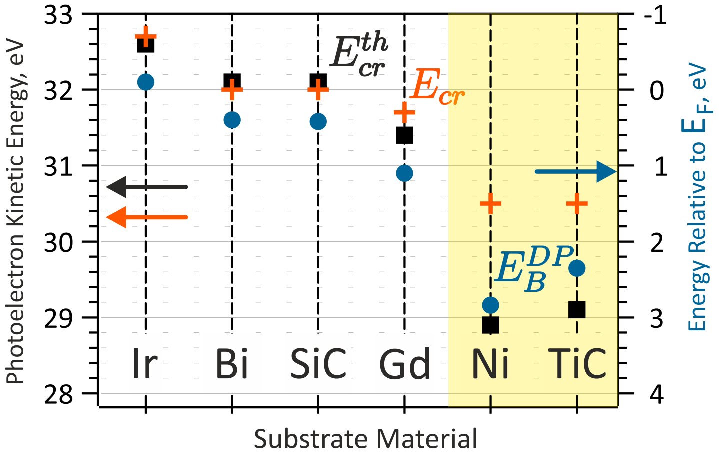

Figure 4.16: The experimentally observed positions of NL crossings E_{cr} (red crosses, left axis) and shifts of the Dirac point of graphene E_B^{DP} (purple circles, right axis) for various substrates. Strongly interacting substrates are marked by a yellow background. One can see that two graphs are very similar in the region of weakly interacting substrates. Moreover, the theoretical ScR crossing positions E_{cr}^{th} (black squares, left axis) are in good agreement with the experimental E_{cr} values with the exception of strongly interacting substrates. The exact energy values are listed in Table 4.1.

previous chapter, and strongly bonded graphene on Ni(111) [Gr/Ni(111)] with its DC modified by the interaction with the substrate and hybridization with Ni 3*d* bands [135].

From the data in the Table 4.1 and Figures 4.16 and 4.17 there is a clear correlation between the E_B^{DP} and the crossing position E_{cr}. Interesting that for Gr/SiC(0001) and Gr/Bi/Ir(111) – two chemically very contrasting substrates with similar graphene lattice parameter and doping – E_{cr} is the same within experimental error.

This correlation comes from the fact that the energy position of the resonances is pinned to the vacuum level of the sample E_{vac}^S [see Fig. 4.15(c)]. The kinetic energy in the experiment is measured relative to the *analyzer* vacuum level E_{vac}^A and since the

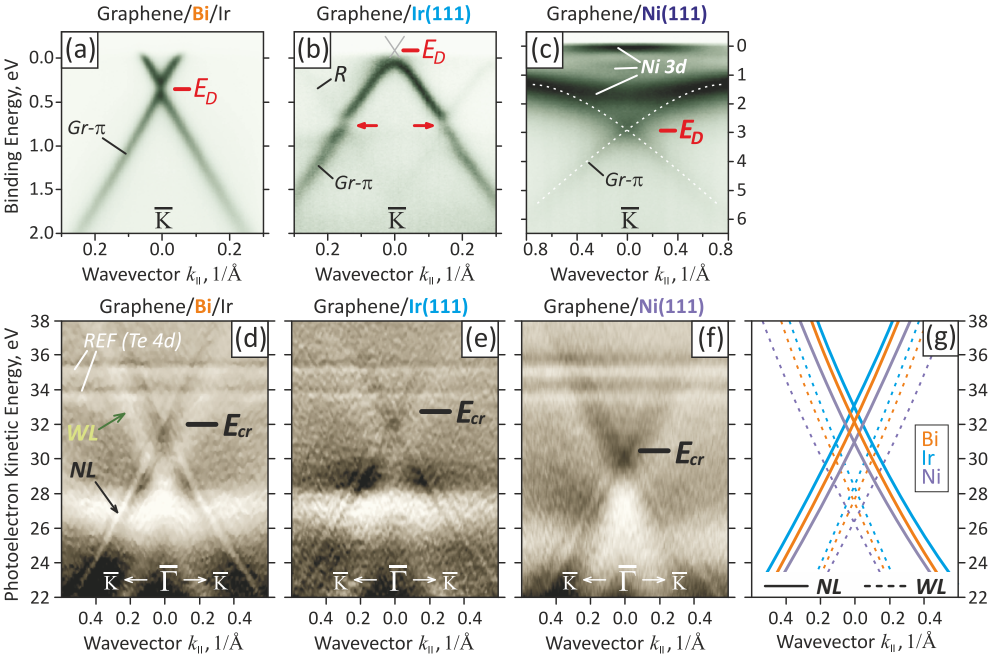

Figure 4.17: The effect of the substrate on ScR and Dirac cones (DC) in graphene. (a–c) ARPES spectra of the DC in (a) Gr/Bi/Ir(111), (b) Gr/Ir(111) and (c) Gr/Ni(111), note the different binding energies of the Dirac point (E_D). (d–f) The corresponding spectra of the ScR area. The crossing kinetic energies E_{cr} of the narrow features (marked as NL) vary between the substrates, they are better visible in (g) where traces of NL and WL for different substrates are overlaid. The changes in E_{cr} are same for both NL and WL and correlate with the shifts of E_D from (a–c).

Fermi levels E_F of sample and analyzer are equalized, the position of the bottom of the resonance parabola is exactly $\Delta E = E^S_{vac} - E^A_{vac} = \Phi_S - \Phi_A$, i.e. unlike typical ARPES features the ScR energy position *depends* on the work function of the sample Φ_S. This explains the large shifts of E_{cr} on different substrates. Moreover, for weakly bound graphene Φ_S is directly related to the doping level E_B^{DP} ($\Phi_S + E_B^{DP} = (4.50 \pm 0.05)$ eV [328]) and this is the origin of the observed correlation between E_{cr} and E_B^{DP}. Finally, one can calculate the expected position of the crossing as $E_{cr}^{th} = \frac{\hbar^2|\vec{\mathbf{G}}|^2}{2m_e} + (\Phi_S - \Phi_A) - E_{dip} \approx \frac{\hbar^2|\vec{\mathbf{G}}|^2}{2m_e} - E_B^{DP} + const$, where $\vec{\mathbf{G}}$ is the reciprocal lattice basis vector and $E_{dip} = E_{thr} - E_{cr}$ is the separation in energy from the threshold to the measured intensity minimum position (this distance can be calculated, but the result depends on the exact shape of the SPB, which is generally unknown). The constant factor can be estimated as $4.5\ \text{eV} - \Phi_\text{A} - \text{E}_\text{dip} = -0.7$ eV, where $\Phi_A = 4.4$ eV for our setup and the value $E_{dip} = 0.8$ eV was extracted from the interference model calculations [see Fig. 4.8(h)]. On the other hand, the calculated values of $(\frac{\hbar^2|\vec{\mathbf{G}}|^2}{2m_e} - E_B^{DP})$ are on average* 0.6 eV higher than the experimental E_{cr} for weakly interacting substrates, which is very close to the estimated value of 0.7 eV. The values ($E_{cr}^{th} = \frac{\hbar^2 |\vec{\mathbf{G}}|^2}{2m_e} - E_B^{DP} - 0.6$ eV) are in fair agreement with the measured values of E_{cr} and correlate with the E_B^{DP}, as shown in Fig. 4.16.

For graphene on strongly interacting substrates such estimates have much larger discrepancies from the experimental data. A possible reason is that the position of the Dirac point is influenced by hybridization of the DC with the substrate states and does not precisely reflect the change in the work function.

However, one should also take into account other possible sources of the discrepancies. First of all, the value of E_{dip}. The distance between graphene and the substrate is significantly lower for strongly interacting substrates, this may lead to different shape of the SPB and different displacement of the intensity dip. As stated above, the variation of E_{dip} in the model calculations for simple barrier shapes was less than 0.5 eV.

Another point of consideration is that variation of only 0.01 Å in the lattice constant a_{gr} results in a $\sim$ 0.25 eV shift of the crossing point. The value $a_{gr} = 2.46$ Å of free-standing graphene is a good approximation only for weakly interacting substrates. In particular, for Gr/Ni(111) the (1×1) LEED pattern and Helium-diffraction data ([329, 330]) suggest that $a_{gr} = 2.49$ Å, equal to the surface lattice of Ni(111). For Gr/TiC(111) the condition of commensurability between (7×7) TiC(111) and $(5\sqrt{3} \times 5\sqrt{3})\mathrm{R}30°$ graphene lattices ([331]) gives $a_{gr} = 2.47$ Å. Unfortunately, up to date there is a lack of experimental structural data with high enough precision for graphene on various substrates. Considering the fact that scattering resonances are a general phenomenon occurring for many 2D materials and crystal surfaces, a better understanding of their features may turn them into a practical tool for precise determination of the surface lattice constant.

4.4.3 Controlling the resonances

Based on the previous theoretical and experimental studies we can understand the basic principles and even perform modeling of the scattering resonances. From our findings it follows that by engineering graphene-metal interfaces one can control the energy position of the ScR in a wide range. Such an effect can be useful for optoelectronic applications as it allows to modify the electron emission spectrum. In this section we make one step further and investigate the possibilities of controlling the ScR by structural modifications of the crystal surface. Graphene is a perfect test system for this study, not only because it exhibits pronounced fine-structures of ScR in ARPES, but also because of the versatility that it provides for chemical and physical modifications.

---

[*] Value 0.6 eV minimizes the mean squared error.

4.4.3.1 Corrugation enhancement

The two-layer model of scattering resonances is based on the approximation of a uniform 1D surface potential barrier $U(z)$. However, lateral variations of the potential are always present on the atomic scale in the vicinity of the surface, their importance for VLEED was demonstrated in Ref. [326]. It is interesting to study the effect of a *nanoscale* periodic in-plane potential modulation on ScR as well. A convenient sample for this purpose is Gr/Ir(111) that has a natural structural corrugation in the form of a moiré pattern with periodicity of $\sim$ 25 Å and small amplitude of $\sim$ 0.3 Å [see Figs. 3.10(a–c,k)]. The ARPES data presented earlier reveals no strong difference between ScR in mildly corrugated graphene on Ir(111) and other substrates. However, one can enhance the moiré superpotential strength in a controlled way by decorating graphene with metallic nanoclusters (quantum dots QDs). As demonstrated in Ref. [258], deposition of Ir atoms on Gr/Ir(111) at room temperature leads to self-assembly of stable Ir QDs of uniform size in the specific valleys of the moiré pattern. Similar behavior was observed for other noble metals as well, such as Pt [332, 333] and Rh [334]. It was shown that such metallic QDs locally pin graphene to the Ir(111) substrate and cause $sp^2 \rightarrow sp^3$ rehybridization [332, 335], that leads to stronger deformation of the graphene sheet and enhancement of the superpotential amplitude. This effect can be tuned by changing the size of QDs that is directly related to the amount of the deposited material.

In our experiments we have performed a decoration of Gr/Ir(111) by Ir nanoclusters of two different sizes corresponding to 0.1 and 0.2 ML of nominal Ir thickness (smaller and larger QDs, respectively). STM measurements reveal that indeed deposition of submonolayer amounts of Ir at room temperature leads to the formation of well-ordered QD arrays with narrow size distribution, Figure 4.18(b) presents the STM image of Gr/Ir(111) after deposition of 0.2 ML of Ir.

The influence of the clusters on the electronic band structure of Gr/Ir(111) has been investigated by ARPES [Fig. 4.18(c–h)]. First of all, we observe that the width of the minigaps (E_m) at the crossings of DC replicas, caused by an umklapp effect of the moiré pattern of graphene, increases with increasing size of Ir QDs [Fig. 4.18(c–e)]. In our experiments the widths E_m were $\sim$ 180 meV, 320 meV and 420 meV for clean Gr/Ir(111), smaller QDs and larger QDs, respectively. This effect is known from the literature and it is attributed to an enhancement of the moiré superpotential by the QD arrays [141, 194]. Despite this, the *positions* and overall shape of ScR features remain the same after QD deposition [Fig. 4.18(f–h)], but their *intensity* changes. The narrow ScR features NL nearly vanish already after deposition of small clusters, WL features are also strongly suppressed, however they remain visible even after deposition of large nanoclusters. Of course, the deposited Ir clusters cover a part of the graphene surface, but the ScR suppression cannot be attributed exclusively to such shadowing of electrons emitted from below the clusters, since we are able to observe the band structure

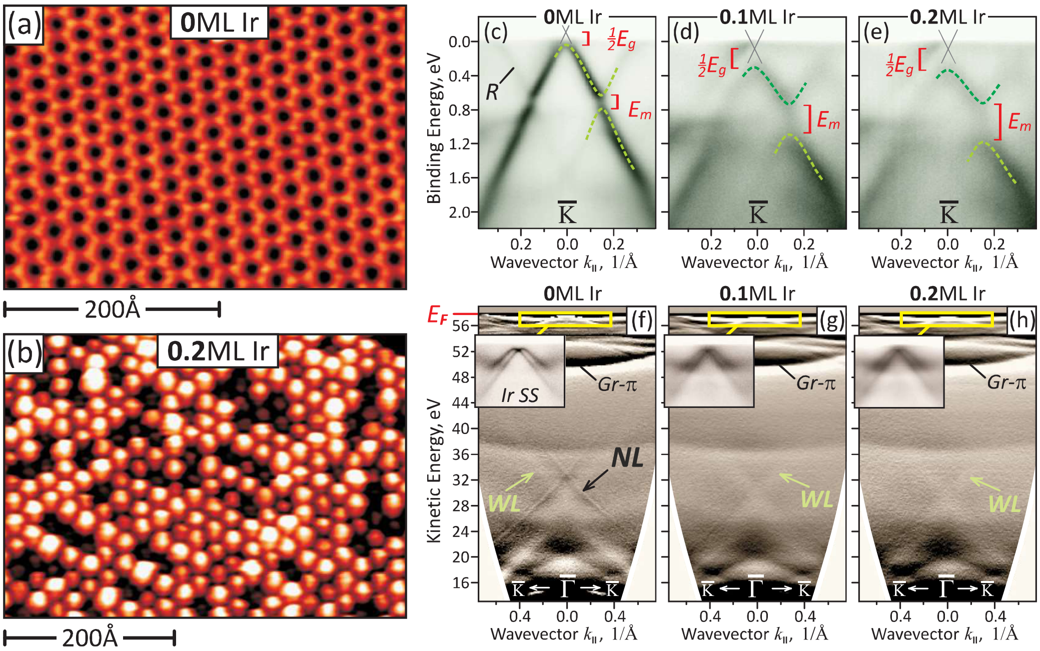

Figure 4.18: Effect of Ir nanoclusters on electron scattering resonances ScR in Gr/Ir(111). (a,b) STM of Gr/Ir(111): (a) as-prepared and (b) after deposition of 0.2 ML of Ir (well-periodic array of quantum dots (QDs) is formed through decoration of the moiré pattern by Ir adatoms). (c–h) ARPES spectra of Gr/Ir(111) taken with $h\nu = 62$ eV without QDs (c,f), after deposition of 0.1 ML Ir (d,g) and 0.2 ML Ir (e,h). Higher amount of Ir leads to larger nanocluster size and at the same time larger moiré-induced umklapp minigaps E_m (c–e), indicating enhancement of the moiré superpotential. At the same time ScR features (f–h) become strongly suppressed already after deposition of 0.1 ML Ir. Insets in (f–h) show preserved Ir(111) surface state.

of graphene and the Ir(111) surface state is preserved [270] [see insets in Figs. 4.18(f–h)]. On the other hand the observation of suppressed ScR is in line with Ref. [336], where the screening of the $n = 1$ image potential state in Gr/Ir(111) decorated by Ir nanoclusters was investigated. The authors observe a rapid non-linear decay of the IPS intensity with increasing nanocluster coverage of graphene and the IPS disappears at coverages above 50%. This effect is attributed to a non-uniform variation of the surface potential across the surface due to clusters and the same explanation is applicable in our case. Indeed, the global work function of Gr/Ir(111) with large cluster coverage is significantly larger than that of bare Gr/Ir(111) ((5.5 ± 0.1) eV and (4.4 ± 0.1) eV, respectively [336]), whereas even small variations in the position of E_{vac} may destroy the part of the ScR close to the threshold (including narrow lines NL) by averaging the fast-oscillating part. Broad lines WL, in contrast, are more stable against such perturbations.

The results of this experiment once again highlight the importance of the shape of the surface potential barrier for scattering resonances and show that suppression of

NL due to variations in work function masks the possible effects of the superpotential enhanced by the nanoclusters. Therefore, there are still many open questions related to the influence of nanoscale corrugation on ScR, e.g. what is the effect of it on the WL structure at very low kinetic energies and do superstructural replicas of ScR exist?

4.4.3.2 Hydrogenation

A more delicate way to enhance the strength of the superpotential in Gr/Ir(111) is *hydrogenation*. Atomic hydrogen deposited on Gr/Ir(111) acts in many aspects similar to Ir clusters: it binds to carbon atoms preferentially at the valleys of the moiré pattern and changes the hybridization of these atoms from sp^2 to sp^3 [265, 337]. This leads to deformation of the flat graphene sheet and formation of alternating bonds to hydrogen and iridium, the latter pin graphene to the substrate enhancing the nanoscale corrugation.

The important difference from deposition of clusters is that hydrogenation disturbs the surface topography to less extent, which is beneficial for a uniform surface potential. Another point to consider is the variation of the work function $\Phi(x,y)$ across the sample that was crucial in the case of clusters. There are experimental evidences that room temperature hydrogenation leads to a *single-sidedly* hydrogenated graphene, in contrast to the symmetric "graphane" structure with hydrogen on both sides [338]. This means that in hydrogenated areas a surface electric dipole appears that might affect $\Phi(x,y)$. Unfortunately, the information about a change of the work function due to hydrogenation is very scarce, however there are theoretical indications that this value is on the scale of 0.1 eV [339]*, much smaller than ~ 1 eV in the case of clusters.

To study the influence of hydrogenation on the ScR features in Gr/Ir(111) an ARPES experiment was conducted. Figure 4.19 demonstrates ARPES spectra taken with $h\nu =$ 62 eV along $\overline{\Gamma \mathrm{M}}$ and covering kinetic energies of both ScR and valence band features. The first panel presents reference data from clean Gr/Ir(111) and the following three were measured after sequential steps of hydrogenation. The degree of hydrogenation (percent of carbon atoms in graphene bonded to atomic hydrogen) in each step was controlled by the time of exposure to the atomic hydrogen (the ratio of total exposures in steps 1–3 is 1:2:4).

First of all, with increasing exposure time we observe broadening of the Gr/Ir(111) bands (indicative of increase in electron scattering rate), but not radical changes in their dispersion that would be expected in case of double-sidedly hydrogenated *graphane* ([340]). At the same time we observe opening of the band gap at the $\overline{\mathrm{K}}$ point after hydrogenation (Fig. 4.20) in agreement with Ref. [265], which confirms that hydrogenation of the surface takes place. The maximal exposure used in the experiment (3^{rd}

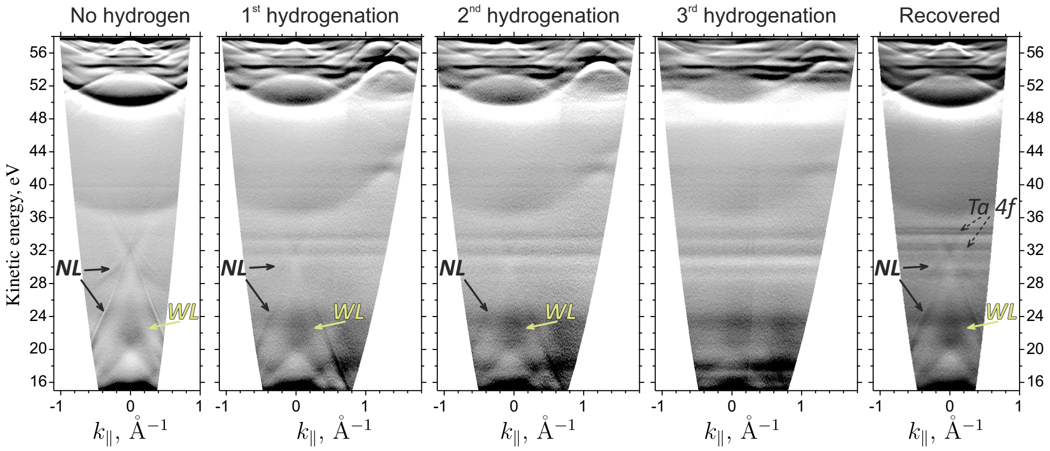

Figure 4.19: ARPES data ($\frac{\mathrm{dI(E,k)}}{\mathrm{d}E}$) of Gr/Ir(111) measured with $h\nu = 62$ eV along $\overline{\Gamma\mathrm{M}}$ showing the effect of hydrogenation on NL and WL of ScR. Initially (left) ScR features are pronounced and they fade with each step of hydrogenation (middle). After annealing hydrogen desorbs from the surface and ScR features are recovered (right). The horizontal lines that appear in the spectrum after hydrogenation and stay after annealing are identified as 4f core levels of Ta in different oxidation states and are attributed to evaporation of small amounts of filament material on the sample surface.

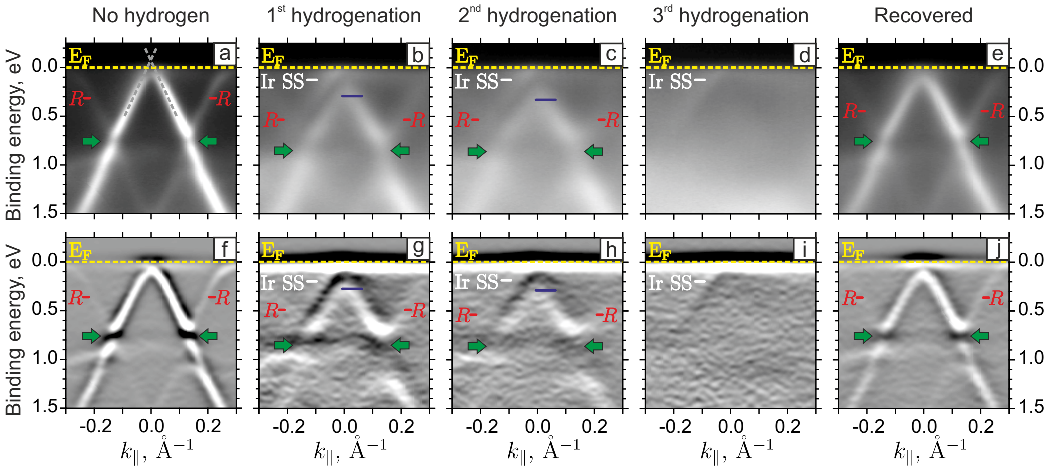

Figure 4.20: ARPES spectra of the Dirac cone in pristine (a), hydrogenated (b–d) and recovered by annealing (e) Gr/Ir(111) measured with $h\nu = 62$ eV. Second derivative ($\frac{\mathrm{d^2I(E,k)}}{\mathrm{d}E^2}$) of the corresponding spectra is presented below (f–j). Wave vector $k_\parallel$ is given relative to $\overline{\mathrm{K}}$. One can see that the apex of the cone (blue dash) moves to higher binding energies indicating the opening of a gap at $\overline{\mathrm{K}}$. Minigaps (green arrows) at the crossings of the main Dirac cone with replica cones (R) are also enhanced.

step) results in a very strong broadening of the Dirac cone [Figs. 4.20(d,i)] which nearly vanishes.

The effect of hydrogenation is also observed in the STM data presented in Fig. 4.21.

---

[*] Calculated for coronene, a small graphene-like organic molecule, on a SiO_2 substrate.

The measurements were performed on a pristine Gr/Ir(111) sample [Fig. 4.21(a) shows a typical moiré pattern, inset — its atomically resolved image] and samples treated equivalently to the 1^{st} and the 3^{rd} hydrogenation steps in the ARPES experiment, i.e. low and high exposure. Already after low hydrogen exposure [Fig. 4.21(b)] one can see separate "donut"-like protrusions that correspond to locally hydrogenated sites in agreement with the literature [265]. High exposure in turn results in a very non-uniform surface topography with large and unevenly shaped hydrogen islands [dark areas in Fig. 4.21(c)]. Hydrogenated areas measured with a low bias voltage [Fig. 4.21(c)] appear dark, that indicates a reduced local density of states close to the Fermi level in agreement with the gapped Dirac cone observed by ARPES. It is also important to note that STM did not reveal any traces of filament material, confirming that its amounts are small.

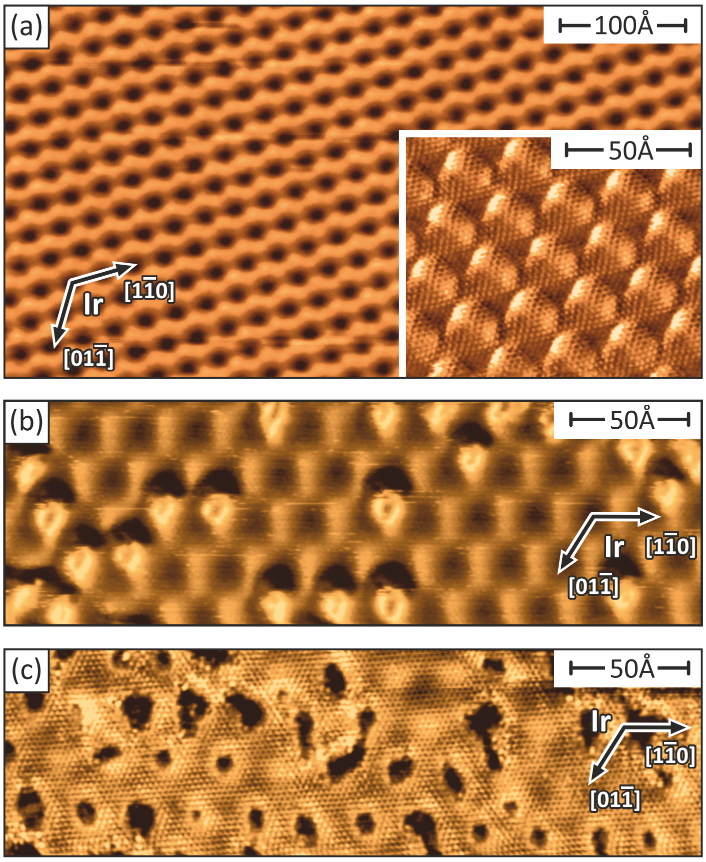

Figure 4.21: STM characterization of hydrogenated Gr/Ir(111). (a) Moiré pattern of pristine graphene/Ir(111) (inset – atomically resolved image). (b) After first hydrogenation, separate "donut"-like protrusion appear. (c) After third hydrogenation, the surface is inhomogeneously covered with hydrogen (black areas). I channel, tunneling parameters (I_t, U_b): (a) 0.45 nA, 0.1 V; inset to (a) 2.1 nA, 2 mV; (b) 0.4 nA, 0.4 V; (c) 0.4 nA, 2 mV.

At the same time with each step of hydrogenation the ScR features are gradually suppressed, while the details of their structure remain the same. After the 3^{rd} step of hydrogenation ScR nearly vanish everywhere except for very low kinetic energies. Interesting is that in contrast to the case of deposition of Ir clusters, NL and WL features disappear *simultaneously*. This indicates that the formation of ScR is disturbed by a different mechanism than the work function stability which should in the first place influence the visibility of NL. Another crucial factor for ScR formation is the long-range surface order that is responsible for the *elastic scattering* involved in the interference model. This order might be compromised by large areas rehybridized toward sp^3. This explanation is in line with the strong broadening observed in the valence band and is also confirmed by atomically-resolved STM data shown in Fig. 4.21(c). STM imaging reveals spatially disordered islands of hydrogen leading to a substantial lateral inhomogeneity of the moiré superpotential of graphene. Finally, hydrogenation can be thermally reversed at temperatures above 450°C, as it was demonstrated in Refs. [341, 342]. Indeed, after annealing at 740°C both Gr/Ir(111) band structure and the ScR features were recovered [Figs. 4.20(e,j) and Fig. 4.19, right]. This demonstrates that the suppression mechanism is directly related to hydrogenation.

4.5 Summary of conclusions

In this chapter we have studied scattering electron resonances as they occur in ARPES using graphene on a variety of substrates as a versatile model system. We start by presenting a detailed description of the unusual features observed in our ARPES experiments at low kinetic energies and prove their equivalence to the VLEED fine structure. The results are in a good qualitative agreement with the existing theory, as verified by our calculations in the framework of the interference model. All the main properties of ScR get a simple explanation in this model: the complex line shape with wide and narrow peaks, the overall geometry and robust free-electron-like parabolic dispersion. By a systematic study of graphene on a wide range of chemically differing substrates we demonstrate that the energy position of the resonances is in a direct relation to the magnitude of charge transfer between graphene and the substrate. This gives a key to control over the position of the resonances. Moreover, we have shown that the scattering resonances in Gr/Ir(111) can be *suppressed* by nanopatterning either by a superlattice of Ir nanoclusters or by atomic hydrogen. We attribute these effects to strong local variations of the work function accompanied by local $sp^2 \rightarrow sp^3$ rehybridization and/or destruction of long-range order of the graphene lattice. However, an unambiguous proof requires advanced theoretical analysis.

The possibilities of engineering the scattering resonances described in this chapter can be applied for optoelectronic devices based on graphene. However, ScR appear not only in graphene, but at all crystalline surfaces. The results of this study expand the general understanding of this phenomenon and are applicable to many other materials. They can help to obtain precise information about the structure and the surface potential barrier of the studied materials during the ARPES experiments.

The scattering resonances have been studied for five decades, but only now they become acknowledged in ARPES and there are plenty of open questions left for future research, such as the deviations from the behavior predicted by the interference model that are observed at very low kinetic energies; determination of exact ScR energy position for graphene on strongly interacting substrates; the possibility of replica-formation in ScR due to a strong superpotential (substrates with larger natural moiré corrugation of graphene can be tested, such as Ru(0001)); spin-dependent effects in ScR caused by a spin-polarized surface potential barrier in graphene on ferromagnetic materials.

The main results of this chapter were published in the journal Applied Physics Letters (Ref. [343]).

Bibliography

[1] K. S. Novoselov, A. K. Geim, S. V. Morozov, D. Jiang, Y. Zhang, S. V. Dubonos, I. V. Grigorieva, and A. A. Firsov, „Electric Field Effect in Atomically Thin Carbon Films“, *Science*, vol. 306, no. 5696, pp. 666–669, 2004 (cit. on pp. 1, 4, 41).

[2] L. Wang, I. Meric, P. Y. Huang, Q. Gao, Y. Gao, H. Tran, T. Taniguchi, K. Watanabe, L. M. Campos, D. A. Muller, J. Guo, P. Kim, J. Hone, K. L. Shepard, and C. R. Dean, „One-Dimensional Electrical Contact to a Two-Dimensional Material“, *Science*, vol. 342, no. 6158, pp. 614–617, 2013 (cit. on p. 1).

[3] S. Datta and B. Das, „Electronic analog of the electro-optic modulator“, *Applied Physics Letters*, vol. 56, no. 7, pp. 665–667, 1990 (cit. on pp. 2, 51).

[4] D. Marchenko, A. Varykhalov, M. R. Scholz, G. Bihlmayer, E. I. Rashba, A. Rybkin, A. M. Shikin, and O. Rader, „Giant Rashba Splitting in Graphene Due to Hybridization with Gold“, *Nature Communications*, vol. 3, p. 1232, 2012 (cit. on pp. 2, 18, 50–53, 56, 67, 69, 70, 81).

[5] C. L. Kane and E. J. Mele, „Quantum Spin Hall Effect in Graphene“, *Physical Review Letters*, vol. 95, no. 22, p. 226 801, 2005 (cit. on pp. 2, 11, 12, 15, 16, 50, 73).

[6] C. Weeks, J. Hu, J. Alicea, M. Franz, and R. Wu, „Engineering a Robust Quantum Spin Hall State in Graphene via Adatom Deposition“, *Physical Review X*, vol. 1, no. 2, p. 021 001, 2011 (cit. on pp. 2, 17, 73).

[7] P. R. Wallace, „The Band Theory of Graphite“, *Physical Review*, vol. 71, no. 9, pp. 622–634, 1947 (cit. on pp. 4, 6, 9).

[8] R. Peierls, „Quelques propriétés typiques des corps solides“, *Annales de l'institut Henri Poincaré*, vol. 5, no. 3, pp. 177–222, 1935 (cit. on p. 4).

[9] L. D. Landau, „On the theory of phase transitions“, *Zhurnal Eksperimental'noi i Teoreticheskoi Fiziki*, vol. 7, pp. 19–32, 1937 (cit. on p. 4).

[10] N. D. Mermin, „Crystalline Order in Two Dimensions“, *Physical Review*, vol. 176, no. 1, pp. 250–254, 1968 (cit. on p. 4).

[11] D. Nelson, T. Piran, and S. Weinberg, *Statistical Mechanics of Membranes and Surfaces*, 2nd. World Scientific, 2004 (cit. on p. 4).

[12] K. S. Novoselov, A. K. Geim, S. V. Morozov, D. Jiang, M. I. Katsnelson, I. V. Grigorieva, S. V. Dubonos, and A. A. Firsov, „Two-dimensional gas of massless Dirac fermions in graphene“, *Nature*, vol. 438, no. 7065, pp. 197–200, 2005 (cit. on p. 4).

[13] A. K. Geim and K. S. Novoselov, „The rise of graphene“, *Nature Materials*, vol. 6, no. 3, pp. 183–191, 2007 (cit. on p. 4).

[14] K. Novoselov, D. Jiang, F. Schedin, T. Booth, V. Khotkevich, S. Morozov, and A. Geim, „Two-dimensional atomic crystals“, *Proceedings of the National Academy of Sciences*, vol. 102, no. 30, pp. 10 451–10 453, 2005 (cit. on p. 4).

[15] C. Lee, X. Wei, J. W. Kysar, and J. Hone, „Measurement of the Elastic Properties and Intrinsic Strength of Monolayer Graphene“, *Science*, vol. 321, no. 5887, pp. 385–388, 2008 (cit. on p. 4).

[16] R. R. Nair, P. Blake, A. N. Grigorenko, K. S. Novoselov, T. J. Booth, T. Stauber, N. M. R. Peres, and A. K. Geim, „Fine Structure Constant Defines Visual Transparency of Graphene“, *Science*, vol. 320, no. 5881, pp. 1308–1308, 2008 (cit. on p. 4).

[17] F. Bonaccorso, Z. Sun, T. Hasan, and A. C. Ferrari, „Graphene photonics and optoelectronics“, *Nature Photonics*, vol. 4, p. 611, 2010 (cit. on p. 4).

[18] J. C. Meyer, A. K. Geim, M. I. Katsnelson, K. S. Novoselov, T. J. Booth, and S. Roth, „The structure of suspended graphene sheets“, *Nature*, vol. 446, no. 7131, pp. 60–63, 2007 (cit. on p. 5).

[19] J.-C. Charlier, P. C. Eklund, J. Zhu, and A. C. Ferrari, „Electron and Phonon Properties of Graphene: Their Relationship with Carbon Nanotubes“, in *Carbon Nanotubes: Advanced Topics in the Synthesis, Structure, Properties and Applications*, A. Jorio, G. Dresselhaus, and M. S. Dresselhaus, Eds., ser. Topics in Applied Physics. Berlin, Heidelberg: Springer, Berlin, Heidelberg, 2008, pp. 673–709 (cit. on p. 6).

[20] S. Reich, J. Maultzsch, C. Thomsen, and P. Ordejón, „Tight-binding description of graphene“, *Physical Review B*, vol. 66, no. 3, p. 035 412, 2002 (cit. on p. 8).

[21] L. Van Hove, „The Occurrence of Singularities in the Elastic Frequency Distribution of a Crystal“, *Physical Review*, vol. 89, no. 6, pp. 1189–1193, 1953 (cit. on p. 9).

[22] A. H. Castro Neto, F. Guinea, N. M. R. Peres, K. S. Novoselov, and A. K. Geim, „The electronic properties of graphene“, *Reviews of Modern Physics*, vol. 81, no. 1, pp. 109–162, 2009 (cit. on p. 9).

[23] P. A. M. Dirac, „The quantum theory of the electron“, *Proceedings of the Royal Society of London A: Mathematical, Physical and Engineering Sciences*, vol. 117, no. 778, pp. 610–624, 1928 (cit. on p. 10).

[24] T. O. Wehling, A. M. Black-Schaffer, and A. V. Balatsky, „Dirac materials“, *Advances in Physics*, vol. 63, no. 1, pp. 1–76, 2014 (cit. on p. 10).

[25] D. P. DiVincenzo and E. J. Mele, „Self-consistent effective-mass theory for intralayer screening in graphite intercalation compounds“, *Physical Review B*, vol. 29, pp. 1685–1694, 4 1984 (cit. on p. 10).

[26] G. W. Semenoff, „Condensed-Matter Simulation of a Three-Dimensional Anomaly“, *Physical Review Letters*, vol. 53, pp. 2449–2452, 26 1984 (cit. on p. 10).

[27] S. A. Wolf, D. D. Awschalom, R. A. Buhrman, J. M. Daughton, S. v. Molnár, M. L. Roukes, A. Y. Chtchelkanova, and D. M. Treger, „Spintronics: A Spin-Based Electronics Vision for the Future“, *Science*, vol. 294, no. 5546, pp. 1488–1495, 2001 (cit. on p. 11).

[28] I. Žutic, J. Fabian, and S. Das Sarma, „Spintronics: Fundamentals and applications“, *Reviews of Modern Physics*, vol. 76, no. 2, pp. 323–410, 2004 (cit. on p. 11).

[29] G. Dresselhaus and M. S. Dresselhaus, „Spin-Orbit Interaction in Graphite“, *Physical Review*, vol. 140, no. 1A, A401–A412, 1965 (cit. on p. 11).

[30] H. Min, J. E. Hill, N. A. Sinitsyn, B. R. Sahu, L. Kleinman, and A. H. MacDonald, „Intrinsic and Rashba spin-orbit interactions in graphene sheets“, *Physical Review B*, vol. 74, no. 16, p. 165 310, 2006 (cit. on pp. 12, 16).

[31] Y. A. Bychkov and E. Rashba, „Properties of a 2D electron gas with lifted spectral degeneracy“, *JETP Letters*, vol. 39, no. 2, p. 78, 1984 (cit. on pp. 12, 50).

[32] Y. A. Bychkov and E. I. Rashba, „Oscillatory effects and the magnetic susceptibility of carriers in inversion layers“, *Journal of Physics C: Solid State Physics*, vol. 17, no. 33, p. 6039, 1984 (cit. on p. 12).

[33] E. I. Rashba, „Graphene with Structure-Induced Spin-Orbit Coupling: Spin-Polarized States, Spin Zero Modes, and Quantum Hall Effect“, *Physical Review B*, vol. 79, no. 16, p. 161 409, 2009 (cit. on pp. 12, 15).

[34] L. L. Foldy and S. A. Wouthuysen, „On the Dirac Theory of Spin 1/2 Particles and Its Non-Relativistic Limit“, *Physical Review*, vol. 78, no. 1, pp. 29–36, 1950 (cit. on p. 12).

[35] L. H. Thomas, „The Motion of the Spinning Electron“, *Nature*, vol. 117, no. 2945, p. 514, 1926 (cit. on p. 12).

[36] G. Bihlmayer, Y. M. Koroteev, P. M. Echenique, E. V. Chulkov, and S. Blugel, „The Rashba-effect at metallic surfaces“, *Surface Science*, Berlin, Germany: 4–9 September 2005, vol. 600, no. 18, pp. 3888–3891, 2006 (cit. on pp. 13, 15).

[37] S. LaShell, B. A. McDougall, and E. Jensen, „Spin Splitting of an Au(111) Surface State Band Observed with Angle Resolved Photoelectron Spectroscopy“, *Physical Review Letters*, vol. 77, no. 16, pp. 3419–3422, 1996 (cit. on p. 14).

[38] M. Hoesch, M. Muntwiler, V. N. Petrov, M. Hengsberger, L. Patthey, M. Shi, M. Falub, T. Greber, and J. Osterwalder, „Spin structure of the Shockley surface state on Au(111)“, *Physical Review B*, vol. 69, no. 24, p. 241 401, 2004 (cit. on p. 14).

[39] C. R. Ast, J. Henk, A. Ernst, L. Moreschini, M. C. Falub, D. Pacile, P. Bruno, K. Kern, and M. Grioni, „Giant Spin Splitting through Surface Alloying“, *Physical Review Letters*, vol. 98, no. 18, p. 186 807, 2007 (cit. on p. 14).

[40] A. Varykhalov, D. Marchenko, M. R. Scholz, E. D. L. Rienks, T. K. Kim, G. Bihlmayer, J. Sánchez-Barriga, and O. Rader, „Ir(111) Surface State with Giant Rashba Splitting Persists under Graphene in Air“, *Physical Review Letters*, vol. 108, no. 6, p. 066 804, 2012 (cit. on pp. 14, 85, 104).

[41] A. Tamai, W. Meevasana, P. D. C. King, C. W. Nicholson, A. de la Torre, E. Rozbicki, and F. Baumberger, „Spin-orbit splitting of the Shockley surface state on Cu(111)“, *Physical Review B*, vol. 87, no. 7, p. 075 113, 2013 (cit. on p. 14).

[42] J. Nitta, T. Akazaki, H. Takayanagi, and T. Enoki, „Gate Control of Spin-Orbit Interaction in an Inverted $\mathrm{In}_{0.53}\mathrm{Ga}_{0.47}\mathrm{As}/\mathrm{In}_{0.52}\mathrm{Al}_{0.48}\mathrm{As}$ Heterostructure“, *Physical Review Letters*, vol. 78, no. 7, pp. 1335–1338, 1997 (cit. on p. 14).

[43] Y. Ho Park, H.-j. Kim, J. Chang, S. Hee Han, J. Eom, H.-J. Choi, and H. Cheol Koo, „Separation of Rashba and Dresselhaus spin-orbit interactions using crystal direction dependent transport measurements“, *Applied Physics Letters*, vol. 103, no. 25, p. 252 407, 2013 (cit. on p. 14).

[44] L. Petersen and P. Hedegard, „A simple tight-binding model of spin-orbit splitting of sp-derived surface states“, *Surface Science*, vol. 459, no. 1, pp. 49–56, 2000 (cit. on p. 15).

[45] M. Gmitra, S. Konschuh, C. Ertler, C. Ambrosch-Draxl, and J. Fabian, „Band-Structure Topologies of Graphene: Spin-Orbit Coupling Effects from First Principles“, *Physical Review B*, vol. 80, no. 23, p. 235 431, 2009 (cit. on pp. 16, 96, 98).

[46] J. C. Boettger and S. B. Trickey, „First-principles calculation of the spin-orbit splitting in graphene“, *Physical Review B*, vol. 75, no. 12, p. 121 402, 2007 (cit. on p. 16).

[47] J. Zhou, Q. Liang, and J. Dong, „Enhanced spin-orbit coupling in hydrogenated and fluorinated graphene“, *Carbon*, vol. 48, no. 5, pp. 1405–1409, 2010 (cit. on p. 17).

[48] A. H. Castro Neto and F. Guinea, „Impurity-Induced Spin-Orbit Coupling in Graphene“, *Physical Review Letters*, vol. 103, no. 2, p. 026 804, 2009 (cit. on p. 17).

[49] J. Balakrishnan, G. K. W. Koon, M. Jaiswal, A. H. C. Neto, and B. Ozyilmaz, „Colossal enhancement of spin-orbit coupling in weakly hydrogenated graphene“, *Nature Physics*, vol. 9, no. 5, pp. 284–287, 2013 (cit. on p. 17).

[50] D. Ma, Z. Li, and Z. Yang, „Strong spin-orbit splitting in graphene with adsorbed Au atoms“, *Carbon*, vol. 50, no. 1, pp. 297–305, 2012 (cit. on p. 17).

[51] J. Hu, J. Alicea, R. Wu, and M. Franz, „Giant Topological Insulator Gap in Graphene with 5*d* Adatoms“, *Physical Review Letters*, vol. 109, no. 26, p. 266 801, 2012 (cit. on p. 17).

[52] Y. Li, P. Tang, P. Chen, J. Wu, B.-L. Gu, Y. Fang, S. B. Zhang, and W. Duan, „Topological insulators in transition-metal intercalated graphene: The role of d electrons in significantly increasing the spin-orbit gap“, *Physical Review B*, vol. 87, no. 24, p. 245 127, 2013 (cit. on p. 17).

[53] I. I. Klimovskikh, M. M. Otrokov, V. Y. Voroshnin, D. Sostina, L. Petaccia, G. Di Santo, S. Thakur, E. V. Chulkov, and A. M. Shikin, „Spin-Orbit Coupling Induced Gap in Graphene on Pt(111) with Intercalated Pb Monolayer“, *ACS Nano*, vol. 11, no. 1, pp. 368–374, 2017 (cit. on p. 17).

[54] F. Calleja, H. Ochoa, M. Garnica, S. Barja, J. J. Navarro, A. Black, M. M. Otrokov, E. V. Chulkov, A. Arnau, A. L. V. d. Parga, F. Guinea, and R. Miranda, „Spatial variation of a giant spin-orbit effect induces electron confinement in graphene on Pb islands“, *Nature Physics*, vol. 11, no. 1, pp. 43–47, 2015 (cit. on p. 17).

[55] L. Brey, „Spin-orbit coupling in graphene induced by adatoms with outer-shell p orbitals“, *Physical Review B*, vol. 92, no. 23, p. 235 444, 2015 (cit. on p. 17).

[56] A. Avsar, J. Y. Tan, T. Taychatanapat, J. Balakrishnan, G. K. W. Koon, Y. Yeo, J. Lahiri, A. Carvalho, A. S. Rodin, E. C. T. O'Farrell, G. Eda, A. H. Castro Neto, and B. Özyilmaz, „Spin–Orbit Proximity Effect in Graphene“, *Nature Communications*, vol. 5, p. 4875, 2014 (cit. on p. 18).

[57] D. Marchenko, J. Sánchez-Barriga, M. R. Scholz, O. Rader, and A. Varykhalov, „Spin Splitting of Dirac Fermions in Aligned and Rotated Graphene on Ir(111)“, *Physical Review B*, vol. 87, no. 11, p. 115 426, 2013 (cit. on pp. 18, 42, 51, 79, 81, 86).

[58] A. M. Shikin, A. G. Rybkin, D. Marchenko, A. A. Rybkina, M. R. Scholz, Oliver Rader, and A. Varykhalov, „Induced Spin–Orbit Splitting in Graphene: The Role of Atomic Number of the Intercalated Metal and π–d Hybridization“, *New Journal of Physics*, vol. 15, no. 1, p. 013 016, 2013 (cit. on pp. 18, 51, 81).

[59] A. Varykhalov, J. Sánchez-Barriga, D. Marchenko, P. Hlawenka, P. S. Mandal, and O. Rader, „Tunable Fermi Level and Hedgehog Spin Texture in Gapped Graphene“, *Nature Communications*, vol. 6, p. 7610, 2015 (cit. on pp. 18, 44, 51, 69, 96).

[60] E. V. Zhizhin, A. Varykhalov, A. G. Rybkin, A. A. Rybkina, D. A. Pudikov, D. Marchenko, J. Sanchez-Barriga, I. I. Klimovskikh, G. G. Vladimirov, O. Rader, and A. M. Shikin, „Spin splitting of Dirac fermions in graphene on Ni intercalated with alloy of Bi and Au“, *Carbon*, vol. 93, pp. 984–996, 2015 (cit. on pp. 18, 51, 81).

[61] E. C. T. O'Farrell, J. Y. Tan, Y. Yeo, G. K. W. Koon, B. Özyilmaz, K. Watanabe, and T. Taniguchi, „Rashba Interaction and Local Magnetic Moments in a Graphene-BN Heterostructure Intercalated with Au“, *Phys. Rev. Lett.*, vol. 117, p. 076 603, 7 2016 (cit. on pp. 18, 51).

[62] D. Marchenko, A. Varykhalov, J. Sánchez-Barriga, T. Seyller, and O. Rader, „Rashba splitting of 100 meV in Au-intercalated graphene on SiC“, *Applied Physics Letters*, vol. 108, no. 17, p. 172 405, 2016 (cit. on pp. 18, 51).

[63] H. Hertz, „Über einen Einfluss des ultravioletten Lichtes auf die electrische Entladung“, *Annalen der Physik*, vol. 267, no. 8, pp. 983–1000, 1887 (cit. on p. 18).

[64] A. Einstein, „Über einen die Erzeugung und Verwandlung des Lichtes betreffenden heuristischen Gesichtspunkt“, *Annalen der Physik*, vol. 322, no. 6, pp. 132–148, 1905 (cit. on p. 18).

[65] S. Hüfner, *Photoelectron spectroscopy: principles and applications.* Springer, Berlin, Heidelberg, 2003 (cit. on pp. 19, 83, 104).

[66] P. D. Innes, „On the Velocity of the Cathode Particles Emitted by Various Metals under the Influence of Röntgen Rays, and Its Bearing on the Theory of Atomic Disintegration“, *Proceedings of the Royal Society of London. Series A, Containing Papers of a Mathematical and Physical Character*, vol. 79, no. 532, pp. 442–462, 1907 (cit. on p. 19).

[67] H. Robinson and W. F. Rawlinson, „The magnetic spectrum of the β rays excited in metals by soft X rays“, *The London, Edinburgh, and Dublin Philosophical Magazine and Journal of Science*, vol. 28, no. 164, pp. 277–281, 1914 (cit. on p. 19).

[68] C. N. Berglund and W. E. Spicer, „Photoemission Studies of Copper and Silver: Theory“, *Physical Review*, vol. 136, no. 4A, A1030–A1044, 1964 (cit. on pp. 19, 22).

[69] A. Damascelli, Z. Hussain, and Z.-X. Shen, „Angle-resolved photoemission studies of the cuprate superconductors“, *Reviews of Modern Physics*, vol. 75, no. 2, pp. 473–541, 2003 (cit. on pp. 19, 27).

[70] L. D. Landau and E. M. Lifshitz, *Quantum Mechanics: Nonrelativistic Theory.* Pergamon Press, Oxford, 1977, vol. 3 (cit. on p. 20).

[71] J. J. Sakurai and J. Napolitano, *Modern quantum mechanics.* Addison-Wesley, 2011 (cit. on p. 20).

[72] J. B. Pendry, „Theory of photoemission“, *Surface Science*, vol. 57, no. 2, pp. 679–705, 1976 (cit. on p. 20).

[73] P. J. Feibelman, „Self-Consistent Calculation of the Surface Photoelectric Effect“, *Physical Review Letters*, vol. 34, no. 17, pp. 1092–1095, 1975 (cit. on p. 20).

[74] B. Feuerbacher, B. Fitton, and R. Willis, *Photoemission and the electronic properties of surfaces.* Wiley, 1978 (cit. on p. 20).

[75] R. Schlaf, „Calibration of photoemission spectra and work function determination“, *Online: http://rsl.eng.usf.edu/Documents/Tutorials/PEScalibration.pdf*, 2014 (cit. on pp. 22, 23).

[76] J. C. Vickerman and I. S. Gilmore, *Surface Analysis: The Principal Techniques, 2^{nd} Edition.* John Wiley & Sons, 2009 (cit. on p. 22).

[77] M. P. Seah and W. A. Dench, „Quantitative electron spectroscopy of surfaces: A standard data base for electron inelastic mean free paths in solids“, *Surface and Interface Analysis*, vol. 1, no. 1, pp. 2–11, 1979 (cit. on pp. 22, 24).

[78] S. Tanuma, C. J. Powell, and D. R. Penn, „Calculations of electron inelastic mean free paths. IX. Data for 41 elemental solids over the 50 eV to 30 keV range“, *Surface and Interface Analysis*, vol. 43, no. 3, pp. 689–713, 2011 (cit. on pp. 23, 24).

[79] S. Hagström, C. Nordling, and K. Siegbahn, „Electron spectroscopy for chemical analyses“, *Physics Letters*, vol. 9, no. 3, pp. 235–236, 1964 (cit. on p. 23).

[80] A. Damascelli, „Probing the Electronic Structure of Complex Systems by ARPES“, *Physica Scripta*, vol. T109, p. 61, 2004 (cit. on p. 25).

[81] G. Rickayzen, *Green's Functions and Condensed Matter*, ser. Dover Books on Physics. Dover Publications, 2013 (cit. on pp. 26, 27).

[82] J. S. Toll, „Causality and the Dispersion Relation: Logical Foundations“, *Physical Review*, vol. 104, pp. 1760–1770, 6 1956 (cit. on p. 27).

[83] M. R. Norman, H. Ding, H. Fretwell, M. Randeria, and J. C. Campuzano, „Extraction of the electron self-energy from angle-resolved photoemission data: Application to $\mathrm{Bi_2Sr_2CaCu_2O_{8+x}}$“, *Physical Review B*, vol. 60, pp. 7585–7590, 10 1999 (cit. on p. 27).

[84] B. Wannberg, „Electron optics development for photo-electron spectrometers“, *Nuclear Instruments and Methods in Physics Research Section A: Accelerators, Spectrometers, Detectors and Associated Equipment*, Special issue in honour of Prof. Kai Siegbahn, vol. 601, no. 1, pp. 182–194, 2009 (cit. on pp. 27–30).

[85] J. L. Wiza, „Multi-Channel-Plate Detector“, *Nuclear Instruments & Methods*, vol. 126, pp. 587–601, 1979 (cit. on p. 28).

[86] T. Zouros and E. Benis, „The hemispherical deflector analyser revisited. I. Motion in the ideal 1/r potential, generalized entry conditions, Kepler orbits and spectrometer basic equation“, *Journal of Electron Spectroscopy and Related Phenomena*, vol. 125, no. 3, pp. 221–248, 2002 (cit. on p. 28).

[87] J. Osterwalder, „Spin-Polarized Photoemission“, in *Magnetism: A Synchrotron Radiation Approach*, E. Beaurepaire, H. Bulou, F. Scheurer, and J.-P. Kappler, Eds. Berlin, Heidelberg: Springer Berlin Heidelberg, 2006, pp. 95–120 (cit. on pp. 31, 32).

[88] D. T. Pierce, R. J. Celotta, G.-C. Wang, W. N. Unertl, A. Galejs, C. E. Kuyatt, and S. R. Mielczarek, „The GaAs spin polarized electron source“, *Review of Scientific Instruments*, vol. 51, no. 4, pp. 478–499, 1980 (cit. on p. 31).

[89] J. Sánchez-Barriga, A. Varykhalov, J. Braun, S.-Y. Xu, N. Alidoust, O. Kornilov, J. Minár, K. Hummer, G. Springholz, G. Bauer, *et al.*, „Photoemission of $\mathrm{Bi_2\,Se_3}$ with Circularly Polarized Light: Probe of Spin Polarization or Means for Spin Manipulation?“, *Physical Review X*, vol. 4, no. 1, p. 011 046, 2014 (cit. on p. 31).

[90] M. Z. Hasan and C. L. Kane, „Colloquium: Topological insulators“, *Reviews of Modern Physics*, vol. 82, pp. 3045–3067, 4 2010 (cit. on p. 31).

[91] W. Gerlach and O. Stern, „Der experimentelle Nachweis der Richtungsquantelung im Magnetfeld“, *Zeitschrift für Physik*, vol. 9, no. 1, pp. 349–352, 1922 (cit. on p. 31).

[92] J. Kessler, *Polarized Electrons*, ser. Springer Series on Atomic, Optical, and Plasma Physics. Springer, 1985 (cit. on pp. 31–33).

[93] G. H. Rutherford and R. Grobe, „Comment on "Stern-Gerlach Effect for Electron Beams"“, *Physical Review Letters*, vol. 81, pp. 4772–4772, 21 1998 (cit. on p. 31).

[94] N. F. Mott, „The scattering of fast electrons by atomic nuclei“, *Proceedings of the Royal Society of London A: Mathematical, Physical and Engineering Sciences*, vol. 124, no. 794, pp. 425–442, 1929 (cit. on pp. 31, 32).

[95] T. Okuda, Y. Takeichi, Y. Maeda, A. Harasawa, I. Matsuda, T. Kinoshita, and A. Kakizaki, „A new spin-polarized photoemission spectrometer with very high efficiency and energy resolution“, *Review of Scientific Instruments*, vol. 79, no. 12, p. 123 117, 2008 (cit. on p. 31).

[96] A. Winkelmann, D. Hartung, H. Engelhard, C.-T. Chiang, and J. Kirschner, „High efficiency electron spin polarization analyzer based on exchange scattering at Fe/W(001)“, *Review of Scientific Instruments*, vol. 79, no. 8, p. 083 303, 2008 (cit. on p. 31).

[97] J. Kirschner and R. Feder, „Spin Polarization in Double Diffraction of Low-Energy Electrons from W(001): Experiment and Theory“, *Physical Review Letters*, vol. 42, pp. 1008–1011, 15 1979 (cit. on p. 31).

[98] C. Tusche, M. Ellguth, A. A. Ünal, C.-T. Chiang, A. Winkelmann, A. Krasyuk, M. Hahn, G. Schönhense, and J. Kirschner, „Spin resolved photoelectron microscopy using a two-dimensional spin-polarizing electron mirror“, *Applied Physics Letters*, vol. 99, no. 3, p. 032 505, 2011 (cit. on p. 31).

[99] D. Pierce, R. Celotta, M. Kelley, and J. Unguris, „Electron spin polarization analyzers for use with synchrotron radiation“, *Nuclear Instruments and Methods in Physics Research Section A: Accelerators, Spectrometers, Detectors and Associated Equipment*, vol. 266, no. 1, pp. 550–559, 1988 (cit. on p. 32).

[100] C. G. Shull, C. T. Chase, and F. E. Myers, „Electron Polarization“, *Physical Review*, vol. 63, pp. 29–37, 1-2 1943 (cit. on p. 32).

[101] G. Busch, M. Campagna, P. Cotti, and H. C. Siegmann, „Observation of Electron Polarization in Photoemission“, *Physical Review Letters*, vol. 22, pp. 597–600, 12 1969 (cit. on p. 32).

[102] N. Sherman and D. F. Nelson, „Determination of Electron Polarization by Means of Mott Scattering“, *Physical Review*, vol. 114, pp. 1541–1542, 6 1959 (cit. on p. 33).

[103] L. Mikaelyan, A. Borovoi, and E. Denisov, „Double Mott scattering of electrons“, *Nuclear Physics*, vol. 47, pp. 328–337, 1963 (cit. on p. 33).

[104] G. Binnig, H. Rohrer, C. Gerber, and E. Weibel, „Surface Studies by Scanning Tunneling Microscopy“, *Physical Review Letters*, vol. 49, no. 1, pp. 57–61, 1982 (cit. on p. 34).

[105] G. Binnig and H. Rohrer, „Scanning tunneling microscopy“, *Surface Science*, vol. 126, no. 1, pp. 236–244, 1983 (cit. on p. 34).

[106] G. Binnig and H. Rohrer, „Scanning tunneling microscopy–from birth to adolescence“, *Reviews of Modern Physics*, vol. 59, no. 3, pp. 615–625, 1987 (cit. on p. 34).

[107] R. Wiesendanger and K. Von Klitzing, *Scanning Probe Microscopy: Analytical Methods*, ser. NanoScience and Technology. Springer, 1998 (cit. on p. 34).

[108] C. J. Chen, *Introduction to scanning tunneling microscopy.* Oxford University Press on Demand, 1993, vol. 4 (cit. on pp. 35, 37).

[109] J. Bardeen, „Tunnelling from a Many-Particle Point of View“, *Physical Review Letters*, vol. 6, pp. 57–59, 2 1961 (cit. on p. 36).

[110] R. Wiesendanger and W. Roland, *Scanning Probe Microscopy and Spectroscopy: Methods and Applications*, ser. Scanning Probe Microscopy and Spectroscopy: Methods and Applications. Cambridge University Press, 1994 (cit. on p. 36).

[111] C. J. Chen, „Origin of atomic resolution on metal surfaces in scanning tunneling microscopy“, *Physical Review Letters*, vol. 65, pp. 448–451, 4 1990 (cit. on pp. 36, 37).

[112] J. Tersoff and D. R. Hamann, „Theory and Application for the Scanning Tunneling Microscope“, *Physical Review Letters*, vol. 50, pp. 1998–2001, 25 1983 (cit. on p. 36).

[113] J. Tersoff and D. R. Hamann, „Theory of the scanning tunneling microscope“, *Physical Review B*, vol. 31, pp. 805–813, 2 1985 (cit. on p. 36).

[114] C. J. Chen, „Tunneling matrix elements in three-dimensional space: The derivative rule and the sum rule“, *Physical Review B*, vol. 42, pp. 8841–8857, 14 1990 (cit. on p. 37).

[115] L. Gross, N. Moll, F. Mohn, A. Curioni, G. Meyer, F. Hanke, and M. Persson, „High-Resolution Molecular Orbital Imaging Using a p-Wave STM Tip“, *Physical Review Letters*, vol. 107, no. 8, p. 086 101, 2011 (cit. on p. 37).

[116] E. A. Wood, „Vocabulary of Surface Crystallography“, *Journal of Applied Physics*, vol. 35, no. 4, pp. 1306–1312, 1964 (cit. on p. 39).

[117] R. L. Park and H. H. Madden, „Annealing changes on the (100) surface of palladium and their effect on CO adsorption“, *Surface Science*, vol. 11, no. 2, pp. 188–202, 1968 (cit. on p. 39).

[118] A. S. Mayorov, R. V. Gorbachev, S. V. Morozov, L. Britnell, R. Jalil, L. A. Ponomarenko, P. Blake, K. S. Novoselov, K. Watanabe, T. Taniguchi, and A. K. Geim, „Micrometer-Scale Ballistic Transport in Encapsulated Graphene at Room Temperature“, *Nano Letters*, vol. 11, no. 6, pp. 2396–2399, 2011, PMID: 21574627 (cit. on p. 41).

[119] K. Parvez, S. Yang, X. Feng, and K. Müllen, „Exfoliation of graphene via wet chemical routes“, *Synthetic Metals*, vol. 210, pp. 123–132, 2015, Reviews of Current Advances in Graphene Science and Technology (cit. on p. 41).

[120] K. V. Emtsev, A. Bostwick, K. Horn, J. Jobst, G. L. Kellogg, L. Ley, J. L. McChesney, T. Ohta, S. A. Reshanov, J. Röhrl, E. Rotenberg, A. K. Schmid, D. Waldmann, H. B. Weber, and T. Seyller, „Towards wafer-size graphene layers by atmospheric pressure graphitization of silicon carbide“, *Nature Materials*, vol. 8, no. 3, pp. 203–207, 2009 (cit. on pp. 41, 123).

[121] B. Deng, Z. Liu, and H. Peng, „Toward Mass Production of CVD Graphene Films“, *Advanced Materials*, vol. 0, no. 0, p. 1 800 996, 2018 (cit. on p. 41).

[122] A. V. Bommel, J. Crombeen, and A. V. Tooren, „LEED and Auger electron observations of the SiC(0001) surface“, *Surface Science*, vol. 48, no. 2, pp. 463–472, 1975 (cit. on p. 41).

[123] A. E. Karu and M. Beer, „Pyrolytic Formation of Highly Crystalline Graphite Films“, *Journal of Applied Physics*, vol. 37, no. 5, pp. 2179–2181, 1966 (cit. on p. 41).

[124] C. Oshima and A. Nagashima, „Ultra-thin epitaxial films of graphite and hexagonal boron nitride on solid surfaces“, *Journal of Physics: Condensed Matter*, vol. 9, no. 1, p. 1, 1997 (cit. on pp. 41, 43).

[125] N. R. Gall’, E. V. Rut’kov, and A. Y. Tontegode, „Two Dimensional Graphite Films on Metals and Their Intercalation“, *International Journal of Modern Physics B*, vol. 11, no. 16, pp. 1865–1911, 1997 (cit. on pp. 41–43).

[126] X. Li, W. Cai, L. Colombo, and R. S. Ruoff, „Evolution of Graphene Growth on Ni and Cu by Carbon Isotope Labeling“, *Nano Letters*, vol. 9, no. 12, pp. 4268–4272, 2009, PMID: 19711970 (cit. on p. 41).

[127] X. Li, W. Cai, J. An, S. Kim, J. Nah, D. Yang, R. Piner, A. Velamakanni, I. Jung, E. Tutuc, S. K. Banerjee, L. Colombo, and R. S. Ruoff, „Large-Area Synthesis of High-Quality and Uniform Graphene Films on Copper Foils“, *Science*, vol. 324, no. 5932, pp. 1312–1314, 2009 (cit. on p. 42).

[128] J. Shelton, H. Patil, and J. Blakely, „Equilibrium segregation of carbon to a nickel (111) surface: A surface phase transition“, *Surface Science*, vol. 43, no. 2, pp. 493–520, 1974 (cit. on p. 42).

[129] M. Eizenberg and J. Blakely, „Carbon monolayer phase condensation on Ni(111)“, *Surface Science*, vol. 82, no. 1, pp. 228–236, 1979 (cit. on p. 42).

[130] A. Y. Tontegode, „Carbon on Transition Metal Surfaces“, *Progress in Surface Science*, vol. 38, no. 3, pp. 201–429, 1991 (cit. on p. 42).

[131] S. Nie, A. L. Walter, N. C. Bartelt, E. Starodub, A. Bostwick, E. Rotenberg, and K. F. McCarty, „Growth from below: Graphene Bilayers on Ir (111)“, *ACS Nano*, vol. 5, no. 3, pp. 2298–2306, 2011 (cit. on p. 42).

[132] T. Wu, X. Zhang, Q. Yuan, J. Xue, G. Lu, Z. Liu, H. Wang, H. Wang, F. Ding, Q. Yu, X. Xie, and M. Jiang, „Fast growth of inch-sized single-crystalline graphene from a controlled single nucleus on Cu–Ni alloys“, *Nature Materials*, vol. 15, no. 1, pp. 43–47, 2016 (cit. on p. 42).

[133] Y. Gamo, A. Nagashima, M. Wakabayashi, M. Terai, and C. Oshima, „Atomic Structure of Monolayer Graphite Formed on Ni (111)“, *Surface Science*, vol. 374, no. 1, pp. 61–64, 1997 (cit. on pp. 42, 54).

[134] A. Shikin, V. Adamchuk, and K.-H. Rieder, „Formation of Quasi-Free Graphene on the Ni (111) Surface with Intercalated Cu, Ag, and Au Layers“, *Physics of the Solid State*, vol. 51, no. 11, pp. 2390–2400, 2009 (cit. on pp. 42, 43).

[135] A. Varykhalov, D. Marchenko, J. Sánchez-Barriga, M. R. Scholz, B. Verberck, B. Trauzettel, T. O. Wehling, C. Carbone, and O. Rader, „Intact Dirac Cones at Broken Sublattice Symmetry: Photoemission Study of Graphene on Ni and Co“, *Physical Review X*, vol. 2, no. 4, p. 041 017, 2012 (cit. on pp. 42, 69, 92, 98, 129).

[136] A. Grüneis and D. V. Vyalikh, „Tunable Hybridization between Electronic States of Graphene and a Metal Surface“, *Physical Review B*, vol. 77, no. 19, p. 193 401, 2008 (cit. on pp. 42, 43).

[137] A. Varykhalov and O. Rader, „Graphene Grown on Co(0001) Films and Islands: Electronic Structure and Its Precise Magnetization Dependence“, *Physical Review B*, vol. 80, no. 3, p. 035 437, 2009 (cit. on p. 42).

[138] D. Usachov, A. Fedorov, M. M. Otrokov, A. Chikina, O. Vilkov, A. Petukhov, A. G. Rybkin, Y. M. Koroteev, E. V. Chulkov, V. K. Adamchuk, *et al.*, „Observation of Single-Spin Dirac Fermions at the Graphene/Ferromagnet Interface“, *Nano Letters*, vol. 15, no. 4, pp. 2396–2401, 2015 (cit. on pp. 42, 50).

[139] D. Eom, D. Prezzi, K. T. Rim, H. Zhou, M. Lefenfeld, S. Xiao, C. Nuckolls, M. S. Hybertsen, T. F. Heinz, and G. W. Flynn, „Structure and Electronic Properties of Graphene Nanoislands on Co (0001)“, *Nano Letters*, vol. 9, no. 8, pp. 2844–2848, 2009 (cit. on p. 42).

[140] I. Pletikosić, M. Kralj, P. Pervan, R. Brako, J. Coraux, A. T. N'Diaye, C. Busse, and T. Michely, „Dirac Cones and Minigaps for Graphene on Ir(111)“, *Physical Review Letters*, vol. 102, no. 5, p. 056 808, 2009 (cit. on pp. 42, 50, 79, 90).

[141] S. Rusponi, M. Papagno, P. Moras, S. Vlaic, M. Etzkorn, P. Sheverdyaeva, D. Pacilé, H. Brune, and C. Carbone, „Highly Anisotropic Dirac Cones in Epitaxial Graphene Modulated by an Island Superlattice“, *Physical Review Letters*, vol. 105, no. 24, p. 246 803, 2010 (cit. on pp. 42, 50, 79, 86, 132).

[142] P. Sutter, J. T. Sadowski, and E. Sutter, „Graphene on Pt(111): Growth and substrate interaction“, *Physical Review B*, vol. 80, p. 245 411, 24 2009 (cit. on p. 42).

[143] J. Sun, Y. Nam, N. Lindvall, M. T. Cole, K. B. Teo, Y. W. Park, and A. Yurgens, „Growth Mechanism of Graphene on Platinum: Surface Catalysis and Carbon Segregation“, *Applied Physics Letters*, vol. 104, no. 15, p. 152 107, 2014 (cit. on p. 42).

[144] P. W. Sutter, J.-I. Flege, and E. A. Sutter, „Epitaxial Graphene on Ruthenium“, *Nature Materials*, vol. 7, no. 5, pp. 406–411, 2008 (cit. on p. 42).

[145] E. Sutter, D. Acharya, J. Sadowski, and P. Sutter, „Scanning Tunneling Microscopy on Epitaxial Bilayer Graphene on Ruthenium (0001)“, *Applied Physics Letters*, vol. 94, no. 13, p. 133 101, 2009 (cit. on p. 42).

[146] D. Castner, B. Sexton, and G. Somorjai, „LEED and thermal desorption studies of small molecules (H_2, O_2, CO, CO_2, NO, C_2H_4, C_2H_2 and C) chemisorbed on the rhodium (111) and (100) surfaces“, *Surface Science*, vol. 71, no. 3, pp. 519–540, 1978 (cit. on p. 42).

[147] A. B. Preobrajenski, M. L. Ng, A. S. Vinogradov, and N. Mårtensson, „Controlling graphene corrugation on lattice-mismatched substrates“, *Physical Review B*, vol. 78, p. 073 401, 7 2008 (cit. on p. 42).

[148] N. R. Gall’, S. N. Mikhajlov, E. V. Rut’kov, and A. Y. Tontegode, „Study of structure and properties of graphite monolayer on rhenium“, *Zhurnal Tekhnicheskoj Fiziki*, vol. 56, no. 4, pp. 732–737, 1986 (cit. on p. 42).

[149] E. Miniussi, M. Pozzo, A. Baraldi, E. Vesselli, R. R. Zhan, G. Comelli, T. O. Mente ş, M. A. Niño, A. Locatelli, S. Lizzit, and D. Alfè, „Thermal Stability of Corrugated Epitaxial Graphene Grown on Re(0001)“, *Physical Review Letters*, vol. 106, p. 216 101, 21 2011 (cit. on p. 42).

[150] N. A. Vinogradov, A. Zakharov, V. Kocevski, J. Rusz, K. Simonov, O. Eriksson, A. Mikkelsen, E. Lundgren, A. Vinogradov, N. Mårtensson, *et al.*, „Formation and Structure of Graphene Waves on Fe (110)“, *Physical Review Letters*, vol. 109, no. 2, p. 026 101, 2012 (cit. on p. 42).

[151] Y. Xue, B. Wu, Y. Guo, L. Huang, L. Jiang, J. Chen, D. Geng, Y. Liu, W. Hu, and G. Yu, „Synthesis of Large-Area, Few-Layer Graphene on Iron Foil by Chemical Vapor Deposition“, *Nano Research*, vol. 4, no. 12, pp. 1208–1214, 2011 (cit. on p. 42).

[152] T. Aizawa, R. Souda, S. Otani, Y. Ishizawa, and C. Oshima, „Bond softening in monolayer graphite formed on transition-metal carbide surfaces“, *Physical Review B*, vol. 42, pp. 11 469–11 478, 18 1990 (cit. on p. 43).

[153] E. Y. Kataev, D. Y. Usachov, A. S. Frolov, A. A. Rulev, A. A. Volykhov, A. Y. Kozmenkova, M. Krivenkov, D. Marchenko, A. Varykhalov, M. V. Kuznetsov, *et al.*, „Native and graphene-coated flat and stepped surfaces of TiC“, *Carbon*, vol. 132, pp. 656–666, 2018 (cit. on pp. 43, 123).

[154] M. Batzill, „The surface science of graphene: Metal interfaces, CVD synthesis, nanoribbons, chemical modifications, and defects“, *Surface Science Reports*, vol. 67, no. 3–4, pp. 83–115, 2012 (cit. on pp. 43, 50).

[155] A. Varykhalov, M. R. Scholz, T. K. Kim, and O. Rader, „Effect of Noble-Metal Contacts on Doping and Band Gap of Graphene“, *Physical Review B*, vol. 82, no. 12, p. 121 101, 2010 (cit. on pp. 43, 50).

[156] C. Enderlein, Y. Kim, A. Bostwick, E. Rotenberg, and K. Horn, „The Formation of an Energy Gap in Graphene on Ruthenium by Controlling the Interface“, *New Journal of Physics*, vol. 12, no. 3, p. 033 014, 2010 (cit. on pp. 43, 50).

[157] A. Varykhalov, J. Sanchez-Barriga, A. M. Shikin, C. Biswas, E. Vescovo, A. Rybkin, D. Marchenko, and O. Rader, „Electronic and Magnetic Properties of Quasifreestanding Graphene on Ni“, *Physical Review Letters*, vol. 101, no. 15, p. 157 601, 2008 (cit. on pp. 43, 51, 53, 56, 69).

[158] Y. S. Dedkov, A. M. Shikin, V. K. Adamchuk, S. L. Molodtsov, C. Laubschat, A. Bauer, and G. Kaindl, „Intercalation of copper underneath a monolayer of graphite on Ni(111)“, *Physical Review B*, vol. 64, p. 035 405, 3 2001 (cit. on p. 43).

[159] S. Forti, A. Stöhr, A. A. Zakharov, C. Coletti, K. V. Emtsev, and U. Starke, „Mini-Dirac cones in the band structure of a copper intercalated epitaxial graphene superlattice“, *2D Materials*, vol. 3, no. 3, p. 035 003, 2016 (cit. on p. 43).

[160] Y. Zhang, Y. Zhang, D. Ma, Q. Ji, W. Fang, J. Shi, T. Gao, M. Liu, Y. Gao, Y. Chen, L. Xu, and Z. Liu, „Mn atomic layers under inert covers of graphene and hexagonal boron nitride prepared on rh(111)“, *Nano Research*, vol. 6, no. 12, pp. 887–896, 2013 (cit. on p. 43).

[161] Y. S. Dedkov, M. Fonin, U. Rüdiger, and C. Laubschat, „Graphene-protected iron layer on Ni(111)“, *Applied Physics Letters*, vol. 93, no. 2, p. 022 509, 2008 (cit. on p. 43).

[162] S. Schumacher, F. Huttmann, M. Petrović, C. Witt, D. F. Förster, C. Vo-Van, J. Coraux, A. J. Martínez-Galera, V. Sessi, I. Vergara, R. Rückamp, M. Grüninger, N. Schleheck, F. Meyer zu Heringdorf, P. Ohresser, M. Kralj, T. O. Wehling, and T. Michely, „Europium underneath graphene on Ir(111): Intercalation mechanism, magnetism, and band structure“, *Physical Review B*, vol. 90, p. 235 437, 23 2014 (cit. on pp. 43, 80).

[163] J. Mao, L. Huang, Y. Pan, M. Gao, J. He, H. Zhou, H. Guo, Y. Tian, Q. Zou, L. Zhang, *et al.*, „Silicon Layer Intercalation of Centimeter-Scale, Epitaxially Grown Monolayer Graphene on Ru (0001)“, *Applied Physics Letters*, vol. 100, no. 9, p. 093 101, 2012 (cit. on p. 43).

[164] O. Vilkov, A. Fedorov, D. Usachov, L. Yashina, A. Generalov, K. Borygina, N. Verbitskiy, A. Grüneis, and D. Vyalikh, „Controlled Assembly of Graphene-Capped Nickel, Cobalt and Iron Silicides“, *Scientific Reports*, vol. 3, 2013 (cit. on p. 43).

[165] N. I. Verbitskiy, A. V. Fedorov, G. Profeta, A. Stroppa, L. Petaccia, B. Senkovskiy, A. Nefedov, C. Wöll, D. Y. Usachov, D. V. Vyalikh, L. V. Yashina, A. A. Eliseev, T. Pichler, and A. Grüneis, „Atomically Precise Semiconductor–Graphene and hBN Interfaces by Ge Intercalation“, *Scientific Reports*, vol. 5, p. 17 700, 2015 (cit. on p. 43).

[166] A. Nagashima, N. Tejima, and C. Oshima, „Electronic states of the pristine and alkali-metal-intercalated monolayer graphite/Ni(111) systems“, *Physical Review B*, vol. 50, pp. 17 487–17 495, 23 1994 (cit. on p. 43).

[167] M. Petrović, I. Š. Rakić, S. Runte, C. Busse, J. Sadowski, P. Lazić, I. Pletikosić, Z.-H. Pan, M. Milun, P. Pervan, *et al.*, „The Mechanism of Caesium Intercalation of Graphene“, *Nature Communications*, vol. 4, 2013 (cit. on p. 43).

[168] C. Virojanadara, A. A. Zakharov, S. Watcharinyanon, R. Yakimova, and L. I. Johansson, „A low-energy electron microscopy and x-ray photo-emission electron microscopy study of Li intercalated into graphene on SiC(0001)“, *New Journal of Physics*, vol. 12, no. 12, p. 125 015, 2010 (cit. on p. 43).

[169] A. Varykhalov, W. Gudat, and O. Rader, „Imaging Buried Molecules: Fullerenes Under Graphene“, *Advanced Materials*, vol. 22, no. 30, pp. 3307–3310, 2010 (cit. on p. 43).

[170] A. T. N'Diaye, J. Coraux, T. N. Plasa, C. Busse, and T. Michely, „Structure of epitaxial graphene on Ir(111)“, *New Journal of Physics*, vol. 10, no. 4, p. 043 033, 2008 (cit. on p. 44).

[171] M. Gao, Y. Pan, L. Huang, H. Hu, L. Z. Zhang, H. M. Guo, S. X. Du, and H.-J. Gao, „Epitaxial growth and structural property of graphene on Pt(111)“, *Applied Physics Letters*, vol. 98, no. 3, p. 033 101, 2011 (cit. on p. 44).

[172] E. Rotenberg and A. Bostwick, „Superlattice effects in graphene on SiC(0001) and Ir(111) probed by ARPES“, *Synthetic Metals*, vol. 210, pp. 85–94, 2015, Reviews of Current Advances in Graphene Science and Technology (cit. on p. 44).

[173] T. Latychevskaia, C. Escher, and H.-W. Fink, „Moiré structures in twisted bilayer graphene studied by transmission electron microscopy“, *Ultramicroscopy*, vol. 197, pp. 46–52, 2019 (cit. on p. 44).

[174] P. Hohenberg and W. Kohn, „Inhomogeneous Electron Gas“, *Phys. Rev.*, vol. 136, B864–B871, 3B 1964 (cit. on p. 45).

[175] W. Kohn and L. J. Sham, „Self-Consistent Equations Including Exchange and Correlation Effects“, *Phys. Rev.*, vol. 140, A1133–A1138, 4A 1965 (cit. on p. 46).

[176] J. P. Perdew, K. Burke, and M. Ernzerhof, „Generalized Gradient Approximation Made Simple“, *Physical Review Letters*, vol. 77, no. 18, p. 3865, 1996 (cit. on pp. 46, 55).

[177] A. Michaelides and M. Scheffler, „An Introduction to the Theory of Crystalline Elemental Solids and their Surfaces“, in *Surface and Interface Science*. John Wiley & Sons, Ltd, 2014, ch. 2, pp. 13–72 (cit. on pp. 46, 105).

[178] A. Varykhalov, „1^2-ARPES: The ultra high resolution photoemission station at the U112-PGM-2a-1^2 beamline at BESSY II“, *Journal of large-scale research facilities*, vol. 4, no. 0, p. 128, 2018 (cit. on pp. 47, 83).

[179] F. Passek and M. Donath, „Spin-split image-potential-induced surface state on Ni(111)“, *Phys. Rev. Lett.*, vol. 69, pp. 1101–1104, 7 1992 (cit. on p. 48).

[180] I. Ekvall, E. Wahlström, D. Claesson, H. Olin, and E. Olsson, „Preparation and characterization of electrochemically etched W tips for STM“, *Measurement Science and Technology*, vol. 10, no. 1, pp. 11–18, 1999 (cit. on p. 48).

[181] A.-D. Müller, F. Müller, M. Hietschold, F. Demming, J. Jersch, and K. Dickmann, „Characterization of electrochemically etched tungsten tips for scanning tunneling microscopy“, *Review of Scientific Instruments*, vol. 70, no. 10, pp. 3970–3972, 1999 (cit. on p. 48).

[182] T. Hagedorn, M. E. Ouali, W. Paul, D. Oliver, Y. Miyahara, and P. Grütter, „Refined tip preparation by electrochemical etching and ultrahigh vacuum treatment to obtain atomically sharp tips for scanning tunneling microscope and atomic force microscope“, *Review of Scientific Instruments*, vol. 82, no. 11, p. 113 903, 2011 (cit. on p. 48).

[183] K. Momma and F. Izumi, „*VESTA3* for Three-Dimensional Visualization of Crystal, Volumetric and Morphology Data“, *Journal of Applied Crystallography*, vol. 44, no. 6, pp. 1272–1276, 2011 (cit. on p. 48).

[184] D. Nečas and P. Klapetek, „Gwyddion: an open-source software for SPM data analysis“, *Central European Journal of Physics*, vol. 10, pp. 181–188, 1 2012 (cit. on p. 48).

[185] X. Liu, C.-Z. Wang, M. Hupalo, H.-Q. Lin, K.-M. Ho, and M. C. Tringides, „Metals on Graphene: Interactions, Growth Morphology, and Thermal Stability“, *Crystals*, vol. 3, no. 1, p. 79, 2013 (cit. on p. 50).

[186] Y. Dedkov, E. Voloshina, and M. Fonin, „Scanning Probe Microscopy and Spectroscopy of Graphene on Metals“, *Physica Status Solidi B: Basic Solid State Physics*, vol. 252, no. 3, pp. 451–468, 2015 (cit. on p. 50).

[187] G. Giovannetti, P. Khomyakov, G. Brocks, V. v. Karpan, J. Van den Brink, and P. Kelly, „Doping Graphene with Metal Contacts“, *Physical Review Letters*, vol. 101, no. 2, p. 026 803, 2008 (cit. on pp. 50–52, 66, 67).

[188] P. Khomyakov, G. Giovannetti, P. Rusu, G. v. Brocks, J. Van den Brink, and P. Kelly, „First-Principles Study of the Interaction and Charge Transfer between Graphene and Metals“, *Physical Review B*, vol. 79, no. 19, p. 195 425, 2009 (cit. on pp. 50, 66, 67).

[189] A. J. Marsden, M.-C. Asensio, J. Avila, P. Dudin, A. Barinov, P. Moras, P. M. Sheverdyaeva, T. W. White, I. Maskery, G. Costantini, *et al.*, „Is Graphene on Copper Doped?“, *Physica Status Solidi Rapid Research Letters*, vol. 7, no. 9, pp. 643–646, 2013 (cit. on p. 50).

[190] V. Karpan, G. Giovannetti, P. Khomyakov, M. Talanana, A. Starikov, M. Zwierzycki, J. Van Den Brink, G. Brocks, and P. Kelly, „Graphite and Graphene As Perfect Spin Filters“, *Physical Review Letters*, vol. 99, no. 17, p. 176 602, 2007 (cit. on p. 50).

[191] O. Rader, A. Varykhalov, J. Sánchez-Barriga, D. Marchenko, A. Rybkin, and A. M. Shikin, „Is There a Rashba Effect in Graphene on 3*d* Ferromagnets?“, *Physical Review Letters*, vol. 102, no. 5, p. 057 602, 2009 (cit. on p. 50).

[192] D. Marchenko, A. Varykhalov, J. Sánchez-Barriga, O. Rader, C. Carbone, and G. Bihlmayer, „Highly Spin-Polarized Dirac Fermions at the Graphene/Co Interface“, *Physical Review B*, vol. 91, no. 23, p. 235 431, 2015 (cit. on pp. 50, 98).

[193] L. Ponomarenko, R. Gorbachev, G. Yu, D. Elias, R. Jalil, A. Patel, A. Mishchenko, A. Mayorov, C. Woods, J. Wallbank, *et al.*, „Cloning of Dirac Fermions in Graphene Superlattices“, *Nature*, vol. 497, no. 7451, pp. 594–597, 2013 (cit. on p. 50).

[194] J. Sánchez-Barriga, A. Varykhalov, D. Marchenko, M. R. Scholz, and O. Rader, „Minigap Isotropy and Broken Chirality in Graphene with Periodic Corrugation Enhanced by Cluster Superlattices“, *Physical Review B*, vol. 85, no. 20, p. 201 413, 2012 (cit. on pp. 50, 79, 86, 132).

[195] F. Kuemmeth, S. Ilani, D. Ralph, and P. McEuen, „Coupling of Spin and Orbital Motion of Electrons in Carbon Nanotubes“, *Nature*, vol. 452, no. 7186, pp. 448–452, 2008 (cit. on p. 50).

[196] A. M. Shikin, G. V. Prudnikova, V. K. Adamchuk, F. Moresco, and K.-H. Rieder, „Surface intercalation of gold underneath a graphite monolayer on Ni(111) studied by angle-resolved photoemission and high-resolution electron-energy-loss spectroscopy“, *Physical Review B*, vol. 62, pp. 13 202–13 208, 19 2000 (cit. on pp. 51, 54).

[197] D. Farías, K. Rieder, A. Shikin, V. Adamchuk, T. Tanaka, and C. Oshima, „Modification of the surface phonon dispersion of a graphite monolayer adsorbed on Ni(111) caused by intercalation of Yb, Cu and Ag“, *Surface Science*, vol. 454-456, pp. 437–441, 2000 (cit. on p. 51).

[198] M. Krivenkov, E. Golias, D. Marchenko, J. Sánchez-Barriga, G. Bihlmayer, O. Rader, and A. Varykhalov, „Nanostructural origin of giant Rashba effect in intercalated graphene“, *2D Materials*, vol. 4, no. 3, p. 035 010, 2017 (cit. on pp. 52, 53, 72).

[199] G. Kresse and J. Hafner, „Ab Initio Molecular Dynamics for Liquid Metals“, *Physical Review B*, vol. 47, no. 1, p. 558, 1993 (cit. on p. 55).

[200] P. E. Blöchl, „Projector Augmented-Wave Method“, *Physical Review B*, vol. 50, no. 24, p. 17 953, 1994 (cit. on p. 55).

[201] S. Grimme, „Semiempirical GGA-Type Density Functional Constructed with a Long-Range Dispersion Correction“, *Journal of Computational Chemistry*, vol. 27, no. 15, pp. 1787–1799, 2006 (cit. on p. 55).

[202] N. P. Lyakishev, Ed., *Phase diagrams of binary metallic systems (in russian).* 1996, vol. 1, pp. 378–379 (cit. on p. 56).

[203] M. J. Kelley, P. W. Gilmour, and D. G. Swartzfager, „Strain effects in surface segregation – The Au/Ni system“, *Journal of Vacuum Science and Technology*, vol. 17, no. 2, pp. 634–637, 1980 (cit. on p. 56).

[204] L. Nielsen, „The Nucleation and Growth of Au on Ni (110) and Ni (111)–A Scanning Tunneling Microscopy Study“, Ph.D. dissertation, Aarhus University, 1995 (cit. on pp. 56–59).

[205] J. Jacobsen, L. Pleth Nielsen, F. Besenbacher, I. Stensgaard, E. Lægsgaard, T. Rasmussen, K. W. Jacobsen, and J. K. Nørskov, „Atomic-Scale Determination of Misfit Dislocation Loops at Metal-Metal Interfaces“, *Physical Review Letters*, vol. 75, no. 3, pp. 489–492, 1995 (cit. on pp. 57–59, 62, 71).

[206] C. C.-W. L. Leon, „Gold-nickel surface alloy chemistry with oxygen and carbon monoxide“, Ph.D. dissertation, Massachusetts Institute of Technology, 2015 (cit. on p. 57).

[207] F. Besenbacher, L. P. Nielsen, and P. T. Sprunger, „Chapter 6 Surface alloying in heteroepitaxial metal-on-metal growth“, in *Growth and Properties of Ultrathin Epitaxial Layers*, ser. The Chemical Physics of Solid Surfaces, D. King and D. Woodruff, Eds., vol. 8, Elsevier, 1997, pp. 207–257 (cit. on p. 59).

[208] I. Meunier, G. Tréglia, J.-M. Gay, B. Aufray, and B. Legrand, „Ag/Cu(111) structure revisited through an extended mechanism for stress relaxation“, *Physical Review B*, vol. 59, pp. 10 910–10 917, 16 1999 (cit. on p. 59).

[209] K. Umezawa, S. Nakanishi, M. Yoshimura, K. Ojima, K. Ueda, and W. M. Gibson, „Ag/Cu(111) surface structure and metal epitaxy by impact-collision ion-scattering spectroscopy and scanning tunneling microscopy“, *Physical Review B*, vol. 63, p. 035 402, 3 2000 (cit. on p. 59).

[210] A. Bendounan, H. Cercellier, Y. Fagot-Revurat, B. Kierren, V. Y. Yurov, and D. Malterre, „Modification of Shockley states induced by surface reconstruction in epitaxial Ag films on Cu(111)“, *Physical Review B*, vol. 67, p. 165 412, 16 2003 (cit. on p. 59).

[211] H. Brune, M. Giovannini, K. Bromann, and K. Kern, „Self-organized growth of nanostructure arrays on strain-relief patterns“, *Nature*, vol. 394, no. 6692, pp. 451–453, 1998 (cit. on p. 60).

[212] K. Aït-Mansour, H. Brune, D. Passerone, M. Schmid, W. Xiao, P. Ruffieux, A. Buchsbaum, P. Varga, R. Fasel, and O. Gröning, „Interface-confined mixing and buried partial dislocations for Ag bilayer on Pt(111)“, *Physical Review B*, vol. 86, 2012 (cit. on p. 60).

[213] M. Schmid, A. Biedermann, H. Stadler, and P. Varga, „Lattice mismatch dislocations in a preferentially sputtered alloy studied by scanning tunneling microscopy“, *Physical Review Letters*, vol. 69, pp. 925–928, 6 1992 (cit. on p. 60).

[214] M. Asano, R. Kawamura, R. Sasakawa, N. Todoroki, and T. Wadayama, „Oxygen Reduction Reaction Activity for Strain-Controlled Pt-Based Model Alloy Catalysts: Surface Strains and Direct Electronic Effects Induced by Alloying Elements“, *ACS Catalysis*, vol. 6, no. 8, pp. 5285–5289, 2016 (cit. on p. 60).

[215] A. G. Rybkin, A. A. Rybkina, M. M. Otrokov, O. Y. Vilkov, I. I. Klimovskikh, A. E. Petukhov, M. V. Filianina, V. Y. Voroshnin, I. P. Rusinov, A. Ernst, A. Arnau, E. V. Chulkov, and A. M. Shikin, „Magneto-Spin-Orbit Graphene: Interplay between Exchange and Spin-Orbit Couplings“, *Nano Letters*, 2018 (cit. on pp. 60, 71).

[216] B. Premlal, M. Cranney, F. Vonau, D. Aubel, D. Casterman, M. M. D. Souza, and L. Simon, „Surface intercalation of gold underneath a graphene monolayer on SiC(0001) studied by scanning tunneling microscopy and spectroscopy“, *Applied Physics Letters*, vol. 94, no. 26, p. 263 115, 2009 (cit. on p. 62).

[217] M. Cranney, F. Vonau, P. B. Pillai, E. Denys, D. Aubel, M. M. D. Souza, C. Bena, and L. Simon, „Superlattice of resonators on monolayer graphene created by intercalated gold nanoclusters“, *EPL (Europhysics Letters)*, vol. 91, no. 6, p. 66 004, 2010 (cit. on p. 62).

[218] M. N. Nair, M. Cranney, F. Vonau, D. Aubel, P. Le Fèvre, A. Tejeda, F. Bertran, A. Taleb-Ibrahimi, and L. Simon, „High van Hove singularity extension and Fermi velocity increase in epitaxial graphene functionalized by intercalated gold clusters“, *Physical Review B*, vol. 85, p. 245 421, 24 2012 (cit. on p. 62).

[219] J. Lahiri, T. Miller, L. Adamska, I. I. Oleynik, and M. Batzill, „Graphene Growth on Ni(111) by Transformation of a Surface Carbide“, *Nano Letters*, vol. 11, no. 2, pp. 518–522, 2011, PMID: 21182255 (cit. on pp. 62, 63).

[220] G. Li, H. Zhou, L. Pan, Y. Zhang, L. Huang, W. Xu, S. Du, M. Ouyang, A. C. Ferrari, and H.-J. Gao, „Role of Cooperative Interactions in the Intercalation of Heteroatoms between Graphene and a Metal Substrate“, *Journal of the American Chemical Society*, vol. 137, no. 22, pp. 7099–7103, 2015 (cit. on p. 63).

[221] G. Kresse and J. Furthmüller, „Efficient iterative schemes for ab initio total-energy calculations using a plane-wave basis set“, *Phys. Rev. B*, vol. 54, pp. 11 169–11 186, 16 1996 (cit. on p. 67).

[222] A. López, L. Colmenárez, M. Peralta, F. Mireles, and E. Medina, „Proximity-induced spin-orbit effects in graphene on Au“, *Phys. Rev. B*, vol. 99, p. 085 411, 8 2019 (cit. on p. 69).

[223] P. Rakyta, A. Kormányos, and J. Cserti, „Effect of Sublattice Asymmetry and Spin-Orbit Interaction on Out-of-Plane Spin Polarization of Photoelectrons“, *Physical Review B*, vol. 83, no. 15, p. 155 439, 2011 (cit. on pp. 69, 77, 96).

[224] J. Sławińska and J. I. Cerdá, „Complex spin texture of Dirac cones induced via spin-orbit proximity effect in graphene on metals“, *Physical Review B*, vol. 98, p. 075 436, 7 2018 (cit. on pp. 71, 72).

[225] J. Sławińska and J. I. Cerdá, „Spin–orbit proximity effect in graphene on metallic substrates: decoration versus intercalation with metal adatoms“, *New Journal of Physics*, vol. 21, no. 7, p. 073 018, 2019 (cit. on p. 71).

[226] E. L. Shirley, L. J. Terminello, A. Santoni, and F. J. Himpsel, „Brillouin-zone-selection effects in graphite photoelectron angular distributions“, *Physical Review B*, vol. 51, pp. 13 614–13 622, 19 1995 (cit. on pp. 74, 75).

[227] I. Gierz, J. Henk, H. Höchst, C. R. Ast, and K. Kern, „Illuminating the dark corridor in graphene: Polarization dependence of angle-resolved photoemission spectroscopy on graphene“, *Physical Review B*, vol. 83, p. 121 408, 12 2011 (cit. on pp. 76, 77, 100).

[228] A. Bostwick, T. Ohta, J. L. McChesney, K. V. Emtsev, T. Seyller, K. Horn, and Eli Rotenberg, „Symmetry breaking in few layer graphene films“, *New Journal of Physics*, vol. 9, no. 10, p. 385, 2007 (cit. on pp. 76, 79).

[229] M. Mucha-Kruczyński, O. Tsyplyatyev, A. Grishin, E. McCann, V. I. Fal’ko, A. Bostwick, and E. Rotenberg, „Characterization of graphene through anisotropy of constant-energy maps in angle-resolved photoemission“, *Physical Review B*, vol. 77, p. 195 403, 19 2008 (cit. on p. 77).

[230] E. Loginova, S. Nie, K. Thürmer, N. C. Bartelt, and K. F. McCarty, „Defects of graphene on Ir(111): Rotational domains and ridges“, *Physical Review B*, vol. 80, p. 085 430, 8 2009 (cit. on p. 78).

[231] L. Meng, R. Wu, L. Zhang, L. Li, S. Du, Y. Wang, and H.-J. Gao, „Multi-oriented moiré superstructures of graphene on Ir(111): experimental observations and theoretical models“, *Journal of Physics: Condensed Matter*, vol. 24, no. 31, p. 314 214, 2012 (cit. on p. 78).

[232] H. Hattab, A. T. N'Diaye, D. Wall, G. Jnawali, J. Coraux, C. Busse, R. van Gastel, B. Poelsema, T. Michely, F.-J. Meyer zu Heringdorf, and M. Horn-von Hoegen, „Growth temperature dependent graphene alignment on Ir(111)“, *Applied Physics Letters*, vol. 98, no. 14, p. 141 903, 2011 (cit. on p. 78).

[233] F. Jean, T. Zhou, N. Blanc, R. Felici, J. Coraux, and G. Renaud, „Topography of the graphene/Ir(111) moiré studied by surface x-ray diffraction“, *Physical Review B*, vol. 91, no. 24, p. 245 424, 2015 (cit. on p. 78).

[234] D. Nobis, M. Potenz, D. Niesner, and T. Fauster, „Image-potential states of graphene on noble-metal surfaces“, *Physical Review B*, vol. 88, p. 195 435, 19 2013 (cit. on p. 80).

[235] H. Vita, S. Böttcher, K. Horn, E. N. Voloshina, R. E. Ovcharenko, T. Kampen, A. Thissen, and Y. S. Dedkov, „Understanding the origin of band gap formation in graphene on metals: graphene on Cu/Ir(111)“, *Scientific Reports*, vol. 4, p. 5704, 2014 (cit. on pp. 80, 98).

[236] I. Klimovskikh, M. Krivenkov, A. Varykhalov, D. Estyunin, and A. Shikin, „Reconstructed Fermi surface in graphene on Ir(111) by Gd-Ir surface alloying“, *Carbon*, vol. 147, pp. 182–186, 2019 (cit. on pp. 80, 123).

[237] L. Li, Y. Wang, L. Meng, R.-t. Wu, and H.-J. Gao, „Hafnium intercalation between epitaxial graphene and Ir(111) substrate“, *Applied Physics Letters*, vol. 102, no. 9, p. 093 106, 2013 (cit. on p. 80).

[238] R. Decker, J. Brede, N. Atodiresei, V. Caciuc, S. Blügel, and R. Wiesendanger, „Atomic-scale magnetism of cobalt-intercalated graphene“, *Physical Review B*, vol. 87, p. 041 403, 4 2013 (cit. on p. 80).

[239] H. Vita, S. Böttcher, P. Leicht, K. Horn, A. B. Shick, and F. Máca, „Electronic structure and magnetic properties of cobalt intercalated in graphene on Ir(111)“, *Physical Review B*, vol. 90, p. 165 432, 16 2014 (cit. on p. 80).

[240] L. Meng, R. Wu, H. Zhou, G. Li, Y. Zhang, L. Li, Y. Wang, and H.-J. Gao, „Silicon intercalation at the interface of graphene and Ir(111)“, *Applied Physics Letters*, vol. 100, no. 8, p. 083 101, 2012 (cit. on p. 80).

[241] E. Grånäs, J. Knudsen, U. A. Schröder, T. Gerber, C. Busse, M. A. Arman, K. Schulte, J. N. Andersen, and T. Michely, „Oxygen Intercalation under Graphene on Ir(111): Energetics, Kinetics, and the Role of Graphene Edges“, *ACS Nano*, vol. 6, no. 11, pp. 9951–9963, 2012, PMID: 23039853 (cit. on p. 80).

[242] E. Grånäs, M. Andersen, M. A. Arman, T. Gerber, B. Hammer, J. Schnadt, J. N. Andersen, T. Michely, and J. Knudsen, „CO Intercalation of Graphene on Ir(111) in the Millibar Regime“, *The Journal of Physical Chemistry C*, vol. 117, no. 32, pp. 16 438–16 447, 2013 (cit. on p. 80).

[243] J. Warmuth, A. Bruix, M. Michiardi, T. Hänke, M. Bianchi, J. Wiebe, R. Wiesendanger, B. Hammer, P. Hofmann, and A. A. Khajetoorians, „Band-gap engineering by Bi intercalation of graphene on Ir(111)“, *Physical Review B*, vol. 93, no. 16, p. 165 437, 2016 (cit. on pp. 80–82, 84, 85, 87, 90, 92, 95, 97).

[244] J. C. F. M. Warmuth, „Structural and Electronic Properties of Bismuth Intercalated Graphene on Iridium“, M.S. thesis, University of Hamburg, 2014 (cit. on pp. 80–82, 85, 90).

[245] C. R. Ast, „A little bit of everything“, *Nature Physics*, vol. 14, no. 9, pp. 874–875, 2018 (cit. on p. 80).

[246] G. Li and S. Wang, „Quantum Spin Hall States in 2D Bismuth-Based Materials“, in, ser. Springer Series in Materials Science, S. Wang and P. Lu, Eds., Singapore: Springer Singapore, 2019, pp. 351–379 (cit. on p. 80).

[247] F. Schindler, A. M. Cook, M. G. Vergniory, Z. Wang, S. S. P. Parkin, B. A. Bernevig, and T. Neupert, „Higher-order topological insulators“, *Science Advances*, vol. 4, no. 6, 2018 (cit. on p. 80).

[248] F. Reis, G. Li, L. Dudy, M. Bauernfeind, S. Glass, W. Hanke, R. Thomale, J. Schäfer, and R. Claessen, „Bismuthene on a SiC substrate: A candidate for a high-temperature quantum spin Hall material“, *Science*, vol. 357, no. 6348, pp. 287–290, 2017 (cit. on p. 80).

[249] C.-H. Hsu, V. Ozolins, and F.-C. Chuang, „First-principles study of Bi and Sb intercalated graphene on SiC(0001) substrate“, *Surface Science*, vol. 616, pp. 149–154, 2013 (cit. on p. 80).

[250] A. Stöhr, S. Forti, S. Link, A. A. Zakharov, K. Kern, U. Starke, and H. M. Benia, „Intercalation of graphene on SiC(0001) via ion implantation“, *Physical Review B*, vol. 94, p. 085 431, 8 2016 (cit. on pp. 80–82, 87).

[251] A. Stöhr, „Structured graphene on SiC: Graphene growth on a patterned substrate and the realization of ballistic np-junctions“, Ph.D. dissertation, Friedrich-Alexander-Universität Erlangen-Nürnberg (FAU), 2016 (cit. on p. 80).

[252] G. C. Burnett, T. J. Monroe, and F. B. Dunning, „High-efficiency retarding-potential Mott polarization analyzer“, *Review of Scientific Instruments*, vol. 65, no. 6, pp. 1893–1896, 1994 (cit. on p. 81).

[253] S. Doniach and M. Šunjić, „Many-electron singularity in X-ray photoemission and X-ray line spectra from metals“, *Journal of Physics C: Solid State Physics*, vol. 3, no. 2, pp. 285–291, 1970 (cit. on p. 83).

[254] A. C. Thompson and D. Vaughan, Eds., *X-ray Data Booklet*, Second. Lawrence Berkeley National Laboratory, University of California, 2001 (cit. on p. 84).

[255] P. Zeller, X. Ma, and S. Günther, „Indexing moiré patterns of metal-supported graphene and related systems: strategies and pitfalls“, *New Journal of Physics*, vol. 19, no. 1, p. 013 015, 2017 (cit. on p. 85).

[256] E. Starodub, A. Bostwick, L. Moreschini, S. Nie, F. E. Gabaly, K. F. McCarty, and E. Rotenberg, „In-plane orientation effects on the electronic structure, stability, and Raman scattering of monolayer graphene on Ir(111)“, *Physical Review B*, vol. 83, p. 125 428, 12 2011 (cit. on p. 86).

[257] M. Kralj, I. Pletikosić, M. Petrović, P. Pervan, M. Milun, A. T. N'Diaye, C. Busse, T. Michely, J. Fujii, and I. Vobornik, „Graphene on Ir(111) characterized by angle-resolved photoemission“, *Physical Review B*, vol. 84, p. 075 427, 7 2011 (cit. on p. 87).

[258] A. T. N'Diaye, T. Gerber, C. Busse, J. Mysliveček, J. Coraux, and T. Michely, „A versatile fabrication method for cluster superlattices“, *New Journal of Physics*, vol. 11, no. 10, p. 103 045, 2009 (cit. on pp. 90, 123, 132).

[259] M. F. Crommie, C. P. Lutz, and D. M. Eigler, „Imaging standing waves in a two-dimensional electron gas“, *Nature*, vol. 363, no. 6429, pp. 524–527, 1993 (cit. on pp. 93, 104).

[260] H. A. Mizes and J. S. Foster, „Long-Range Electronic Perturbations Caused by Defects Using Scanning Tunneling Microscopy“, *Science*, vol. 244, no. 4904, pp. 559–562, 1989 (cit. on p. 93).

[261] G. M. Rutter, J. N. Crain, N. P. Guisinger, T. Li, P. N. First, and J. A. Stroscio, „Scattering and interference in epitaxial graphene“, *Science*, vol. 317, no. 5835, pp. 219–222, 2007 (cit. on p. 93).

[262] A. Rossi, S. Piccinin, V. Pellegrini, S. de Gironcoli, and V. Tozzini, „Nano-Scale Corrugations in Graphene: A Density Functional Theory Study of Structure, Electronic Properties and Hydrogenation“, *J. Phys. Chem. C*, vol. 119, no. 14, pp. 7900–7910, 2015 (cit. on p. 98).

[263] G. Sclauzero and A. Pasquarello, „Carbon rehybridization at the graphene/SiC(0001) interface: Effect on stability and atomic-scale corrugation“, *Physical Review B*, vol. 85, no. 16, p. 161 405, 2012 (cit. on p. 98).

[264] D. Haberer, D. V. Vyalikh, S. Taioli, B. Dora, M. Farjam, J. Fink, D. Marchenko, T. Pichler, K. Ziegler, S. Simonucci, M. S. Dresselhaus, M. Knupfer, B. Büchner, and A. Grüneis, „Tunable Band Gap in Hydrogenated Quasi-Free-Standing Graphene“, *Nano Letters*, vol. 10, no. 9, pp. 3360–3366, 2010 (cit. on pp. 98, 123).

[265] R. Balog, B. Jørgensen, L. Nilsson, M. Andersen, E. Rienks, M. Bianchi, M. Fanetti, E. Lægsgaard, A. Baraldi, S. Lizzit, Z. Sljivancanin, F. Besenbacher, B. Hammer, T. G. Pedersen, P. Hofmann, and L. Hornekær, „Bandgap opening in graphene induced by patterned hydrogen adsorption“, *Nature Materials*, vol. 9, no. 4, p. 315, 2010 (cit. on pp. 98, 134, 136).

[266] H.-C. Mertins, C. Jansing, M. Krivenkov, A. Varykhalov, O. Rader, H. Wahab, H. Timmers, A. Gaupp, A. Sokolov, M. Tesch, and P. M. Oppeneer, „Giant magneto-optical Faraday effect of graphene on Co in the soft x-ray range“, *Physical Review B*, vol. 98, no. 6, p. 064 408, 2018 (cit. on p. 98).

[267] N. Knorr, H. Brune, M. Epple, A. Hirstein, M. Schneider, and K. Kern, „Long-range adsorbate interactions mediated by a two-dimensional electron gas“, *Physical Review B*, vol. 65, no. 11, p. 115 420, 2002 (cit. on p. 104).

[268] P. M. Echenique and J. B. Pendry, „The existence and detection of rydberg states at surfaces“, *Journal of Physics C: Solid State Physics*, vol. 11, no. 10, p. 2065, 1978 (cit. on pp. 104, 108, 114, 122).

[269] P. M. Echenique and M. E. Uranga, „Image potential states at surfaces“, *Surface Science*, vol. 247, no. 2, pp. 125–132, 1991 (cit. on p. 104).

[270] J. Sánchez-Barriga, G. Bihlmayer, D. Wortmann, D. Marchenko, O. Rader, and A. Varykhalov, „Effect of structural modulation and thickness of a graphene overlayer on the binding energy of the Rashba-type surface state of Ir(111)“, *New Journal of Physics*, vol. 15, no. 11, p. 115 009, 2013 (cit. on pp. 104, 133).

[271] N. V. Smith, „Phase analysis of image states and surface states associated with nearly-free-electron band gaps“, *Physical Review B*, vol. 32, no. 6, pp. 3549–3555, 1985 (cit. on pp. 105, 114, 122).

[272] E. G. McRae, „Electronic surface resonances of crystals“, *Reviews of Modern Physics*, vol. 51, no. 3, pp. 541–568, 1979 (cit. on pp. 105, 108, 109, 111, 114).

[273] J. C. L. Bosse, J. Lopez, C. Gaubert, Y. Gauthier, and R. Baudoing, „Threshold effects in LEED: Resonance or interference effects?“, *Journal of Physics C: Solid State Physics*, vol. 15, no. 15, p. 3425, 1982 (cit. on pp. 105, 106, 108, 111, 116, 118).

[274] R. Jones and P. Jennings, „LEED fine structure: Origins and applications“, *Surface Science Reports*, vol. 9, no. 4, pp. 165–196, 1988 (cit. on pp. 105, 108, 118).

[275] J. C. L. Bosse, J. Lopez, C. Gaubert, Y. Gauthier, and R. Baudoing, „A general picture of threshold effects in LEED“, *Journal of Physics C: Solid State Physics*, vol. 15, no. 29, p. 6087, 1982 (cit. on pp. 106, 108, 110, 111, 116, 118).

[276] U. Burgbacher, J. Braun, A. K. Brüning, A. B. Schmidt, and M. Donath, „Spin-dependent surface barrier from very-low-energy electron diffraction fine structures: A feasibility study“, *Physical Review B*, vol. 87, no. 19, p. 195 411, 2013 (cit. on pp. 106, 108, 110, 113, 127).

[277] F. Wicki, J.-N. Longchamp, T. Latychevskaia, C. Escher, and H.-W. Fink, „Mapping unoccupied electronic states of freestanding graphene by angle-resolved low-energy electron transmission“, *Physical Review B*, vol. 94, p. 075 424, 7 2016 (cit. on pp. 106, 108, 109, 126).

[278] I. Estermann and O. Stern, „Beugung von molekularstrahlen“, *Zeitschrift für Physik*, vol. 61, no. 1-2, pp. 95–125, 1930 (cit. on p. 107).

[279] J. E. Lennard-Jones and A. F. Devonshire, „Diffraction and Selective Adsorption of Atoms at Crystal Surfaces“, *Nature*, vol. 137, no. 3478, pp. 1069–1070, 1936 (cit. on p. 107).

[280] A. F. Devonshire, „The interaction of atoms and molecules with solid surfaces V–The diffraction and reflexion of molecular rays“, *Proceedings of the Royal Society of London A: Mathematical, Physical and Engineering Sciences*, vol. 156, no. 887, pp. 37–44, 1936 (cit. on p. 107).

[281] S. Kikuchi and S. Nakagawa, „Die anomale Reflexion der schnellen Elektronen an die Einkristalloberflächen“, *Scientific Papers of the Institute of Physical and Chemical Research*, vol. 21, p. 256, 1933 (cit. on p. 108).

[282] S. Miyake, K. Kohra, and M. Takagi, „The nature of the specular reflexion of electrons from a crystal surface“, *Acta Crystallographica*, vol. 7, no. 5, pp. 393–401, 1954 (cit. on p. 108).

[283] S. Miyake and K. Hayakawa, „Resonance effects in low and high energy electron diffraction by crystals“, *Acta Crystallographica Section A*, vol. 26, no. 1, pp. 60–70, 1970 (cit. on p. 108).

[284] E. G. McRae and C. W. Caldwell Jr, „Low-energy electron diffraction study of lithium fluoride (100) surface“, *Surface Science*, vol. 2, pp. 509–515, 1964 (cit. on p. 108).

[285] C. Grimes, „Electrons in surface states on liquid helium“, *Surface Science*, vol. 73, pp. 379–395, 1978 (cit. on p. 108).

[286] J. Lauzier, L. de Bersuder, and V. Hoffstein, „Observation of Surface-State Resonances in Low-Energy Electron-Diffraction Rotation Diagrams for Al“, *Physical Review Letters*, vol. 27, no. 11, pp. 735–738, 1971 (cit. on p. 108).

[287] P. J. Jennings, „Surface barrier effects in low-energy electron diffraction“, *Surface Science*, vol. 25, no. 3, pp. 513–525, 1971 (cit. on p. 108).

[288] E. McRae, „Surface-state resonances in low-energy electron diffraction“, *Surface Science*, vol. 25, no. 3, pp. 491–512, 1971 (cit. on pp. 108, 109).

[289] J. Rundgren and G. Malmstrom, „Transmission and reflection of low-energy electrons at the surface barrier of a metal“, *Journal of Physics C: Solid State Physics*, vol. 10, no. 23, p. 4671, 1977 (cit. on p. 108).

[290] R. E. Dietz, E. G. McRae, and R. L. Campbell, „Saturation of the Image Potential Observed in Low-Energy Electron Reflection at Cu(001) Surface“, *Physical Review Letters*, vol. 45, pp. 1280–1284, 15 1980 (cit. on pp. 108, 111, 118).

[291] J. M. Baribeau and J.-D. Carette, „Rydberg surface states and surface resonances“, *Physica B+C*, vol. 106, no. 2, pp. 221–226, 1981 (cit. on p. 108).

[292] E. G. McRae and M. L. Kane, „Calculations on the effect of the surface potential barrier in LEED“, *Surface Science*, vol. 108, no. 3, pp. 435–445, 1981 (cit. on pp. 108, 114).

[293] J. Lopez, J. C. Le Bossé, C. Gaubert, R. Baudoing, and Y. Gauthier, „Dynamical effects of the surface potential barrier in very low energy electron diffraction“, *Surface Science*, vol. 126, no. 1, pp. 286–293, 1983 (cit. on p. 108).

[294] C. Gaubert, R. Baudoing, Y. Gauthier, and J. Rundgren, „General aspects of beam threshold effects in LEED“, *Surface Science*, vol. 147, no. 1, pp. 162–178, 1984 (cit. on p. 108).

[295] M. N. Read and A. S. Christopoulos, „Resonant electron surface-barrier scattering on W(001)“, *Physical Review B*, vol. 37, no. 17, pp. 10 407–10 410, 17 1988 (cit. on pp. 108, 111).

[296] E. E. Krasovskii, J. Höcker, J. Falta, and J. I. Flege, „Surface resonances in electron reflection from overlayers“, *Journal of Physics: Condensed Matter*, vol. 27, no. 3, p. 035 501, 2014 (cit. on p. 108).

[297] V. N. Strocov, R. Claessen, G. Nicolay, S. Hüfner, A. Kimura, A. Harasawa, S. Shin, A. Kakizaki, H. I. Starnberg, P. O. Nilsson, and P. Blaha, „Three-dimensional band mapping by angle-dependent very-low-energy electron diffraction and photoemission: Methodology and application to Cu“, *Phys. Rev. B*, vol. 63, p. 205 108, 20 2001 (cit. on p. 108).

[298] O. Y. Vilkov, E. E. Krasovskii, A. V. Fedorov, A. G. Rybkin, A. M. Shikin, C. Laubschat, J. Budagosky, D. V. Vyalikh, and D. Y. Usachov, „Angle-resolved secondary photoelectron emission from graphene interfaces“, *Physical Review B*, vol. 99, p. 195 421, 19 2019 (cit. on pp. 108, 109, 119, 121).

[299] M. Bovet, V. N. Strocov, F. Clerc, C. Koitzsch, D. Naumović, and P. Aebi, „Excited States Mapped by Secondary Photoemission“, *Physical Review Letters*, vol. 93, p. 107 601, 10 2004 (cit. on pp. 108, 113, 119).

[300] A. Winkelmann, M. Ellguth, C. Tusche, A. A. Ünal, J. Henk, and J. Kirschner, „Momentum-resolved photoelectron interference in crystal surface barrier scattering“, *Physical Review B*, vol. 86, no. 8, p. 085 427, 2012 (cit. on p. 108).

[301] A. Zaporozhchenko-Zymaková, D. Kutnyakhov, K. Medjanik, C. Tusche, O. Fedchenko, S. Chernov, M. Ellguth, S. A. Nepijko, H. J. Elmers, and G. Schönhense, „Momentum-resolved photoelectron absorption in surface barrier scattering on Ir(111) and graphene/Ir(111)“, *Physical Review B*, vol. 96, no. 15, p. 155 108, 2017 (cit. on pp. 108, 109, 124).

[302] H. Hibino, H. Kageshima, F.-Z. Guo, F. Maeda, M. Kotsugi, and Y. Watanabe, „Two-dimensional emission patterns of secondary electrons from graphene layers formed on SiC(0001)“, *Applied Surface Science*, 9th International Conference on Atomically Controlled Surfaces, Interfaces and Nanostructures 2007 (ASCIN-9), vol. 254, no. 23, pp. 7596–7599, 2008 (cit. on pp. 108, 109, 119, 126).

[303] P. O. Nilsson, K. Karlsson, and J. Rundgren, „Prediction of image-state excitation by secondary beams in inverse-photoemission spectroscopy“, *Phys. Rev. B*, vol. 47, pp. 12 968–12 971, 19 1993 (cit. on p. 108).

[304] S. Yang, R. A. Bartynski, G. P. Kochanski, S. Papadia, T. Fondén, and M. Persson, „Surface barrier resonances on a simple metal“, *Physical Review Letters*, vol. 70, no. 6, pp. 849–852, 1993 (cit. on p. 108).

[305] M. Budke, V. Renken, H. Liebl, G. Rangelov, and M. Donath, „Inverse photoemission with energy resolution better than 200 meV“, *Review of Scientific Instruments*, vol. 78, no. 8, p. 083 903, 2007 (cit. on p. 108).

[306] M. Winter, E. V. Chulkov, and U. Höfer, „Trapping of Image-Potential Resonances on a Free-Electron-like Surface“, *Phys. Rev. Lett.*, vol. 107, p. 236 801, 23 2011 (cit. on p. 108).

[307] D. Gugel, D. Niesner, C. Eickhoff, S. Wagner, M. Weinelt, and T. Fauster, „Two-photon photoemission from image-potential states of epitaxial graphene“, *2D Materials*, vol. 2, no. 4, p. 045 001, 2015 (cit. on p. 108).

[308] R. Arafune, N. Takagi, and H. Ishida, „Spin-orbit interaction in unoccupied surface states“, *Progress in Surface Science*, vol. 93, no. 4, pp. 177–188, 2018, Special Issue in Honor of Prof. Maki Kawai (cit. on p. 108).

[309] K. Artmann, „Zur Theorie der Kikuchi-Enveloppen“, *Zeitschrift für Physik A Hadrons and nuclei*, vol. 124, no. 1-2, pp. 80–104, 1947 (cit. on p. 109).

[310] S. Papadia, M. Persson, and L.-A. Salmi, „Image-potential-induced resonances at free-electron-like metal surfaces“, *Phys. Rev. B*, vol. 41, pp. 10 237–10 239, 14 1990 (cit. on pp. 109, 116).

[311] M. Nekovee and J. E. Inglesfield, „Threshold Behaviour of Surface Density of States at the Vacuum Level“, *Europhysics Letters (EPL)*, vol. 19, no. 6, pp. 535–540, 1992 (cit. on pp. 109, 121).

[312] M. Grass, J. Braun, G. Borstel, R. Schneider, H. Durr, T. Fauster, and V. Dose, „Unoccupied electronic states and surface barriers at Cu surfaces“, *Journal of Physics: Condensed Matter*, vol. 5, no. 5, pp. 599–614, 1993 (cit. on pp. 109, 121).

[313] G. Butti, S. Caravati, G. P. Brivio, M. I. Trioni, and H. Ishida, „Image potential states and electronic structure of Na/Cu(111)“, *Phys. Rev. B*, vol. 72, p. 125 402, 12 2005 (cit. on pp. 109, 121).

[314] R. O. Jones, P. J. Jennings, and O. Jepsen, „Surface barrier in metals: A new model with application to W(001)“, *Phys. Rev. B*, vol. 29, pp. 6474–6480, 12 1984 (cit. on p. 110).

[315] L. A. MacColl, „Numerical Calculations of the Reflection of Electrons by Metals“, *Phys. Rev.*, vol. 56, pp. 699–702, 7 1939 (cit. on p. 110).

[316] S. M. Thurgate, C. Sun, and G. Hitchen, „Surface structural determination by VLEED analysis“, in *Surface Science*, Springer, 1996, pp. 29–37 (cit. on p. 111).

[317] N. D. Lang and W. Kohn, „Theory of Metal Surfaces: Induced Surface Charge and Image Potential“, *Phys. Rev. B*, vol. 7, pp. 3541–3550, 8 1973 (cit. on p. 114).

[318] J. D. Jackson, *Classical electrodynamics*, 3rd ed. Wiley, 1999, pp. 154–155 (cit. on p. 114).

[319] P. L. de Andres, P. M. Echenique, D. Niesner, T. Fauster, and A. Rivacoba, „One-dimensional potential for image-potential states on graphene“, *New Journal of Physics*, vol. 16, no. 2, p. 023 012, 2014 (cit. on p. 114).

[320] M. Ghaznavi, Z. L. Mišković, and F. O. Goodman, „Nonlinear screening of external charge by doped graphene“, *Phys. Rev. B*, vol. 81, p. 085 416, 8 2010 (cit. on p. 114).

[321] G. V. Wolf and Y. P. Chuburin, „Fano resonances in low-energy electron transmission through crystalline films“, *Journal of Physics: Condensed Matter*, vol. 21, no. 18, p. 185 007, 2009 (cit. on p. 119).

[322] G. V. Wolf and Y. P. Chuburin, „Lifetime of resonance states of the continuous electronic spectrum of a quantum-well Cu(001) film“, *Physics of the Solid State*, vol. 53, no. 7, pp. 1499–1503, 2011 (cit. on p. 119).

[323] V. U. Nazarov, E. E. Krasovskii, and V. M. Silkin, „Scattering resonances in two-dimensional crystals with application to graphene“, *Physical Review B*, vol. 87, no. 4, p. 041 405, 2013 (cit. on pp. 119, 120).

[324] U. Fano, „Effects of Configuration Interaction on Intensities and Phase Shifts“, *Phys. Rev.*, vol. 124, pp. 1866–1878, 6 1961 (cit. on p. 119).

[325] A. R. P. Rau, „Perspectives on the Fano Resonance Formula“, *Physica Scripta*, vol. 69, no. 1, pp. C10–C13, 2004 (cit. on p. 119).

[326] E. Tamura and R. Feder, „Three-dimensional surface potential barrier in electron-solid scattering: Theory and application to W(001)“, *Solid State Communications*, vol. 58, no. 10, pp. 729–733, 1986 (cit. on pp. 121, 132).

[327] R. A. Krakowski and D. R. Olander, „Dissociation of Hydrogen on Tantalum Using a Modulated Molecular Beam Technique“, *The Journal of Chemical Physics*, vol. 49, no. 11, pp. 5027–5041, 1968 (cit. on p. 123).

[328] D. Niesner and T. Fauster, „Image-potential states and work function of graphene“, *Journal of Physics: Condensed Matter*, vol. 26, no. 39, p. 393 001, 2014 (cit. on p. 130).

[329] A. Tamtögl, E. Bahn, J. Zhu, P. Fouquet, J. Ellis, and W. Allison, „Graphene on Ni(111): Electronic Corrugation and Dynamics from Helium Atom Scattering“, *J. Phys. Chem. C*, vol. 119, no. 46, pp. 25 983–25 990, 2015 (cit. on p. 131).

[330] E. Bahn, A. Tamtögl, J. Ellis, W. Allison, and P. Fouquet, „Structure and dynamics investigations of a partially hydrogenated graphene/Ni(111) surface“, *Carbon*, vol. 114, pp. 504–510, 2017 (cit. on p. 131).

[331] H. Itoh, T. Ichinose, C. Oshima, T. Ichinokawa, and T. Aizawa, „Scanning tunneling microscopy of monolayer graphite epitaxially grown on a TiC(111) surface“, *Surface Science Letters*, vol. 254, no. 1, pp. L437–L442, 1991 (cit. on p. 131).

[332] J. Knudsen, P. J. Feibelman, T. Gerber, E. Grånäs, K. Schulte, P. Stratmann, J. N. Andersen, and T. Michely, „Clusters binding to the graphene moiré on Ir(111): X-ray photoemission compared to density functional calculations“, *Phys. Rev. B*, vol. 85, p. 035 407, 3 2012 (cit. on p. 132).

[333] T. Gerber, E. Granas, U. A. Schroder, P. Stratmann, K. Schulte, J. N. Andersen, J. Knudsen, and T. Michely, „Stability and Reactivity of Graphene-Templated Nanoclusters“, *The Journal of Physical Chemistry C*, vol. 120, no. 46, pp. 26 290–26 299, 2016 (cit. on p. 132).

[334] A. Cavallin, M. Pozzo, C. Africh, A. Baraldi, E. Vesselli, C. Dri, G. Comelli, R. Larciprete, P. Lacovig, S. Lizzit, and D. Alfè, „Local Electronic Structure and Density of Edge and Facet Atoms at Rh Nanoclusters Self-Assembled on a Graphene Template", *ACS Nano*, vol. 6, no. 4, pp. 3034–3043, 2012 (cit. on p. 132).

[335] P. J. Feibelman, „Pinning of graphene to Ir(111) by flat Ir dots", *Phys. Rev. B*, vol. 77, p. 165 419, 16 2008 (cit. on p. 132).

[336] K. Jochmann and T. M. Bernhardt, „The influence of metal cluster lattices on the screening of image potential state electrons on graphene", *The Journal of Chemical Physics*, vol. 149, no. 16, p. 164 706, 2018 (cit. on p. 133).

[337] J. H. Jørgensen, A. G. Čabo, R. Balog, L. Kyhl, M. N. Groves, A. M. Cassidy, A. Bruix, M. Bianchi, M. Dendzik, M. A. Arman, L. Lammich, J. I. Pascual, J. Knudsen, B. Hammer, P. Hofmann, and L. Hornekaer, „Symmetry-Driven Band Gap Engineering in Hydrogen Functionalized Graphene", *ACS Nano*, vol. 10, no. 12, pp. 10 798–10 807, 2016 (cit. on p. 134).

[338] A. L. Jørgensen, D. A. Duncan, C. F. P. Kastorp, L. Kyhl, Z. Tang, A. Bruix, M. Andersen, B. Hammer, T.-L. Lee, L. Hornekær, and R. Balog, „Chemically-resolved determination of hydrogenated graphene–substrate interaction", *Physical Chemistry Chemical Physics*, vol. 21, pp. 13 462–13 466, 25 2019 (cit. on p. 134).

[339] B. R. Matis, J. S. Burgess, F. A. Bulat, A. L. Friedman, B. H. Houston, and J. W. Baldwin, „Surface doping and band gap tunability in hydrogenated graphene", *ACS nano*, vol. 6, no. 1, pp. 17–22, 2012 (cit. on p. 134).

[340] S. Lebègue, M. Klintenberg, O. Eriksson, and M. I. Katsnelson, „Accurate electronic band gap of pure and functionalized graphane from GW calculations", *Phys. Rev. B*, vol. 79, p. 245 117, 24 2009 (cit. on p. 134).

[341] D. C. Elias, R. R. Nair, T. M. G. Mohiuddin, S. V. Morozov, P. Blake, M. P. Halsall, A. C. Ferrari, D. W. Boukhvalov, M. I. Katsnelson, A. K. Geim, and K. S. Novoselov, „Control of Graphene's Properties by Reversible Hydrogenation: Evidence for Graphane", *Science*, vol. 323, no. 5914, pp. 610–613, 2009 (cit. on p. 137).

[342] R. Balog, M. Andersen, B. Jørgensen, Z. Sljivancanin, B. Hammer, A. Baraldi, R. Larciprete, P. Hofmann, L. Hornekær, and S. Lizzit, „Controlling hydrogenation of graphene on Ir (111)", *ACS nano*, vol. 7, no. 5, pp. 3823–3832, 2013 (cit. on p. 137).

[343] M. Krivenkov, D. Marchenko, J. Sánchez-Barriga, O. Rader, and A. Varykhalov, „Suppression of electron scattering resonances in graphene by quantum dots", *Applied Physics Letters*, vol. 111, no. 16, p. 161 605, 2017 (cit. on p. 138).

This page was intentionally left empty.

Publications related to this thesis

[1] M. Krivenkov, D. Marchenko, E. Golias, J. Sánchez-Barriga, O. Rader, and A. Varykhalov, „Origin of the band gap in Bi-intercalated graphene on Ir(111)“, *2D Materials (under review)*, 2020.

[2] M. Krivenkov, E. Golias, D. Marchenko, J. Sánchez-Barriga, G. Bihlmayer, O. Rader, and A. Varykhalov, „Nanostructural origin of giant Rashba effect in intercalated graphene“, *2D Materials*, vol. 4, no. 3, p. 035 010, 2017.

[3] M. Krivenkov, D. Marchenko, J. Sánchez-Barriga, O. Rader, and A. Varykhalov, „Suppression of electron scattering resonances in graphene by quantum dots“, *Applied Physics Letters*, vol. 111, no. 16, p. 161 605, 2017.

Other publications

[4] M. Sajedi, M. Krivenkov, D. Marchenko, A. Varykhalov, J. Sánchez-Barriga, E. D. L. Rienks, and O. Rader, „Is there a giant Rashba effect in the valence band of lead halide perovskites?“, *Physical Review Letters (submitted)*, 2020.

[5] I. Klimovskikh, M. Krivenkov, A. Varykhalov, D. Estyunin, and A. Shikin, „Reconstructed Fermi surface in graphene on Ir(111) by Gd-Ir surface alloying“, *Carbon*, vol. 147, pp. 182–186, 2019.

[6] L. M. Schoop, A. Topp, J. Lippmann, F. Orlandi, L. Müchler, M. G. Vergniory, Y. Sun, A. W. Rost, V. Duppel, M. Krivenkov, S. Sheoran, P. Manuel, A. Varykhalov, B. Yan, R. K. Kremer, C. R. Ast, and B. V. Lotsch, „Tunable Weyl and Dirac states in the nonsymmorphic compound CeSbTe“, *Science Advances*, vol. 4, no. 2, 2018.

[7] J. J. Frick, A. Topp, S. Klemenz, M. Krivenkov, A. Varykhalov, C. R. Ast, A. B. Bocarsly, and L. M. Schoop, „Single-Crystal Growth and Characterization of the Chalcopyrite Semiconductor CuInTe2 for Photoelectrochemical Solar Fuel Production“, *The Journal of Physical Chemistry Letters*, vol. 9, no. 23, pp. 6833–6840, 2018.

[8] H.-C. Mertins, C. Jansing, M. Krivenkov, A. Varykhalov, O. Rader, H. Wahab, H. Timmers, A. Gaupp, A. Sokolov, M. Tesch, and P. M. Oppeneer, „Giant magneto-optical Faraday effect of graphene on Co in the soft x-ray range“, *Physical Review B*, vol. 98, no. 6, p. 064 408, 2018.

[9] E. Golias, M. Krivenkov, A. Varykhalov, J. Sánchez-Barriga, and O. Rader, „Band Renormalization of Blue Phosphorus on Au(111)“, *Nano Letters*, vol. 18, no. 11, pp. 6672–6678, 2018, PMID: 30281315.

[10] E. Y. Kataev, D. Y. Usachov, A. S. Frolov, A. A. Rulev, A. A. Volykhov, A. Y. Kozmenkova, M. Krivenkov, D. Marchenko, A. Varykhalov, M. V. Kuznetsov, *et al.*, „Native and graphene-coated flat and stepped surfaces of TiC“, *Carbon*, vol. 132, pp. 656–666, 2018.

[11] L. M. Schoop, A. Topp, J. Lippmann, F. Orlandi, L. Müchler, M. G. Vergniory, Y. Sun, A. W. Rost, V. Duppel, M. Krivenkov, *et al.*, „Tunable Weyl and Dirac states in the nonsymmorphic compound CeSbTe“, *Science Advances*, vol. 4, no. 2, eaar2317, 2018.

[12] H.-C. Mertins, C. Jansing, M. Gilbert, M. Krivenkov, J. Sánchez-Barriga, A. Varykhalov, O. Rader, H. Wahab, H. Timmers, A. Gaupp, *et al.*, „Magneto-optical reflection spectroscopy on graphene/Co in the soft x-ray range“, in *Journal of Physics: Conference Series*, IOP Publishing, vol. 903, 2017, p. 012 025.

[13] J. Sánchez-Barriga, M. Battiato, M. Krivenkov, E. Golias, A. Varykhalov, A. Romualdi, L. Yashina, J. Minár, O. Kornilov, H. Ebert, *et al.*, „Subpicosecond spin dynamics of excited states in the topological insulator $\mathrm{Bi_2Te_3}$“, *Physical Review B*, vol. 95, no. 12, p. 125 405, 2017.

[14] I. Shvets, I. Klimovskikh, Z. Aliev, M. Babanly, J. Sánchez-Barriga, M. Krivenkov, A. Shikin, and E. Chulkov, „Impact of stoichiometry and disorder on the electronic structure of the $\mathrm{PbBi_2Te}_{4-x}\mathrm{Se}_x$ topological insulator“, *Physical Review B*, vol. 96, no. 23, p. 235 124, 2017.

[15] A. Topp, M. G. Vergniory, M. Krivenkov, A. Varykhalov, F. Rodolakis, J. L. McChesney, B. V. Lotsch, C. R. Ast, and L. M. Schoop, „The effect of spin-orbit coupling on nonsymmorphic square-net compounds“, *Journal of Physics and Chemistry of Solids*, 2017.

[16] A. Topp, R. Queiroz, A. Grüneis, L. Müchler, A. W. Rost, A. Varykhalov, D. Marchenko, M. Krivenkov, F. Rodolakis, J. L. McChesney, *et al.*, „Surface floating 2D bands in layered nonsymmorphic semimetals: ZrSiS and related compounds“, *Physical Review X*, vol. 7, no. 4, p. 041 073, 2017.

[17] C. Jansing, H.-C. Mertins, M. Gilbert, H. Wahab, H. Timmers, S.-H. Choi, A. Gaupp, M. Krivenkov, A. Varykhalov, O. Rader, *et al.*, „X-ray natural birefringence in reflection from graphene“, *Physical Review B*, vol. 94, no. 4, p. 045 422, 2016.

[18] D. Kutnyakhov, S. Chernov, K. Medjanik, R. Wallauer, C. Tusche, M. Ellguth, S. Nepijko, M. Krivenkov, J. Braun, S. Borek, *et al.*, „Spin texture of time-reversal symmetry invariant surface states on W(110)“, *Scientific reports*, vol. 6, p. 29 394, 2016.

[21] L. Müchler, A. Topp, R. Queiroz, M. Krivenkov, A. Varykhalov, J. Cano, C. R. Ast, and L. M. Schoop, „Modular Arithmetic with Nodal Lines: Drumhead Surface States in ZrSiTe", *Physical Review X*, vol. 10, p. 011 026, 1 2020.

[22] A. Varykhalov, F. Freyse, I. Aguilera, M. Battiato, M. Krivenkov, D. Marchenko, G. Bihlmayer, S. Blügel, O. Rader, and J. Sánchez-Barriga, „Effective mass enhancement and ultrafast electron dynamics of Au(111) surface state coupled to a quantum well", *Phys. Rev. Research*, vol. 2, p. 013 343, 1 2020.

[23] J. R. Chamorro, A. Topp, Y. Fang, M. J. Winiarski, C. R. Ast, M. Krivenkov, A. Varykhalov, B. J. Ramshaw, L. M. Schoop, and T. M. McQueen, „Dirac fermions and possible weak antilocalization in LaCuSb2", *APL Materials*, vol. 7, no. 12, p. 121 108, 2019.

[24] I. A. Shvets, I. I. Klimovskikh, Z. S. Aliev, M. B. Babanly, F. J. Zúñiga, J. Sánchez-Barriga, M. Krivenkov, A. M. Shikin, and E. V. Chulkov, „Surface electronic structure of the wide band gap topological insulator $PbBi_4Te_4Se_3$", *Phys. Rev. B*, vol. 100, p. 195 127, 19 2019.

Summary

The current thesis is focused on the properties of graphene supported by metallic substrates and specifically on the behaviour of electrons in such systems. Methods of scanning tunneling microscopy, electron diffraction and photoemission spectroscopy were applied to study the structural and electronic properties of graphene. The purpose of the first part of this work is to introduce the most relevant aspects of graphene physics and the methodical background of experimental techniques used in the current thesis.

The scientific part of this work starts with the extensive study by means of scanning tunneling microscopy of the nanostructures that appear in Au intercalated graphene on Ni(111). This study was aimed to explore the possible structural explanations of the Rashba-type spin splitting of ~ 100 meV experimentally observed in this system — much larger than predicted by theory. It was demonstrated that gold can be intercalated under graphene not only as a dense monolayer, but also in the form of well-periodic arrays of nanoclusters, a structure previously not reported. Such nanocluster arrays are able to decouple graphene from the strongly interacting Ni substrate and render it quasi-free-standing, as demonstrated by our DFT study. At the same time calculations confirm strong enhancement of the proximity-induced SOI in graphene supported by such nanoclusters in comparison to monolayer gold. This effect, attributed to the reduced graphene-Au distance in the case of clusters, provides a large Rashba-type spin splitting of ~ 60 meV.

The obtained results not only provide a possible mechanism of SOI enhancement in this particular system, but they can be also generalized for graphene on other strongly interacting substrates intercalated by nanostructures of heavy noble d metals.

Even more intriguing is the proximity of graphene to heavy *sp*-metals that were predicted to induce an *intrinsic* SOI and realize a spin Hall effect in graphene. Bismuth is the heaviest stable *sp*-metal and its compounds demonstrate a plethora of exciting physical phenomena. This was the motivation behind the next part of the current thesis, where structural and electronic properties of a previously unreported phase of Bi-intercalated graphene on Ir(111) were studied by means of scanning tunneling microscopy, spin- and angle-resolved photoemission spectroscopy and electron diffraction. Photoemission experiments revealed a remarkable, nearly ideal graphene band structure with strongly suppressed signatures of interaction between graphene and the Ir(111) substrate, moreover, the characteristic moiré pattern observed in graphene on Ir(111) by electron diffraction and scanning tunneling microscopy was strongly suppressed after intercalation. The whole set of experimental data evidences that Bi forms a dense intercalated layer that efficiently decouples graphene from the substrate. The interaction manifests itself only in the n-type charge doping (~ 0.4 eV) and a relatively small band gap at the Dirac point (~ 190 meV). The origin of this minor band gap is quite intriguing and in this work it was possible to exclude a wide range of mechanisms that could be responsible for it, such as induced intrinsic spin-orbit interaction, hybridization with the substrate states and corrugation of the graphene lattice. The main origin of the band gap was attributed to the A-B symmetry breaking and this conclusion found support in the careful analysis of the interference effects in photoemission that provided the band gap estimate of ~ 140 meV.

While the previous chapters were focused on adjusting the properties of graphene by proximity to heavy metals, graphene on its own is a great object to study various physical effects at crystal surfaces. The final part of this work is devoted to a study of surface scattering resonances by means of photoemission spectroscopy, where this effect manifests itself as a distinct modulation of photoemission intensity. Though scattering resonances were widely studied in the past by means of electron diffraction, studies about their observation in photoemission experiments started to appear only recently and they are very scarce.

For a comprehensive study of scattering resonances graphene was selected as a versatile model system with adjustable properties. After the theoretical and historical introduction to the topic of scattering resonances follows a detailed description of the unusual features observed in the photoemission spectra obtained in this work and finally the equivalence between these features and scattering resonances is proven. The obtained photoemission results are in a good qualitative agreement with the existing theory, as verified by our calculations in the framework of the interference model. This simple model gives a suitable explanation for the general experimental observations.

The possibilities of engineering the scattering resonances were also explored. A systematic study of graphene on a wide range of substrates revealed that the energy position of the resonances is in a direct relation to the magnitude of charge transfer between graphene and the substrate. Moreover, it was demonstrated that the scattering resonances in graphene on Ir(111) can be *suppressed* by nanopatterning either by a superlattice of Ir nanoclusters or by atomic hydrogen. These effects were attributed to strong local variations of work function and/or destruction of long-range order of the graphene lattice. The tunability of scattering resonances can be applied for optoelectronic devices based on graphene. Moreover, the results of this study expand the general understanding of the phenomenon of scattering resonances and are applicable to many other materials besides graphene.

Zusammenfassung

Die vorliegende Arbeit beschäftigt sich mit den Eigenschaften von Graphen auf metallischen Substraten und speziell mit dem Verhalten von Elektronen in solchen Systemen. Methoden der Rastertunnelmikroskopie, Elektronenbeugung und Photoemissionsspektroskopie wurden angewendet, um die strukturellen und elektronischen Eigenschaften von Graphen zu untersuchen. Ziel des ersten Teils dieser Arbeit ist es, die wichtigsten Aspekte der Graphenphysik und den methodischen Hintergrund der in der vorliegenden Arbeit verwendeten experimentellen Techniken vorzustellen.

Der wissenschaftliche Teil dieser Arbeit beginnt mit der umfassenden Untersuchung von Nanostrukturen, die in Au-interkaliertem Graphen auf Ni(111) auftreten, mittels Rastertunnelmikroskopie. Diese Studie zielte darauf ab, die möglichen strukturellen Erklärungen der experimentell in diesem System beobachteten Rashba-Spin-Aufspaltung von $\sim$ 100 meV zu untersuchen — die viel größer als theoretisch vorhergesagt ist.

Es wurde gezeigt, dass Gold unter Graphen nicht nur als dichte Monolage interkaliert werden kann, sondern auch in Form von exakt periodischen Anordnungen von Nanoclustern, einer Struktur, die bisher nicht beschrieben wurde. Solche Nanocluster-Arrays können Graphen von dem stark wechselwirkenden Ni-Substrat entkoppeln und es quasi freistehend machen, wie unsere Dichtefunktionaltheorie-Studie zeigt. Gleichzeitig bestätigen die Dichtefunktionaltheorie-Rechnungen eine starke Erhöhung der durch Proximity induzierten Spin-Bahn-Wechselwirkung in Graphen durch solche Nanocluster im Vergleich zu einer homogenen Gold-Monolage. Dieser Effekt, der im Falle von Clustern auf den verringerten Graphen-Au-Abstand zurückgeführt wird, liefert eine große Spinaufspaltung vom Rashba-Typ von $\sim$ 60 meV.

Die erhaltenen Ergebnisse liefern nicht nur einen möglichen Mechanismus zur Erhöhung der Spin-Bahn-Wechselwirkung in diesem speziellen System, sondern können auch auf Graphen auf anderen stark wechselwirkenden Substraten verallgemeinert werden, die mit Nanostrukturen von schweren Edelmetallen interkaliert sind.

Noch faszinierender ist die Nähe von Graphen zu schweren *sp*-Metallen, von denen vorhergesagt wurde, dass sie einen intrinsischen Spin-Bahn-Wechselwirkung induzieren und einen Spin-Hall-Effekt in Graphen realisieren. Wismut ist das schwerste stabile *sp*-Metall und seine Verbindungen zeigen eine Vielzahl aufregender physikalischer Phänomene. Dies war die Motivation für den nächsten Teil der vorliegenden Arbeit, in dem strukturelle und elektronische Eigenschaften einer bisher nicht beschriebenen Phase von Bismuth-interkaliertem Graphen auf Ir(111) mittels Rastertunnelmikroskopie, spin-

und winkelaufgelöster Photoemissionsspektroskopie und Elektronenbeugung untersucht. Photoemissionsexperimente ergaben eine bemerkenswerte, nahezu ideale Graphenbandstruktur mit stark unterdrückten Wechselwirkungssignaturen zwischen Graphen und dem Ir(111)-Substrat. Außerdem wird das charakteristische Moiré-Muster, das für Graphen auf Ir(111) mit Elektronenbeugung und Rastertunnelmikroskopie beobachtet wurde, nach der Interkalation stark unterdrückt. Die gesamten experimentellen Daten belegen, dass Bi eine dichte interkalierte Schicht bildet, die Graphen effizient vom Substrat entkoppelt. Die Wechselwirkung manifestiert sich nur in der Ladungsdotierung vom n-Typ ($\sim 0,4$ eV) und einer relativ kleinen Bandlücke am Dirac-Punkt (~ 190 meV). Den Ursprung dieser kleinen Bandlücke zu ermitteln ist sehr komplex, und in dieser Arbeit konnten eine Vielzahl von Mechanismen ausgeschlossen werden, die dafür verantwortlich sein könnten, wie etwa induzierte intrinsische Spin-Bahn-Wechselwirkung, Hybridisierung mit den Substratzuständen und Riffelung des Graphen-Gitters. Der Hauptursprung der Bandlücke wurde einem Bruch der A-B-Symmetrie zugeschrieben, und diese Schlussfolgerung stützte sich auf eine eingehende Analyse der Interferenzeffekte bei der Photoemission, die eine Abschätzung der Bandlücke von ~ 140 meV lieferte.

Während sich die vorherigen Kapitel auf die Anpassung der Eigenschaften von Graphen durch die Nähe zu Schwermetallen konzentrierten, ist Graphen allein ein großartiges Objekt, um verschiedene physikalische Effekte an Kristalloberflächen zu untersuchen. Der letzte Teil dieser Arbeit befasst sich mit der Untersuchung von Oberflächenstreuresonanzen mittels Photoemissionsspektroskopie, wobei sich dieser Effekt in einer deutlichen Modulation der Photoemissionsintensität manifestiert. Obwohl Streuresonanzen in der Vergangenheit häufig mittels Elektronenbeugung untersucht wurden, erschienen einige wenige Studien über ihre Beobachtung in Photoemissionsexperimenten erst vor kurzem.

Für eine umfassende Untersuchung der Streuresonanzen wurde Graphen als vielseitiges Modellsystem mit einstellbaren Eigenschaften ausgewählt. Nach der theoretischen und historischen Einführung in das Thema Streuresonanzen folgt eine detaillierte Beschreibung der ungewöhnlichen Merkmale, die in den in dieser Arbeit erhaltenen Photoemissionsspektren beobachtet wurden, und schließlich wird die Äquivalenz zwischen diesen Merkmalen und Streuresonanzen bewiesen. Die erhaltenen Photoemissionsergebnisse stimmen qualitativ gut mit der bestehenden Theorie überein, wie unsere Berechnungen im Rahmen des Interferenzmodells belegen. Dieses einfache Modell liefert eine geeignete Erklärung für die gesamtheit der experimentellen Beobachtungen.

Möglichkeiten, die Streuresonanzen zu modifizieren wurden ebenfalls untersucht. Eine systematische Untersuchung von Graphen auf einer Vielzahl von Substraten ergab, dass die Energieposition der Resonanzen in direktem Zusammenhang mit der Größe des Ladungstransfers zwischen Graphen und Substrat steht. Darüber hinaus wurde gezeigt, dass die Streuresonanzen in Graphen auf Ir(111) durch Nanostrukturierung entweder durch ein Übergitter von Ir-Nanoclustern oder durch atomaren Wasserstoff *unterdrückt* werden können. Diese Effekte wurden auf starke lokale Variationen der Austrittsarbeit und/oder die Zerstörung der langreichweitigen Ordnung des Graphengitters. Die Abstimmbarkeit von Streuresonanzen kann für optoelektronische Bauelemente auf der Basis von Graphen verwendet werden. Darüber hinaus erweitern die Ergebnisse dieser Studie das allgemeine Verständnis des Phänomens der Streuresonanzen und sind neben Graphen auch auf viele andere Materialien anwendbar.

Page 175 (Curriculum Vitae) contains personal data.
Hence, it is not part of this online publication.

Declaration

I herewith declare that I have produced this paper without the prohibited assistance of third parties and without making use of aids other than those specified; notions taken over directly or indirectly from other sources have been identified as such. This paper has not previously been presented in identical or similar form to any other German or foreign examination board.

The thesis work was conducted from 2015 to 2020 under the supervision of apl. Prof. Dr. Oliver Rader at Helmholtz-Zentrum Berlin für Materialien und Energie and Mathematisch-Naturwissenschaftlichen Fakultät der Universität Potsdam.

Berlin, 2020